# Extracting physics from fixed topology simulations

DISSERTATION
zur Erlangung des Doktorgrades
der Naturwissenschaften

vorgelegt beim Fachbereich Physik der
Goethe-Universität Frankfurt
in Frankfurt am Main

von
Arthur Dromard
aus Bayeux, Frankreich

Frankfurt am Main, July 2016

vom Fachbereich Physik der

Goethe Universität Frankfurt

als Dissertation angenommen.

Dekan: Prof. Dr. Rene Reifarth

Gutachter: Prof. Dr. Marc Wagner
Prof. Dr. Wolfgang Bietenholz

Datum der Disputation: 27 October 2016

*To Sandra, who endured an absent-minded companion working on weird subjects*

# Contents

# Deutsche Zusammenfassung

Das Standardmodell ist eine der größten Errungenschaften der modernen theoretischen Physik. Es beschreibt die Physik der Elementarteilchen mit Hilfe von drei Kräften. Dabei handelt es sich um die Elektrodynamik, die schwache und die starke Wechselwirkung. Während die Elektrodynamik sowie die schwache Wechselwirkung bereits verstanden sind, ist dies nicht der Fall für die starke Wechselwirkung. Ebenso fundamental wie die beiden anderen Kräfte, ist die starke Wechselwirkung verantwortlich für die Entstehung aller Hadronen, welche in Mesonen und Baryonen klassifiziert werden. Ein sehr bekanntes Beispiel für erstere ist das Pion und für letztere das Proton sowie das Neutron, aus welchen der Kern eines jeden Atoms besteht. Diese fundamentale Kraft scheint durch eine Theorie namens Quantenchromodynamik (QCD) beschrieben werden zu können. Dieser Theorie zur Folge, handelt es sich bei Hadronen nicht um elementare Teilchen, sondern um Objekte, die aus Quarks und Gluonen zusammengesetzt sind. Letztere sind die Vektorteilchen der Kraft, das heisst es handelt sich um Bosonen mit Spin 1. Bei den Quarks, welche die Materie-Bestandteile darstellen, handelt es sich um Fermionen mit Spin 1/2. Die Beschreibung der Wechselwirkung erforderte das Einführen einer neuen Quantenzahl, die sogenannte Farbladung, welche in drei verschiedenen Ausführung existiert, blau, grün und rot. Die Namenswahl ist wohlgemerkt kein Zufall. Beispielsweise sind Objekte, welche aus drei Quarks zusammengesetzt sind, stets farbneutral, in der gleichen Art und Weise wie das Mischen der drei Primärfarben weiss ergibt. Hingegen konnten Zustände mit einer bestimmten Farbe experimentell nicht nachgewiesen werden. Quarks und Gluonen scheinen in farbneutralen, hadronischen Zuständen begrenzt zu sein. Diese Eigenschaft der QCD wird mit dem Begriff Confinement bezeichnet und resultiert aus der starken Kopplung bei niedriger Energie oder großer Distanz. Hingegen ist die Kopplungskonstante der QCD für große Energien (bzw. kleine Distanzen) klein, das heisst, dass Quarks und Gluonen kaum wechselwirken und nahezu frei sind, wodurch eine störungstheoretische Behandlung der QCD möglich wird. Diese Eigenschaft bezeichnet man auch als asymptotische Freiheit. Die Möglichkeit der QCD beide Verhaltensweisen zu beschreiben, ist eine ihrer herausragendsten Eigenschaften. Wie dem auch sei, ist bislang keines der beiden Phänomene ausreichend erforscht. Benötigt wird somit eine Methode, mit welcher man das Regime untersuchen kann, in dem störungstheoretische Behandlung möglich ist, als auch jenes, das vom sog. Confinement bestimmt wird.

Die einzige bekannte Methode, welche die Kriterien erfüllt, um eine solche Untersuchung zu ermöglichen, ist die sog. Gitter QCD, bzw. im allgemeinen Gittereichtheorie. Dabei wird die Theorie diskretisiert und auf einem vier dimensionalen euklidischen Raum-Zeit Gitter formuliert. Auf diese Weise ist die Theorie auf natürliche Weise regularisiert und mathematisch wohl definiert. Auf der anderen Seite erlaubt der sog. Pfadintegral-Formalismus die Behandlung der Theorie als ein System der statistischen Mechanik, welches beispielsweise durch einen eine Markov Kette erzeugenden Monte Carlo Algorithmus berechnet werden kann. Diese Vorgehensweise wurde erstmals von Wilson in 1974 [1] vorgeschlagen. Kurz darauf führte Creutz die ersten numerischen Simulationen der Yang-Mills Theorie [2] mit einem sog. heat-bath Monte Carlo Algorithmus aus.

Dabei stellte sich heraus, dass diese Methodik extrem rechenintensiv ist. In ihren Anfängen wurde die Methode stark kritisiert, da mit ihr nicht physikalische Parameter simuliert wurden, wie etwa eine extrem hohe Pionmasse, große Gitterabstände $a$ sowie keine dynamischen Quarks. Mit dem Fortschreiten der Computer Technologie und der Erfindung Super-Computer wurden die Simulationen jedoch realistischer und kamen den physikalischen Parametern näher. Nichtsdestotrotz musste man noch immer die Probleme der diskretisierten und endlichen Raum-Zeit bewältigen. Verschiedene Techniken wurde entwickelt, um den Kontinuums-Limes sowie den Limes unendlichen Volumens abzuschätzen bzw. zu extrapolieren. Dabei gilt, je kleiner der Gitterabstand und je größer die Gitter Ausdehnung, desto besser funktioniert die Extrapolation in die genannten Limite.

Die Simulationen sind bis heute noch sehr kostspielig und zur Zeit stellen Ausdehnungen von $L \approx 4$fm und $a = 0.08$ fm typische physikalische Gitterausdehnungen dar. Wie dem auch sei, wurde durch die Simulationen von reiner Yang-Mills Theorie und anderer niedriger dimensionaler Modelle beobachtet, dass die Topologie bei kleinem Gitterabstand $a$ einfriert [3]. Dies wurde auch kürzlich in Simulationen voller QCD festgestellt [4, 5]. Der typische Gitterabstand, ab welchem das Problem in Erscheinung tritt, ist $a \approx 0.05$ fm. Dieser Wert hängt jedoch auch von der simulierten Quarkmasse sowie dem verwendeten Algorithmus ab. Das Einfrieren der Topologie führt zu Ergebnissen, die sich von den physikalischen Ergebnissen unterscheiden, wodurch die Vorhersagen der Gitter QCD ihre Bedeutung verlieren. Eine Lösung für dieses Problem zu finden ist eine der größten Aufgabe für die Zukunft der Gitter QCD [6]. In jüngerer Vergangenheit wurden zur Behandlung des Problems verschiedene Methoden vorgeschlagen. Eine der bekanntesten dieser Methoden ist die Verwendung offener Randbedingungen [7], was jedoch gewisse Probleme birgt, wie etwa die Brechung der Translationsinvarianz. Ein weiterer Vorschlag basiert auf einer Gleichung von Brower, Chandrasekharan, Negele und Wiese (BCNW) in [8]. Diese Gleichung verknüpft den physikalischen Wert von Massen oder Observablen mit deren Gegenstücken bei eingefrorener Topologie.

Das hauptsächliche Ziel dieser Arbeit war es, eine weitestgehend vollständige Untersuchung dieser Möglichkeit für QCD vorzunehmen, um herauszufinden, ob die Methode praktikabel ist und effizient für Gitter Simulationen verwendet werden kann. Diese Studie eröffnete ebenfalls die Möglichkeit entscheidende Kriterien für die Anwendung sowie die Grenzen der Methode zu finden. Insbesondere legten wir den Fokus bei den Tests darauf, Teilchenmassen sowie die topologische Ladung zu extrahieren.

Zunächst untersuchten wir die Methode theoretisch. Eine sorgfältige Untersuchung der erzielten Näherungen zur Berechnung der Formel, ermöglichte die Identifizierung von vier Kriterien ((**C1**),(**C2**),(**C3**) und (**C4**)) zur Bestimmung der Masse. Dabei beschränkt **(C1)** die mögliche räumliche Reichweite, für welche die Methode gültig ist, sowie die topologischen Sektoren. Das Kriterium **(C2)** bestimmt den maximalen Zeit Wert für die Bestimmung der Masse. **(C3)** ist ein Maß für die Möglichkeit die gewöhnlichen auftretenden Effekte endlicher Größe zu vernachlässigen, unter Vorgabe einer minimalen räumlichen Ausdehnung. **(C4)** liefert eine Beschränkung durch einen minimalen Zeit Wert, welcher der Vermeidung der Kontamination der Resultate durch angeregte Zustände dient.

Der zweite Schritt bestand darin, die Formel bis zur dritten Ordnung in 1/V zu entwickeln, um eine höhere Präzision zu erzielen oder um Fehler abzuschätzen, für den Fall das eine niedrigere Ordnung der Gleichung verwendet wird. Darüber hinaus untersuchten wir die Konsequenzen der Paritätsbrechung aufgrund fixierter Topologie bei Korrelatoren von Paritätspartnern. Insbesondere haben wir gezeigt, dass eine Fixierung der Topologie zu $1/V$ Korrekturen bei Größen führt, die einen leichteren Paritätspartner besitzen. In diesem Fall muss eine Matrix anstelle eines einzelnen Korrelators gefittet werden.

Der darauffolgende Schritt bestand darin, eine Reihe von Tests mit verschiedenen Modellen durchzuführen.

Die Tests wurden zunächst für das O(2)-Modell mit einem Kasten-Potential ausgeführt. Dabei handelte es sich jedoch nicht um eine Simulation, sondern um eine direkte Berechnung mit beliebiger Präzision. Dies erlaubte uns eine exakte Untersuchung aller Parameter sowie die Konsequenzen der Missachtung der aufgeführten Kriterien. Es war uns weiterhin möglich die Entwicklung der BCNW-Relation bis zur dritten Ordnung zu testen und die mit der höheren Entwicklung einhergehenden Verbesserungen aufzuzeigen. Anschließend nahmen wir Tests an QCD ähnlicheren Modellen, darunter eines mit Fermionen und Confinement, vor, um das zugrunde liegende Probleme zu studieren. Dabei handelte es sich um das Schwinger-Modell sowie um ein Modell in vier Dimensionen, reine Yang-Mills Theorie. Bei diesen Tests war jedoch die Statistik nicht ausreichend, um die Auswirkungen der Verbesserungen der BCNW-Relation nachzuweisen. Wie dem auch sei, ist es uns gelungen die problematischen Kriterien zu identifizieren. Unter Betrachtung unserer Resultate schien es, dass die Bedingungen **(C2)** und **(C4)** einfach zu erfüllen sind. Im Gegensatz dazu bereitet **(C1)** Schwierigkeiten, sofern die Simulationen in hohen topologischen Sektoren gefangen ist. Dieser Fall tritt allerdings selten auf, da die topologische Ladung einer Gauss Verteilung unterliegt, aufgrund der die Wahrscheinlichkeit für hohe topologische Sektoren sehr gering ist. Es besteht auch die Möglichkeit, eine Wirkung zu verwenden, welche die Topologie fixiert und es somit erlaubt einen bestimmten topologischen Sektoren festzulegen, sodass die Bedingung **(C1)** dadurch respektiert wird. Die letzte Bedingung **(C3)** bezieht sich nicht speziell auf Simulationen bei fixierter Topologie, sondern auf gewöhnliche endliche Volumen Effekte. Für diese Art von Effekten existieren bereits Lösungen. Dieses Problem ist insbesondere bei sehr kostspieligen Simulationen von Bedeutung, wie etwa solche, die mit chiralen Fermionen durchgeführt werden. Diese stellen gleichzeitig die Fermion Spezies dar, für welche das Problem des Einfrierens der Topologie am schwerwiegendsten ist. Durch unsere Tests konnte diese Bedingung als die restriktivste identifiziert werden, insbesondere hinsichtlich der Anwendung der Methode auf QCD. Aus diesem Grund suchten wir erfolgreich nach einer Lösung um die Einschränkungen durch die **(C3)** Bedingung zu reduzieren. Unsere Lösung bestand darin, gewöhnliche endliche Volumen Effekte bei fixierter Topologie zu berechnen. Dies führte zu einer neuen Gleichung, die wir mit Erfolg an SU(2) und QCD testen konnten.

Wir erwähnten ebenfalls, die topologische Suszeptibilität bestimmen zu wollen, um zumindest herausfinden zu können, ob die Bedingung **(C1)** erfüllt ist. Das Verfahren zur Bestimmung der Masse sollte uns ebenfalls die Möglichkeit eröffnen, die topologische Suszeptibilität zu berechnen. Es stellte sich jedoch heraus, dass die der Suszeptibilität anhaftenden statistischen Fehler, die aus dieser Methode resultieren, sehr groß sind. Die Methode ist somit zur Bestimmung der topologischen Suszeptibilität nicht geeignet. Wir untersuchten daraufhin zwei verschiedene Methoden, welche den Vorteil besitzen, nur ein Volumen sowie einen topologischen Sektor benötigen.

Bei der ersten handelt es sich um die AFHO-Methode [11]. Sie basiert auf der BCNW-Relation, wodurch die gleichen Kriterien erfüllt werden müssen. Die Methode besteht darin, den topologischen Ladungsdichte Korrelator bei fixierter Topologie zu berechnen. Getestet wurde die Methode in SU(2) und in QCD. Die durchgeführten Tests ließen den Schluss zu, dass die Ergebnisse mit denen aus Simulationen bei nicht fixierter Topologie übereinstimmen und kleinere statistische Fehler besitzen, verglichen mit den Ergebnissen der Suszeptibilität bei Bestimmung durch die BCNW Gleichung.

Bei der zweiten getesteten Methode handelt es sich um die Slab Methode [12, 13]. Die Methode beruht auf Berechnungen in Unter-Volumina und unterliegt nicht den Bedingungen der ersten, BCNW basierten Methode. Die primäre Bedingung hierbei ist, dass der Wert der Kurtosis null oder zumindest klein genug ist, um vernachlässigbar zu sein. A priori lässt sich jeder topologische Sektor verwenden und es existieren keine Einschränkungen bezüglich des Volumens. Wir testeten die Methode an QCD Konfigurationen und bemerkten

einige Auffälligkeiten. Zunächst funktioniert die Methode nicht wie erwartet, da eine Konstante zur theoretichen Formel addiert werden muss. Darüber hinaus treten einige Abweichungen für kleine Unter-Volumina sowie für große topologische Sektoren mit $|Q| > 4$ auf. Diese Abweichungen wurden untersucht. Bezüglich der Konstante scheint ein Zusammenhang zum Glätten der Konfigurationen zu bestehen, während es sich bei den Abweichungen bezüglich der Unter-Volumina um gewöhnliche endliche Volumen-Effekte handelt, welche durch den "gradient flow" verstärkt werden. Unter Beachtung dieser Umstände ist es jedoch gelungen die topologische Suszeptibilität erfolgreich zu bestimmen. Das einzige bestehende Probleme ist die fehlende Erklärung zu diesen Abweichungen, auch wenn bereits einige Ideen dazu existieren.

Es kann geschlossen werden, dass die BCNW Methode effizient ist, um physikalische Ergebnisse aus fixierten Topologie Simulationen zu extrahieren. Die Anwendung kann in zwei Schritte unterteilt werden:

1. Zunächst müssen wir die topologische Suszeptibilität berechnen, um zu bestimmen, welche topologischen Sektoren die Bedingung **(C1)** erfüllen. Dafür können die AFHO sowie die Slab-Methode für mittlere Volumen verwendet werden. Im Falle der Verwendung der AFHO Methode muss anschließend überprüft werden, ob die Bedingung **(C1)** eingehalten wurde.
2. Im zweiten Schritt kann die BCNW Methode unter Beachtung der vier Bedingungen und unter Verwendung der im ersten Schritt berechneten topologischen Suszeptibilität angewandt werden.

Wir beenden die Zusammenfassung mit einigen Vorschlägen für nachfolgende Arbeiten. Diese können sich auf zwei Bereiche aufteilen. Der erste betrifft direkt die BCNW Methode während der zweite die Bestimmung der topologischen Suszeptibilität betrifft.

Bezüglich der BCNW Methode:

- Es sollten Tests für die QCD entwickelt werden, um ein drittes Volumen integrieren zu können (laufende Arbeit).
- Ein zweiter Test, welcher noch durchgeführt werden muss, ist die Extraktion der Masse zweier Paritätspartner.

Betreffend der topologischen Suszeptibilität:

- Ausstehend ist die Durchführung einer vollständigen Untersuchung der bei der AFHO Methode auftretenden gewöhnlichen endlichen Volumen Effekte.
- Weiterhin die Ausführung einer theoretischen Studie zu den Abweichungen der Slab Methode.

Zusammenfassend ist festzuhalten, dass die Ergebnisse dieser Arbeit beweisen, dass Simulationen bei fixierter oder eingefrorener Topologie unter Verwendung der BCNW Methode durchgeführt werden können. Insbesondere haben wir die Kriterien bestimmt, unter deren Einhaltung die Methode als gültig betrachtet werden kann und nahmen Verbesserung vor, welche zu einer großen Reichweite an Anwendungen führte. Es wurden

Untersuchungen sowie erfolgreiche Tests zu zwei Methoden zur Extraktion der topologischen Suszeptibilität vorgenommen. Wir glauben, dass die beschriebenen Methoden in den kommenden Jahren oft Anwendung finden werden.

# Introduction

The Standard Model is one of the greatest successes of modern theoretical physics. Itl describes the physics of elementary particles by means of three forces, the electro-magnetisc, the weak and the strong interactions. The electro-magnetic and the weak interaction are rather well understood in comparison to the strong interaction. The latest is as fundamental as the others, it is responsible for the formation of all hadrons which are classified into mesons and baryons. Well-known examples of the former is the pion and of the latter is the proton and the neutron, which form the nucleus of every atom. This fundamental force is believed to be described by the Quantum Chromodynamics (QCD) theory. According to this theory, hadrons are not elementary particles but are composed of quarks and gluons. The latter are the vector particles of the force and so are bosons of spin 1 and the former constitute the matter and are fermions with spin 1/2. To describe the interaction a new quantum number had to be introduced: the color charge which exists in three different types (blue, green and red). The name has not been chosen arbitrary as elements created from three quarks of different colors are colorless in the same way that mixing the three primary colors leads to white. However, experimentally no colored structure has ever been observed. The quarks and the gluons seem to be confined in colorless hadrons. This property of QCD is called confinement and results from a large coupling constant at low energy (or large distance). For high energy (or small distance), the perturbative analysis of QCD permits to establish the coupling constant to be small and quarks and gluons are almost free. This property is called asymptotic freedom. The possibility for QCD to describe both behaviors is one of its amazing characteristics. However, both phenomena are not well understood and one needs a method to study both the pertubative and the confining regime.

The only known method which fulfills the above criteria is Lattice QCD and more generally Lattice Quantum Field Theory (LQFT). It consists of a discretization of the spacetime and a formulation of QCD on a four-dimensional Euclidean spacetime grid of spacing $a$. In this way, the theory is naturally regularized and mathematically well-defined. On the other hand, the path integral formalism allows the theory to be treated as a Statistical Mechanics system which can be evaluated via a Markov chain Monte-Carlo algorithm. This method was first suggested by Wilson in 1974 [1] and shortly after Creutz performed the first numerical simulations of Yang-Mills theory [2] using a heath-bath Monte-Carlo algorithm. It appears that this method is extremely demanding in computational power. In its early days the method was criticized as the only feasible simulations involved non-physical values such as extremely large quark masses, large lattice spacing $a$ and no dynamical quarks. With the progress of the computers and the appearance of the super-computer, the studies have come close to the physical point. But one still needs to deal with discrete space time and finite volume. Several techniques have been developed to estimate the infinite volume limit and the continuum limit. The smaller the lattice spacing and the larger the volume, the better the extrapolation to continuum and infinite volume limits is.

The simulations are still very expensive and for the moment a typical length of the box is $L \approx 4$fm and $a \approx 0.08$fm. However, it has been realized simulating pure Yang-Mills theory and other lower dimensional models that the topology is freezing at small $a$ [3]. It was also observed recently on full QCD simulations [4,5]. The typical lattice spacing for which this problem appears in QCD is $a \approx 0.05$fm but this value depends on the quark mass used and on the algorithm. The freezing of topology leads to results which differ from physical results. Solving this issue is important for the future of LQCD [6]. Recently several methods to overcome the problem have been suggested, one of the most popular is the used of open boundary conditions [7] but this promising method has still its own issues, mainly the breaking of translation invariance. Another suggestion is

based on a relation derived by Brower, Chandrasekharan, Negele and Wiese (BCNW) in [8]. This relation links the physical values of masses or observables to their fixed topology counterparts.

The aim of this thesis is to discuss the latter solution with the first rather complete investigation of the problem on different models including QCD. A first study was realized before the thesis in [9, 10]. It was done with low statistics and authors were not able to make a clear statement on the procedure. In this thesis, we have investigated the practicability of the method, the conditions of applications and different ideas to improve it. The organization of the thesis is the following.

In chapter 1, we review some basic knowledge on QCD and quantum field theory in general, needed to understand the thesis. An important part of this chapter is an introduction to topology in Quantum Field Theory. We explain some important notions such as the topological charge, instantons and the $\theta$-vacuum.

The second chapter is a short introduction to lattice quantum field theory. We show how QCD can be numerically simulated and how the fields can be discretized. Then we explain quickly how we simulate QCD and how we extract interesting values from lattice simulations. This will allow us to explain in detail the problem of the freezing of topology and other simulation problems linked with topology.

Chapter 3 will focus on the topological charge. This quantity is special on the lattice since one can find several definitions that are not completely equivalent. After introducing them, we will have a closer look at the field theoretical definitions used in this work. The UV-fluctuation problem and procedures that solve it will be discussed in detail, in addition we will present the links that exist between the different processes. At the end, we will compare numerically the different definitions.

Chapters 4 and 5 are respectively the theoretical part and the numerical test of the method to extract physical results from fixed topology simulations based on the BCNW-equation. The theoretical part will demonstrate the BCNW-equation for observables and masses. Next the problem of parity mixing will be studied. The numerical part will present numerical tests on three different models: the 1D O(2) model with a square well potential, the pure 4D SU(2) Yang-Mills theory and the Schwinger model.

Chapter 6 corresponds to the extension of the BCNW-equation to include ordinary finite volume effects in order to apply the BCNW-method in QCD. The first part will explain what ordinary finite volume effects are and how they are affected by a fixed topology. Then we will compute the extension of the BCNW-equation which includes the ordinary finite volume effects. The second part will present the numerical tests of the previous equations obtained for the 4D SU(2) Yang-Mills theory and QCD.

Chapter 7 will present two methods to extract the topological susceptibility from fixed topology simulations. These methods are necessary as the previous chapter will conclude on a difficult extraction of this quantity using the BCNW-method. The first part will then present the Aoki, Fukaya, Hashimoto and Onogi (AFHO) method [11] with numerical tests on SU(2) and QCD. And finally the second part will present the Slab method [12, 13] with numerical tests on QCD.

This thesis is based on several publications where I made a major contributions and is essentially a summary of my contributions to these papers. In particular, chapters 3, 4 and 5 are based on the following published papers [14–16]. The chapters 3, 6 and 7 are based on the following proceedings [17–20] and the following papers [21–23] which are in preparation.

# Chapter 1

# Quantum Field Theory and Topology

## 1.1 Quantum ChromoDynamics

### 1.1.1 The QCD Lagrangian

Quantum ChromoDynamics (QCD) is a gauge theory of the strong interaction between quarks and gluons, elementary constituents of hadrons. The theory is based on the principle of local gauge invariance with a non-Abelian SU(3) gauge group [24]. The Lagrangian density of the theory is composed of three different parts:

$$\mathcal{L}_{QCD} = \mathcal{L}_{quark} + \mathcal{L}_{YM} + \mathcal{L}_{int}, \tag{1.1.1}$$

where $\mathcal{L}_{quarks}$ describes the dynamics of free quarks, $\mathcal{L}_{YM}$ the gluons interacting with each other and $\mathcal{L}_{int}$ the interaction part that couples quarks and gluons. Let us first consider the gluonic part:

$$\mathcal{L}_{YM} = -\frac{1}{4} F^a_{\mu\nu}(x) F^{\mu\nu}_a(x). \tag{1.1.2}$$

Before explaining the different mathematical elements inside the Lagrangian, we will first explain what it describes. The notation is explained in the Appendix A.1. The Yang-Mills part of the Lagrangian describes the dynamics of the gluons which are the vector particles of the strong interaction. In that sense, they are not the matter in the common language. They represented the quantization of a force. So in a world described uniquely by a Yang-Mills Lagrangian, there is no fermionic matter and the Lagrangian describes the dynamics of the vacuum of the theory and its excitations (glueballs).

Now, let us describe the different elements of the Lagrangian. $F^a_{\mu\nu}$ is the field strength tensor, which is directly related to the gluon field components $A^a_\mu$:

$$F^a_{\mu\nu}(x) = \partial_\mu A^a_\nu(x) - \partial_\nu A^a_\mu(x) - g f^{abc} A^b_\mu(x) A^c_\nu(x), \tag{1.1.3}$$

where $g$ is the bare coupling constant and $f^{abc}$ the structure constants of SU(3) defined in A.1. This purely bosonic part of the Lagrangian is invariant with respect to a local SU(3) gauge transformation. This SU(3) gauge is called the color gauge and frequently noted $\mathrm{SU(3)}_c$.

The free quark part of the Lagrangian can be expressed as:

$$\mathcal{L}_{quark} = \sum_{f=1}^{N_f} \bar{\psi}_f(x) \left( i\gamma^\mu \partial_\mu - m_f \right) \psi_f(x), \tag{1.1.4}$$

where $N_f$ is the number of flavours and $\psi_f$ is the quark field corresponding to flavour $f$ , $m_f$ is the $f-$flavour bare quark mass and $\gamma^\mu$ are the Dirac matrices generating the Clifford algebra. This part describes the dynamics

of the quarks without interaction. The mass $m_f$ appears as a parameter when we look only at QCD. However, if we consider the complete Standard Model, the mass of the quark is the results of the interaction between massless quarks and the Higgs bosons.

The last part of the QCD Lagrangian is $\mathcal{L}_{int}$:

$$\mathcal{L}_{int} = g \sum_{f=1}^{N_f} \bar{\psi}_f(x) \gamma^\mu A_\mu(x) \psi_f(x), \tag{1.1.5}$$

where $A_\mu(x) = A_\mu^a T_a$ with $T_a$ the generators of SU(3) defined in Appendix A.1. As the only term mixing fermions and bosons, it represents the interaction of the quarks with the gluon fields. It is interesting to remark that $\mathcal{L}_{quark}$ is not invariant under $\mathrm{SU}(3)_c$ gauge transformation as $\mathcal{L}_{int}$ but their sums is gauge invariant. For this reason, they are rarely considered independently and we will rather consider the following part:

$$\mathcal{L}_{ferm} = \mathcal{L}_{quark} + \mathcal{L}_{int} = \sum_{f=1}^{N_f} \bar{\psi}_f(x) \left( i\gamma^\mu D_\mu - m_f \right) \psi_f(x), \tag{1.1.6}$$

where we have introduced the covariant derivative $D_\mu$, defined by:

$$D_\mu(x) = \partial_\mu - igA_\mu(x). \tag{1.1.7}$$

Thus:

$$\mathcal{L}_{QCD} = \sum_{f=1}^{N_f} \bar{\psi}_f(x) \left( i\gamma^\mu D_\mu - m_f \right) \psi_f(x) - \frac{1}{4} F_{\mu\nu}^a(x) F_a^{\mu\nu}(x) \tag{1.1.8}$$

and the action is given by:

$$S_{QCD}[\psi, \bar{\psi}, A] = \int d^4x \mathcal{L}_{QCD}. \tag{1.1.9}$$

### 1.1.2 Path integral

An elegant way to quantize a classical theory is to use the Feynman path integral formalism. This quantization method is particularly important for lattice field theory. We can sketch the idea behind the method rather easily. A classical particle to go from one point to the other will use the trajectory which will minimize the action. This behavior is called the least action principle. As the particle is classical, its trajectory can be perfectly defined at any time and the path it follows is unique and clear. (Two paths with the same action can exist but the particle will choose one and stay on it).

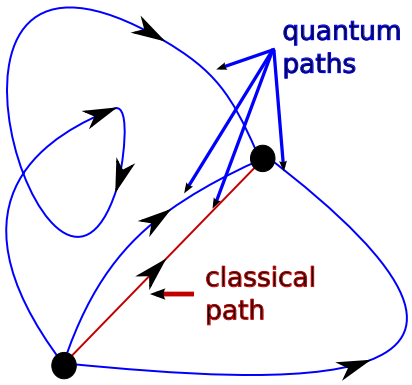


Figure 1.1.1: Sketch of path integrals

In quantum physic the situation is different (cf. figure 1.1.1), a trajectory cannot be defined and a particle will virtually use all the paths with a finite action. Nevertheless we can still speak about probabilities to measure the particle on one path. This probability depends of the value of the action in the same way that in statistical physics, the probability to find the system in one state depends on its energy. In that sense, the classical path is not the only one but becomes the path with the maximum probability. And the expectation value of an observable can be computed by:

$$\langle \mathcal{O} \rangle = \frac{1}{Z} \int D\bar{\psi} D\psi DA \mathcal{O}[\psi, \bar{\psi}, A] e^{iS_{QCD}[\psi,\bar{\psi},A]} \tag{1.1.10}$$

with the partition function:

$$Z = \int D\bar{\psi} D\psi DA e^{iS_{QCD}[\psi,\bar{\psi},A]}. \tag{1.1.11}$$

From a practical point of view, it is not feasible to numerically compute the previous path integral as $e^{iS_{QCD}[\psi,\bar{\psi},A]}$ is an oscillating factor. Thus it is advantageous for many numerical applications to perform a Wick rotation:

$$t_E = it, \tag{1.1.12}$$

which is equivalent to change from a Minkowski space to an Euclidean space. The idea is to make all the calculus in the Euclidean space and then perform an analytical continuation of the function to the physical space. This is possible only if the correlation function satisfies the Osterwalder-Schrader reflection positivity [25]. From this condition we have that the transition probabilities between gauge-invariant states are non-negative and the quantum mechanical Hamiltonian has only real and positive eigenvalues [26].

Then we infer that the expectation value of an observable is given by:

$$\langle \mathcal{O} \rangle = \frac{1}{Z^E} \int D\bar{\psi} D\psi DA \mathcal{O}[\psi, \bar{\psi}, A] e^{-S^E_{QCD}[\psi,\bar{\psi},A]} \tag{1.1.13}$$

with

$$Z^E = \int D\bar{\psi} D\psi DA e^{-S^E_{QCD}[\psi,\bar{\psi},A]} \tag{1.1.14}$$

and

$$\mathcal{L}^E_{QCD} = \sum_{f=1}^{N_f} \bar{\psi}_f(x) \left(\gamma^\mu D_\mu + m_f\right) \psi_f(x) + \frac{1}{4} F^a_{\mu\nu}(x) F^{\mu\nu}_a(x), \tag{1.1.15}$$

where the anticommutation property of $\gamma_\mu$ is changed to:

$$\{\gamma_\mu, \gamma_\nu\} = 2\delta_{\mu\nu}. \tag{1.1.16}$$

As expected the oscillating exponential appearing in eq. (1.1.10) and eq. (1.1.11) is replaced by a well-behaved factor $e^{-S^E_{QCD}[\psi,\bar{\psi},A]}$. The statistical point of view of the path integral formalism is now clearly visible, as the partition function can be interpreted as the partition function of a mechanical system in which the exponential factor $e^{-S^E_{QCD}[\psi,\bar{\psi},A]}$ plays the role of the Boltzmann factor. Numerically and so practically the problem becomes much simpler as it can be simulated by a Monte-Carlo algorithm. The principle of such algorithm will be explained in section 2.2.

## 1.2 Topology in quantum field theory

Topology is the study and the classification of objects which are equivalent by continuous deformations. In field theory the objects studied are field configurations. In that sense, the topology in quantum field theory is the study of the fields under continuous deformations. In the models studied, the non-trivial topology is coming from the gauge part of our theory. As we observed in section 1.1.1, the fermionic part interacts with the gluonic part and fermions and observables will be affected by different topologies. In this section, several notions of topology in field theory will be quickly introduced. For a more complete description, we refer to [27–30]. In a first part, we shall present the topology of the QCD vacuum. Then we will focus on non-trivial gauge configurations called topological objects. We will be essentially interested in one of them called instantons. To finish, we will look at

the implications for QCD.

### 1.2.1 Finite action and winding number

Let us now consider the SU(2) Yang-Mills theory in Euclidean spacetime before coming back to SU(3). Let us define a $3-$sphere of constant radius $r$ in Euclidean spacetime. Having a finite action requires that the Lagrangian density goes as $r^{-6}$ when $r$ tends to infinity. That leads to

$$A_\mu(r) \underset{r\to\infty}{=} 0. \tag{1.2.1}$$

In the previous statement, the invariance under gauge transformation has not been taken into account. The general solution is then that $A_\mu$ should tend to a pure gauge:

$$A_\mu(x) \underset{r\to\infty}{=} \frac{1}{g} G(x)\partial_\mu G^{-1}(x), \tag{1.2.2}$$

where $G(x) \in$ SU(2).

It is easy to realize that SU(2) is isomorphic to $S^3$. Let us take an element $U$ of SU(2), which can be written as:

$$U = \exp(\frac{i}{2}\vec{u}.\vec{\sigma}), \tag{1.2.3}$$

where $\vec{\sigma}$ are the Pauli matrices. $U$ can be defined by 3 reals ($u_1$,$u_2$ and $u_3$). Moreover using the fact that Pauli matrices are nilpotent it can be proved that this 3 dimensional vector space is periodic in any of the 3 directions with a same periodicity of $4\pi$ which demonstrate the isomorphism with $S^3$. In order to study the equivalence of the previous expression, one has to study the topology of the mapping of the $3-$sphere in our Euclidean space and the SU(2) group symmetry of our theory. It is equivalent to study the mapping of a $3-$sphere on a $3-$sphere. In terms of topology, the result is:

$$\pi_3(S^3) = \mathbb{Z}, \tag{1.2.4}$$

meaning that there is an infinity of non-equivalent ways to map SU(2) to $S^3$. For each of these different mappings an integer is attributed :

$$n_W = \frac{1}{24\pi^2}\int d^3x\epsilon^{ijk}\,\mathrm{Tr}\left[(U\partial_i U^\dagger)(U\partial_j U^\dagger)(U\partial_k U^\dagger)\right]. \tag{1.2.5}$$

This winding number represents the number of times that the $3-$sphere is wrapped by $U(x)$ when $x$ varies on $\mathbb{R}^4$. Let us show that this number is a topological invariant and so that is not modified by continuous transformations. We consider an infinitesimal transformation $\delta U(x) = U(x)\delta T(x)$

$$\delta(U\partial_i U^\dagger) = \delta U\partial_i U^\dagger + U\partial_i\delta U^\dagger = U(\delta T)\partial_i U^\dagger - U(\delta T)\partial_i U^\dagger - U(\partial_i\delta T)U^\dagger = -U(\partial_i\delta T)U^\dagger \tag{1.2.6}$$

$$\begin{aligned}\delta n_W &\propto \int d^3x\epsilon^{ijk}\,\mathrm{Tr}\left[U(\partial_i\delta T)U^\dagger(U\partial_j U^\dagger)(U\partial_k U^\dagger)\right]\\ &\propto \int d^3x\epsilon^{ijk}\,\mathrm{Tr}\left[(\partial_i\delta T)(\partial_j U)(\partial_k U^\dagger)\right] = 0,\end{aligned} \tag{1.2.7}$$

where we used the integration by parts for the first step and the antisymmetry of $\epsilon$ in the final step. The winding number can also be expressed in terms of the vector potential,

$$n_w = \frac{g^2}{16\pi^2}\int d^3x\epsilon_{ijk}(A_i^a\partial_j A_k^a - \frac{g}{3}\epsilon^{abc}A_i^a A_j^b A_k^c). \tag{1.2.8}$$

The topological structure of SU(3) is directly related to the fact that SU(2)$\subset$SU(3) and so SU(3) possesses

the same topological structure than SU(2).

### 1.2.2 Instantons

Let us return to the Euclidean gauge action:

$$S_E = \frac{1}{4}\int d^4x F^a_{\mu\nu}F^a_{\mu\nu}. \tag{1.2.9}$$

We can determine the Bogomol'nyi bound, meaning the minimum of the action for a given topology:

$$S_E = \frac{1}{4}\int d^4x \left(\pm F^a_{\mu\nu}\tilde{F}^a_{\mu\nu} + \frac{1}{2}(F^a_{\mu\nu} \mp \tilde{F}^a_{\mu\nu})^2\right) \geq \pm\frac{1}{4}\int d^4x F^a_{\mu\nu}\tilde{F}^a_{\mu\nu}, \tag{1.2.10}$$

with $\tilde{F}^a_{\mu\nu}$ the dual of $F^a_{\mu\nu}$ expressed as $\tilde{F}^a_{\mu\nu} = \epsilon_{\mu\nu\rho\sigma}F^a_{\rho\sigma}$. The last integral can be rewritten using Stoke's theorem:

$$\int d^4x F^a_{\mu\nu}\tilde{F}^a_{\mu\nu} = \frac{32\pi^2}{g^2}\int d\sigma_\mu K_\mu \tag{1.2.11}$$

with

$$K_\mu = \frac{g^2}{16\pi^2}\epsilon_{\mu\nu\rho\sigma}(A^a_\nu\partial_\rho A^a_\sigma - \frac{g}{3}\epsilon^{abc}A^a_\nu A^b_\rho A^c_\sigma). \tag{1.2.12}$$

We observe that this quantity is related to $n_w$ and so it is called the topological current. In contrast to $n_w$, $K_\mu$ is oriented, leading to:

$$Q = \int d\sigma_\mu K_\mu = n_w(\infty) - n_w(-\infty) = \frac{g^2}{32\pi^2}\int d^4x F^a_{\mu\nu}\tilde{F}^a_{\mu\nu}, \tag{1.2.13}$$

where $Q$ is the topological charge. The Bogomol'nyi bound can be expressed in terms of the topological charge:

$$S_E \geq \frac{8\pi^2}{g^2}|Q|. \tag{1.2.14}$$

The field tensor which minimizes the action is such that:

$$\tilde{F}^a_{\mu\nu} = \pm F^a_{\mu\nu}. \tag{1.2.15}$$

Those self-dual (reciprocally anti self-dual) configurations are called instantons (anti-instantons). They possess a topological charge of $Q = +1$ $(-1)$ and are classical solutions of the equations of motion as they minimize locally the action.

An analytic expression of such self-dual fields can be computed via a spherical ansatz:

$$A^a_\mu = -\frac{2}{g}\frac{\eta_{a\mu\nu}x_\nu}{x^2+\rho^2}, \tag{1.2.16}$$

where $\rho$ is the size of the instantons and can be an arbitrary positive number. $\eta_{a\mu\nu}$ is the 't Hooft symbol defined as:

$$\eta_{a\mu\nu} = \begin{cases} \epsilon_{a\mu\nu} & \mu,\nu = 1,2,3 \\ \delta_{a\mu} & \nu = 0 \\ -\delta_{a\nu} & \mu = 0. \end{cases} \tag{1.2.17}$$

The previous result eq. (1.2.16) seems to lead to a $F_{\mu\nu}$ which falls as $1/x^2$, but the leading term in

eq. (1.2.16) is a pure gauge and by choosing judiciously the gauge, the following expression is obtained:

$$A_\mu^a = -\frac{2}{g}\frac{\eta_{a\mu\nu}x_\nu\rho^2}{x^2\left(x^2+\rho^2\right)}, \tag{1.2.18}$$

which leads to a $F_{\mu\nu}$ which falls as $1/|x|^4$ and a finite action.

### 1.2.3 Periodicity of Yang-Mills vacuum and Tunneling

For a moment, let us go back to the Minkowski space. We have seen previously that $A_\mu$ needs to tend to a pure gauge at the infinity to have a finite Euclidean action. The pure gauge plays also an important role as the vacuum of the Yang-Mills theory. The Hamiltonian density of the Yang-Mills theory can be expressed as:

$$\mathcal{H}_{\mathcal{YM}} = \frac{1}{2}\left(E^2+B^2\right), \tag{1.2.19}$$

with $E$ the electric field and $B$ the magnetic field. The vacuum will correspond to configurations minimizing the Hamiltonian density, so with $E=0$ and $B=0$. Those configurations are the pure gauge defined in eq. (1.2.2). As seen previously, the attribution of a topological winding number to them is possible. The existence of topologically non-equivalent configurations proves the existence of many different classical vacua with different winding numbers. If it is not possible to change $Q$ by continuous transformations (gauge transformations which vanishes at infinity), this is possible to do it by large gauge transformations (they cannot be continuously deformed to $\mathbb{1}$). As those gauge transformations cannot be pure gauges, they possess an energy. If we were in classical theory, the story would end here with different vacua. However, in quantum field theory tunneling exists, and the quantum vacuum is a superposition of those states.

Let us first describe the property of such a tunneling. We assume a tunneling that happens at a time $t$ to change the winding number by one unit. Such difference between winding numbers has already been studied in eq. (1.2.13) and is the topological charge. This implies that we can attribute a topological charge $Q=\pm1$ to the process of tunneling. It can be proven that the probability of tunneling is given by:

$$P \propto \exp\left(-\frac{8\pi^2}{g^2}\right) = \exp\left(-S_{E,inst}\right), \tag{1.2.20}$$

which is directly related to the action of a single instanton configuration. This result is a direct link between the instantons in Euclidean space and tunneling in Minkowski space, showing that they are two aspects of the same thing.

### 1.2.4 $\theta$-Vacuum and action

The question of the nature of the quantum vacuum has not yet found an answer. Let us come back to our Euclidean space where topology is easier to interpret. Starting from a partition function in a box of size $V_s \times T$ with a given topological charge $n$

$$Z(V_s,T,n) = N\int DA e^{-S_E}\delta_{Q,n}, \tag{1.2.21}$$

where the $\delta_{Q,n}$ assures that we consider only configurations for which the topological charge $Q[A]$ is $Q[A]=n$, we can express our partition function as partition functions of two subvolumes $V_s\times T_1$ and $V_s\times T_2$. As the action is an additive quantity, partition functions have to be multiplied. The topological charge of the subvolumes $n_1$ and $n_2$ will take all possible values such that $n_1+n_2=n$ with $n$ fixed. In addition we suppose that no instanton

are located on the boundaries ( i.e. surface effects are neglected). At the end, we get

$$Z(V_s,T,n)=\sum_{n=n_1+n_2} Z(V_s,T_1,n_1)Z(V_s,T_2,n_2). \tag{1.2.22}$$

Such convolution behavior is not the one expected if $n$ was a true quantum number. We expect a multiplication instead. However, it is well known that a Fourier transform changes a convolution into a multiplication,

$$Z(V_s,T,\theta)=\sum_n e^{in\theta}Z(V_s,T,n)=N\int DAe^{-S_E}e^{iQ\theta}. \tag{1.2.23}$$

Therefore $Z(V_s,T,\theta)$ is given by:

$$Z(V_s,T,\theta)=Z(V_s,T_1,\theta)Z(V_s,T_2,\theta). \tag{1.2.24}$$

From this analysis, it appears that the quantum vacuum is the $\theta$-vacuum: $|\theta\rangle=\sum e^{in\theta}|n\rangle,\ n\in\mathbb{Z}$. The eq. (1.2.23) leads to the definition of an action which takes into account the topology:

$$S_E(\theta)=S_E-iQ[A]\theta. \tag{1.2.25}$$

Thus the Lagrangian density of QCD on the $\theta$-vacuum is given by:

$$\mathcal{L}_{QCD}(\theta)=\sum_{f=1}^{N_f}\bar{\psi_f}(x)\left(i\gamma_\mu D_\mu+m_f\right)\psi_f(x)+\frac{1}{4}F^a_{\mu\nu}(x)F^{\mu\nu}_a(x)-i\theta\frac{g^2}{32\pi^2}F^a_{\mu\nu}(x)\tilde{F}^a_{\mu\nu}(x). \tag{1.2.26}$$

To summarize this subsection, we have seen by straightforward analysis that the true vacuum was $|\theta\rangle$, the $\theta$-vacuum and that the Lagrangian could be modified by inserting a topological term.

The existence of the $\theta$-term leads to several questions. The first one is the influence of this $\theta$-term on the ground state energy. To answer this question, we will discuss the problem in a diluted instanton gas neglecting interactions between them. The energy, that is needed to change from a topological vacuum $|i\rangle$ to a topological vacuum $|j\rangle$ is given by:

$$\langle j|\exp(-\mathcal{H}t)|i\rangle=\sum_{n_+}\sum_{n_-}\frac{\delta_{n_+-n_-,j-i}}{n_+!n_-!}\left(C\cdot t\cdot e^{-S_{inst}}\right)^{n_++n_-}, \tag{1.2.27}$$

where $n_+$ is the number of instantons, $n_-$ the number of anti-instantons, $C$ is a constant and $S_{inst}$ is the action of a vacuum with one instanton. A Poisson distribution has been assumed as we consider that there is no interaction between instantons. Then the energy of the ground state on the $\theta$-vacuum is given by:

$$\begin{aligned}\langle\theta|\exp(-\mathcal{H}t)|\theta\rangle&=\sum_{n_+}\sum_{n_-}\frac{e^{i(n_+-n_-)\theta}}{n_+!n_-!}\left(C\cdot V\cdot t\cdot e^{-S_{inst}}\right)^{n_++n_-}\\&=\exp\left(2C\cdot V\cdot te^{-S_{inst}}\cos(\theta)\right).\end{aligned} \tag{1.2.28}$$

Leading to an energy density of the vacuum:

$$E(\theta)/V=-2Ce^{-S_{inst}}cos(\theta). \tag{1.2.29}$$

It is interesting to observe the symmetry between $\theta$ and $-\theta$ in the energy. This corresponds to the invariance of physics under the interchange of instantons and anti-instantons [27].

A second question that is legitimate to ask, is how the equation of motion are modified. We have already

used in eq. (1.2.11) that

$$\mathrm{Tr}\left(F_{\mu\nu}\tilde{F}_{\mu\nu}\right) = \frac{16\pi^2}{g^2}\partial_\mu K_\mu. \tag{1.2.30}$$

From this equation, it appears that the $\theta$-term in our Lagrangian is the divergence of a topological current. As a divergence term, it does not modify the equations of motion.

The last question which appears is what is the value of $\theta$ in QCD. This question is particularly important as for $\theta \neq 0 \mod (\pi)$ the parity P as well as the CP symmetry are broken. The answer of this question can be measured experimentally, in particular if CP is broken by the $\theta$-term the neutron acquires an electric dipole momentum. Its measurement leads to

$$\theta < 10^{-10}. \tag{1.2.31}$$

Explaining this value of $\theta \approx 0$ is known as the strong CP problem as there is no reason in QCD for $\theta$ to take this particular value. The axion model has been suggested as a solution [31, 32]. In this extension of QCD the axion mechanism transforms the constant $\theta$ parameter in a dynamical field. As we can observe in eq. (1.2.29), the energy is minimal for $\theta = 0$ and so $|\theta = 0\rangle$ becomes the natural vacuum of the theory. So far no axions have been observed experimentally.

### 1.2.5 The topological charge distribution and the topological susceptibility

The naive picture of a diluted instanton distribution can also be used to have some insights about the distribution of the topological charge. Once again we can assume a Poisson distribution for the instantons as well as the anti-instantons. Then the probability to have $n_+(n_-)$ instantons (anti-instantons) is given by

$$p(n_\pm) = \frac{e^{-\lambda_\pm}\lambda_\pm^{n_\pm}}{n_\pm!}, \tag{1.2.32}$$

where $\lambda_+(\lambda_-)$ is the average number of instantons (anti-instantons).

Therefore the probability to have a topological charge $Q$ is given by:

$$p(Q) = \sum_{n_+}\sum_{n_-}\frac{e^{-\lambda_+}\lambda_+^{n_+}}{n_+!}\frac{e^{-\lambda_-}\lambda_-^{n_-}}{n_-!}\delta_{Q,n_+-n_-}. \tag{1.2.33}$$

This kind of distribution is well-known in statistics and is called the Skellam distribution. It is easy to show that in case of $Q \in \mathbb{Z}$ the distribution is:

$$p(Q) = e^{-(\lambda_+ + \lambda_-)}\left(\frac{\lambda_+}{\lambda_-}\right)^{Q/2} I_Q(2\sqrt{\lambda_1\lambda_2}), \tag{1.2.34}$$

with $I_Q$ the modified Bessel function of the first kind. In our case the instantons and anti-instantons are similar objects with only one topological charge of opposite sign to distinguish them. So we can assume that $\lambda_- = \lambda_+ = \lambda$ which implies $\langle Q\rangle$. Then the distribution is given by:

$$p(Q) = e^{-2\lambda}I_Q(2\lambda). \tag{1.2.35}$$

The study of the distribution gives us that the average of this distribution is 0 and the variance is given by:

$$\langle Q^2\rangle - \langle Q\rangle^2 = \langle Q^2\rangle = 2\lambda, \tag{1.2.36}$$

with a non-zero kurtosis. In case of a large $\lambda$, the distribution is close to a normal distribution especially for large topological charges. That suggests to generally assume a normal distribution for the topological charge. In case of a normal distribution, the kurtosis is zero and the value of $\langle Q^2\rangle$ gives all necessary information

about the distribution. Now if we are at finite spacetime volume $V$, this value can be related to the topological susceptibility $\chi_{\mathrm{t}}$ by the following relation:

$$\langle Q^2 \rangle = \chi_{\mathrm{t}}\, V. \tag{1.2.37}$$

The topological susceptibility can be defined in a more general way. In fact, the topological susceptibility is related to the $\theta$-dependence of the vacuum energy by the following expression:

$$\left.\frac{\partial^2 E_0}{\partial \theta^2}\right|_{\theta=0} = \chi_{\mathrm{t}}\,. \tag{1.2.38}$$

This quantity is particularly important in the process of explaining the large $\eta'$-mass in QCD via the Witten-Veneziano formula [33, 34]:

$$\frac{4N_f}{f_\pi^2}\,{\chi_{\mathrm{t}}}^{quenched} = m_{\eta'}^2 + m_\eta^2 - 2m_K^2, \tag{1.2.39}$$

or for the axion abundance in the universe [35] as it is related to the mass of the axions:

$$\chi_{\mathrm{t}} = (m_a f_a)^2 \tag{1.2.40}$$

with $m_a$ the mass of the axion and $f_a$ the axion decay constant. This quantity will also appear all along the thesis.

# Chapter 2

# Quantum Field Theory on the Lattice

## 2.1 QCD and Lattice

As seen previously, QCD is the theory which describes the strong interaction. As its coupling is too strong to make a meaningful pertubative study, a numerical method has been developed which is the lattice QCD theory. In this chapter, we will quickly introduce this method. For a more complete descriptions the reader is invited to refer to [36–38].

### 2.1.1 Discretization of the gauge field

The name lattice comes from the fact that we are working with a grid made of links which are related to the potential vector by:

$$\hat{U}(x, x + a\hat{\mu}) = \hat{U}_\mu(x) = e^{igaA_\mu(x)}, \tag{2.1.1}$$

where $\hat{\mu}$ the unit vector in the $\mu$ direction and $a$ is the lattice spacing , the distance between two points on the lattice. $\hat{U}_\mu(x)$ is the gauge field on the lattice. It is a variable defined on the link connecting site $x$ and $x + \hat{\mu}$ and which belongs to the gauge group of the theory.

The simplest gauge field lattice action is probably the Wilson action, but the choice of the lattice action is not unique. However, each action should converge to the continuum action when the lattice spacing $a$ goes to zero, known as the continuum limit. The Wilson action for SU(3) gauge theory on the lattice reads

$$\hat{S}_{Wilson}[\hat{U}] = \frac{\beta}{3} \sum_x \sum_{1 \le \mu < \nu \le 4} \left(1 - \mathrm{Re}\,\mathrm{Tr}\,\hat{P}(x, \mu, \nu)\right), \tag{2.1.2}$$

where $\hat{P}$ is called the plaquette and is the smallest loop on the lattice,

$$\hat{P}(x, \mu, \nu) = \hat{P}_{\mu\nu}(x) = \hat{U}_\mu(x)\hat{U}_\nu(x + a\hat{\mu})\hat{U}_{-\mu}(x + a\hat{\mu} + a\hat{\nu})\hat{U}_{-\nu}(x + a\hat{\nu}). \tag{2.1.3}$$

In order to link $\beta$ with the coupling constant, a good idea is to rewrite the Wilson action similarly as in Yang-Mills SU(3) theory. Using the fact that

$$\hat{P}_{\mu\nu} = e^{iga^2 F_{\mu\nu}} = \mathbb{1} + iga^2\, F_{\mu\nu} - \frac{g^2 a^4}{2}\, F_{\mu\nu}\, F_{\mu\nu} + \mathcal{O}(a^6). \tag{2.1.4}$$

The Wilson action can be rewritten as:

$$\begin{aligned}\hat{S}_{Wilson} &= \frac{\beta}{3}\sum_x\sum_{\mu<\nu}\left(1-\mathrm{Re}\,\mathrm{Tr}\left(\mathbb{1}+iga^2\,F_{\mu\nu}-\frac{g^2a^4}{2}\,F_{\mu\nu}\,F_{\mu\nu}+\mathcal{O}(a^6)\right)\right)\\ &= \frac{g^2a^4}{2}\frac{\beta}{3}\sum_x\sum_{\mu<\nu}\mathrm{Tr}\left(F_{\mu\nu}\,F_{\mu\nu}+\mathcal{O}(a^2)\right)\\ &= \frac{g^2a^4}{4}\frac{\beta}{6}\sum_x\sum_{\mu,\nu}F_{\mu\nu_b}F^b_{\mu\nu}+\mathcal{O}(a^2),\end{aligned} \tag{2.1.5}$$

As the discretization of $\int \mathrm{d}^4x \to a^4\sum_x$, we obtain:

$$\beta = \frac{6}{g^2} \tag{2.1.6}$$

and corrections due to the discretization are of the order $\mathcal{O}(a^2)$.

### 2.1.2 Discretization of the fermion field

**Naive Discretization**

The discretization of the fermion field is a bit more subtle than the discretization of the gauge fields. We can start here with the naive discretization of the one-flavor continuum free fermion action. The action is given by:

$$S^{free}_{quark} = \int d^4x\bar{\psi}(x)D\psi(x), \tag{2.1.7}$$

where $D$ is the Dirac operator:

$$D = \gamma_\mu\partial_\mu + m, \tag{2.1.8}$$

with $m$ the mass of the quark. Once again the discretization is not unique, but all local discretizations have the same continuum limit. One choice for the lattice derivative is:

$$\hat{\partial}_\mu\psi(x) = \frac{1}{2a}\left(\psi(x+a\hat{\mu})-\psi(x-a\hat{\mu})\right). \tag{2.1.9}$$

Thus the previous action becomes:

$$\hat{S}^{free}_{quark} = a^4\sum_x\sum_\mu\bar{\psi}(x)\left(\gamma_\mu\hat{\partial}_\mu+m\right)\psi(x). \tag{2.1.10}$$

The lattice Dirac operator is:

$$\hat{D}_{naive} = \gamma_\mu\hat{\partial}_\mu + m. \tag{2.1.11}$$

In order to give the fermion propagator a simple expression, one usually expresses it in the momentum space. The Fourier transform of $\hat{\partial}_\mu$ is given by:

$$\tilde{p}_\mu = \frac{1}{a}\sin(a\hat{p}_\mu), \tag{2.1.12}$$

leading to the following propagator:

$$\hat{D}^{-1}_{naive}(p) = \frac{-i\tilde{p}_\mu\gamma_\mu + m\mathbb{1}}{\sum_\mu\tilde{p}^2_\mu + m^2}. \tag{2.1.13}$$

If we consider the massless fermion case, the pole of the propagator is given for $\tilde{p}_\mu = 0$, which corresponds to $\hat{p}_\mu = (0,0,0,0)$ but also for any momentum component that is equal to $\pi/a$. The fermion corresponding to

momentum 0 is the physical one and the one obtained in the continuum. The other ones are unphysical fermions (called doublers) due to discretization. In four-dimensional spacetime, we have $2^4 - 1 = 15$ doublers.

**Wilson fermions**

The first way to overcome the problem is to introduce an additional term proportional to the lattice spacing which will suppress these doublers but converges to 0 in the continuum limit. Before writing down the new Dirac operator, we need to introduce the forward lattice derivative $\nabla_\mu$ and the backward derivative $\nabla^*_\mu$:

$$a\nabla_\mu\psi(x) = \psi(x + a\hat{\mu}) - \psi(x) \text{ and } a\nabla^*_\mu\psi(x) = \psi(x) - \psi(x - a\hat{\mu}). \tag{2.1.14}$$

With that definition we can rewrite:

$$\hat{\partial}_\mu\psi(x) = \frac{1}{2}\left(\nabla_\mu + \nabla^*_\mu\right)\psi(x), \tag{2.1.15}$$

and the new Wilson Dirac operator is given by:

$$\hat{D}_{Wilson} = \frac{1}{2}\left(\gamma_\mu\left(\nabla_\mu + \nabla^*_\mu\right) - ar\nabla^*_\mu\nabla_\mu\right) + m, \tag{2.1.16}$$

where $r$ is the Wilson parameter and the new term is called the Wilson term.

This trick successfully suppresses the doublers, however there is a price to pay for solving the problem. First, the Wilson term leads to an $\mathcal{O}(a)$ leading cut-off dependence in the observables (which is more than for the gauge action). This default can be fixed by using Symanzik improved action or by adding a twisted mass term that will be introduced in the next paragraph. The second part concerns the chiral symmetry. The continuum action (like the naive discretization) is chirally symmetric when the quark mass is zero. However, the Wilson term is a momentum dependent mass term and breaks explicitly the chiral symmetry. An important consequence of this symmetry breaking is that the quark mass requires additive renormalization.

There is no simple solution for this problem. In fact a No-Go theorem has been proven by Nielsen and Ninomiya [39], which states that it is not possible that a lattice Dirac operator $\hat{D}$ fulfills at the same time the following conditions:

1. Locality: the norm of the Dirac operator $\hat{D}$ decays at least exponentially as the function of the distance.
2. Translation invariance: The Fourier transform of the Dirac operator exists and equals $\hat{D}(p) = i\gamma_\mu p_\mu + \mathcal{O}(ap^2)$ for $p \ll \pi/a$.
3. No fermion doublers
4. Chiral Symmetry: $\{\hat{D}, \gamma_5\} = 0$.

A solution was found [40] for this problem in the form of overlap or domain-wall fermions. We will not describe them in this thesis but the reader can refer to [38] for an introduction to this subject. The solution is to find a Dirac operator which respects the 3 first points and respects an approximate version of the forth point

$$\{\hat{D}, \gamma_5\} = a\hat{D}\gamma_5\hat{D}. \tag{2.1.17}$$

Then the chiral symmetry is restored in the continuum limit.

Before looking at the twisted mass Dirac operator, we need to have a look at the gauge symmetry of our theory. Until here the derivatives used are not the covariant derivatives. If in our action the mass term is gauge invariant, the other term is not.

Lets have a look at the forward lattice derivative:

$$\bar{\psi}(x)\left(\gamma_\mu\nabla_\mu\right)\psi(x) = \bar{\psi}(x)\gamma_\mu\psi(x + a\hat{\mu}) - \bar{\psi}(x)\gamma_\mu\psi(x). \tag{2.1.18}$$

And so under a unitary gauge transformation we have:

$$\bar{\psi}(x)\nabla_\mu\psi(x) \to \bar{\psi}(x)G^\dagger(x)G(x+a\hat{\mu})\psi(x+a\hat{\mu}) - \bar{\psi}(x)G^\dagger(x)G(x)\psi(x). \tag{2.1.19}$$

The second part is gauge invariant, but the first one is not, and as a consequence, the action is not gauge invariant. One can modify the derivative into a covariant derivative:

$$\hat{D}_\mu\psi(x) = \frac{1}{2a}\left(\hat{U}_\mu(x)\psi(x+a\hat{\mu}) - \hat{U}^\dagger_\mu(x-a\hat{\mu})\psi(x-a\hat{\mu})\right). \tag{2.1.20}$$

The forward derivative becomes:

$$a\nabla_\mu\psi(x) = \hat{U}_\mu(x)\psi(x+a\hat{\mu}) - \psi(x) \tag{2.1.21}$$

and the backward derivative:

$$a\nabla^*_\mu\psi(x) = \psi(x) - \hat{U}^\dagger_\mu(x-a\hat{\mu})\psi(x-a\hat{\mu}). \tag{2.1.22}$$

The gauge transformation becomes:

$$\begin{aligned}\bar{\psi}(x)\nabla_\mu\psi(x) \to &\bar{\psi}(x)G^\dagger(x)G(x)\hat{U}_\mu(x)G^\dagger(x+a\hat{\mu})G(x+a\hat{\mu})\psi(x+a\hat{\mu}) \\ &- \bar{\psi}(x)G^\dagger(x)G(x)\psi(x),\end{aligned} \tag{2.1.23}$$

which is gauge invariant.

**Wilson twisted mass fermions**

At first Wilson twisted mass fermions were developed to deal with unphysically small eigenvalues of the Dirac operator (Dirac zero modes). In quenched QCD, those eigenvalues lead to what is called exceptional configurations. They are large fluctuations which are not compensated by the fermionic determinant. The problem is that under this conditions the chiral limit is almost not possible to obtain. With dynamical quarks, the fermionic determinant compensates those large fluctuations but some technicals problems as a long autocorrelation time remain.

Another property of twisted mass fermions is the systematic $\mathcal{O}(a)$-improvement. It is possible to tune a parameter in order to suppress the $\mathcal{O}(a)$ errors existing in the simple Wilson fermions.

We first have to define the twisted quark fields ($\chi$) which are related to the physical field by an axial transformation

$$\psi(x) \to \chi(x) = e^{i\omega\gamma_5\tau_3/2}\psi(x), \quad \bar{\psi}(x) \to \bar{\chi}(x) = \bar{\psi}(x)e^{i\omega\gamma_5\tau_3/2}, \tag{2.1.24}$$

where $\omega$ is an angle called the twisted angle. The action is then defined by

$$\hat{S}_{TM} = a^4\sum_x \bar{\chi}(x)\hat{D}_{TM}\chi(x), \tag{2.1.25}$$

with

$$\hat{D}_{TM} = \hat{D}_{Wilson}(m) + i\mu\gamma_5\tau_3, \tag{2.1.26}$$

where $\mu$ is an additional mass parameter. The action is left invariant by this transformation if someone considers the following transformations for the masses:

$$\begin{aligned} m \to &m\cos(\omega) + \mu\sin(\omega) \\ \mu \to &-m\sin(\omega) + \mu\cos(\omega). \end{aligned} \tag{2.1.27}$$

The maximum twist is the special case $\omega = \pi/2$. This value corresponds to sending the bare quark mass to zero or, equivalently, taking the additive mass renormalization into account, to its critical values $m_c$. Finding this parameter is not trivial but one will be rewarded by an automatic $\mathcal{O}(a)$-improvement [41,42](but punished by $m_{\pi^\pm} \neq m_{\pi^0}$. The two solutions which exist are to tune the quark mass such that the pion mass vanishes or alternatively one can tune the untwisted PCAC mass defined by

$$m_{PCAC} = \frac{\sum_x \langle \partial_0 A_0^a(\vec{x},t) P^a(0)\rangle}{2\sum_x \langle P^a(\vec{x},t), P^a(0)\rangle}, \quad a = 1,2 \tag{2.1.28}$$

to zero [43]. The second method appears to work really efficiently in practical simulations.

The action is then

$$\hat{S}_{MTM} = a^4 \sum_x \bar{\chi}(x)\hat{D}_{MTM}\chi(x), \tag{2.1.29}$$

with

$$\hat{D}_{TM} = \hat{D}_{Wilson}(m_c) + i\mu\gamma_5\tau_3. \tag{2.1.30}$$

The automatic $\mathcal{O}(a)$-improvement makes the maximal twisted mass formulation really practical for simulations and will be used for QCD results in this thesis.

#### Other fermion discretizations

As mentioned before there exist several fermion discretizations which have not been used during the thesis and will not be discussed in detail.

There are essentially chirally symmetric fermion discretizations, in which we can find the overlap fermions or the domain wall fermions or perfect action. They both have an automatic chiral symmetry in the continuum limit. However, they are extremely costly in terms of computation time and both have extremely long autocorrelation time for topological observables and have some additional issues when the topological sectors is changed [44]. Another kind of chirally symmetric fermions are the Creutz fermions. They are much cheaper. However, they break a lot of discrete symmetries as parity, time reflection or charge conjugation which implies some fine tunning to restore theses symmetries in the continuum limit.

A complete different kind of fermion discretization is the staggered fermions where the doublers are treated by the rooting of the Dirac operators.

### 2.1.3 Scale setting

On the lattice, every quantity is given in units of the lattice spacing $a$. The lattice spacing is fixed by choosing the value $\beta$, nevertheless the value of $\beta$ does not give us the corresponding value in physical units. Thus one needs a method to know the value of $a$ in fm, in order to compare predictions with experimental results. Several methods exist, the most common one is to determine the ratio between the Sommer parameter $r_0$ and the lattice spacing $a$ [38].

The method implying the Sommer parameter is based on the force between two static quarks. For sufficiently heavy quarks, the quark-antiquark bound states can be described by an effective non-relativistic Schrödinger equation and the force $F(r)$ can be studied. From comparing with experimental data from $\bar{b}b$ or $\bar{c}c$ spectra one can establish very crudely that:

$$F(r_0)r_0^2 = 1.65 \tag{2.1.31}$$

corresponds to $r_0 \approx 0.5$fm. The force[1] cannot be computed directly on the lattice but the potential can be. The potential is expressed as

$$V(r) = A + \frac{B}{r} + \sigma r \Rightarrow F(r) = -\frac{B}{r^2} + \sigma, \tag{2.1.32}$$

[1]Note: The force is defined in that case with the opposite sign of the usual convention. $F(r) = \mathrm{d}\,V(r)/\,\mathrm{d}\,r$.

with $A,\ B$ and $\sigma$ some constant. $\sigma$ is called the string tension. By fitting the potential on the lattice, we obtains the results for $A$, $B$ and $\sigma$. This allows us with the help of eq. (2.1.31) to determine the ratio $r_0/a$ and so the lattice spacing $a$.

In hadronic spectroscopy, the approach is different since experimental values exist for the lowest states. They can be used to fix their scale and so give predictions for heavier states. In this thesis, we will mostly not be interested in giving results in physics units. However, we will still generally give the physical value of the lattice spacing $a$ which has been computed using the Sommer parameter method.

## 2.2 Simulating QCD

In this section we will describe the general idea of the numerical computation algorithms in lattice-QCD. Then we will describe how we extract the meaningful results as observables and masses.

### 2.2.1 General idea

We already stated in section 1.1.2 that we can numerically approximate the path integral by a Monte-Carlo method. The path integral is a high-dimensional integral over all possible gauge fields and fermions field configurations. The integration of Grassmann-valued fermion fields can always be performed analytically, leaving an integral over only the gauges fields, weighted by Boltzmann factor $e^{-S_{eff}}$, where $S_{eff}$ is an effective action. The majority of the gauge field configurations has a very large action, so their weights are negligible in the value of the integral. Therefore it is primordial to perform importance sampling. The latter is a method which favors the configurations with the lowest action, the ones which contribute the most to the integral value. If the sampling is representative, meaning that the configurations are distributed according to the action and there are enough of them, then an average value of an observable $\bar{\mathcal{O}}$ can be estimated as

$$\bar{\mathcal{O}} = \frac{1}{N}\sum_{i=1}^{N} \mathcal{O}[U_i], \tag{2.2.1}$$

where $O[U_i]$ is the value of the observable on the configuration $U_i$.

To obtain a serie of configurations $U_i$, a Monte-Carlo algorithm is generally used performing small updates of the configuration $U_i$ to obtain the next configuration $U_{i+1}$. The succession of the configurations $U_i$ is called the Markov Chain. To give the correct average, the chain has to obey ergodicity and detailed balance. The latter is expressed as:

$$e^{-S[U]}P(U \to U') = e^{-S[U']}P(U' \to U), \tag{2.2.2}$$

with $P(U \to U')$ the probability of transition from configuration $U$ to $U'$.

In the beginning of this part, we mentioned that the Grassmann-valued fermion fields have been integrated analytically meaning that our partition function defined in eq. (1.1.14) can be rewritten as:

$$Z = \int DU e^{-S_{YM}[U]} \prod_{i=1}^{N_f} \det(\hat{D}_i[U]), \tag{2.2.3}$$

where $\det(\hat{D}_i[U])$ is the result of the integration over the fermion fields $\psi_i$, it is the determinant of the Dirac operator matrix for fermions of flavour $i$. This form of the partition function implies that the distribution that has to be simulated depends of $\det(\hat{D}_i[U])$. The cost to take into account this determinant is by far the most expensive part of the Monte-Carlo simulation.

### 2.2.2 Hybrid Monte Carlo

The Hybrid Monte-Carlo algorithm [45] is composed of two main steps: a molecular dynamics update of gauge field and a Metropolis accept/reject step.

To explain the first step we will take the example of a real scalar field $q$. The Hamiltonian for the system is given by:

$$H = \frac{1}{2}p^2 + S[q], \tag{2.2.4}$$

where $S[q]$ is the action of the gauge theory that we want to simulate and $p$ is the conjugate variable of $q$. From this Hamiltonian, we get the classical Hamilton equations:

$$\begin{aligned} \dot{p} &= -\frac{\partial H}{\partial q} &&= -\frac{\partial S}{\partial q} \\ \dot{q} &= \frac{\partial H}{\partial p} &&= \quad p, \end{aligned} \tag{2.2.5}$$

where the dot represents the derivative with respect to Monte-Carlo time (Computer time). These equations are called the molecular dynamic equations as they represent the evolution of classical points. Solving these equations one obtains a trajectory in phase space, i.e the value of $p(\tau)$ and $q(\tau)$ for each Monte-Carlo time $\tau$. The HMC is now given by:

1. Generate a initial configuration for $p$ according to the distribution $\exp(-\frac{1}{2}p^2)$. It will correspond to $p(\tau = 0)$.

2. The molecular dynamics update: Solve numerically eq. (2.2.5) to obtain $p(\tau)$ and $q(\tau)$ from their initial values. From energy conservation principle, the Hamiltonian should be conserved up to numerical integration errors.

3. The Metropolis accept/reject step: the new configuration is accepted with a probability of:

   $$P = \min(1, e^{-(H(\tau)-H(0))}). \tag{2.2.6}$$

   Here $H(\tau) - H(0)$ can be different than 0 due to numerical errors. If the configuration is rejected, then $q(\tau) = q(0)$.

4. Repeat the steps 2-3 to have the number of configurations desired with initial values, i.e. values obtained at the end of step 3 of the preceding configuration. (also 1. has to be repeated from time to time)

For simulating an SU(N) theory on the lattice, the process is the same but one has:

$$\begin{aligned} &p = \pi^a_{x,\mu} \text{ and } p^2 = \sum_{x,\mu,a} \pi^a_{x,\mu}\pi^a_{x,\mu} \\ &q = U_{x,\mu} \text{ and } \dot{U}_{x,\mu} = \pi_{x,\mu}U_{x,\mu}. \end{aligned} \tag{2.2.7}$$

To simulate QCD with dynamical quarks, the previous algorithm can be used. But this is not efficient, as the fermion determinant is a highly non-local quantity and for each step, one has to compute it again completely. To overcome this problem, the pseudo-fermion method is used. It consists in replacing the fermions fields by auxiliary bosonic fields and expressing the determinant as a Gaussian integral over these fields [38]. Despite this improvement, simulating the fermionic part is by far the most computation time consuming part.

### 2.2.3 Observables in lattice

As we have observed previously in Section 1.1.2, in Euclidean physics we can compute any expected value of an observable $\mathscr{O}$ using statistical physics:

$$\langle \mathscr{O} \rangle = \frac{1}{Z^E} \int D\bar{\psi} D\psi DA \mathscr{O}[\psi, \bar{\psi}, A] e^{-S^E_{QCD}[\psi, \bar{\psi}, A]}. \tag{2.2.8}$$

This expectation value can be related to the Monte-Carlo average via the Birkhoff's theorem of ergodicity . Meaning that if the simulation is performed correctly, for $N \to \infty$, the numerical average $\bar{\mathscr{O}}$ tends to $\langle \mathscr{O} \rangle$. Then one is supposed to be able to compute any observable on the lattice with enough statistics. The convergence of the numerical average to the expectation value depends on the observable, but most of the time an order of $\mathcal{O}(1000)$ is enough.

In QCD we are essentially interested in extracting the hadron properties, especially a lot of effort is done to compute the mass of different hadrons [46–49]. To extract the mass of hadrons, one computes generally one or several particular observables which are two-point correlation functions defined by:

$$C(t) = \langle 0 | O(t) \bar{O}(0) | 0 \rangle, \tag{2.2.9}$$

where $O$ is an operator which has the same quantum numbers than the hadron that we are looking for. The operator can be seen as an element which excites the vacuum creating different independent states such that one of them corresponds to the particle that we are interested in. Since:

$$O(t) = e^{Ht} O e^{-Ht}, \tag{2.2.10}$$

one can express our two point function such that:

$$C(t) = \sum_n \langle 0 | e^{Ht} O e^{-Ht} | n \rangle \langle n | O^\dagger | 0 \rangle = \sum_n |\langle 0 | O | n \rangle|^2 e^{-(E_n - E_0)t}, \tag{2.2.11}$$

where $E_n$ is the energy of the state $|n\rangle$. For large Euclidean time separation $t$, the highest energy states is suppressed and we obtained (in case of connected two point function):

$$C(t) = |\langle 0 | O | 1 \rangle|^2 e^{-(E_1 - E_0)t} + \mathcal{O}(e^{-(E_2 - E_0)t}. \tag{2.2.12}$$

The difference of energies between the state $|1\rangle$ and the vacuum $|0\rangle$ corresponds to the mass of the particle $m_1 = E_1 - E_0$. From the previous equation one can define the mass in the following way:

$$m_1 \underset{t \to \infty}{=} -\frac{d}{dt} \ln(C(t)). \tag{2.2.13}$$

On the lattice one can apply the same method. However, we have generally a finite temporal extension $T$ and to conserve the translation invariant, it is standard to impose periodic boundary conditions. This leads to a slightly different correlation function:

$$\hat{C}(t) \cong 2 \left| \langle 0 | \hat{O} | 1 \rangle \right|^2 e^{-\frac{T}{2}(E_1 - E_0)} \cosh\left( (E_1 - E_0) \left( t - \frac{T}{2} \right) \right). \tag{2.2.14}$$

Then one gets the mass from the fit of the a $\cosh$ or one has to solve the equation:

$$\frac{\hat{C}(t)}{\hat{C}(t+1)} = \frac{\cosh\left( (E_1 - E_0)\left( t - \frac{T}{2} \right) \right)}{\cosh\left( (E_1 - E_0)\left( t + 1 - \frac{T}{2} \right) \right)}. \tag{2.2.15}$$

As an example a suitable operator to extract the charged pion mass is given by:

$$\hat{O} = \frac{1}{\sqrt{V_s}} \int \mathrm{d}^3 r \; \bar{d}(\vec{r})\gamma_5 u(\vec{r}) \tag{2.2.16}$$

where $d(\vec{r})$ and $u(\vec{r})$ are the down and up quark field respectively.

## 2.3 Topology freezing and fixing

### 2.3.1 Topology freezing

Strictly speaking the notion of topological sectors does not exist on the lattice in most of its formulations. In the continuum, a topological sector can be seen as an ensemble of configurations separated by an infinite action leading to the impossibility to have continuous deformation from one sector to the others. On the lattice, we can still define what we call a pseudo topological sector (called topological sector when no confusion with the continuum is possible) which is a set of configurations separated by a large Euclidean action and that becomes the topological sector in the continuum limit. In that sense, the pseudo topological sectors are no topological sectors and a transition between them is possible via a continuous transformation.

For our Monte-Carlo algorithm the previous statement is a positive aspect of the discretization. To obtain a meaningful result, the algorithm has to reproduce the physical distribution of the configurations and especially the distribution among different topological sectors. The possibility to change the pseudo topological sector arises from two aspects. The first one corresponds to the fact that we do not have an infinite action barrier and the second one is that a Monte-Carlo step is not a continuous transformation. However, as the action barrier is large, the transition between topological sector is statistically suppressed which implies a large autocorrelation time.

An important problem arises when we reduce the lattice spacing. As mentioned before, the possibility of transition is due to the discretization and one can expect that transitions become rarer when the lattice spacing is reduced. This is due to the Monte-Carlo steps which become smaller and to the energy barrier which turns larger. This leads to an increase of the topological autocorrelation time with a reduction of the lattice spacing. At some lattice spacings, the autocorrelation time becomes so large that generating configurations to obtain a proper distribution among pseudo topological sectors is not practically doable. This problem is well known and has been called “topology freezing” or “topological slowing down”. Several studies have been pursued to understand the evolution of the autocorrelation time. It appears that it is probably following an exponential law [3]. This phenomenon is difficult to study as it depends on a lot of different parameters as the quark mass. In figure 2.3.1[2], we observe the transition probability between topological sectors as a function of the bare coupling $\hat{g}$ and the bare mass of quark $\hat{m}/\hat{g}$ for the Schwinger model (a short description of the model with the setup of the simulation, which gives these results, can be found in Appendix A.2.1.2). The bare coupling is proportional to the lattice spacing and we observe this exponential behavior mentioned before with a saturation for a large lattice spacing. In the dark blue region, the topology is frozen.

This problem depends also on the kind of fermions used. For dynamical Wilson fermions, the problem becomes important for lattice spacing $a \leq 0.05$fm which corresponds to fine lattices but researchers start to use it. For overlap or domain wall fermions the problem appears at much coarser lattices and they are generally forced to work at fixed topology.

**Open boundary conditions** One solution called open boundary conditions has been suggested [7]. By letting one side of the box “open”, while the others are kept periodic, one allows the instantons to “leave the box”. Thus the action barrier between previous topological sectors disappears and the topological charge can

[2]This figure has been produced by Christopher Czaban during his master thesis.

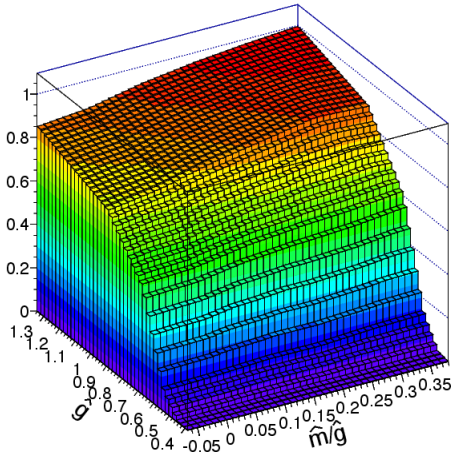


Figure 2.3.1: The probability for a transition to another topological sector per HMC trajectory as a function of $\hat{g} = 1/\sqrt{\beta}$ in the Schwinger Model (varying the lattice spacing in physical units) and $\hat{m}/\hat{g} = \hat{m}\sqrt{\beta}$ (varying the bare quark mass in physical units) for $\hat{g}\hat{L} = \hat{L}/\sqrt{\beta} = 24/\sqrt{5}$ (spacetime extension and coupling constant in physical units fixed).

fluctuate continuously. In that sense, these conditions solve the previous problem and the topology is not frozen anymore.

However, this solution raises several problems on which we have little control. The main problem is the breaking of the translation invariance. With periodic boundary conditions this symmetry of the QFT is conserved, but with open boundary conditions a translation in a open side direction will probably not conserve the results. The second problem is the loss of notion of topology. In an open spacetime, topology does not exist. In open boundary condition lattice, the topological sectors disappear completely (allowing the fluctuation of the topological charge) leading to a non-integer topological charge which is mot anymore a topological number.

The problem of translation invariance has already been studied in several occasions [7, 50, 51]. It appears that close to the open boundaries, results are largely different from the periodic results. Nevertheless when we get far away from the boundaries, the periodic boundary results are reproduced up to statistical errors. This "far away" notion has been numerically studied and it appears that to be safe, one has to consider to measure the observable in the sub-volume located between $T/4$ and $3T/4$ when $T$ is the extension of the lattice in the open boundary direction [52]. So one loses merely $50\%$ of the simulated lattice. There are also less conservative results where $30\%$ of the lattice was lost [53].

On topology, an interesting study was proposed in [52], where the autocorrelation for the topological charge has been computed not for the complete volume but for the sub-volume where the effects of translation invariance breaking are negligible. In that context, it appears that for very small lattice spacings the open boundary conditions are interesting but not as good as expected. Especially, the efficiency of open boundaries to overcome the topology freezing are inversely proportional to the extension of the lattice in the open boundary direction. Another study [53] underlines the same kind of effects. They observe that the number of instantons plus the number of anti-instantons is roughly the same between periodic boundary conditions and open boundary conditions in the safe region.

### 2.3.2 Topology fixing

Another problem which can appear with the topology is when we are using a mixed action, having different kinds of fermions in the sea and in the valence. Generally, the idea is to be able to keep some properties of the valence fermions when reducing the cost in the computing time. However, if overlap valence quarks with

Wilson sea quarks are used, the zero-modes of the valence quarks are not compensated by the zero-modes of the sea quarks. The consequence is an ill-behaved comtinuum limit [55, 91]. A possible solution to this problem is to fix the topology to zero via a topology conserving gauge action [56–58]. As for overlap quarks the probability to obtain positive and negative zero-modes in the same configuration is infinitesimally small, fixing the topology at zero will avoid zero modes to appear. Then the continuum limit obtained is expected to behave normally.

# Chapter 3

# Topological charge on the lattice

In the continuum, the topological charge is unique. All the different definitions that we will defined in this section, lead to the same integer. On the lattice, the situation is different and several problems appear. Due to the discretization the topological charge is not unique anymore and several definitions potentially lead to different results. In the following chapter, we introduce different possibilities to compute the topological charge. Then we will see how the gauge field definition is affected by UV-fluctuations and how the problem can be solved. We will present recent works to link the different possibilities to overcome the problem of UV-fluctuations. In the last section, we compare the definitions and give the pros and cons of each of them.

## 3.1 Different definitions

The definitions are of three kinds: fermionic ones based on the properties of the Dirac operator, the field ones based on gluonic fields and the geometric ones based on differential geometry properties of the vacuum. This last definition is generally used for low dimensional theories as O(2)-theory on a circle or two dimensional O(3)-theory, but it complicates to apply on SU(N). Especially this method is valid in SU(N) uniquely for smooth configurations [59] and so it is barely used in QCD and we will not present it.

### 3.1.1 Fermionic definition

#### 3.1.1.1 The index definition

The index definition can only be used with a Ginsparg-Wilson operator as it allows exact zero modes of the Dirac operator. The idea is to link the number of zero modes to the topological charge $Q$ using the well-known Atiyah-Singer index theorem [60]. According to this theorem, the topological charge is expressed as:

$$Q = n_- - n_+, \tag{3.1.1}$$

where $n_\pm$ are, respectively, the number of zero modes in the positive and in the negative chirality sector. The topological charge obtained is clearly an integer, it does not need any renormalization. However, the definition is affected by a dependence on the $s$ parameter of the kernel of the Dirac operator which can be interpreted as a cut-off effect. In practice, this method is extremely costly as it needs several inversions of the Dirac operator.

#### 3.1.1.2 The spectral flow definition

This definition is closely related to the previous one. One considers the mass dependence of the eigenvalues of the Hermitian Wilson-Dirac operator $D^\dagger D + m^2$. Looking at the evolution of each eigenvalue as a function of $m$, one can compute the topological charge by counting the number of times that the eigenvalue changes

from positive to negative sign and making the difference with the number of time that eigenvalue changes from negative to positive sign. This method is completely equivalent to the measure of the index of the overlap operator at a corresponding value of the $s$ parameter. In this definition, the mass range is a cut-off effect. This definition has all advantages of the Dirac operator at lower cost. In practice, having a continuous evolution of the eigenvalue as a function of mass is not possible.Therefore the method might suffer from difficulties in an unambiguous resolution of the crossing.

### 3.1.2 Field definition

The field definition is the most natural one as it uses explicitly the tensor field $F_{\mu\nu}$. In this definition the topological charge is defined as:

$$Q = \frac{1}{16\pi^2} \int \mathrm{d}\, x^4 \,\mathrm{Tr}\left(F_{\mu\nu}(x)\tilde{F}_{\mu\nu}(x)\right). \tag{3.1.2}$$

On the lattice, the definition suffers for several issues. In particular the naive computation of the topological charge leads to completely wrong results due to UV-fluctuations. This problem and its solution will be discussed later in section 3.2. Moreover some information on the instanton is lost due to the discretization, leading to an approximation of the results of the integrals which results in a non-integer value for the topological charge.

#### 3.1.2.1 Basic operator

In order to better understand the previous remarks, it is interesting to look closer at the field definition of the topological charge in terms of lattice fields. When we express eq. (3.1.2) on the lattice, we obtain the following expression:

$$\hat{Q} = \frac{1}{32\pi^2} \sum_n \sum_{\mu,\nu,\rho,\sigma} \epsilon_{\mu\nu\rho\sigma} \hat{F}_{\mu\nu} \hat{F}_{\rho\sigma} + \mathcal{O}(a^2), \tag{3.1.3}$$

where $\hat{F}_{\mu\nu} = \mathrm{Im}(\hat{P}_{\mu\nu}) + \mathcal{O}(a)$ with $\hat{P}_{\mu\nu}$ is the plaquette in the ($\mu$,$\nu$) plane.

As it can be observed in eq. (3.1.3), the operator $\hat{Q}$ is defined with an $a^2$ error which is at finite lattice spacing the reason to have a non-integer topological charge, meaning that in the continuum limit one should obtain a right topological charge. To understand this error better, the interpretation of the topological charge as the number of instantons subtracted by the number of anti-instantons helps. These instantons are pseudo-particles with a non local field. For one instanton, the value of $\mathrm{Tr}\left(F_{\mu\nu}(x)\tilde{F}_{\mu\nu}(x)\right)$ is always positive and if the maximum is not on lattice point, the sum $\sum_n \sum_{\mu,\nu,\rho,\sigma} \epsilon_{\mu\nu\rho\sigma} \hat{F}_{\mu\nu} \hat{F}_{\rho\sigma}$ is underestimated leading to a value of the topological charge slightly smaller than one. For the anti-instantons the same reasoning can be done leading to a topological charge slightly larger than minus one. From this reasoning, it can be estimated that the absolute value of the topological charge of the configuration is in average slightly smaller than the topological charge estimated by the number of instantons. This observation leads to a simple solution to deal with the problem previously mentioned in [61].

To reduce these lattice artifacts and improve the convergence towards the continuum limit, an estimator $Q_i$ is defined as:

$$Q_i = \mathrm{round}(\alpha \hat{Q}), \tag{3.1.4}$$

where $\mathrm{round}(x)$ denotes the closest integer to $x$ and $\alpha$ is a rescaling factor close to 1 and determined in such a way to minimize:

$$\left\langle \left(\alpha \hat{Q} - Q_i\right)^2 \right\rangle. \tag{3.1.5}$$

On figure 3.1.1, we can see the influence of the procedure to obtain a topological charge close to an integer. It can be observed on the left, that peaks are not centered on the integer but on smaller values as mentioned

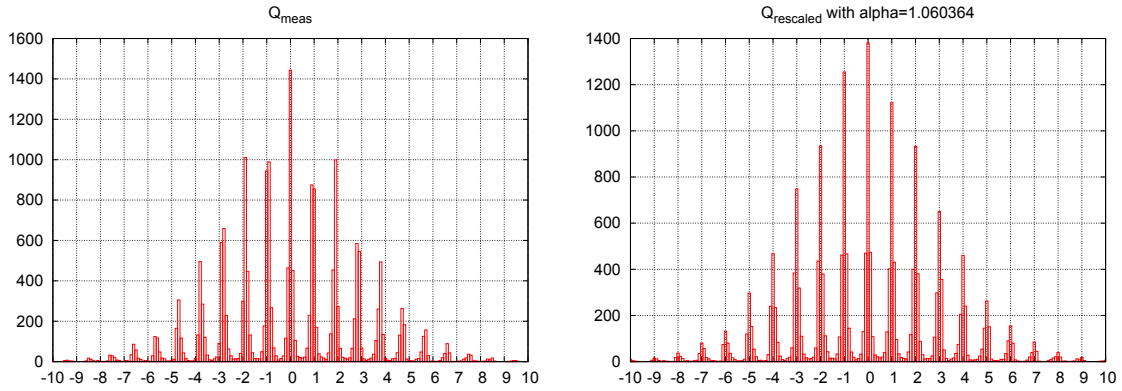


Figure 3.1.1: Topological charge distribution computed with the field definition at flow time $\tau = 8\tau_0$ for the set of configurations defined in section A.2.3.2 for a spatial extend of $\hat{L} = 16$ . On the left: The topological charge has been directly measured by the field definition with clover improvement. On the right: The topological charge has been rescaled with $\alpha \approx 1.06$.

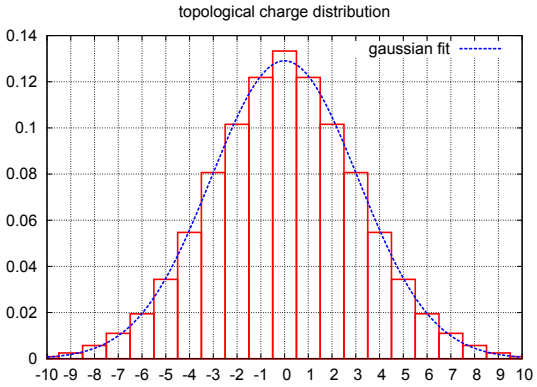


Figure 3.1.2: Normalized distribution of the integer topological charge after symmetrization between negative and positive topological charges for $8\tau_0$ using the set of configuration defined in section A.2.3.2 for a spatial extend of $\hat{L} = 16$. The dashed line represents a Gaussian fit to the distribution.

in the previous paragraph. That implies that this is difficult to attribute integer topological charges to many configurations without making errors. On the right, after the procedure, peaks are centered on integers and the amount of configurations for which it is difficult to attribute the integer topological charges is strongly suppressed. This process is particularly beneficial if one does not want to invest to much computation time. We can associate an integer to each of these configurations with little chance to make an error(depends on $\beta$ resp. $a$). In figure 3.1.2, we used the previous method and the results is a distribution nicely in agreement with a Gaussian distribution.

#### 3.1.2.2 Operator improvement

The rescaling method is rather easy to implement but the method consists only of a minimization of the average of the $\mathcal{O}(a^2)$ effects and not of a suppression of them. It is possible to make some improvement by using different operators, leading to a reduction of the errors or to the suppression of $\mathcal{O}(a^2)$ or even $\mathcal{O}(a^4)$ errors. Those techniques imply relations with higher loop operators.

Let us first consider the clover improvement which is the easiest improvement to apply. The procedure

| Improvements | Clover | Symanzik | 3Loops | 4Loops | 5Loops |
|---|---|---|---|---|---|
| $\alpha$ | $1.060(8)$ | $1.022(7)$ | $1.002(10)$ | $0.998(5)$ | $1.001(4)$ |

Table 3.1.1: Results of the rescaling parameter for a flow time $\tau = 8\tau_0$ using the set of configuration defined in section A.2.3.2 for a spatial extend of $\hat{L} = 16$.

consists of replacing the plaquette $\hat{P}^{\mu\nu}$ by an operator $\hat{P}_c^{\mu\nu}$ involving a greater number of loops, defined as:

$\hat{P}_c^{\mu\nu} =$ 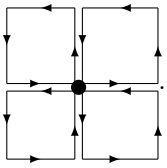 . (3.1.6)

This first improvement will reduce the $\mathcal{O}(a^2)$, however, they will not be suppressed and a rescaling will still be necessary (cf. table 3.1.1). The next step involves rectangular loops ($2 \times 1$), this improvement is called the Symanzik improvement [62] which has only $\mathcal{O}(a^4)$ artifacts, but it is still not sufficient to make a rescaling useless (cf. table 3.1.1). To get distribution peaks on integer (rescaling parameter equal 1 up to some statical error), one has to suppress any lattice artifact below $\mathcal{O}(a^6)$ [63]. In order to do so, one can consider the following operator for the topological charge :

$$\hat{Q}_{Imp}(c_5) = \frac{1}{32\pi^2} \sum_n \sum_{\mu,\nu,\rho\sigma} \epsilon_{\mu\nu\rho\sigma} \sum_{i=1}^{5} \frac{c_i}{m_i^2 n_i^2} \hat{F}^{\mu\nu}_{(m_i,n_i)} \hat{F}^{\rho\sigma}_{(m_i,n_i)} \tag{3.1.7}$$

where the operator $\hat{F}^{\mu\nu}_{(m_i,n_i)}$ is defined as:

$\hat{F}^{\mu\nu}_{(m_i,n_i)} = \frac{1}{8}\mathrm{Im}\Big($ 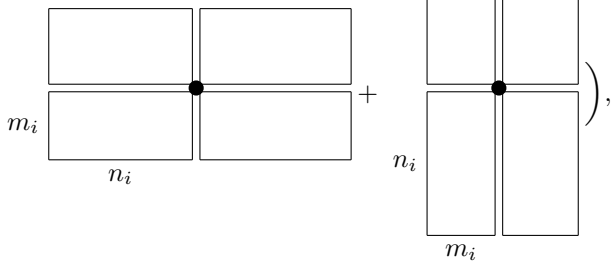 $\Big)$, (3.1.8)

with $(m_i,n_i)$=(1,1), (2,2), (1,2), (1,3) and (3,3), $c_1 = (19-55c_5)/9$, $c_2 = (1-64c_5)/9$ , $c_3 = (-64+640c_5)/45$ and $c_4 = (1/5-2c_5)$. The value of $c_5$ can be chosen to be $1/10$ for which only the three square loops contribute ((1,1), (2,2) and (3,3)), 0 thus only the four loops (1,1), (2,2), (1,2), (1,3) contribute or $1/20$ where all the five loops contribute. Only those three values allow the suppression of $\mathcal{O}(a^4)$ lattice artifact. The difference between them are the amplitude of the $\mathcal{O}(a^6)$ lattice artifacts. All three values of $c_5$ give a value of $\alpha$ compatible with 1 (cf. table 3.1.1). This leads to the conclusion that the values obtained are closed to an integer and that rescaling is not necessary. Others improvements exist as the Iwasaki improvement [64].

## 3.2 Field definition and UV-fluctuations

In the previous section, the most problematic part of the field definition has been avoided. As we mentioned before, the field definition cannot be employed naively and one has to apply a smoothing procedure.

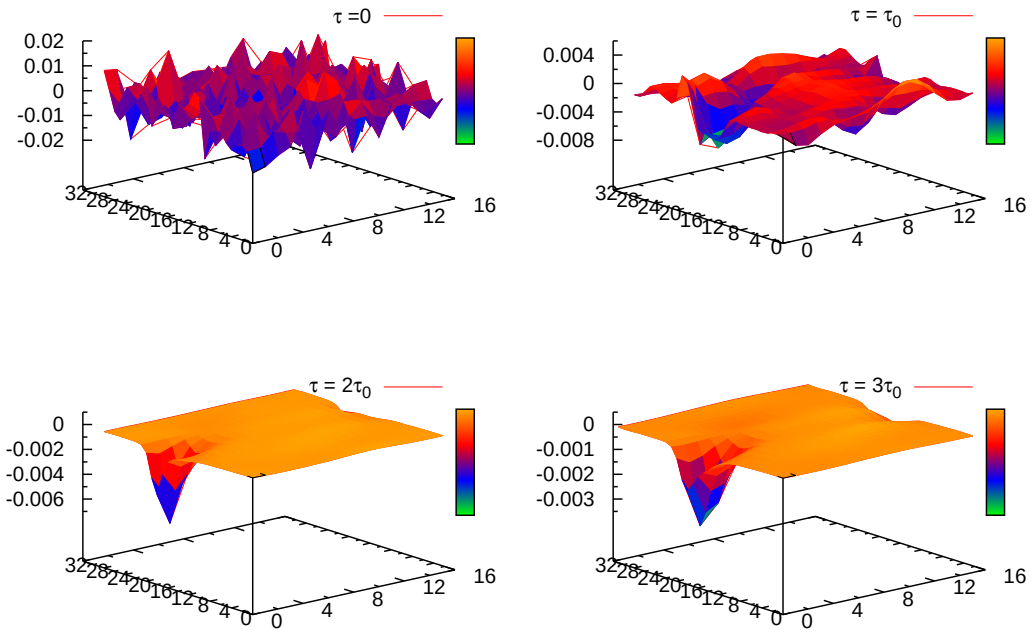


Figure 3.2.1: Topological charge density as a function of $t$ and $x_3$ for the plane defined by $x_1 = 7$ and $x_2 = 4$ for 4 different flow times (cf. section 3.2.2.3) . **Top left:** flow time $\tau = 0$, no smoothing has been done. **Top right:** flow time $\tau = \tau_0$. **Bottom left:** flow time $\tau = 2\tau_0$. **Bottom right:** flow time $\tau = 3\tau_0$.

### 3.2.1 The problem of the UV-fluctuation

The UV-fluctuations on the lattice are particularly bothersome with respect to the computation of the topological charge. They appear as statistical noise and so they should cancel each other for a large number of configurations. This is the case when we can average over independent configurations, but it is not the case when we compute a value on one configuration. The reason is that the number of non-correlated points on the lattice is much too small.

For the topological charge computation the fluctuations appear as peaks which are computed by the operator as they were instantons, which can lead to a completely wrong result (cf. the first steps of figure 3.2.2). In order to avoid this problem one has to smooth out the UV-fluctuations. On figure 3.2.1, we can see an illustration of the a smoothing process (gradient flow: cf. section 3.2.2.3) on a configuration of the ensemble defined in A.2.3.2 for $\hat{L} = 16$. At flow time equal zero, no smoothing has been realized and it is not possible to see any structure due to the large UV-fluctuation (cf. the scale of the top left plot of figure 3.2.1 compared to the other scales). At $\tau = \tau_0$, some smoothing has already been applied and we can see an anti-instanton emerged from the noise. At $\tau = 2\tau_0$ and $\tau = 3\tau_0$, the anti-instanton is clearly visible and the noise is negligible. Note, that with flow time the anti-instanton signal spreads on the lattice.

### 3.2.2 Smoothing procedure

A lot of different kinds of smoothing procedures exist, they are generally close to each other and we will see in section 3.3.1 that one can link some of them perturbatively. Here we will not present all processes but we will focus on three of them, from the older to the newer: the cooling [66], the APE-smearing [67] and the gradient flow [68].

#### 3.2.2.1 Cooling

Cooling has been the first procedure introduced to get rid of UV-fluctuations. The cooling method proceeds in discrete steps, which locally minimize the gauge action. The process is done first for one link and then it propagates through the lattice. A cooling step is defined by the modification of all links. Then the procedure is repeated to achieve the local minimization of the action.

In order to precisely describe the process, let us define our notation: $\hat{U}_\mu(x)$ is a link and $\hat{S}_{l\,\mu}(x)$ is the staple associated to $\hat{U}_\mu(x)$. The SU(N) action is the following:

$$S = \frac{2N}{g_0^2} \sum_{x,\mu>0} \left(1 - \frac{1}{N}\text{Re}\left(\text{Tr}\left(\hat{U}_\mu(x)\hat{S}_{l\,\mu}^{\dagger}(x)\right)\right)\right). \tag{3.2.1}$$

Now we explain a cooling step in detail:

- Start with a link $\hat{U}_\mu(x)$. To minimize the action one has to maximize $\hat{U}_\mu(x)\hat{S}_{l\,\mu}^{\dagger}(x)$, which means replacing $\hat{U}_\mu(x)$ by:
$$\hat{U}_\mu(x) = \text{Proj}_{\text{SU(N)}}\left(\hat{S}_{l\,\mu}(x)\right). \tag{3.2.2}$$
- Here is important to stress that the link is replaced directly, which means that for computing the other links (e.g. $\hat{U}_\mu(x+\mu)$ or $\hat{U}_\nu(x)$), the already updated link is used.
- Replace all the links of the lattice using the same process. The step is over when all links have been replaced.

The cooling step is repeated $n_c$ times, reducing the action more and more. If the algorithm would only suppress the UV-fluctuations, the larger $n_c$ is, the better it is. Unfortunately this is not the case, this algorithm is a discrete transformation of the configurations and so can destroy the topology. In reality it appears rather often that some instantons are destroyed in the cooling process (cf. figure 3.2.2), leading ultimately to $Q = 0$ for a very large amount of cooling steps.

So when dealing with cooling one has to find a compromise between obtaining a topological charge not too much affected by UV-fluctuations and avoiding to destroy topology. This compromise is not easily achieved and it is difficult to estimate if the topology of the configuration has already been changed. Another problem which appears when we measure quantities on a cooled configuration is the diffusion process. As it can be observed, the cooling procedure is a kind of averaging over links transporting information present on one link to other links. This diffusion process increases the correlation between the links and makes the extraction of local quantities difficult.

In order to fix the problem of non-stability of the topology under cooling several attempts have been made. One which is probably most interesting is the improved cooling [63]. The idea is rather similar to the improvement of the topological charge operator. As the problem is coming from the fact that the process is discrete, we can limit this effect by minimizing an improved version of the action:

$$\hat{S}_{Imp}(c_5) = \sum_{i=1}^{5} \frac{c_i}{m_i^2 n_i^2} \hat{S}_{(m_i,n_i)}, \tag{3.2.3}$$

with

$$\hat{S}_{(m_i,n_i)} = \frac{2N}{g_0^2} \sum_{x,\mu,\nu} (1 - \frac{1}{N}\text{Re}(\text{Tr}( \tag{3.2.4}$$

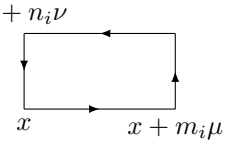


$$)))$$

and $c_i$ and $(m_i, n_i)$ defined as in the eq. (3.1.7). Applying an improved cooling leads to a much more stable topological charge [63].

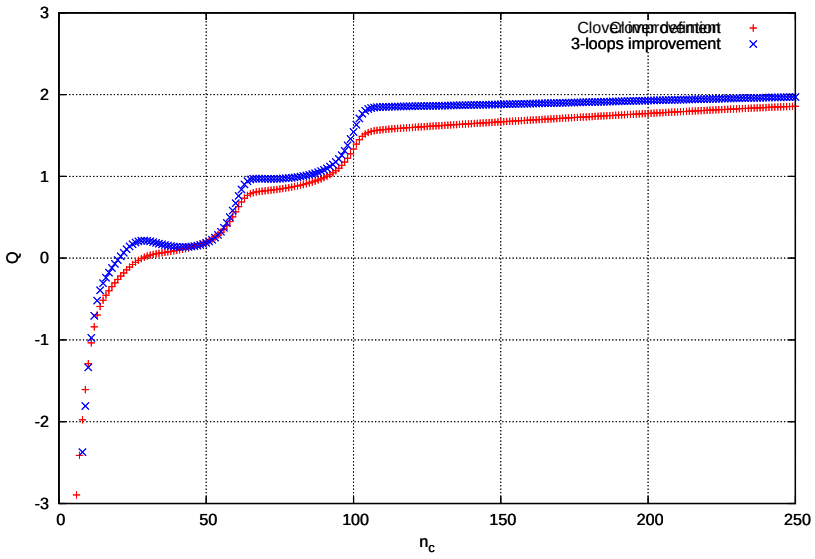


Figure 3.2.2: Topological charge as a function of the non improved cooling steps for clover improved and 3-loops improved topological charge operator. Two destructions of anti-instantons can be observed around step 60 and step 100.

#### 3.2.2.2 APE-smearing

The APE-smearing is a discrete procedure that eliminates short-distance fluctuations by averaging them. In that sense, it suppresses the UV-fluctuations as the average of them is 0 (random noise), when the topology should be preserved as the instantons are not compensated by the anti-instantons if the topological charge is different than 0. Moreover, the averaging is just local and should not destroy large structures. The procedure is defined by the following steps:

- $\hat{U}_\mu^{(n)}(x)$ with $n$ the number of APE steps is replaced by $\hat{U}_\mu^{(n+1)}(x)$.

$$\hat{U}_\mu^{(n+1)}(x) = \text{Proj}_{\text{SU(N)}} \left[ (1-\alpha)\hat{U}_\mu^{(n)}(x) + \frac{\alpha}{6}\hat{S}_{l_\mu}^{(n)}(x) \right], \tag{3.2.5}$$

  with $\alpha$ the smearing parameter.

- As it can be observed, in contrast to cooling, the update of the links is done in parallel, i.e. the expression of the updated link can not include already updated links.

- A step of APE-smearing is the update of all links.

The APE-smearing suffers unfortunately from the same problems as cooling, i.e the possibility to smooth out the topology and the diffusion. Here the adjustable parameter $\alpha$ represents a small advantage to avoid to smear out a topological object. The presence of $\alpha$ allows to adjust the "speed" of the smoothing. With a small $\alpha$, smearing becomes smoother making the detection of the destruction of an instanton easier. A small $\alpha$ also increases the time needed to get rid of UV-fluctuations. On the other side, a large $\alpha$ corresponds to a fast smearing. For $\alpha$ too large a problem appears as the convergence of the algorithm is not sure. For configurations issue from the B39.16 ensemble (c.f. Appendix A.2.3.1) , we have observed a non-convergence of the algorithm for $\alpha \geq 0.7$.

To reduce the problem of the destruction of instantons, one can improve the APE-smearing process. The method is equivalent to the cooling in the sense that the staple has to be modified as:

$$\hat{S}_{l\,Imp}^{\ \mu}(c_5) = \sum_{i=1}^{5} \frac{c_i}{m_i^2 n_i^2} \hat{S}_{l(m_i,n_i)}^{\ \mu}, \tag{3.2.6}$$

where $\hat{S}_{l(m_i,n_i)}^{\ \mu}$ is such as $\hat{U}^{\mu}(x)\hat{S}_{l(m_i,n_i)}^{\dagger\mu}(x)$ is the sum of all loops of size $m_i \times n_i$ or $n_i \times m_i$ which include the link $\hat{U}^{\mu}(x)$. For example, $\hat{S}_{l(1,2)}^{\ \mu}$ is given by:

$$\hat{S}_{l(1,2)}^{\ \mu} = \sum_{\nu\neq\mu}$$

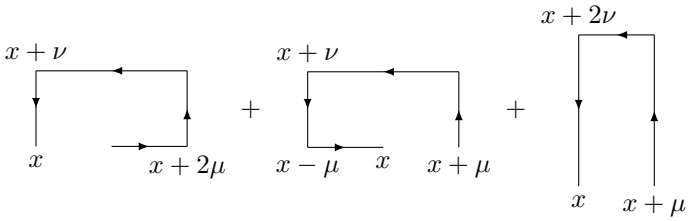


$$+ (\nu \rightarrow -\nu). \tag{3.2.7}$$

#### 3.2.2.3 Gradient Flow

The gradient flow is the most recent method. In contrast to the other methods, it can be considered independently of the simple procedure of smoothing. One can consider the gradient flow equation as the equation of evolution of a field in 5D

$$\begin{aligned} \dot{V}_{\mu}(x,\tau) &= -g_0^2[\partial_{x,\mu} S(V(\tau))]V_{\mu}(x,\tau) \\ V_{\mu}(x,0) &= U_{\mu}(x) \end{aligned}, \tag{3.2.8}$$

where $\tau$ is the flow time (the coordinate in the 5th dimension), $\dot{f}$ means the derivative of $f$ with respect to flow time $\tau$ and $\partial_{x,\mu}$ is the link derivative that can be defined as:

$$\partial_{x,\mu} f(U) = i \sum_a T^a \frac{\mathrm{d}}{\mathrm{d}\, s} f(e^{isX^a} U)\bigg|_{s=0}, \tag{3.2.9}$$

with

$$X^a = \begin{cases} T^a & \text{if } (y,\nu) = (x,\mu) \\ 0 & \text{otherwise} \end{cases}. \tag{3.2.10}$$

This leads to

$$g_0^2 \partial_{x,\mu} S(\hat{U}_{\mu}^{GF}(\tau)) = \frac{1}{2}\left(\Omega_{\mu} - \Omega_{\mu}^{\dagger}\right) - \frac{1}{2N}\,\mathrm{Tr}\left(\Omega_{\mu} - \Omega_{\mu}^{\dagger}\right), \tag{3.2.11}$$

with $\Omega_{\mu} = \hat{U}_{\mu}\hat{S}_{l\,\mu}$.

This equation is clearly a diffusive process reducing locally the field (in that sense, it is close to cooling) and its implication leads to a smoothing of the configuration. The diffusion process can be studied and specially we can compute the radius of diffusion which is given by $\sqrt{8\tau}$. In contrast to other processes, the gradient flow is a continuous process and therefore is not destroying topologies.

An interesting property of the gradient flow concerns the scale setting. Perturbation theory suggests that the energy density of the gauge field $\langle E \rangle$ scales the continuum limit like a physical quantity of dimension $4$. The scaling behavior of $\langle E \rangle$ can be checked by defining a reference scale $\tau_0$ through the implicit equation:

$$\tau^2 \langle E \rangle\big|_{\tau=\tau_0} = 0.3. \tag{3.2.12}$$

If $\langle E \rangle$ is physical, the dimensionless ratio $\tau_0/r_0^2$, with $r_0$ the Sommer parameter (cf. section 2.1.3) is independent of the lattice spacing $a$ up to corrections vanishing in the continuum limit. Then $\tau_0$ becomes the equivalent of $r_0$ to set the scale, but in this case no fitting is necessary.

**Numerical implementation** In order to implement the gradient flow on the lattice, eq. (3.2.8) can be rewritten as:

$$\dot{V}(x,\tau) = Z(V(x,\tau))V(x,\tau), \tag{3.2.13}$$

with $V(x,\tau)$ belongs to the Lie group $G$ of all gauge fields ($G$ =SU(3) for QCD) and $Z(V(x,\tau))$ belongs to the Lie algebra of $G$. From this point of view, the gradient flow equation is an ordinary first-order differential equation. Once we have noticed it, solving numerically the equation is easy and just needs the implementation of the Runge-Kutta scheme, that can be expressed as (following the paper of [68]):

$$\begin{aligned} W_0 &= V(x,\tau) \\ W_1 &= \exp\left(\frac{1}{4}Z_0\right) W_0 \\ W_2 &= \exp\left(\frac{8}{9}Z_1 - \frac{17}{36}Z_0\right) W_1 \\ V(x,\tau+\epsilon) &= \exp\left(\frac{3}{4}Z_2 - \frac{8}{9}Z_1 + \frac{17}{36}Z_0\right) W_2, \end{aligned} \tag{3.2.14}$$

where $Z_i = \epsilon Z(W_i)$, $i = 0,1,2$. This scheme corresponds to a second order Runge-Kutta scheme leading to an error of $\mathcal{O}(\epsilon^3)$. Empirically one finds that the integration is numerically stable in the direction of positive flow time and a step of $\epsilon = 0.01$ is sufficient. Figure 3.2.1 represents the influence of gradient flow on the topological charge density. The noise is reduced by the procedure and the topological structure appears clearly.

## 3.3 Comparing the definition

Hard work has been done in collaboration to publish an extensive comparison for most of the topological charge definitions [17, 22]. In this part, we will restrain ourself to topological charge definition used in the thesis. We will first have a look at the perturbative matching of cooling, APE-smearing and gradient flow. Then we will see the correlation between the topological charge and the results obtained for the topological susceptibility in each case. And to finish, we will sum-up the pros and cons of all different topological charge definitions described in the thesis. For an extensive comparison the reader is invited to read [17, 22].

### 3.3.1 Smoothing process and matching

A first relation was found in [69] between gradient flow and cooling, and in [70] the authors have extended the results to the improved cooling procedure. Here, we will repeat the calculus for cooling, but also look at the matching between gradient flow and APE. Those results will be published in [21], including more smoothing processes that we will not mention here.

In order to simplify the notation we will use $\hat{U}_\mu^{GF}$ for the gradient flow, $\hat{U}_\mu^{cool}$ for cooling and $\hat{U}_\mu^{APE}$ for APE smearing. We will also call $\Omega_\mu(x) = \hat{U}_\mu(x)\hat{S}_{l\,\mu}^{\dagger}(x)$.

For sufficiently smoothed configurations, we consider that all links are close to the unity element of the gauge group. In this approximation the link can be written as:

$$\hat{U}_\mu = 1 + i\sum_a u_\mu^a(x)T^a + \mathcal{O}(u^2), \tag{3.3.1}$$

where $u_\mu^a$ are infinitesimal quantities. And the staple is expressed as:

$$\hat{S}_{l\,\mu} = 6 + i\sum_a s_\mu^a(x)T^a, \tag{3.3.2}$$

where $s_\mu^a$ is also an infinitesimal quantity, and the constant 6 is coming from the sum in the 3 directions different from $\mu$, and the factor 2 from the fact that we have to consider positive and negative directions. $\Omega_\mu$ can now be expressed perturbatively:

$$\Omega_\mu(x) = 6 + i\sum_a (6u_\mu^a(x) - s_\mu^a(x))T^a. \tag{3.3.3}$$

The diverse solutions of smoothing: eq. (3.2.2), eq. (3.2.5) and eq. (3.2.8), can be rewritten perturbatively.

**Gradient flow** Using eqs. (3.2.11) and (3.3.3), one can express pertubatively the derivative of the action as:

$$g_0^2\partial_{x,\mu}S(\hat{U}_\mu^{GF}(\tau)) = i\sum_a \left(6u_{\mu,}^{GF,a}(\tau) - s_\mu^{APE,a}(\tau)\right)T^a \tag{3.3.4}$$

Then the gradient flow equation (3.2.8) leads to :

$$\begin{aligned}
\hat{U}_\mu^{GF}(\tau+\epsilon) - \hat{U}_\mu^{GF}(\tau) &= -i\epsilon\sum_a \left(6u_\mu^{GF,a}(\tau) - s_\mu^{GF,a}(\tau)\right)T^a \times \left(1 + i\sum_b u_\mu^{GF,b}(\tau)T^b\right) \\
&\Leftrightarrow \hat{U}_\mu^{GF}(\tau+\epsilon) = \hat{U}_\mu^{GF}(\tau) - i\epsilon\sum_a \left(6u_\mu^{GF,a}(\tau) - s_\mu^{GF,a}(\tau)\right)T^a \\
&\Leftrightarrow u_\mu^{GF,a}(\tau+\epsilon) = u_\mu^{GF,a}(\tau) - \epsilon\left(6u_\mu^{GF,a}(\tau) - s_\mu^{GF,a}(\tau)\right).
\end{aligned} \tag{3.3.5}$$

**Cooling:** For cooling we start from eq. (3.2.2) to express it pertubatively:

$$\begin{aligned}
\hat{U}_{n+1,\mu}^{cool}(x) = \text{Proj}_{\text{SU(N)}}\left(\hat{S}_{l\,n,\mu}^{\;cool}(x)\right) &\Rightarrow 1 + i\sum_a u_{n+1,\mu}^{cool,a}(x)T^a = \text{Proj}_{\text{SU(N)}}\left(6 + i\sum_a s_{n,\mu}^{cool,a}(x)T^a\right) \\
&\Rightarrow 1 + i\sum_a u_{n+1,\mu}^{cool,a}(x)T^a = 1 + i\sum_a \frac{s_{n,\mu}^{cool,a}(x)}{6}T^a \\
&\Rightarrow u_{n+1,\mu}^{cool,a}(x) = \frac{s_{n,\mu}^{cool,a}(x)}{6}.
\end{aligned} \tag{3.3.6}$$

It can easily be rewritten in a way close to the gradient flow:

$$u_{n+1,\mu}^{c,a}(x) = u_{n,\mu}^{c,a}(x) - \frac{1}{6}\left(6u_{n,\mu}^{c,a}(x) - s_{n,\mu}^{c,a}(x)\right). \tag{3.3.7}$$

The two perturbative equations eqs. (3.3.7) and (3.3.5) give a one-to-one correspondence between cooling and gradient flow if $\epsilon$ is taken such that $\epsilon = 1/6$. However, we have not yet considered how the updating is done. The staple in gradient flow is constructed with gauge links all computed at the same flow time $\tau$. On the contrary to gradient flow, the staple in the cooling process contains updated and non updated links. The number of already updated links in the staple depends on the position of the link in the lattice. However, the average of updated links and non-updated links in a staple can be computed via a diffusive model. It appears on average that a staple contains as much updated link that non-updated. The presence of already half of updated links in the staple appears as a general increase of the cooling algorithm speed by a factor of 2. This modifies the one-to-one correspondence to:

$$\tau = \frac{n_c}{3}. \tag{3.3.8}$$

**APE-smearing:** The computation for the APE-smearing is very close to cooling . Starting from eq. (3.2.5), we get:

$$\begin{aligned}
&\hat{U}^{APE}_{n+1,\mu}(x) = \text{Proj}_{\text{SU(N)}}\left[(1-\alpha)\hat{U}^{APE}_{n,\mu}(x) + \frac{\alpha}{6}\hat{S}_l{}^{APE}_{n,\mu}(x)\right] \\
&\Rightarrow 1 + i\sum_a u^{APE,a}_{n+1,\mu}(x)T^a = \text{Proj}_{\text{SU(N)}}\left(1 + i\sum_a\left((1-\alpha)u^{APE,a}_{n,\mu}(x) + \frac{\alpha}{6}s^{APE,a}_{n,\mu}(x)\right)T^a\right) \\
&\Rightarrow u^{APE,a}_{n+1,\mu}(x) = (1-\alpha)u^{APE,a}_{n,\mu}(x) + \frac{\alpha}{6}s^{APE,a}_{n,\mu}(x) \\
&\Rightarrow u^{APE,a}_{n+1,\mu}(x) = u^{APE,a}_{n,\mu}(x) - \frac{\alpha}{6}\left(6u^{APE,a}_{n,\mu}(x) - s^{APE,a}_{n,\mu}(x)\right).
\end{aligned} \tag{3.3.9}$$

This leads to an one-to-one correspondence between APE-smearing and gradient flow if $\epsilon$ is taken such that $\epsilon = \alpha/6$. As links are updated in the same way by both algorithm, no additional factor is needed. Thus the result is:

$$\tau = \alpha\frac{n_{APE}}{6}. \tag{3.3.10}$$

The one-to-one correspondence between gradient flow and cooling and the one-to-one correspondence between gradient flow and APE-smearing implies an one-to-one correspondence between APE-smearing and cooling:

$$n_c = \alpha\frac{n_{APE}}{2}. \tag{3.3.11}$$

These different correspondences relate the different processes between them and prove that they are only different kinds of discretizations of the gradient flow equations. This observation gives a theoretical justification for all of them while so far cooling and APE-smearing were only technical tricks. This equivalence also allows for the comparison of smoothed configurations between them. Moreover using the scaling properties of the gradient flow and the matching, we can use cooling or APE-smearing to set the scale.

In figure 3.3.1 we observed the action value of a configuration selected randomly in the ensemble defined in A.2.3.2 with the spatial extend $\hat{L} = 16$. At small gradient flow times, the curves do not agree, while for large flow time they agree perfectly. This observation makes perfect sense as the relations obtained before are perturbative relations. At small flow times, the UV-fluctuations are still important and the configurations are highly non-perturbative and the approximation eq. (3.3.1) is not valid anymore. For large gradient flow times, the configuration are smooth and the UV-fluctuations are negligible. This leads to small differences at small flow times and almost equal values for large flow times as observed in the plot. This confirms the correspondences obtained.

### 3.3.2 Correlation and choice of operators

We have seen previously different methods to compute the topological charge. In the case of the field definition we were able to link several smoothing procedures perturbatively. However, it is difficult to know if the different processes are equivalent or not, i.e. whether we obtain the same values whatever methods and operators we used. We already answered partially the question by saying that the topological charge is not unique on the lattice. However, to have a more complete answer to the question, we have a look at the correlation between the different methods used to compute the topological charge. In table 3.3.1 and in figure 3.3.2 the results of the correlation for 6 different methods are presented[1]. We can first observe that the field definition without smoothing procedure is not correlated to the others, which is clearly the effect of the UV-fluctuations (cf. section 3.2) and mostly statistical fluctuations are computed. The study of the array reveals an extremely strong correlation ($> 95\%$) between methods of the same kind (fermionic or bosonic) which can be expected due to the similitudes of the methods. The most interesting point is the correlation between fermionic and bosonic definitions which are superior to $80\%$.

[1] Results of the index have been computed by K. Cichy and for the spectral flow by F. Bruckmann.

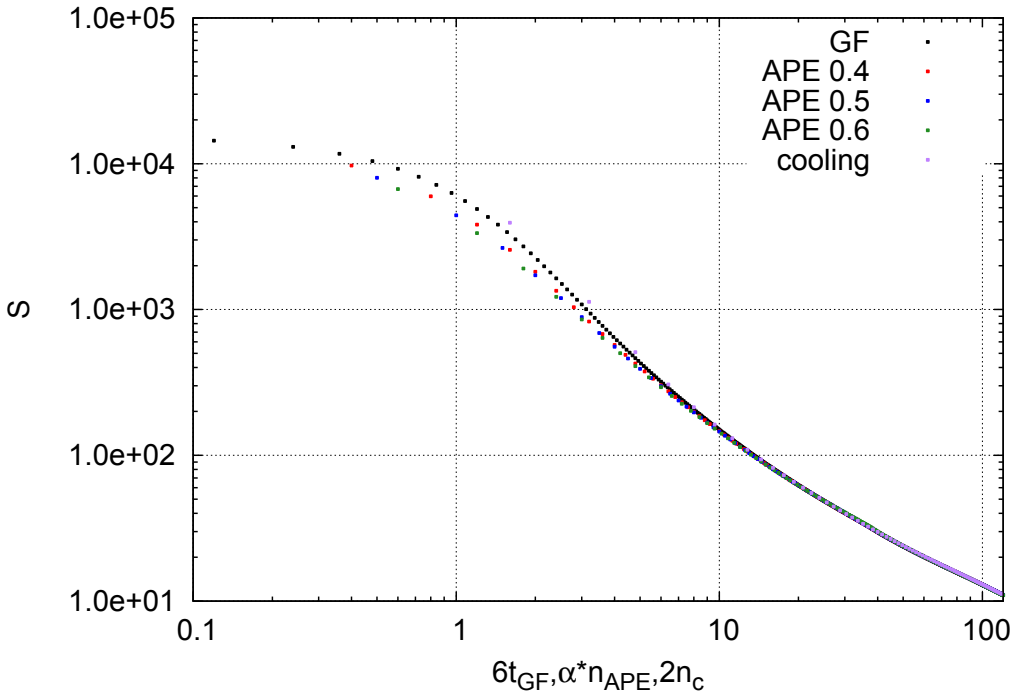


Figure 3.3.1: Evolution of the action under smoothing for gradient flow (GF), APE smearing ($\alpha = 0.4,\ 0.5$ and $0.6$) and cooling for a random configuration from the ensemble defined in A.2.3.2 with the spatial extend $\hat{L} = 16$. The abscissa has been adjusted to match the relations (3.3.8), (3.3.10) and (3.3.11).

Another interesting question is the comparison of field definitions with smoothing between them and with different numbers of smoothing steps. It appears that the correlation is always $> 90\%$ for different levels of smoothing. The comparison has been done between topological charges measured at $\tau_0$ (or equivalent) and $3\tau_0$ (or equivalent). Between the different smoothing procedures the correlation is extremely high as mentioned before. The correlation between the same amounts of smoothing (using the equivalence (3.3.8), (3.3.10) and (3.3.11)) is higher than between different amounts of smoothing, as expected.

A question has not been properly answered yet: Which method should be used? In order to answer this question, we have to sum-up the properties of each definition in the table 3.3.2. From this table, it appears that the only advantage of the index definition is to have an integer. This can be compensated for the field definition as we have seen before. The conclusion of the summary is that if we need to implement an operator to compute the topological charge the field definition with a gradient flow smoothing is probably the best choice. Nevertheless, as we have observed, every definition studied gives similar results. Hence there is little reason to change the method if we already have one.

| | Index | SF | Field NS | Field GF | Field Cool | Field APE |
|---|---|---|---|---|---|---|
| Index | 1 | 0.95(0) | 0.18(6) | 0.82(2) | 0.81(2) | 0.82(2) |
| SF | 0.95(0) | 1 | 0.17(4) | 0.81(2) | 0.80(1) | 0.83(1) |
| Field NS | 0.18(6) | 0.17(4) | 1 | 0.14(4) | 0.14(4) | 0.14(4) |
| Field GF | 0.82(2) | 0.81(2) | 0.14(4) | 1 | 0.96(0) | 0.98(0) |
| Field Cool | 0.81(2) | 0.80(1) | 0.14(4) | 0.96(0) | 1 | 0.95(0) |
| Field APE | 0.82(2) | 0.83(1) | 0.14(4) | 0.98(0) | 0.95(0) | 1 |

Table 3.3.1: Correlation between different topological charge definitions for the ensemble defined in section A.2.3.1. The definition used are: the index definition with $s = 0.4$, spectral flow (SF) with $s = 0.5$, the clover field definition but not smooth (NS), the clover field definition with gradient flow (GF) at $3\tau_0$, with cooling (Cool) for $n_c \approx 9\tau_0$ and with APE smearing with $\alpha = 0.5$ and $n_{APE} \approx 36\tau_0$.

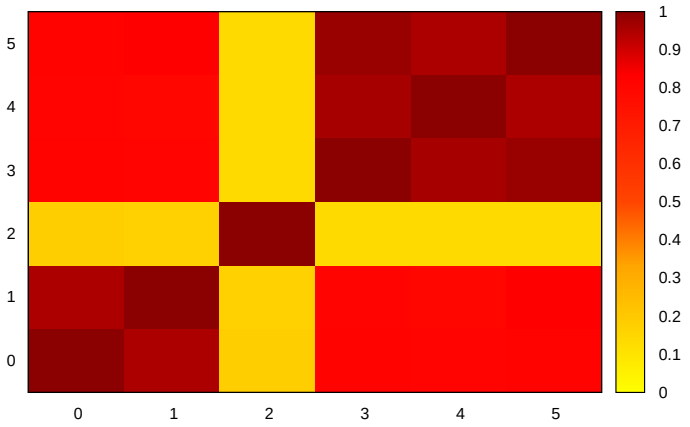


Figure 3.3.2: Representation of the table 3.3.1.

| Kind | Fermionic | | Bosonic | | |
|---|---|---|---|---|---|
| Method | Index | SF | GF | Cooling | APE |
| Integer | yes | yes | no | no | no |
| Specific operator | overlap | overlap | no | no | no |
| Theoretical sound definition | yes | yes | yes | linked GF | linked GF |
| Destruction of topology | no | no | no | yes | yes |
| Computation time | +++ | ++ | = | - | - |
| Parameter dependence | $s$ | $m$ | flow time | $n_c$ | $n_{APE}$ |

Table 3.3.2: Summary of pros and cons for the method of computation of the topological charge. In the computation time dependence, $+$ means that the method is costly compared to gradient flow, several $+$ mean extremely costly (several orders of magnitudes). $-$ means that the method is cheaper.

# Chapter 4

# The BCNW-equation

As we have observed in Section 2.3, it is interesting to understand the error made when we are performing computations at fixed topology and to develop a method to extract physical results from fixed or frozen topology simulations. In this chapter, we will introduce the theoretical part necessary to find such a method. We will particularly focus on the BCNW-equation and the different extensions that we calculated.

## 4.1 The partition function $Z_{Q,V}$ at fixed topology and finite spacetime volume

In this section we calculate the dependence of the Euclidean QCD partition function at fixed topological charge $Q$ on the spacetime volume $V$, denoted as $Z_{Q,V}$, up to $\mathcal{O}(1/V^3)$.

### 4.1.1 Calculation of the $1/V$ expansion of $Z_{Q,V}$

We have seen in section 1.2.4 that the partition function of the $\theta$-vacuum can be expressed as:

$$\mathcal{Z}_{\theta,V} \equiv \int DA\, D\psi\, D\bar{\psi}\, e^{-S_{E,\theta}[A,\bar{\psi},\psi]} = \sum_n e^{-E_n(\theta,V_s)T} \tag{4.1.1}$$

where $T$ is the periodic time extension, $V_s$ the spatial volume, $V = TV_s$, $E_n(\theta, V_s)$ is the energy eigenvalue of the $n$-th eigenstate of the Hamiltonian and $S_{E,\theta}$ the Euclidean QCD action with the $\theta$ term. Similarly, the Euclidean QCD partition function at fixed topological charge $Q$ and finite spacetime volume $V$ is defined as

$$Z_{Q,V} \equiv \int DA\, D\psi\, D\bar{\psi}\, \delta_{Q,Q[A]} e^{-S_E[A,\bar{\psi},\psi]}. \tag{4.1.2}$$

with $S_E$ the Euclidean QCD action without $\theta$ term. Using

$$\delta_{Q,Q[A]} = \frac{1}{2\pi} \int_{-\pi}^{+\pi} d\theta\, e^{i(Q-Q[A])\theta} \tag{4.1.3}$$

it is easy to see that $Z_{Q,V}$ and $\mathcal{Z}_{\theta,V}$ are related by a Fourier transform as mentioned in section 1.2.4,

$$Z_{Q,V} = \frac{1}{2\pi} \int_{-\pi}^{+\pi} d\theta\, e^{iQ\theta}\, \mathcal{Z}_{\theta,V}. \tag{4.1.4}$$

In our non interacting instanton model we have found that $E_n(\theta, V_s) = E_n(-\theta, V_s)$ (cf. eq. (1.2.29)). This

result can be generalized to many quantum field theories. They need to possess quasi-particles and quasi-anti-particles which are topological objects distributed according to the same law. It represents the symmetry between instantons and anti-instantons and implies $(d/d\theta)E_n(\theta, V_s)|_{\theta=0} = 0$. Using this together with eq. (4.1.1) one can express the topological susceptibility according to

$$\chi_{\mathrm{t}} = \lim_{V_s\to\infty} \frac{E_0^{(2)}(\theta, V_s)}{V_s}\bigg|_{\theta=0} = e_0^{(2)}(\theta)\Big|_{\theta=0} \tag{4.1.5}$$

(throughout this chapter $X^{(n)}$ denotes the $n$-th derivative of the quantity $X$ with respect to $\theta$). Moreover, the effects of ordinary finite volume effects, i.e. finite volume effects not associated with fixed topology will be described in chapter 6. These are expected to be suppressed exponentially with increasing spatial volume $V_s$ and they will be neglected in this chapter (cf. section 4.3 for a discussion). In other words we assume $V_s$ to be sufficiently large such that $E_0(\theta, V_s) \approx e_0(\theta)V_s$, where $e_0(\theta)$ is the energy density of the vacuum.

At sufficiently large $T$ the partition function is dominated by the vacuum, i.e.

$$\mathcal{Z}_{\theta,V} = e^{-E_0(\theta,V_s)T}\Big(1 + \mathcal{O}(e^{-\Delta E(\theta)T})\Big), \tag{4.1.6}$$

where $\Delta E(\theta) = E_1(\theta, V_s) - E_0(\theta, V_s)$. The exponentially suppressed correction will be omitted in the following (cf. section 4.3 for a discussion). To ease the notation, we define

$$f(\theta) \equiv f(\theta, Q, V) \equiv e_0(\theta) - \frac{iQ\theta}{V}. \tag{4.1.7}$$

Using also eq. (4.1.6) the partition function at fixed topology eq. (4.1.4) can be written according to

$$Z_{Q,V} = \frac{1}{2\pi}\int_{-\pi}^{+\pi} d\theta\, e^{-f(\theta)V}, \tag{4.1.8}$$

where the integral eq. (4.1.8) can be approximated by means of the saddle point method. To this end, we expand $f(\theta)V$ around its minimum $\theta_s$ and replace $\int_{-\pi}^{+\pi}$ by $\int_{-\infty}^{+\infty}$, which introduces another exponentially suppressed error (cf. section 4.3 for a discussion),

$$Z_{Q,V} = \frac{1}{2\pi}\int_{-\infty}^{+\infty} d\theta\, \exp\bigg( - f(\theta_s)V - \frac{f^{(2)}(\theta_s)V}{2}(\theta-\theta_s)^2 - \sum_{n=3}^{\infty}\frac{f^{(n)}(\theta_s)V}{n!}(\theta-\theta_s)^n\bigg). \tag{4.1.9}$$

$\theta_s$ can be determined as a power series in $1/\mathcal{E}_2V$. Due to $E_n(+\theta, V_s) = E_n(-\theta, V_s)$, the expansion of the vacuum energy density around $\theta = 0$ is

$$e_0(\theta) = \sum_{k=0}^{\infty}\frac{\mathcal{E}_{2k}\theta^{2k}}{(2k)!} \quad , \quad \mathcal{E}_k \equiv e_0^{(k)}(\theta)\Big|_{\theta=0} \tag{4.1.10}$$

(note that $\mathcal{E}_2 = \chi_{\mathrm{t}}$). Consequently,

$$f(\theta)V = \sum_{k=0}^{\infty}\frac{\mathcal{E}_{2k}\theta^{2k}}{(2k)!}V - iQ\theta. \tag{4.1.11}$$

It is straightforward to solve the defining equation for $\theta_s$, $d/d\theta f(\theta)V|_{\theta=\theta_s} = 0$, with respect to $\theta_s$[1],

$$\theta_s = i\Big(\frac{Q}{\mathcal{E}_2 V}\Big) + \mathcal{O}\Big(\frac{1}{(\mathcal{E}_2 V)^3}\Big). \tag{4.1.12}$$

Finally the saddle point method requires to deform the contour of integration to pass through the saddle point, which is just a constant shift of the real axis by the purely imaginary $\theta_s$. We introduce the real coordinate $s = (\theta - \theta_s)(f^{(2)}(\theta_s)V)^{1/2}$ parameterizing the shifted contour of integration yielding

$$Z_{Q,V} = \frac{e^{-f(\theta_s)V}}{2\pi(f^{(2)}(\theta_s)V)^{1/2}} \int_{-\infty}^{+\infty} ds\, \exp\Big( -\frac{1}{2}s^2 - \sum_{n=3}^{\infty} \frac{f^{(n)}(\theta_s)V}{n!(f^{(2)}(\theta_s)V)^{n/2}} s^n \Big). \tag{4.1.13}$$

After defining

$$||h(s)|| \equiv \frac{1}{\sqrt{2\pi}} \int_{-\infty}^{+\infty} ds\, e^{-s^2/2} h(s) \tag{4.1.14}$$

a more compact notation for the eq. (4.1.13) is

$$Z_{Q,V} = \frac{e^{-f(\theta_s)V}}{(2\pi f^{(2)}(\theta_s)V)^{1/2}} \underbrace{\Big|\Big| \exp\Big( -\sum_{n=3}^{\infty} \frac{f^{(n)}(\theta_s)V}{n!(f^{(2)}(\theta_s)V)^{n/2}} s^n \Big)\Big|\Big|}_{\equiv G}, \tag{4.1.15}$$

where $G$ can also be written as

$$G = 1 + \sum_{k=1}^{\infty} \frac{(-1)^k}{k!} \Big|\Big| \Big( \sum_{n=3}^{\infty} \frac{f^{(n)}(\theta_s)V}{n!(f^{(2)}(\theta_s)V)^{n/2}} s^n \Big)^k \Big|\Big|. \tag{4.1.16}$$

We now insert $f(\theta)V$ and $\theta_s$ (eqs. (4.1.11) and (4.1.12)) and perform the integration over $s$ order by order in $1/\mathcal{E}_2 V$ (note that $\theta_s \sim 1/\mathcal{E}_2 V$). To this end we use the relations

$$\begin{aligned}
f^{(2n)}(\theta_s)V &= \sum_{l=n}^{\infty} \frac{\mathcal{E}_{2l} V}{(2l-2n)!} \theta_s^{2l-2n} \quad , \quad n = 1, 2, \dots \\
f^{(2n-1)}(\theta_s)V &= \sum_{l=n}^{\infty} \frac{\mathcal{E}_{2l} V}{(2l-2n+1)!} \theta_s^{2l-2n+1} \quad , \quad n = 2, 3, \dots \\
||s^{2n-1}|| &= 0 \quad , \quad ||s^{2n}|| = (2n-1)!! = \frac{(2n)!}{2^n n!} = 1 \times 3 \times 5 \times \dots \times (2n-1) \quad , \quad n = 0, 1, \dots
\end{aligned} \tag{4.1.17}$$

The terms in eq. (4.1.16) are

- for $k = 1$ proportional to $1/(\mathcal{E}_2 V)^{n/2-1}$,
- for $k = 2$ proportional to $1/(\mathcal{E}_2 V)^{(n_1+n_2)/2-2}$,
- for $k = 3$ proportional to $1/(\mathcal{E}_2 V)^{(n_1+n_2+n_3)/2-3}$, ...

Moreover, $n$, $n_1 + n_2$, $n_1 + n_2 + n_3$, ... have to be even, otherwise the corresponding term in eq. (4.1.16) vanishes, due to eq. (4.1.17). Finally every odd $n$ and $n_j$ contributes in leading order in $\theta_s$ one power of $\theta_s \sim 1/\mathcal{E}_2 V$. Therefore, up to $\mathcal{O}(1/(\mathcal{E}_2 V)^3)$ it is sufficient to consider the following terms:

[1]Throughout this work errors in $1/\mathcal{E}_2 V$ are proportional to either $1/(\mathcal{E}_2 V)^4$ or $1/(\mathcal{E}_2 V)^5$. For errors proportional to $1/(\mathcal{E}_2 V)^4$ we also keep track of powers of $Q$, e.g. we distinguish $\mathcal{O}(1/(\mathcal{E}_2 V)^4)$ and $\mathcal{O}(Q^2/(\mathcal{E}_2 V)^4)$, etc. For errors proportional to $1/(\mathcal{E}_2 V)^5$, we do not show powers of $Q$, i.e. we just write $\mathcal{O}(1/(\mathcal{E}_2 V)^5)$. We also estimate $\mathcal{E}_n/\mathcal{E}_2 = \mathcal{O}(1)$, for which numerical support can be found in [71].

- $k = 1, n = 4$:
$$\left\| \frac{f^{(4)}(\theta_s)V}{4!(f^{(2)}(\theta_s)V)^2} s^4 \right\| = \frac{1}{\mathcal{E}_2 V} \frac{\mathcal{E}_4}{8\mathcal{E}_2} + \mathcal{O}\left( \frac{1}{(\mathcal{E}_2 V)^3} \right). \tag{4.1.18}$$

- $k = 1, n = 6$:
$$\left\| \frac{f^{(6)}(\theta_s)V}{6!(f^{(2)}(\theta_s)V)^3} s^6 \right\| = \frac{1}{(\mathcal{E}_2 V)^2} \frac{\mathcal{E}_6}{48\mathcal{E}_2} + \mathcal{O}\left( \frac{1}{(\mathcal{E}_2 V)^2} \theta_s^2 \right). \tag{4.1.19}$$

- $k = 2, n_1 = n_2 = 4$:
$$\left\| \frac{(f^{(4)}(\theta_s)V)^2}{(4!)^2(f^{(2)}(\theta_s)V)^4} s^8 \right\| = \frac{1}{(\mathcal{E}_2 V)^2} \frac{35\mathcal{E}_4^2}{192\mathcal{E}_2^2} + \mathcal{O}\left( \frac{1}{(\mathcal{E}_2 V)^2} \theta_s^2 \right). \tag{4.1.20}$$

Inserting these expressions into eq. (4.1.16) leads to

$$G = 1 + \frac{1}{\mathcal{E}_2 V}\left( -\frac{\mathcal{E}_4}{8\mathcal{E}_2} \right) + \frac{1}{(\mathcal{E}_2 V)^2}\left( -\frac{\mathcal{E}_6}{48\mathcal{E}_2} + \frac{35\mathcal{E}_4^2}{384\mathcal{E}_2^2} \right) + \mathcal{O}\left( \frac{1}{(\mathcal{E}_2 V)^3}\ ,\ \frac{1}{(\mathcal{E}_2 V)} \theta_s^2 \right) \tag{4.1.21}$$

The remaining terms in eq. (4.1.15) expanded in powers of $1/V$ are

$$f(\theta_s)V = \mathcal{E}_0 V + \frac{1}{\mathcal{E}_2 V} \frac{1}{2} Q^2 + \mathcal{O}\left( \frac{1}{(\mathcal{E}_2 V)^3} \right) \tag{4.1.22}$$

and

$$f^{(2)}(\theta_s)V = \mathcal{E}_2 V \left( 1 - \frac{1}{(\mathcal{E}_2 V)^2} \frac{\mathcal{E}_4}{2\mathcal{E}_2} Q^2 + \mathcal{O}\left( \frac{1}{(\mathcal{E}_2 V)^3} Q^2 \right) \right). \tag{4.1.23}$$

Combining eqs. (4.1.15), (4.1.21), (4.1.22) and (4.1.23) yields the final result for $Z_{Q,V}$,

$$\begin{aligned} Z_{Q,V} = \frac{1}{\sqrt{2\pi\mathcal{E}_2 V}} \Bigg( & \exp\left( -E_0(0, V_s)T - \frac{1}{\mathcal{E}_2 V} \frac{1}{2} Q^2 \right) \left( 1 - \frac{1}{(\mathcal{E}_2 V)^2} \frac{\mathcal{E}_4}{2\mathcal{E}_2} Q^2 \right)^{-1/2} \\ & \times \left( 1 - \frac{1}{\mathcal{E}_2 V} \frac{\mathcal{E}_4}{8\mathcal{E}_2} + \frac{1}{(\mathcal{E}_2 V)^2}\left( -\frac{\mathcal{E}_6}{48\mathcal{E}_2} + \frac{35\mathcal{E}_4^2}{384\mathcal{E}_2^2} \right) \right) + \mathcal{O}\left( \frac{1}{\mathcal{E}_2^3 V^3}\ ,\ \frac{1}{\mathcal{E}_2^3 V^3} Q^2 \right) \Bigg). \end{aligned} \tag{4.1.24}$$

Now we can consider that $E_0(0, V_s) = 0$ as only differences of energy are interesting in physic. We rewrite that $\chi_{\mathrm{t}} = \mathcal{E}_2$. We get:

$$Z_{Q,V} = \frac{1}{\sqrt{2\pi\,\chi_{\mathrm{t}}\,V}} \left( \exp\left( -\frac{1}{\chi_{\mathrm{t}}\,V} \frac{1}{2} Q^2 \right) \times \left( 1 - \frac{1}{8\,\chi_{\mathrm{t}}\,V} \frac{\mathcal{E}_4}{\chi_{\mathrm{t}}} \right) + \mathcal{O}\left( \frac{1}{{\chi_{\mathrm{t}}}^2\,V^2} \right) \right) \quad . \tag{4.1.25}$$

Here, the partition function at fixed topology gives us the probability distribution of the topological charge. From this expression, we observe that the partition function tends to be a Gaussian distribution for large volume, which is consistent with the calculus in the section 1.2.5 and the figure 3.1.2.

### 4.1.2 Observables

More important than knowing the partition function at fixed topology is to know the relation for observables between their fixed topology value and their physical value. The behavior at fixed topology of any observables can be computed by the same means. Starting with the expectation values for an observable at fixed topology:

$$\mathscr{O}_{Q,V} = \langle O_1 O_2 \dots O_n \rangle_{Q,V} = \int DA\, D\psi\, D\bar{\psi}\, \delta_{Q,Q[A]} O_1 O_2 \dots O_n e^{-S_E[A,\bar{\psi},\psi]}. \tag{4.1.26}$$

As mentioned in section 1.2.4, $\mathscr{O}_{Q,V}$ and $\mathscr{O}(\theta)$ are related by a Fourier transform,

$$\mathcal{O}_{Q,V} = \frac{1}{2\pi}\frac{1}{Z_{Q,V}}\int d\theta Z(\theta)\mathcal{O}(\theta)\exp(i\theta Q) \tag{4.1.27}$$

with $\mathcal{O}(\theta)$ the expectation values of our observable on the $\theta$-vacuum. Inserting the equations eqs. (4.1.6) and (4.1.7) leads to:

$$\mathcal{O}_{Q,V} = \frac{1}{2\pi}\frac{1}{Z_{Q,V}}\int d\theta\mathcal{O}(\theta)e^{-f(\theta)V}. \tag{4.1.28}$$

Then, the expansion of $\mathcal{O}(\theta)$ around the saddle point $\theta_s$ :

$$\mathcal{O}(\theta) = \sum_k \frac{(\theta_s-\theta)^{2k}}{2k!}\mathcal{O}^{(2k)}(\theta_s), \tag{4.1.29}$$

is inserted in eq. (4.1.28),

$$Z_{Q,V}\mathcal{O}_{Q,V} = \frac{1}{2\pi}\int d\theta\sum_k \frac{(\theta_s-\theta)^{2k}}{2k!}\mathcal{O}^{(2k)}(\theta_s)e^{-f(\theta)V}. \tag{4.1.30}$$

The use of the parameter $s$ defined in the previous section allows us to rewrite our previous results as:

$$Z_{Q,V}\mathcal{O}_{Q,V} = \frac{1}{2\pi}\sum_k \frac{\mathcal{O}^{(2k)}(\theta_s)}{2k!}\int d\theta\frac{s^{2k}}{(f^{(2)}(\theta_s)V)^{k/2}}e^{-f(\theta)V} \tag{4.1.31}$$

Similarly to eq. (4.1.13), the expansion of $e^{-f(\theta)V}$ around our saddle point leads to:

$$\begin{aligned} Z_{Q,V}\mathcal{O}_{Q,V} &= \sum_k \frac{\mathcal{O}^{(2k)}(\theta_s)}{2k!}\frac{e^{-f(\theta_s)V}}{(f^{(2)}(\theta_s)V)^{1/2}}\times \\ &\times\int_{-\infty}^{+\infty} ds\,\frac{s^{2k}}{(f^{(2)}(\theta_s)V)^k}\exp\Big(-\frac{1}{2}s^2-\sum_{n=3}^{\infty}\frac{f^{(n)}(\theta_s)V}{n!(f^{(2)}(\theta_s)V)^{n/2}}s^n\Big) \\ &= \sum_k \frac{\mathcal{O}^{(2k)}(\theta_s)}{2k!}\frac{e^{-f(\theta_s)V}}{(f^{(2)}(\theta_s)V)^{1/2}}\times \\ &\times\left|\left|\frac{s^{2k}}{(f^{(2)}(\theta_s)V)^k}\left(\sum_{l=0}^{\infty}\frac{(-1)^l}{l!}\Big(\sum_{n=3}^{\infty}\frac{f^{(n)}(\theta_s)V}{n!(f^{(2)}(\theta_s)V)^{n/2}}s^n\Big)^l\right)\right|\right|. \end{aligned} \tag{4.1.32}$$

The terms in eq. (4.1.32) are

- for $l=1$ proportional to $1/(\mathcal{E}_2V)^{n/2+k-1}$,
- for $l=2$ proportional to $1/(\mathcal{E}_2V)^{(n_1+n_2)/2+2k-2}$,
- for $l=3$ proportional to $1/(\mathcal{E}_2V)^{(n_1+n_2+n_3)/2+3k-3}$, ...

Therefore, to write our relation to the second order in $1/\mathcal{E}_2V$ it is sufficient to consider the following terms:

- $k=1,\ l=0$

$$\frac{\mathcal{O}^{(2)}(\theta_s)}{2!}\left|\left|\frac{s^2}{(f^{(2)}(\theta_s)V)}\right|\right| = \frac{\mathcal{O}^{(2)}(\theta_s)}{2(f^{(2)}(\theta_s)V)} \tag{4.1.33}$$

- $k=1,\ l=1,\ n=4$

$$\begin{aligned}&\frac{\mathscr{O}^{(2)}(\theta_s)}{2!}\left|\left|-\frac{f^{(4)}(\theta_s)V}{4!(f^{(2)}(\theta_s)V)^3}s^6\right|\right|+\mathcal{O}\left(\frac{1}{(\mathcal{E}_2V)^3}\right)\\&=-\frac{\mathscr{O}^{(2)}(\theta_s)}{2}\left(\frac{5!!f^{(4)}(\theta_s)V}{4!(f^{(2)}(\theta_s)V)^3}\right)+\mathcal{O}\left(\frac{1}{(\mathcal{E}_2V)^3}\right)\end{aligned}\tag{4.1.34}$$

- $k=2,\ l=0$

$$\begin{aligned}&\frac{\mathscr{O}^{(4)}(\theta_s)}{4!}\left(\left|\left|\frac{s^4}{(f^{(2)}(\theta_s)V)^2}\right|\right|\right)+\mathcal{O}\left(\frac{1}{(\mathcal{E}_2V)^3}\right)\\&=\frac{3}{4!}\frac{\mathscr{O}^{(4)}(\theta_s)}{(f^{(2)}(\theta_s)V)^2}+\mathcal{O}\left(\frac{1}{(\mathcal{E}_2V)^3}\right)\end{aligned}\tag{4.1.35}$$

- All the others terms are negligible.

Inserting these expressions into eq. (4.1.32) leads to:

$$\begin{aligned}Z_{Q,V}\mathscr{O}_{Q,V}&=Z_{Q,V}\mathscr{O}(\theta_s)+\frac{e^{-f(\theta_s)V}}{(f^{(2)}(\theta_s)V)^{1/2}}\frac{\mathscr{O}^{(2)}(\theta_s)}{2!}\left(\frac{1}{(f^{(2)}(\theta_s)V)}-\frac{5!!f^{(4)}(\theta_s)V}{4!(f^{(2)}(\theta_s)V)^3}\right)\\&+\frac{e^{-f(\theta_s)V}}{(f^{(2)}(\theta_s)V)^{1/2}}\frac{3}{4!}\frac{\mathscr{O}^{(4)}(\theta_s)}{(f^{(2)}(\theta_s)V)^2}+\mathcal{O}\left(\frac{1}{\mathcal{E}_2^3V^3}\ ,\ \frac{1}{\mathcal{E}_2^3V^3}Q^2\right)\\&=Z_{Q,V}\left(\mathscr{O}(\theta_s)+\frac{\mathscr{O}^{(2)}(\theta_s)}{2\mathcal{E}_2V}\left(1-\frac{1}{\mathcal{E}_2V}\frac{\mathcal{E}_4}{\mathcal{E}_2}(\frac{5}{8}-\frac{1}{8})\right)+\frac{\mathscr{O}^{(4)}(\theta_s)}{8(\mathcal{E}_2V)^2}\right)\\&+\mathcal{O}\left(\frac{1}{\mathcal{E}_2^3V^3}\ ,\ \frac{1}{\mathcal{E}_2^3V^3}Q^2\right)\end{aligned}\tag{4.1.36}$$

Now we divide both sides of the previous equation to get to the following expression for $\mathscr{O}_{Q,V}$:

$$\mathscr{O}_{Q,V}=\mathscr{O}(\theta_s)+\frac{\mathscr{O}^{(2)}(\theta_s)}{2\mathcal{E}_2V}\left(1-\frac{1}{\mathcal{E}_2V}\frac{\mathcal{E}_4}{2\mathcal{E}_2}\right)+\frac{\mathscr{O}^{(4)}(\theta_s)}{8(\mathcal{E}_2V)^2}+\mathcal{O}\left(\frac{1}{\mathcal{E}_2^3V^3}\ ,\ \frac{1}{\mathcal{E}_2^3V^3}Q^2\right).\tag{4.1.37}$$

The result in this form is not useful as we want a relation with the physical observable $\mathscr{O}(0)$ but the result can be developed around 0 using:

$$\mathscr{O}(\theta_s)=\mathscr{O}(0)-\frac{\mathscr{O}^{(2)}(0)}{2}\frac{Q^2}{(\mathcal{E}_2V)^2}+\mathcal{O}\left(\frac{1}{\mathcal{E}_2^3V^3}\ ,\ \frac{1}{\mathcal{E}_2^3V^3}Q^2\right)\tag{4.1.38}$$

and

$$\mathscr{O}^{(2)}(\theta_s)=\mathscr{O}^{(2)}(0)-\frac{\mathscr{O}^{(4)}(0)}{2}\frac{Q^2}{(\mathcal{E}_2V)^2}+\mathcal{O}\left(\frac{1}{\mathcal{E}_2^3V^3}\ ,\ \frac{1}{\mathcal{E}_2^3V^3}Q^2\right).\tag{4.1.39}$$

And finally an observable at fixed topology is given by:

$$\mathscr{O}_{Q,V}=\mathscr{O}(0)+\frac{\mathscr{O}^{(2)}(0)}{2\mathcal{E}_2V}\left(1-\frac{1}{\mathcal{E}_2V}\left(\frac{1}{2}\frac{\mathcal{E}_4}{\mathcal{E}_2}+Q^2\right)\right)+\frac{\mathscr{O}^{(4)}(0)}{8(\mathcal{E}_2V)^2}+\mathcal{O}\left(\frac{1}{\mathcal{E}_2^3V^3}\ ,\ \frac{1}{\mathcal{E}_2^3V^3}Q^2\right).\tag{4.1.40}$$

Here the expression of [8] is retrieved if one neglects the kurtosis and the term $\mathscr{O}^{(4)}(0)$:

$$\mathscr{O}_{Q,V}=\mathscr{O}(0)+\frac{\mathscr{O}^{(2)}(0)}{2\mathcal{E}_2V}\left(1-\frac{Q^2}{\mathcal{E}_2V}\right)+\mathcal{O}\left(\frac{1}{\mathcal{E}_2^2V^2}\ ,\ \frac{1}{\mathcal{E}_2^3V^3}Q^2\right)\tag{4.1.41}$$

This equation will be refereed to as the BCNW-equation for an observable.

### 4.1.3 Mass at fixed topology and finite spacetime volume

The mass is extracted from the two-point correlation functions at fixed topological charge $Q$ and finite spacetime volume $V$, which are defined as

$$C_{Q,V}(t) \equiv \frac{1}{Z_{Q,V}} \int DA\, D\psi\, D\bar{\psi}\, \delta_{Q,Q[A]} O^\dagger(t) O(0) e^{-S_E[A,\bar{\psi},\psi]}. \tag{4.1.42}$$

$O$ denotes a suitable hadron creation operator, i.e. $O$ has the same quantum numbers as the mass of the particle that we want to study. We could have used the result of the previous section to compute the two-point correlation functions at fixed topological charge $Q$, but we are interested in the mass, which requires an exponential form for the relation. For this reason the previous form is not suitable and it is easier to start from the scratch. However, the calculus is similar and several steps will be omitted to avoid repetition. As previously, the two-point correlation function can be computed from the Fourier transform:

$$C_{Q,V}(t) = \frac{1}{2\pi Z_{Q,V}} \int_{-\pi}^{+\pi} d\theta\, \mathcal{Z}_{\theta,V} \mathcal{C}_{\theta,V}(t) e^{iQ\theta}. \tag{4.1.43}$$

$\mathcal{C}_{\theta,V}(t)$ can be expressed in terms of energy eigenstates $|n;\theta,V_s\rangle$ and eigenvalues,

$$\mathcal{C}_{\theta,V}(t)\mathcal{Z}_{\theta,V} = \sum_{n,m} \Big| \langle m;\theta,V_s|O|n;\theta,V_s\rangle \Big|^2 e^{-E_m(\theta,V_s)t} e^{-E_n(\theta,V_s)(T-t)}. \tag{4.1.44}$$

When applied to the vacuum $|0;\theta,V_s\rangle$, the hadron creation operator $O$ creates a state, which has the quantum numbers of the hadron of interest $H$, which are assumed to be not identical to those of the vacuum, even at $\theta \neq 0$. These states are denoted by $|H,n;\theta,V_s\rangle$, the corresponding eigenvalues by $E_{H,n}(\theta,V_s)$. $H$ is typically the lowest state in that sector[2], i.e. $|H,0;\theta,V_s\rangle$ with mass $M_H(\theta) \equiv E_{H,0}(\theta,V_s) - E_0(\theta,V_s)$ (in this section we again neglect ordinary finite volume effects, i.e. finite volume effects not associated with fixed topology; cf. section 4.3.2 for a discussion). Using this notation one can rewrite eq. (4.1.44) accordingly

$$\begin{aligned}
&\mathcal{C}_{\theta,V}(t)\mathcal{Z}_{\theta,V} = \\
&\quad = \alpha(\theta,V_s) e^{-E_0(\theta,V_s)T} e^{-M_H(\theta)t} + \mathcal{O}(e^{-E_0(\theta,V_s)T} e^{-M_H^*(\theta)t}) + \mathcal{O}(e^{-E_0(\theta,V_s)T} e^{-M_H(\theta)(T-t)}) \\
&\quad = \alpha(\theta,V_s) e^{-E_0(\theta,V_s)T} e^{-M_H(\theta)t} \Big(1 + \mathcal{O}(e^{-(M_H^*(\theta)-M_H(\theta))t}) + \mathcal{O}(e^{-M_H(\theta)(T-2t)})\Big),
\end{aligned} \tag{4.1.45}$$

where $\alpha(\theta,V_s) \equiv |\langle H,0;\theta,V_s|O|0;\theta,V_s\rangle|^2$ and $M_H^*(\theta) \equiv E_{H,1}(\theta,V_s) - E_0(\theta,V_s)$ is the mass of the first excitation with the quantum numbers of $H$.

For suitably normalized hadron creation operators $O$, e.g. operators

$$O \equiv \frac{1}{\sqrt{V_s}} \int d^3r\, O'(\mathbf{r}), \tag{4.1.46}$$

where $O'(\mathrm{r})$ is a local operator, i.e. an operator exciting quark and gluon fields only at or close to $\mathbf{r}$, $\alpha$ is independent of $V_s$, i.e. $\alpha = \alpha(\theta)$. Moreover, for operators $O$ respecting either $POP = +O$ or $POP = -O$, i.e. operators with definite parity $P$, one can show $\alpha(+\theta) = \alpha(-\theta)$ by using $P|n;-\theta,V_s\rangle = \eta_n(\theta,V_s)|n;+\theta,V_s\rangle$, where $\eta_n(\theta,V_s)$ is a non-unique phase. In the following we assume that $O$ is suitably normalized and has

[2]Note that parity is not a symmetry at $\theta \neq 0$. Therefore, states with defined parity at $\theta = 0$, which have lighter parity partners (e.g. positive parity mesons), have to be treated and extracted as excited states at $\theta \neq 0$ and, consequently, also at fixed topology. This more complicated case is discussed in section 4.2.

defined parity. Then $\alpha(\theta)$ can be written as a power series around $\theta = 0$ according to

$$\alpha(\theta) = \sum_{k=0}^{\infty} \frac{\alpha^{(2k)}(0)\theta^{2k}}{(2k)!} = \alpha(0) \exp\Bigg( \underbrace{\ln\Bigg( \sum_{k=0}^{\infty} \frac{\alpha^{(2k)}(0)\theta^{2k}}{(2k)!\alpha(0)} \Bigg)}_{\equiv -\beta(\theta) = -\sum_{k=1}^{\infty} \frac{\beta^{(2k)}(0)\theta^{2k}}{(2k)!}} \Bigg). \tag{4.1.47}$$

Inserting $\alpha(\theta)$ in eq. (4.1.45) and neglecting exponentially suppressed corrections (cf. section 4.3.2 for a discussion) leads to

$$\mathcal{C}_{\theta,V}(t)\mathcal{Z}_{\theta,V} = \alpha(0) e^{-(e_0(\theta)V + M_H(\theta)t + \beta(\theta))}. \tag{4.1.48}$$

In analogy to eq. (4.1.7) we define

$$f_{\mathcal{C}}(\theta) \equiv f_{\mathcal{C}}(\theta, Q, V) \equiv e_0(\theta) + \frac{M_H(\theta)t + \beta(\theta) - iQ\theta}{V}. \tag{4.1.49}$$

For two-point correlation functions at fixed topology we then arrive at a similar form as for $Z_{Q,V}$ (eq. (4.1.8)),

$$C_{Q,V}(t) Z_{Q,V} = \frac{\alpha(0)}{2\pi} \int_{-\pi}^{+\pi} d\theta \, e^{-f_{\mathcal{C}}(\theta)V}. \tag{4.1.50}$$

With

$$\mathcal{F}_{2k} \equiv \mathcal{E}_{2k} + \frac{M_H^{(2k)}(0)t + \beta^{(2k)}(0)}{V} = \mathcal{E}_{2k}\left(1 + \frac{x_{2k}}{\mathcal{E}_{2k}V}\right) \quad , \quad x_{2k} \equiv M_H^{(2k)}(0)t + \beta^{(2k)}(0) \tag{4.1.51}$$

the expansion of the exponent is

$$f_{\mathcal{C}}(\theta)V = \sum_{k=0}^{\infty} \frac{\mathcal{F}_{2k}\theta^{2k}}{(2k)!} V - iQ\theta. \tag{4.1.52}$$

Up to $\mathcal{O}(1/(\mathcal{E}_2 V)^3)$ its minimum can be approximated by using eq. (4.1.12),

$$\begin{aligned} \theta_{s,\mathcal{C}} &= i\left(\frac{1}{\mathcal{F}_2 V} Q\right) + \mathcal{O}\left(\frac{1}{(\mathcal{F}_2 V)^3}\right) \\ &= i\left(\frac{1}{\mathcal{E}_2 V(1 + x_2/\mathcal{E}_2 V)} Q\right) + \mathcal{O}\left(\frac{1}{(\mathcal{E}_2 V)^3}\right). \end{aligned} \tag{4.1.53}$$

$C_{Q,V}(t)Z_{Q,V}$ can be written in the same form as $Z_{Q,V}$ (eq. (4.1.15)),

$$C_{Q,V}(t) Z_{Q,V} = \frac{\alpha(0) e^{-f_{\mathcal{C}}(\theta_{s,\mathcal{C}})V}}{\sqrt{2\pi}(f_{\mathcal{C}}^{(2)}(\theta_{s,\mathcal{C}})V)^{1/2}} \underbrace{\left\| \exp\Bigg( -\sum_{n=3}^{\infty} \frac{f_{\mathcal{C}}^{(n)}(\theta_{s,\mathcal{C}})V}{n!(f_{\mathcal{C}}^{(2)}(\theta_{s,\mathcal{C}})V)^{n/2}} s^n \Bigg) \right\|}_{\equiv G_{\mathcal{C}}}. \tag{4.1.54}$$

Using eqs. (4.1.21) and (4.1.24) yields an explicit expression up to $\mathcal{O}(1/(\mathcal{E}_2 V)^2)$,

$$\begin{aligned} C_{Q,V}(t) Z_{Q,V} &= \frac{\alpha(0)}{\sqrt{2\pi\mathcal{F}_2 V}} \Bigg( \exp\Bigg( -\mathcal{F}_0 V - \frac{1}{\mathcal{F}_2 V}\frac{1}{2}Q^2\Bigg) \\ &\quad \Bigg(1 - \frac{1}{(\mathcal{F}_2 V)^2}\frac{\mathcal{F}_4}{2\mathcal{F}_2}Q^2\Bigg)^{-1/2} G_{\mathcal{C}} + \mathcal{O}\Bigg(\frac{1}{(\mathcal{E}_2 V)^3}Q^4\Bigg)\Bigg) \\ &= \frac{1}{\sqrt{2\pi\mathcal{E}_2 V}} \frac{\alpha(0)}{\sqrt{1 + x_2/\mathcal{E}_2 V}} \\ &\quad \Bigg( \exp\Bigg( -E_0 T - M_H(0) t - \frac{1}{\mathcal{E}_2 V(1 + x_2/\mathcal{E}_2 V)}\frac{1}{2}Q^2\Bigg) \\ &\quad \Bigg(1 - \frac{1}{(\mathcal{E}_2 V)^2}\frac{\mathcal{E}_4(1 + x_4/\mathcal{E}_4 V)}{2\mathcal{E}_2(1 + x_2/\mathcal{E}_2 V)^3}Q^2\Bigg)^{-1/2} G_{\mathcal{C}} + \mathcal{O}\Bigg(\frac{1}{(\mathcal{E}_2 V)^3}Q^4\Bigg)\Bigg) \end{aligned} \tag{4.1.55}$$

with

$$\begin{aligned} G_{\mathcal{C}} &= 1 - \frac{1}{\mathcal{F}_2 V}\frac{\mathcal{F}_4}{8\mathcal{F}_2} + \frac{1}{(\mathcal{F}_2 V)^2}\Bigg( -\frac{\mathcal{F}_6}{48\mathcal{F}_2} + \frac{35\mathcal{F}_4^2}{384\mathcal{F}_2^2}\Bigg) \\ &\quad + \mathcal{O}\Bigg(\frac{1}{(\mathcal{E}_2 V)^3}\,,\, \frac{1}{(\mathcal{E}_2 V)^3}Q^2\Bigg) \\ &= 1 - \frac{1}{\mathcal{E}_2 V}\frac{\mathcal{E}_4(1 + x_4/\mathcal{E}_4 V)}{8\mathcal{E}_2(1 + x_2/\mathcal{E}_2 V)^2} \\ &\quad + \frac{1}{(\mathcal{E}_2 V)^2}\Bigg( -\frac{\mathcal{E}_6(1 + x_6/\mathcal{E}_6 V)}{48\mathcal{E}_2(1 + x_2/\mathcal{E}_2 V)^3} + \frac{35\mathcal{E}_4^2(1 + x_4/\mathcal{E}_4 V)^2}{384\mathcal{E}_2^2(1 + x_2/\mathcal{E}_2 V)^4}\Bigg) \\ &\quad + \mathcal{O}\Bigg(\frac{1}{(\mathcal{E}_2 V)^3}\,,\, \frac{1}{(\mathcal{E}_2 V)^3}Q^2\Bigg). \end{aligned} \tag{4.1.56}$$

After inserting $Z_{Q,V}$ (eq. (4.1.24)) it is straightforward to obtain the final result for two-point correlation functions at fixed topology,

$$\begin{aligned} C_{Q,V}(t) &= \frac{\alpha(0)}{\sqrt{1 + x_2/\mathcal{E}_2 V}} \\ &\quad \exp\Bigg( -M_H(0) t - \frac{1}{\mathcal{E}_2 V}\Bigg(\frac{1}{1 + x_2/\mathcal{E}_2 V} - 1\Bigg)\frac{1}{2}Q^2\Bigg) \\ &\quad \Bigg(1 - \frac{1}{(\mathcal{E}_2 V)^2}\frac{\mathcal{E}_4}{2\mathcal{E}_2}Q^2\Bigg)^{+1/2} \Bigg(1 - \frac{1}{(\mathcal{E}_2 V)^2}\frac{\mathcal{E}_4(1 + x_4/\mathcal{E}_4 V)}{2\mathcal{E}_2(1 + x_2/\mathcal{E}_2 V)^3}Q^2\Bigg)^{-1/2} \frac{G_{\mathcal{C}}}{G} \\ &\quad + \mathcal{O}\Bigg(\frac{1}{(\mathcal{E}_2 V)^3}Q^4\Bigg), \end{aligned} \tag{4.1.57}$$

where $G$ and $G_{\mathcal{C}}$ are given in eqs. (4.1.21) and (4.1.56) (note that after inserting $G$ and $G_{\mathcal{C}}$ in eq. (4.1.57) the error is $\mathcal{O}(1/(\mathcal{E}_2 V)^3\ ,\ Q^2/(\mathcal{E}_2 V)^3\ ,\ Q^4/(\mathcal{E}_2 V)^3)$). For some applications it might be helpful to have an expression for two-point correlation functions at fixed topology, which is of the form

$$C_{Q,V}(t) = \text{const} \times \exp\Bigg( -M_H(0) t + \text{fixed topology corrections as a power series in } 1/\mathcal{E}_2 V\Bigg), \tag{4.1.58}$$

i.e. where fixed topology effects only appear in the exponent and are sorted according to powers of $1/\mathcal{E}_2 V$.

Such an expression can be obtained in a straightforward way from eq. (4.1.57),

$$C_{Q,V}(t) = \alpha(0)\exp\left( - M_H(0)t - \frac{1}{\mathcal{E}_2 V}\frac{x_2}{2} - \frac{1}{(\mathcal{E}_2 V)^2}\left(\frac{x_4 - 2(\mathcal{E}_4/\mathcal{E}_2)x_2 - 2x_2^2}{8} - \frac{x_2}{2}Q^2\right)\right) + \mathcal{O}\left(\frac{1}{(\mathcal{E}_2 V)^3}\ ,\ \frac{1}{(\mathcal{E}_2 V)^3}Q^2\ ,\ \frac{1}{(\mathcal{E}_2 V)^3}Q^4\right). \tag{4.1.59}$$

Note that the order of the error is the same for both eq. (4.1.57) and eq. (4.1.59). Considering this expression a mass at fixed topology could be defined as:

$$\begin{aligned} M_{Q,V}(t) &= -\frac{1}{C_{Q,V}(t)}\frac{\partial C_{Q,V}(t)}{\partial t} \\ &= M_H(0) + \frac{M_H^{(2)}(0)}{2\chi_t V}\left(1 - \frac{Q^2}{\chi_t V} - \frac{1}{2}\frac{\mathcal{E}_4}{\chi_t^2 V}\right) + \frac{M_H^{(4)}(0)}{8(\chi_t V)^2} \\ &+ \frac{M_H^{(2)}(0)}{2(\chi_t V)^2}\left(M_H^{(2)}(0)t + \beta^{(2)}(0)\right) + \mathcal{O}\left(\frac{1}{(\mathcal{E}_2 V)^3}\ ,\ \frac{1}{(\mathcal{E}_2 V)^3}Q^2\ ,\ \frac{1}{(\mathcal{E}_2 V)^3}Q^4\right). \end{aligned} \tag{4.1.60}$$

The equation (4.1.60) shows that the mass at fixed topology is time dependent. This issue is a consequence of the non-locality of the theory at fixed topology. For this reason, the authors of [8] have decided to limit the expansion to:

$$M_{Q,V} = M_H(0) + \frac{M_H^{(2)}(0)}{2\chi_t V}\left(1 - \frac{Q^2}{\chi_t V}\right) + \mathcal{O}\left(\frac{1}{(\chi_t V)^2}\right) \tag{4.1.61}$$

which consists of the first order expression to which the topological charge dependent term has been added. We will refer to this equation as the BCNW-equation for the mass. Note that to the order given in eq. (4.1.61), this equation is similar to the BCNW-equation for an observable (cf. eq. (4.1.41)) but this is not the case at the complete second order.

### 4.1.4 Extensions

We have decided up to here to limit the calculus to the second order. In the article [14], we expand the expression up to the third order to improve the precision, which can be useful in case of variables which are topologically sensitive (large second derivative by $\theta$) as the $\eta'$-meson mass or for really fine precision. For example, for $\chi_t V = 10$, the first order corresponds to $\sim 5\%$, $5‰$ for the second order and $1‰$ for the third order (if the quantity measured and its second derivative by $\theta$ are of the same order). Such a precision can already be achieved for variable like the static quark-anti quark potential or the pion mass. Moreover for topological charge such that $|Q|/\chi_t V$ close to 1, the convergence of the formula can be rather slow and one needs higher orders. The calculus is not presented in this thesis, interested readers can refer to our publication [14] where the calculus is presented in details[3] .

We get then the following results:

- For the partition function :

[3] Here we do not consider it necessary to reproduce them as they are very similar to those presented for lowest order but are lengthy.

$$\begin{aligned} Z_{Q,V} =& \frac{1}{\sqrt{2\pi\mathcal{E}_2 V}}\Bigg( \exp\Bigg( - E_0(0,V_s)T - \frac{1}{\mathcal{E}_2 V}\frac{1}{2}Q^2 - \frac{1}{(\mathcal{E}_2 V)^3}\frac{\mathcal{E}_4}{24\mathcal{E}_2}Q^4\Bigg) \\ & \Bigg(1 - \frac{1}{(\mathcal{E}_2 V)^2}\frac{\mathcal{E}_4}{2\mathcal{E}_2}Q^2\Bigg)^{-1/2}\Bigg(1 - \frac{1}{\mathcal{E}_2 V}\frac{\mathcal{E}_4}{8\mathcal{E}_2} + \frac{1}{(\mathcal{E}_2 V)^2}\Bigg( - \frac{\mathcal{E}_6}{48\mathcal{E}_2} + \frac{35\mathcal{E}_4^2}{384\mathcal{E}_2^2}\Bigg) \\ & + \frac{1}{(\mathcal{E}_2 V)^3}\Bigg( - \frac{\mathcal{E}_8}{384\mathcal{E}_2} + \frac{7\mathcal{E}_4\mathcal{E}_6}{128\mathcal{E}_2^2} - \frac{385\mathcal{E}_4^3}{3072\mathcal{E}_2^3} + \Bigg(\frac{\mathcal{E}_6}{16\mathcal{E}_2} - \frac{\mathcal{E}_4^2}{3\mathcal{E}_2^2}\Bigg)Q^2\Bigg) \\ & + \mathcal{O}\Bigg(\frac{1}{\mathcal{E}_2^4 V^4}\,,\ \frac{1}{\mathcal{E}_2^4 V^4}Q^2\,,\ \frac{1}{\mathcal{E}_2^4 V^4}Q^4\Bigg)\Bigg). \end{aligned} \tag{4.1.62}$$

- For an observable:

$$\begin{aligned} \mathscr{O}_{Q,V} =& \mathscr{O}(0) + \frac{\mathscr{O}^{(2)}(0)}{2\mathcal{E}_2 V} + \frac{1}{(\mathcal{E}_2 V)^2}\Bigg(\frac{\mathscr{O}^{(4)}(0) - 2(\mathcal{E}_4/\mathcal{E}_2)\mathscr{O}^{(2)}(0)}{8} - \frac{\mathscr{O}^{(2)}(0)}{2}Q^2\Bigg) \\ & + \frac{1}{(\mathcal{E}_2 V)^3}\Bigg(\frac{\mathscr{O}^{(6)}(0) - 8(\mathcal{E}_4/\mathcal{E}_2)\mathscr{O}^{(4)}(0) - 3(\mathcal{E}_6/\mathcal{E}_2)\mathscr{O}^{(2)}(0) + 16(\mathcal{E}_4/\mathcal{E}_2)^2\mathscr{O}^{(2)}(0)}{48}\Bigg) \\ & - \frac{\mathscr{O}^{(4)}(0)}{4(\mathcal{E}_2 V)^3}Q^2 + \mathcal{O}\Bigg(\frac{1}{(\mathcal{E}_2 V)^4}\,,\ \frac{1}{(\mathcal{E}_2 V)^4}Q^2\,,\ \frac{1}{(\mathcal{E}_2 V)^4}Q^4\Bigg) \end{aligned} \tag{4.1.63}$$

- For the two-point correlations functions:

$$\begin{aligned} C_{Q,V}(t) =& \alpha(0)\exp\Bigg( - M_H(0)t - \frac{1}{\mathcal{E}_2 V}\frac{x_2}{2} - \frac{1}{(\mathcal{E}_2 V)^2}\Bigg(\frac{x_4 - 2(\mathcal{E}_4/\mathcal{E}_2)x_2 - 2x_2^2}{8} - \frac{x_2}{2}Q^2\Bigg) \\ & - \frac{1}{(\mathcal{E}_2 V)^3}\Bigg(\frac{16(\mathcal{E}_4/\mathcal{E}_2)^2 x_2 + x_6 - 3(\mathcal{E}_6/\mathcal{E}_2)x_2 - 8(\mathcal{E}_4/\mathcal{E}_2)x_4 - 12x_2x_4 + 18(\mathcal{E}_4/\mathcal{E}_2)x_2^2 + 8x_2^3}{48} \\ & - \frac{x_4 - 3(\mathcal{E}_4/\mathcal{E}_2)x_2 - 2x_2^2}{4}Q^2\Bigg)\Bigg) + \mathcal{O}\Bigg(\frac{1}{(\mathcal{E}_2 V)^4}\,,\ \frac{1}{(\mathcal{E}_2 V)^4}Q^2\,,\ \frac{1}{(\mathcal{E}_2 V)^4}Q^4\Bigg). \end{aligned} \tag{4.1.64}$$

## 4.2 Parity mixing

As mentioned previously in section 1.2.4, parity $P$ is not a symmetry at $\theta \neq 0$. Therefore, states at $\theta \neq 0$ cannot be classified according to parity and it is not possible to construct two-point correlation functions $\mathcal{C}_{\theta,V}(t)$, where only $P = -$ or $P = +$ states contribute. Similarly, $C_{Q,V}(t)$ contains contributions both of states with $P = -$ or $P = +$, since it is obtained by Fourier transforming $\mathcal{C}_{\theta,V}(t)$ (cf. eq. (4.1.43)). Consequently, one has to determine the masses of $P = -$ and $P = +$ parity partners from the same two-point correlation functions[4]. While usually there are little problems for the lighter state (in the case of mesons typically the $P = -$ ground state), its parity partner (the $P = +$ ground state) has to be treated as an excitation. To precisely determine the mass of an excited state, a single correlator is in most cases not sufficient. For example, to extract a first excitation it is common to study at least a $2 \times 2$ correlation matrix formed by two hadron creation operators, which generate significant overlap to both the ground state and the first excitation.

We discuss the determination of $P = -$ and $P = +$ parity partners from fixed topology computations in a simple setup: a $2 \times 2$ correlation matrix

$$C_{Q,V}^{jk}(t) \equiv \frac{1}{Z_{Q,V}}\int DA\, D\psi\, D\bar{\psi}\, \delta_{Q,Q[A]} O_j^\dagger(t) O_k(0) e^{-S_E[A,\bar{\psi},\psi]} \tag{4.2.1}$$

with hadron creation operators $O_-$ and $O_+$ generating at unfixed topology and small $\theta$ mainly $P = -$ and

[4]Note the similarity to twisted mass lattice QCD, where parity is not an exact symmetry either, and where $P = -$ and $P = +$ states are usually extracted from the same correlation matrix (cf. e.g. [46–49, 72–74]).

$P = +$, respectively. An example for such operators is

$$O_- \equiv \frac{1}{\sqrt{V_s}} \int d^3r\, \bar{c}(\mathbf{r})\gamma_5 u(\mathbf{r}) \quad , \quad O_+ \equiv \frac{1}{\sqrt{V_s}} \int d^3r\, \bar{c}(\mathbf{r}) u(\mathbf{r}) \tag{4.2.2}$$

corresponding to the $D$ meson and its parity partner $D_0^*$. Without loss of generality we assume that the ground state (at $\theta = 0$) has $P = -$, denoted by $H_-$, and the first excitation has $P = +$, denoted by $H_+$.

In the following we derive expressions for the four elements of the correlation matrix $C^{jk}_{Q,V}(t)$, $j, k \in \{-, +\}$. We proceed similarly as in section 4.1.3. This time, however, we consider the two lowest states $H_-$ and $H_+$ (not only a single state),

$$\mathcal{C}^{jk}_{\theta,V}(t)\mathcal{Z}_{\theta,V} = \left(\alpha^{jk}_-(\theta, V_s)e^{-M_{H_-}(\theta)t} + \alpha^{jk}_+(\theta, V_s)e^{-M_{H_+}(\theta)t}\right)e^{-E_0(\theta,V_s)T} \tag{4.2.3}$$

(which is the generalization of eq. (4.1.45) with exponentially suppressed corrections from higher excitations neglected), where

$$\alpha^{jk}_n(\theta) \equiv A^{j,\dagger}_n(\theta)A^k_n(\theta) \quad , \quad A^j_n(\theta) \equiv \langle H_n; \theta | O_j | 0; \theta \rangle. \tag{4.2.4}$$

The overlap of the trial states $O_j|0;\theta\rangle$ and the lowest states $|H_n\rangle$, $A^j_n(\theta)$ and $\alpha^{jk}_n(\theta)$, has to be treated in a more general way, since the leading order of their $\theta$ expansion can be proportional to a constant, to $\theta$ or to $\theta^2$ depending on the indices $j$, $k$ and $n$. Since at $\theta = 0$ parity is a symmetry, $A^+_-(\theta = 0) = A^-_+(\theta = 0) = 0$. Consequently,

- $A^+_-(\theta) = \mathcal{O}(\theta)$, $A^-_+(\theta) = \mathcal{O}(\theta)$,

while

- $A^-_-(\theta) = \mathcal{O}(1)$, $A^+_+(\theta) = \mathcal{O}(1)$.

From the definition of $\alpha^{jk}_n(\theta)$ (eq. (4.2.4)) one can conclude

- $\alpha^{--}_-(\theta) = \mathcal{O}(1)$, $\alpha^{++}_+(\theta) = \mathcal{O}(1)$,
- $\alpha^{-+}_\pm(\theta) = \mathcal{O}(\theta)$, $\alpha^{+-}_\pm(\theta) = \mathcal{O}(\theta)$,
- $\alpha^{++}_-(\theta) = \mathcal{O}(\theta^2)$, $\alpha^{--}_+(\theta) = \mathcal{O}(\theta^2)$.

Using $PO_\pm P = \pm O_\pm$ and $P|n; +\theta, V_s\rangle = \eta_n(\theta, V_s)|n; -\theta, V_s\rangle$, where $\eta_n(\theta, V_s)$ is a non-unique phase, one can show

- $\alpha^{++}_n(+\theta) = +\alpha^{++}_n(-\theta)$, $\alpha^{--}_n(+\theta) = +\alpha^{--}_n(-\theta)$ (i.e. only even powers of $\theta$ in the corresponding expansions),
- $\alpha^{+-}_n(+\theta) = -\alpha^{+-}_n(-\theta)$, $\alpha^{-+}_n(+\theta) = -\alpha^{-+}_n(-\theta)$ (i.e. only odd powers of $\theta$ in the corresponding expansions).

Technically it is straightforward to consider not only the ground state $H_-$, but also a first excitation $H_+$: the contributions of the two states are just summed in eq. (4.2.3), i.e. one can independently determine their Fourier transform and, hence, their contribution to the correlation matrix at fixed topology, $C^{jk}_{Q,V}(t)$. Additional calculations have to be done, however, for off-diagonal elements, where $\alpha^{\pm\mp}_n(+\theta) = -\alpha^{\pm\mp}_n(-\theta)$, and for contributions to diagonal matrix elements, where $\alpha^{\pm\pm}_n(\theta) = \mathcal{O}(\theta^2)$ (cf. the following two subsections). Contributions to diagonal matrix elements, where $\alpha^{\pm\pm}_n(\theta) = \mathcal{O}(1)$, have already been determined (cf. section 4.1.3).

### 4.2.1 Calculation of $\alpha_-^{-+}(\theta), \alpha_+^{-+}(\theta), \alpha_-^{+-}(\theta)$ and $\alpha_+^{+-}(\theta)$

We proceed as in section 4.1.3. $\alpha(\theta)$ can be written as a power series around $\theta = 0$,

$$\alpha(\theta) = \sum_{k=0}^{\infty} \frac{\alpha^{(2k+1)}(0)\theta^{2k+1}}{(2k+1)!} = \alpha^{(1)}(0)\theta \exp\Bigg( \underbrace{\ln\Bigg( \sum_{k=0}^{\infty} \frac{\alpha^{(2k+1)}(0)\theta^{2k}}{(2k+1)!\alpha^{(1)}(0)} \Bigg)}_{\equiv -\beta(\theta) = -\sum_{k=1}^{\infty} \frac{\beta^{(2k)}(0)\theta^{2k}}{(2k)!}} \Bigg). \tag{4.2.5}$$

The corresponding contribution to $\mathcal{C}_{\theta,V}^{jk}(t)\mathcal{Z}_{\theta,V}$ (cf. eq. (4.2.3)) is

$$\alpha(\theta) e^{-M_H(\theta)t} e^{-E_0(\theta,V_s)T} = \alpha^{(1)}(0)\theta e^{-(e_0(\theta)V + M_H(\theta)t + \beta(\theta))}. \tag{4.2.6}$$

As before we define

$$f_{\mathcal{C}}(\theta) \equiv f_{\mathcal{C}}(\theta, Q, V) \equiv e_0(\theta) + \frac{M_H(\theta)t + \beta(\theta) - iQ\theta}{V}. \tag{4.2.7}$$

For the contribution to the correlation matrix at fixed topology $C_{Q,V}^{jk}(t)Z_{Q,V}$ we then obtain

$$\frac{\alpha^{(1)}(0)}{2\pi} \int_{-\pi}^{+\pi} d\theta\, \theta e^{-f_{\mathcal{C}}(\theta)V}, \tag{4.2.8}$$

where $f_{\mathcal{C}}(\theta)V$ is defined by eqs. (4.1.51) and (4.1.52). Consequently, its minimum $\theta_{s,\mathcal{C}}$ is given by eq. (4.1.53) and eq. (4.2.8) can be written as

$$\begin{aligned} &\frac{\alpha^{(1)}(0)e^{-f_{\mathcal{C}}(\theta_{s,\mathcal{C}})V}}{(2\pi f_{\mathcal{C}}^{(2)}(\theta_{s,\mathcal{C}})V)^{1/2}} \left\| \left( \theta_{s,\mathcal{C}} + \frac{s}{(f_{\mathcal{C}}^{(2)}(\theta_{s,\mathcal{C}})V)^{1/2}} \right) \exp\Bigg( -\sum_{n=3}^{\infty} \frac{f_{\mathcal{C}}^{(n)}(\theta_{s,\mathcal{C}})V}{n!(f_{\mathcal{C}}^{(2)}(\theta_{s,\mathcal{C}})V)^{n/2}} s^n \Bigg) \right\| = \\ &\quad = \frac{\alpha^{(1)}(0)e^{-f_{\mathcal{C}}(\theta_{s,\mathcal{C}})V}}{(2\pi f_{\mathcal{C}}^{(2)}(\theta_{s,\mathcal{C}})V)^{1/2}} \Big( \theta_{s,\mathcal{C}} G_{\mathcal{C}} + H_{\mathcal{C}} \Big), \end{aligned} \tag{4.2.9}$$

where $G_{\mathcal{C}}$ is defined in eq. (4.1.54) and

$$\begin{aligned} H_{\mathcal{C}} &\equiv \left\| \frac{s}{(f_{\mathcal{C}}^{(2)}(\theta_{s,\mathcal{C}})V)^{1/2}} \exp\Bigg( -\sum_{n=3}^{\infty} \frac{f_{\mathcal{C}}^{(n)}(\theta_{s,\mathcal{C}})V}{n!(f_{\mathcal{C}}^{(2)}(\theta_{s,\mathcal{C}})V)^{n/2}} s^n \Bigg) \right\| = \\ &= \sum_{k=1}^{\infty} \frac{(-1)^k}{k!} \left\| \frac{s}{(f_{\mathcal{C}}^{(2)}(\theta_{s,\mathcal{C}})V)^{1/2}} \Bigg( \sum_{n=3}^{\infty} \frac{f_{\mathcal{C}}^{(n)}(\theta_{s,\mathcal{C}})V}{n!(f_{\mathcal{C}}^{(2)}(\theta_{s,\mathcal{C}})V)^{n/2}} s^n \Bigg)^k \right\|. \end{aligned} \tag{4.2.10}$$

As in section 4.1.1 it is easy to identify and calculate all terms of $H_{\mathcal{C}}$ up to $\mathcal{O}(1/(\mathcal{E}_2 V)^2)$:

- $k = 1, n = 3$ ($\propto 1/V^2$):

$$\left\| \frac{f_{\mathcal{C}}^{(3)}(\theta_{s,\mathcal{C}})V}{3!(f_{\mathcal{C}}^{(2)}(\theta_{s,\mathcal{C}})V)^2} s^4 \right\| = \frac{1}{\mathcal{F}_2 V} \frac{\mathcal{F}_4}{2\mathcal{F}_2} \theta_{s,\mathcal{C}} + \mathcal{O}\Big( \frac{1}{(\mathcal{E}_2 V)^4} \Big). \tag{4.2.11}$$

Inserting these expressions into eq. (4.2.10) leads to

$$H_{\mathcal{C}} = -\frac{1}{\mathcal{F}_2 V} \frac{\mathcal{F}_4}{2\mathcal{F}_2} \theta_{s,\mathcal{C}} + \mathcal{O}\Big( \frac{1}{(\mathcal{E}_2 V)^4} \Big). \tag{4.2.12}$$

The final explicit expression up to $\mathcal{O}(1/(\mathcal{E}_2 V)^2)$ for the contribution to $C^{jk}_{Q,V}(t)Z_{Q,V}$ (eq. (4.2.9)) is

$$\frac{\alpha^{(1)}(0)}{\sqrt{2\pi\mathcal{F}_2 V}}\Bigg(\exp\Bigg(-\mathcal{F}_0 V-\frac{1}{\mathcal{F}_2 V}\frac{1}{2}Q^2\Bigg)\Bigg(1-\frac{1}{(\mathcal{F}_2 V)^2}\frac{\mathcal{F}_4}{2\mathcal{F}_2}Q^2\Bigg)^{-1/2} \times\Big(\theta_{s,\mathcal{C}}G_{\mathcal{C}}+H_{\mathcal{C}}\Big)+\mathcal{O}\Bigg(\frac{1}{(\mathcal{E}_2 V)^3}Q^4\Bigg)\Bigg). \tag{4.2.13}$$

After dividing by $Z_{Q,V}$ (eq. (4.1.24)), it is straightforward to obtain the final result. In exponential form eq. (4.1.58) it is

$$C^{jk}_{Q,V}(t)\leftarrow\frac{i\alpha^{(1)}(0)Q}{\mathcal{E}_2 V}\exp\Bigg(-M_H(0)t-\frac{1}{\mathcal{E}_2 V}\Bigg(\frac{(\mathcal{E}_4/\mathcal{E}_2)+3x_2}{2}\Bigg)\Bigg)+\mathcal{O}\Bigg(\frac{1}{(\mathcal{E}_2 V)^3}\Bigg). \tag{4.2.14}$$

### 4.2.2 Calculation of $\alpha^{++}_{-}(\theta)$ and $\alpha^{--}_{+}(\theta)$

We proceed as in section 4.1.3. $\alpha(\theta)$ can be written as a power series around $\theta=0$,

$$\alpha(\theta)=\sum_{k=1}^{\infty}\frac{\alpha^{(2k)}(0)\theta^{2k}}{(2k)!}=\frac{\alpha^{(2)}(0)}{2}\theta^2\exp\Bigg(\underbrace{\ln\Bigg(\sum_{k=0}^{\infty}\frac{2\alpha^{(2k+2)}(0)\theta^{2k}}{(2k+2)!\alpha^{(2)}(0)}\Bigg)}_{\equiv-\beta(\theta)=-\sum_{k=1}^{\infty}\frac{\beta^{(2k)}(0)\theta^{2k}}{(2k)!}}\Bigg). \tag{4.2.15}$$

The corresponding contribution to $\mathcal{C}^{jk}_{\theta,V}(t)\mathcal{Z}_{\theta,V}$ (cf. eq. (4.2.3)) is

$$\alpha(\theta)e^{-M_H(\theta)t}e^{-E_0(\theta,V_s)T}=\frac{\alpha^{(2)}(0)}{2}\theta^2 e^{-(e_0(\theta)V+M_H(\theta)t+\beta(\theta))}. \tag{4.2.16}$$

As before we define

$$f_{\mathcal{C}}(\theta)\equiv f_{\mathcal{C}}(\theta,Q,V)\equiv e_0(\theta)+\frac{M_H(\theta)t+\beta(\theta)-iQ\theta}{V}. \tag{4.2.17}$$

For the contribution to the correlation matrix at fixed topology $C^{jk}_{Q,V}(t)Z_{Q,V}$ we then obtain

$$\frac{\alpha^{(2)}(0)}{4\pi}\int_{-\pi}^{+\pi}d\theta\,\theta^2 e^{-f_{\mathcal{C}}(\theta)V}, \tag{4.2.18}$$

where $f_{\mathcal{C}}(\theta)V$ is defined by eqs. (4.1.51) and (4.1.52). Consequently, its minimum $\theta_{s,\mathcal{C}}$ is given by eq. (4.1.53) and eq. (4.2.18) can be written as

$$\begin{aligned}&\frac{\alpha^{(2)}(0)e^{-f_{\mathcal{C}}(\theta_{s,\mathcal{C}})V}}{2(2\pi f^{(2)}_{\mathcal{C}}(\theta_{s,\mathcal{C}})V)^{1/2}}\Bigg\|\Bigg(\theta_{s,\mathcal{C}}+\frac{s}{(f^{(2)}_{\mathcal{C}}(\theta_{s,\mathcal{C}})V)^{1/2}}\Bigg)^2\exp\Bigg(-\sum_{n=3}^{\infty}\frac{f^{(n)}_{\mathcal{C}}(\theta_{s,\mathcal{C}})V}{n!(f^{(2)}_{\mathcal{C}}(\theta_{s,\mathcal{C}})V)^{n/2}}s^n\Bigg)\Bigg\|=\\ &\quad=\frac{\alpha^{(2)}(0)e^{-f_{\mathcal{C}}(\theta_{s,\mathcal{C}})V}}{2(2\pi f^{(2)}_{\mathcal{C}}(\theta_{s,\mathcal{C}})V)^{1/2}}\Big(\theta^2_{s,\mathcal{C}}G_{\mathcal{C}}+2\theta_{s,\mathcal{C}}H_{\mathcal{C}}+I_{\mathcal{C}}\Big),\end{aligned} \tag{4.2.19}$$

where $G_{\mathcal{C}}$ is defined in eq. (4.1.54), $H_{\mathcal{C}}$ is defined in eq. (4.2.10) and

$$\begin{aligned}I_{\mathcal{C}}&\equiv\Bigg\|\frac{s^2}{f^{(2)}_{\mathcal{C}}(\theta_{s,\mathcal{C}})V}\exp\Bigg(-\sum_{n=3}^{\infty}\frac{f^{(n)}_{\mathcal{C}}(\theta_{s,\mathcal{C}})V}{n!(f^{(2)}_{\mathcal{C}}(\theta_{s,\mathcal{C}})V)^{n/2}}s^n\Bigg)\Bigg\|=\\ &=\sum_{k=0}^{\infty}\frac{(-1)^k}{k!}\Bigg\|\frac{s^2}{f^{(2)}_{\mathcal{C}}(\theta_{s,\mathcal{C}})V}\Bigg(\sum_{n=3}^{\infty}\frac{f^{(n)}_{\mathcal{C}}(\theta_{s,\mathcal{C}})V}{n!(f^{(2)}_{\mathcal{C}}(\theta_{s,\mathcal{C}})V)^{n/2}}s^n\Bigg)^k\Bigg\|.\end{aligned} \tag{4.2.20}$$

As in section 4.1.1 it is easy to identify and calculate all terms of $I_\mathcal{C}$ up to $\mathcal{O}(1/(\mathcal{E}_2V)^2)$:

- $k=0$ ($\propto 1/V$):
$$\left\| \frac{s^2}{f_\mathcal{C}^{(2)}(\theta_{s,\mathcal{C}})V} \right\| = \frac{1}{\mathcal{F}_2 V} + \mathcal{O}\Big(\frac{1}{(\mathcal{E}_2V)^3}\Big). \tag{4.2.21}$$

- $k=1, n=4$ ($\propto 1/V^2$):
$$\left\| \frac{f_\mathcal{C}^{(4)}(\theta_{s,\mathcal{C}})V}{4!(f_\mathcal{C}^{(2)}(\theta_{s,\mathcal{C}})V)^3} s^6 \right\| = \frac{1}{(\mathcal{F}_2V)^2}\frac{5\mathcal{F}_4}{8\mathcal{F}_2} + \mathcal{O}\Big(\frac{1}{(\mathcal{E}_2V)^3}\Big). \tag{4.2.22}$$

Inserting these expressions into eq. (4.2.20) leads to

$$I_\mathcal{C} = \frac{1}{\mathcal{F}_2V} + \frac{1}{(\mathcal{F}_2V)^2}\Big(-\frac{5\mathcal{F}_4}{8\mathcal{F}_2}\Big) + \mathcal{O}\Big(\frac{1}{(\mathcal{E}_2V)^3}\Big). \tag{4.2.23}$$

The final explicit expression up to $\mathcal{O}(1/(\mathcal{E}_2V)^3)$ for the contribution to $C^{jk}_{Q,V}(t)Z_{Q,V}$ (eq. (4.2.19)) is

$$\begin{aligned}\frac{\alpha^{(2)}(0)}{2\sqrt{2\pi\mathcal{F}_2V}}\Big(\exp\Big(-\mathcal{F}_0V - \frac{1}{\mathcal{F}_2V}\frac{1}{2}Q^2\Big)\Big(1-\frac{1}{(\mathcal{F}_2V)^2}\frac{\mathcal{F}_4}{2\mathcal{F}_2}Q^2\Big)^{-1/2} \\ \times\Big(\theta_{s,\mathcal{C}}^2 G_\mathcal{C} + 2\theta_{s,\mathcal{C}}H_\mathcal{C} + I_\mathcal{C}\Big) + \mathcal{O}\Big(\frac{1}{(\mathcal{E}_2V)^3}Q^4\Big)\Big).\end{aligned} \tag{4.2.24}$$

After dividing by $Z_{Q,V}$ (eq. (4.1.24)), it is straightforward to obtain the final result. In exponential form eq. (4.1.58) it is

$$C^{jk}_{Q,V}(t) \leftarrow \frac{\alpha^{(2)}(0)}{2\mathcal{E}_2V}\exp\Big(-M_H(0)t - \frac{1}{\mathcal{E}_2V}\Big(\frac{(\mathcal{E}_4/\mathcal{E}_2)+3x_2}{2} + Q^2\Big)\Big) + \mathcal{O}\Big(\frac{1}{(\mathcal{E}_2V)^3}\Big). \tag{4.2.25}$$

### 4.2.3 The $2\times 2$ correlation matrix at fixed topology at $\mathcal{O}(1/\mathcal{E}_2V)$

The $2\times2$ correlation matrix $C^{jk}_{Q,V}(t)$, $j,k\in\{-,+\}$ can be obtained by properly adding the results eqs. (4.1.59), (4.2.14) and (4.2.25). To first order in $1/\mathcal{E}_2V$ it is given by

$$\begin{aligned}C^{--}_{Q,V}(t) &= \alpha_-^{--}(0)\exp\Big(-M_{H_-}(0)t - \frac{1}{\mathcal{E}_2V}\frac{x^{--}_{2,-}}{2}\Big) + \frac{\alpha_+^{--,(2)}(0)}{2\mathcal{E}_2V}\exp\Big(-M_{H_+}(0)t\Big) \\ &\quad + \mathcal{O}\Big(\frac{1}{(\mathcal{E}_2V)^2}\Big)\end{aligned} \tag{4.2.26}$$

$$\begin{aligned}C^{++}_{Q,V}(t) &= \alpha_+^{++}(0)\exp\Big(-M_{H_+}(0)t - \frac{1}{\mathcal{E}_2V}\frac{x^{++}_{2,+}}{2}\Big) + \frac{\alpha_-^{++,(2)}(0)}{2\mathcal{E}_2V}\exp\Big(-M_{H_-}(0)t\Big) \\ &\quad + \mathcal{O}\Big(\frac{1}{(\mathcal{E}_2V)^2}\Big)\end{aligned} \tag{4.2.27}$$

$$\begin{aligned}C^{\mp\pm}_{Q,V}(t) &= \frac{i\alpha_-^{\mp\pm,(1)}(0)Q}{\mathcal{E}_2V}\exp\Big(-M_{H_-}(0)t\Big) + \frac{i\alpha_+^{\mp\pm,(1)}(0)Q}{\mathcal{E}_2V}\exp\Big(-M_{H_+}(0)t\Big) \\ &\quad + \mathcal{O}\Big(\frac{1}{(\mathcal{E}_2V)^2}\Big),\end{aligned} \tag{4.2.28}$$

where $x^{\pm\pm}_{2,\pm} = M^{(2)}_{H_\pm}t + \beta^{\pm\pm,(2)}_\pm$ and $\beta^{\pm\pm,(2)}_\pm = -\alpha^{\pm\pm,(2)}_\pm(0)/\alpha^{\pm\pm}_\pm(0)$ (cf. eq. (4.1.47)). The quantities $\alpha^{jk}_n$ are products of the more fundamental $A^j_n$ (cf. eq. (4.2.4)) and, therefore, are not independent and fulfill certain

constraints. Since the diagonal elements of $\mathcal{C}^{jk}_{\theta,V}(t)$ are real and $\geq 0$,

- $\alpha^{--}_{-}(0), \alpha^{++}_{+}(0), \alpha^{++,(2)}_{-}(0), \alpha^{--,(2)}_{+}(0) \geq 0$ and real (4 real parameters),
- $\alpha^{--,(2)}_{-}(0), \alpha^{++,(2)}_{+}(0)$ real (2 real parameters).

Moreover, from $(\mathcal{C}^{jk}_{\theta,V}(t))^* = \mathcal{C}^{kj}_{\theta,V}(t)$ follows

- $(\alpha^{-+,(1)}_{-}(0))^* = \alpha^{+-,(1)}_{-}(0)$ and $(\alpha^{-+,(1)}_{+}(0))^* = \alpha^{+-,(1)}_{+}(0)$ (4 real parameters).

Quite often one can define the hadron creation operators $O_-$ and $O_+$ in such a way that the off-diagonal elements of $\mathcal{C}^{jk}_{\theta,V}(t)$ are real (or purely imaginary), which reduces the number of real parameters contained in $\alpha^{jk}_n$ from 10 to 8. There are further parameters, $M_{H_-}(0)$, $M_{H_+}(0)$, $M^{(2)}_{H_-}(0)$, $M^{(2)}_{H_+}(0)$ and $\mathcal{E}_2$, i.e. in total 13 parameters.

Eqs. (4.2.26) to (4.2.28) clearly show that parity mixing at fixed topology is already present at order $1/\mathcal{E}_2 V$. In particular this will cause problems when trying to extract the mass of a hadron which has a lighter parity partner, from a single two-point correlation function: e.g. the first term in $C^{++}_{Q,V}(t)$ (eq. (4.2.27)) is suited to determine a positive parity meson; however, there is a contamination by the corresponding lighter negative parity meson due to the second term, which is only suppressed proportional to $1/\mathcal{E}_2 V$ with respect to the spacetime volume: Since the first term is exponentially suppressed with respect to the temporal separation compared to the second term ($\propto e^{-(M_{H_+}-M_{H_-})t}$), a precise determination of $M_{H_+}$ from the single correlator $C^{++}_{Q,V}(t)$ seems extremely difficult and would probably require extremely precise simulation results. Using the full $2\times 2$ correlation matrix eqs. (4.2.26) to (4.2.28) should, however, stabilize a fit to extract $M_{H_+}$ and $M_{H_-}$ at the same time (this is discussed in detail in section 5.2.1.4), similar to what is usually done at ordinary unfixed topology computations, when determining excited states.

This parity mixing at fixed topology has already been observed and discussed in the context of the $\eta$ meson in [11]. When considering the correlation function $C^{--}_{Q,V}(t)$ with a suitable $\eta$ meson creation operator, e.g.

$$O_- \equiv \frac{1}{\sqrt{V_s}} \int d^3r \left( \bar{u}(\mathbf{r})\gamma_5 u(\mathbf{r}) + \bar{d}(\mathbf{r})\gamma_5 d(\mathbf{r}) \right), \tag{4.2.29}$$

one finds

$$C^{--}_{Q,V}(t) = \alpha^{--}_{\eta}(0) \exp\left( -M_\eta(0)t - \frac{1}{\mathcal{E}_2 V}\frac{x^{--}_{2,\eta}}{2} \right) + \frac{\alpha_0^{--,(2)}(0)}{2\mathcal{E}_2 V} + \mathcal{O}\left(\frac{1}{(\mathcal{E}_2 V)^2}\right), \tag{4.2.30}$$

where $M_{H_+} = 0$ has been used ($H_+$ takes in this context the role of the "vacuum state"). Using $\alpha_0^{--,(2)}(0) = -2\mathcal{E}_2^2$ from [11] shows that there is a time independent contribution $-\mathcal{E}_2/V$ to the correlation function $C^{--}_{Q,V}(t)$ as in [11].

It is straightforward to extend eqs. (4.2.26) to (4.2.28) to larger correlation matrices formed by more than the two operators $O_-$ and $O_+$. Similarly, it is easy to include further states besides $H_-$ and $H_+$. In both cases one just has to properly add the expressions eqs. (4.1.59), (4.2.14) and (4.2.25) and assign suitable indices. In appendix C, eqs. (4.2.26) to (4.2.28) are expressed up to $\mathcal{O}(1/(\chi_t V)^3)$.

## 4.3 Discussion of the errors

In this section we discuss in which regime of parameters our $1/V$ expansions of two-point correlation function at fixed topology eqs. (4.1.57) and (4.1.59) are accurate approximations.

### 4.3.1 Errors proportional to $1/\chi_t V$

In section 4.1.4 the spacetime dependence of two-point correlation functions $C_{Q,V}(t)$ has been derived up to $1/V^3$. More precisely, the error is

$$\mathcal{O}\left(\frac{1}{(\chi_t V)^4}\ ,\ \frac{1}{(\chi_t V)^4}Q^2\ ,\ \frac{1}{(\chi_t V)^4}Q^4\right) \tag{4.3.1}$$

(cf. eq. (4.1.57), the text below eqs. (4.1.57) and (4.1.59)). This error will be small, if

**(C1)** $\quad 1/\chi_t V \ll 1 \quad , \quad |Q|/\chi_t V \ll 1$**.**

In other words, computations at fixed topology require large spacetime volumes $V$ (in units of the topological susceptibility $\chi_t = \mathcal{E}_2$), while the topological charge $|Q|$ may not be too large. However, in view of the calculus one can also argue that the conditions should rather be that $Q^2/\chi_t V \ll 1$ instead of $|Q|/\chi_t V \ll 1$. We can call this second condition **(C1')**. Making a clear separation between this two conditions is not easy as fulfilling the condition **(C1')** implies that the condition **(C1)** is fulfilled. We have also used $\mathcal{F}_2 = \chi_t + \mathcal{O}(1/\chi_t V)$, which requires

**(C2)** $\quad |x_2| = |M_H^{(2)}(0)t + \beta^{(2)}(0)| \lesssim 1$**.**

The time dependence of this constraint excludes the use of large values of $t$.

### 4.3.2 Exponentially suppressed errors

In sections 4.1.1 and 4.1.3 several exponentially suppressed corrections have been neglected:

1. **Ordinary finite volume effects, i.e. finite volume effects not associated with fixed topology:**
   Such finite volume effects also appear in QCD simulations, where topology is not fixed. These effects are expected to be proportional to $e^{-m_\pi(\theta)L}$, where $m_\pi(\theta)$ is the mass of the pion (the lightest hadron mass) and $L$ is the periodic spatial extension (cf. chapter 6).

2. **Contributions of excited states to the partition function and to two-point correlation functions:**
   Excited states contribute to the partition function $\mathcal{Z}_{\theta,V}$ proportional to $e^{-\Delta E(\theta)T}$ (cf. eq. (4.1.6)) where $\Delta E(\theta) = E_1(\theta, V_s) - E_0(\theta, V_s)$ is the mass of the lightest hadron, i.e. $\Delta E(\theta) = m_\pi(\theta)$.
   The corresponding dominating terms in a two-point correlation function $\mathcal{C}_{\theta,V}(t)\mathcal{Z}_{\theta,V}$ are proportional to $e^{-(M_H^*(\theta)-M_H(\theta))t}$ and $e^{-M_H(\theta)(T-2t)}$ (cf. eq. (4.1.45)), where $M_H(\theta)$ is the mass of the hadron of interest and $M_H^*(\theta) - M_H(\theta)$ the difference to its first excitation.

3. **Changing the integration limits in** eq. **(4.1.8) from** $\int_{-\pi}^{+\pi}$ **to** $\int_{-\infty}^{+\infty}$**:**
   The relative error is expected to be suppressed exponentially by the second term in the exponential in (4.1.9) and, therefore, proportional to

$$\exp\left(-\frac{\chi_t V}{2}(\pi - \theta_s)^2\right) \approx \exp\left(-\frac{\pi^2 \chi_t V}{2}\right). \tag{4.3.2}$$

In zero temperature QCD simulations typically $L \lesssim T$. For sufficiently large values of $m_\pi(\theta)L$, e.g.

**(C3)** $\quad m_\pi(\theta)L \gtrsim 5 \gg 1$

as typically required in QCD simulations but difficult to reach. Corrections (1) and for the partition function also (2) should essentially be negligible. To be able to ignore corrections (2) for two-point correlation functions, one needs

**(C4)** $\quad (M_H^*(\theta) - M_H(\theta))t \gg 1 \quad , \quad M_H(\theta)(T - 2t) \gg 1$**.**

Corrections (3) can be neglected, if $\chi_t V \gg 1$, which is already part of **(C1)**.

# Chapter 5

# Numerical tests of the BCNW-equations

In the previous chapter the BCNW-equations and their extensions (higher order, parity, ...) have been derived mathematically in the continuum limit. It this chapter we will present a method to extract physical masses from fixed topology based on the BCNW-equation. In the second part of this chapter, several numerical results on different models will be presented to conclude on the viability of the method.

## 5.1 A method to extract physical masses

A straightforward method to determine physical hadron masses (i.e. hadron masses at unfixed topology) from fixed topology simulations based on the $1/V$ expansion eq. (4.1.61) is proposed in [8]:

1. Perform simulations at fixed topology for different topological charges $Q$ and spacetime volumes $V$. Determine the fixed topology hadron masses $M_{Q,V}$ for each simulation.

2. Determine the hadron mass $M_H(0)$ (the hadron mass at unfixed topology), $M_H^{(2)}(0)$ and $\chi_t$ by fitting eq. (4.1.61) to the fixed topology hadron mass $M_{Q,V}$ obtained in step 1.

Note, however, that two-point correlation functions at fixed topology do not decay exponentially $\propto e^{-M_{Q,V}t}$ at large temporal separations $t$ (cf. e.g. eq. (4.1.57)), as their counterparts at unfixed topology do. Therefore, determining a fixed topology and finite volume mass $M_{Q,V}$ is not clear without ambiguity. One could e.g. define $M_{Q,V}$ at some temporal separation $t_M$, where the $1/V$ expansion is a good approximation, i.e. where the conditions **(C2)** and **(C4)** from section 4.3 are fulfilled, using eq. (5.2.3), i.e.

$$M_{Q,V} \equiv M_{Q,V}^{\text{eff}}(t_M) = -\frac{\mathrm{d}}{\mathrm{d}\,t} \ln\left(C_{Q,V}(t)\right)\Big|_{t=t_M}. \tag{5.1.1}$$

However, it is possible that statistical errors on the mass hide this time dependence. In that case a plateau for the mass can be found and the determination of the mass can be done in the usual manner.

To exploit the input data and also the derived $1/V$ expansions for the two-point correlation functions at fixed topology, we propose another method:

1. Perform simulations at fixed topology for different topological charges $Q$ and spacetime volumes $V$. Determine $C_{Q,V}(t)$ for each simulation.

2. Determine the physical hadron mass $M_H(0)$ by performing a single $\chi^2$ minimizing fit of the preferred $1/V$ expansions of $C_{Q,V}(t)$ with respect to its parameters (cf. section 5.2.1.3 for a detailed summary of available expansions and their parameters) to the two-point correlation functions obtained in step 1. This input from step 1 is limited to those $Q$, $V$ and $t$ values, for which the conditions **(C1)**, **(C2)** and **(C4)** from section 4.3 are fulfilled.

Note that this method can also be applied when using correlation matrices at fixed topology. Then the corresponding expansions, e.g. eqs. (4.2.26) to (4.2.28), have to be fitted simultaneously to all elements of the correlation matrix.

## 5.2 The 1D O(2)-model

The case of the O(2)-model without potential is treated in appendix B. It represents a specific case as the $\theta \to -\theta$ symmetry is only a "global" symmetry (in the sens that if each energy levels does not respect the symmetry, however if you take the quantity $E_n(\theta) + E_{-n}(\theta)$ then the symmetry is respected as $E_n(\theta) = E_{-n}(-\theta)$ ) and the condition $E_n(\theta) = E_n(-\theta)$ is not fulfilled which is the reason it is not included in the main part of the thesis. However, this is an analytically solvable case, where it can be proved that some quantities follow the BCNW-equation. Proofs, numerical results and test are presented in the appendix B and interested readers are invited to have a close look on it. In this section, we are interested in the O(2)-model with a square well potential that respects the condition $E_n(\theta) = E_n(-\theta)$. It is solvable numerically up to an arbitrary precision using tools such as Mathematica. This latter property allows us to make extensive tests which include higher order of the BCNW-equation.

### 5.2.1 A particle in a square well

The square well potential is given by

$$U(\varphi) \equiv \begin{cases} 0 & \text{if } -\rho/2 < \varphi < +\rho/2 \\ U_0 & \text{otherwise} \end{cases} \tag{5.2.1}$$

($U_0 > 0$ is the depth and $\rho > 0$ the width of the well). We use the creation operator $O \equiv \sin(\varphi)$ for which one can show $\langle 0;\theta|O|0;\theta\rangle = 0$ [1]

#### 5.2.1.1 Solving the model numerically

For the square well potential eq. (5.2.1) the Schrödinger equation cannot be solved analytically, but numerically up to arbitrary precision, i.e. no simulations are required. For these numerical computations we express all dimensionful quantities in units of $\beta$, i.e. we work with dimensionless quantities. For the numerical results presented in this section we use $U_0 = 5.0$ and $\rho = 0.9 \times 2\pi$.

We proceeded as follows:

1. Solve Schrödinger's equation
2. Use the resulting energy eigenvalues $E_0(\theta)$ and $E_1(\theta)$ to determine
   - $\mathcal{E}_n = E_0^{(n)}(0)$, $n = 0, 2, 4, 6, 8$.
   - $M_H^{(n)}(0) = (d/d\theta)^n (E_1(\theta) - E_0(\theta))|_{\theta=0}$, $n = 0, 2, 4, 6, 8$

   and the resulting wave functions $\psi_0(\varphi;\theta)$ and $\psi_1(\varphi;\theta)$ to determine
   - $\alpha^{(n)}(0)$, $n = 0, 2, 4, 6, 8$,

[1] A complicated theory like QCD has many symmetries and, therefore, many orthogonal sectors of states, which are labeled by the corresponding quantum numbers (total angular momentum, charge conjugation, flavor quantum numbers). In such a theory one typically chooses an operator exciting states, which do not have the quantum numbers of the vacuum, i.e. where $\langle 0;\theta, V_s|O|0;\theta, V_s\rangle = 0$, due to symmetry. In the simple quantum mechanical model parity is the only symmetry, which is broken at $\theta \neq 0$. Therefore, constructing an appropriate creation operator is less straightforward because $\langle 0;\theta|O|0;\theta\rangle = 0$ is not guaranteed by obvious symmetries but has to be shown explicitly.

- $\beta^{(n)}(0)$, $n = 2, 4, 6, 8$,

where

$$\alpha(\theta) = \left| \int_0^{2\pi} d\varphi \, (\psi_1(\varphi;\theta))^* \sin(\varphi)\psi_0(\varphi;\theta) \right|^2 \quad , \quad \beta(\theta) = -\ln\left(\frac{\alpha(\theta)}{\alpha(0)}\right). \tag{5.2.2}$$

These are the parameters of the two-point correlation function $C_{Q,T}(t)$, (eqs. (4.1.57) and (4.1.59)).

3. Calculate $\mathcal{C}_{\theta,T}(t)$ using sufficiently many low lying energy eigenvalues and corresponding wave functions from step 1 such that the exponentially suppressed error is negligible already for very small temporal separations (cf. eqs. (A.2.6) and (4.1.44)).

4. Perform a Fourier transformation numerically to obtain $C_{Q,T}(t)$, the exact correlation function at fixed topology.

5. Define and calculate the effective mass

$$M^{\text{eff}}_{Q,T}(t) \equiv -\frac{d}{dt} \ln\Big(C_{Q,T}(t)\Big). \tag{5.2.3}$$

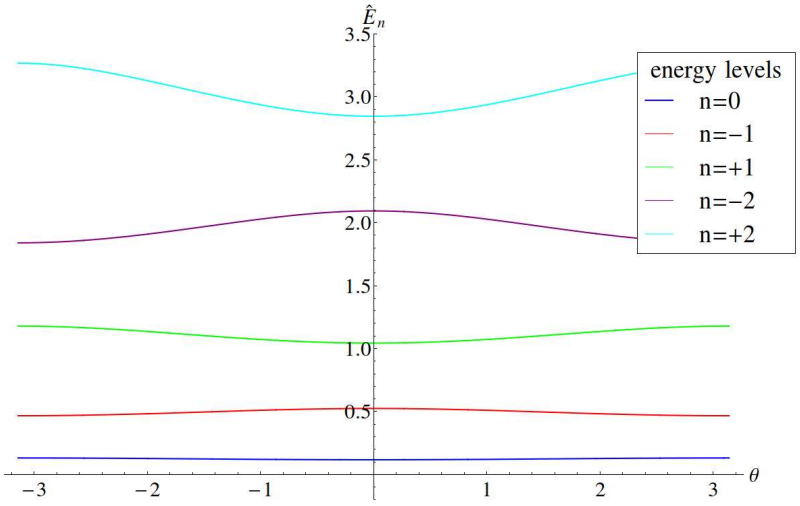


Figure 5.2.1: The low lying energy eigenvalues $E_n$ for the square well potential (5.2.1) with $U_0 = 5.0$ and $\rho = 0.9 \times 2\pi$ as functions of $\theta$.

#### 5.2.1.2 Effective masses at fixed topology

In figure 5.2.2 we show effective masses $M^{\text{eff}}_{Q,T}(t)$ (eq. (5.2.3)) as functions of the temporal separation $t$ for different topological sectors $Q$ and $T = 6.0/\mathcal{E}_2 \approx 930.2$. As usual, at small temporal separations the effective masses are quite large and strongly decreasing due to the presence of excited states. At large temporal separations there are also severe deviations from a constant behavior. This contrasts ordinary quantum mechanics or quantum field theory (i.e. at unfixed topology) and is caused by topology fixing. This effect is also visible in the $1/V$ expansion of the two-point correlation function, in particular in eq. (4.1.59), where the exponent is not purely linear in $t$ for large $t$, but contains also terms proportional to $t^2$ and $t^3$. At intermediate temporal separations there are plateau-like regions, which become smaller with increasing topological charge $Q$.

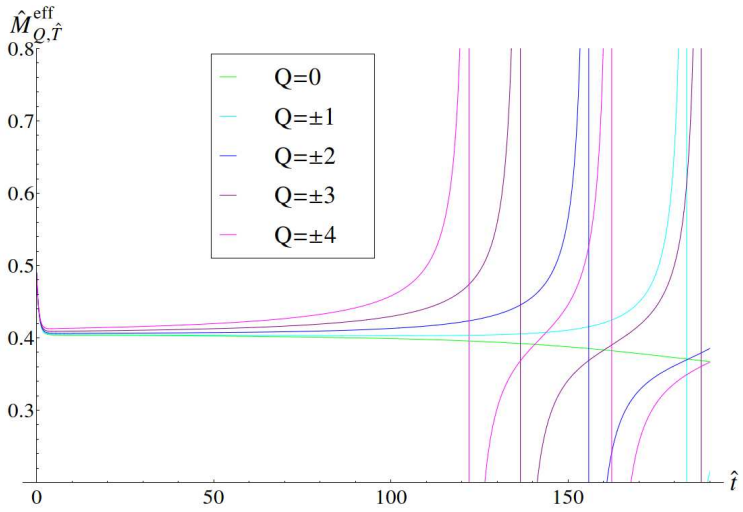


Figure 5.2.2: Effective masses $M^{\text{eff}}_{Q,T}(t)$ as functions of the temporal separation $\hat{t}$ for different topological sectors $Q$ and $T = 6.0/\mathcal{E}_2 \approx 930.2$.

#### 5.2.1.3 Comparison of the $1/V$ expansions of $C_{Q,T}(t)$ and the exact result

In figure 5.2.3 we show effective masses derived from the $1/V$ expansions of two-point correlation functions[2] eqs. (4.1.57) (left column) and (4.1.59) (right column) using the definition eq. (5.2.3). The first, second and third row correspond to $Q = 0$, $|Q| = 1$ and $|Q| = 2$, respectively. To illustrate the relative importance of $1/V$, $1/V^2$ and $1/V^3$ terms, we also show versions of eqs. (4.1.57) and (4.1.59), which are only derived up to $\mathcal{O}(1/V)$ and $\mathcal{O}(1/V^2)$. While less accurate, these expressions contain a smaller number of parameters, which might be an advantage, when e.g. fitting to results from lattice simulations (such a fitting is discussed in section 5.2.1.4). In detail the following curves are shown with $V \to T$ :

- $M^{\text{eff}}_{Q,T}(t)$ from eq. (4.1.57), derived up to $\mathcal{O}(1/V)$:

$$
\begin{aligned}
C_{Q,V}(t) &= \frac{\alpha(0)}{\sqrt{1+x_2/\mathcal{E}_2 V}} \exp\left( - M_H(0)t - \frac{1}{\mathcal{E}_2 V}\left(\frac{1}{1+x_2/\mathcal{E}_2 V} - 1\right)\frac{1}{2}Q^2\right)\frac{G_{\mathcal{C}}}{G} \\
G_{\mathcal{C}} &= 1 - \frac{1}{\mathcal{E}_2 V}\frac{\mathcal{E}_4(1+x_4/\mathcal{E}_4 V)}{8\mathcal{E}_2(1+x_2/\mathcal{E}_2 V)^2} \\
G &= 1 - \frac{1}{\mathcal{E}_2 V}\frac{\mathcal{E}_4}{8\mathcal{E}_2};
\end{aligned}
\tag{5.2.4}
$$

  **8 parameters** ($\mathcal{E}_2$, $\mathcal{E}_4$, $M_H(0)$, $M_H^{(2)}(0)$, $M_H^{(4)}(0)$, $\alpha(0)$, $\beta^{(2)}(0)$, $\beta^{(4)}(0)$) which appear implicitly in $x_2$ and $x_4$

[2]Note that in quantum mechanics a $1/V$ expansion is a $1/T$ expansion.

- $M^{\text{eff}}_{Q,T}(t)$ from eq. (4.1.57), derived up to $\mathcal{O}(1/V^2)$:

$$\begin{aligned} C_{Q,V}(t) &= \frac{\alpha(0)}{\sqrt{1+x_2/\mathcal{E}_2V}} \\ &\quad \exp\Big( - M_H(0)t - \frac{1}{\mathcal{E}_2V}\Big(\frac{1}{1+x_2/\mathcal{E}_2V} - 1\Big)\frac{1}{2}Q^2\Big) \\ &\quad \Big(1 - \frac{1}{(\mathcal{E}_2V)^2}\frac{\mathcal{E}_4}{2\mathcal{E}_2}Q^2\Big)^{1/2}\Big(1 - \frac{1}{(\mathcal{E}_2V)^2}\frac{\mathcal{E}_4(1+x_4/\mathcal{E}_4V)}{2\mathcal{E}_2(1+x_2/\mathcal{E}_2V)^3}Q^2\Big)^{-1/2}\frac{G_{\mathcal{C}}}{G} \\ G_{\mathcal{C}} &= 1 - \frac{1}{\mathcal{E}_2V}\frac{\mathcal{E}_4(1+x_4/\mathcal{E}_4V)}{8\mathcal{E}_2(1+x_2/\mathcal{E}_2V)^2} \\ &\quad + \frac{1}{(\mathcal{E}_2V)^2}\Big( - \frac{\mathcal{E}_6(1+x_6/\mathcal{E}_6V)}{48\mathcal{E}_2(1+x_2/\mathcal{E}_2V)^3} + \frac{35\mathcal{E}_4^2(1+x_4/\mathcal{E}_4V)^2}{384\mathcal{E}_2^2(1+x_2/\mathcal{E}_2V)^4}\Big) \\ G &= 1 - \frac{1}{\mathcal{E}_2V}\frac{\mathcal{E}_4}{8\mathcal{E}_2} + \frac{1}{(\mathcal{E}_2V)^2}\Big( - \frac{\mathcal{E}_6}{48\mathcal{E}_2} + \frac{35\mathcal{E}_4^2}{384\mathcal{E}_2^2}\Big); \end{aligned} \tag{5.2.5}$$

  **11 parameters** ($\mathcal{E}_2$, $\mathcal{E}_4$, $\mathcal{E}_6$, $M_H(0)$, $M_H^{(2)}(0)$, $M_H^{(4)}(0)$, $M_H^{(6)}(0)$, $\alpha(0)$, $\beta^{(2)}(0)$, $\beta^{(4)}(0)$, $\beta^{(6)}(0)$).

- $M^{\text{eff}}_{Q,T}(t)$ from eq. (4.1.57) (which is derived up to $\mathcal{O}(1/V^3)$);
  **14 parameters** ($\mathcal{E}_2$, $\mathcal{E}_4$, $\mathcal{E}_6$, $\mathcal{E}_8$, $M_H(0)$, $M_H^{(2)}(0)$, $M_H^{(4)}(0)$, $M_H^{(6)}(0)$, $M_H^{(8)}(0)$, $\alpha(0)$, $\beta^{(2)}(0)$, $\beta^{(4)}(0)$, $\beta^{(6)}(0)$, $\beta^{(8)}(0)$).

- $M^{\text{eff}}_{Q,T}(t)$ from eq. (4.1.59), up to $\mathcal{O}(1/V)$:

$$C_{Q,V}(t) = \alpha(0)\exp\Big( - M_H(0)t - \frac{1}{\mathcal{E}_2V}\frac{x_2}{2}\Big); \tag{5.2.6}$$

  **5 parameters** ($\mathcal{E}_2$, $M_H(0)$, $M_H^{(2)}(0)$, $\alpha(0)$, $\beta^{(2)}(0)$).

- $M^{\text{eff}}_{Q,T}(t)$ from eq. (4.1.59), up to $\mathcal{O}(1/V^2)$:

$$\begin{aligned} &C_{Q,V}(t) = \\ &\quad = \alpha(0)\exp\Big( - M_H(0)t - \frac{1}{\mathcal{E}_2V}\frac{x_2}{2} - \frac{1}{(\mathcal{E}_2V)^2}\Big(\frac{x_4 - 2(\mathcal{E}_4/\mathcal{E}_2)x_2 - 2x_2^2}{8} - \frac{x_2}{2}Q^2\Big)\Big); \end{aligned} \tag{5.2.7}$$

  **8 parameters** ($\mathcal{E}_2$, $\mathcal{E}_4$, $M_H(0)$, $M_H^{(2)}(0)$, $M_H^{(4)}(0)$, $\alpha(0)$, $\beta^{(2)}(0)$, $\beta^{(4)}(0)$).

- $M^{\text{eff}}_{Q,T}(t)$ from eq. (4.1.59) (which is derived up to $\mathcal{O}(1/V^3)$);
  **11 parameters** ($\mathcal{E}_2$, $\mathcal{E}_4$, $\mathcal{E}_6$, $M_H(0)$, $M_H^{(2)}(0)$, $M_H^{(4)}(0)$, $M_H^{(6)}(0)$, $\alpha(0)$, $\beta^{(2)}(0)$, $\beta^{(4)}(0)$, $\beta^{(6)}(0)$).

Note that the definition eq. (5.2.3) of $M^{\text{eff}}_{Q,T}(t)$ eliminates $\alpha(0)$, i.e. effective masses have one parameter less than the corresponding two-point correlation functions. For comparison we also include the exact result already shown and discussed in figure 5.2.2. Finally, the dashed line indicates the "hadron mass" $M_H(0)$ at unfixed topology, to demonstrate the effect of topology fixing on effective masses.

The validity of the shown $1/V$ expansions has been discussed in section 4.3 and summarized in terms of four conditions, which we check for the quantum mechanical example with parameters $\hat{U}_0 = 5.0$, $\rho = 0.9 \times 2\pi$ and $\hat{T} = 6.0/\hat{\mathcal{E}}_2$:

- **(C1)**:
  $1 \gg 1/\mathcal{E}_2T = 1/6.0$ and $1 \gg |Q|/\mathcal{E}_2T = 0\ ,\ 1/6.0\ ,\ 1/3.0$ for $|Q| = 0\ ,\ 1\ ,\ 2$, i.e. fulfilled. $|Q| = 3, 4, \ldots$ might need a larger $T$ extent.

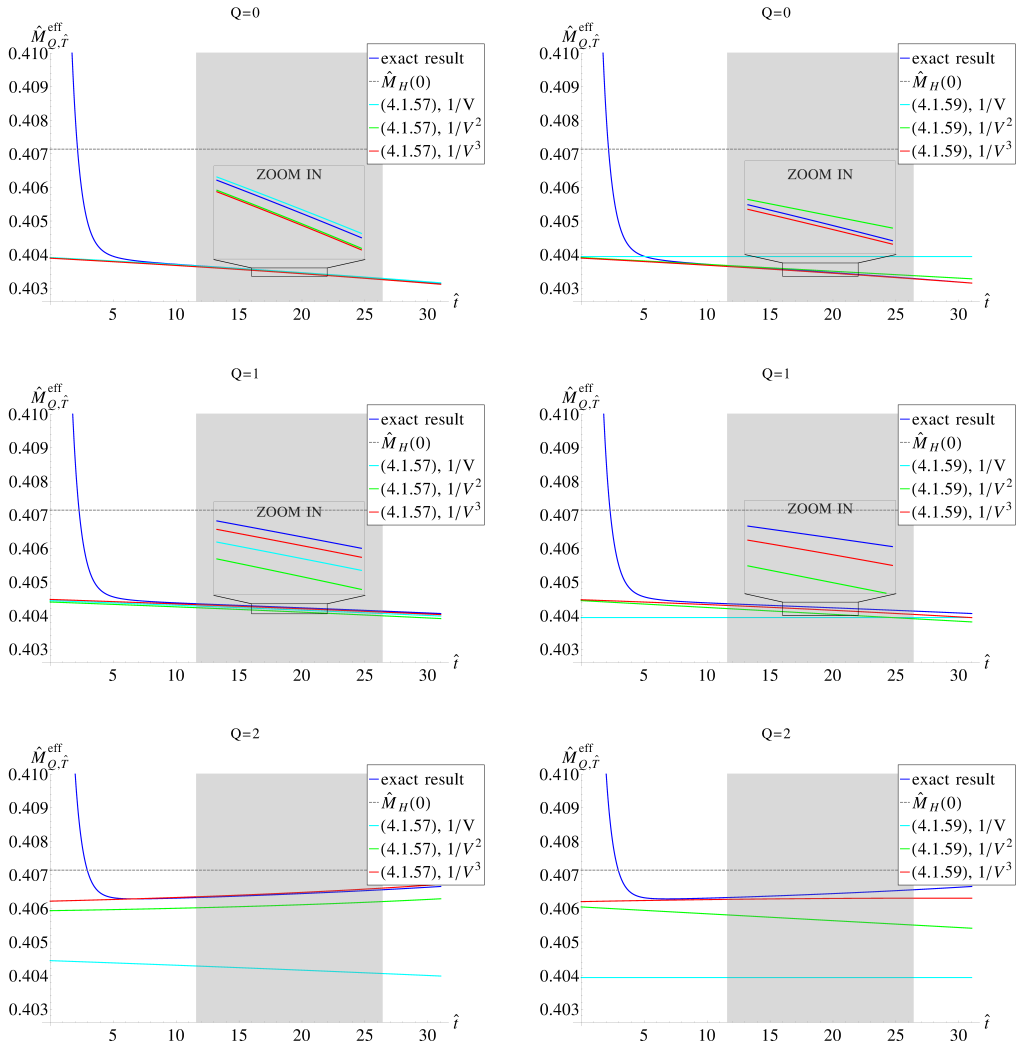


Figure 5.2.3: Effective masses $M^{\rm eff}_{Q,T}(t)$ derived from the $1/\hat{V}$ expansions of two-point correlation functions as functions of the temporal separation $t$ in different topological sectors $Q$ and $\hat{T} = 6.0/\mathcal{E}_2 \approx 930.2$.

- **(C2)**:
  Solving **(C2)**, $|x_2| = |M_H^{(2)}(0)t + \beta^{(2)}(0)| \lesssim 1$, with respect to $t$ and inserting the numbers from table 6.3.1 yields $t \lesssim |(1+\beta^{(2)}(0))/M_H^{(2)}(0)| \approx 26.2$. For significantly larger $t$ values the accuracy of the $1/V$ expansion is expected to suffer. The "safe region", $t \lesssim 26.2$, is shaded in light gray in figure 5.2.3.

- **(C3)**:
  Figure 5.2.1 shows that $M_H(\theta)$ (the analog of $m_\pi$ in QCD) is minimal at $\theta = \pm\pi$, $M_H(\pm\pi) = 0.336$. $m_\pi L$ corresponds to $M_H(\pm\pi)T$ and $M_H(\pm\pi)T = 6.0 \times M_H(\pm\pi)/\mathcal{E}_2 \approx 312.6 \gg 1$, i.e. the condition is clearly fulfilled.

- **(C4)**:
  Figure 5.2.1 shows that $M_H^*(\theta) - M_H(\theta)$ is minimal at $\theta = 0$, $M_H^*(0) - M_H(0) = 0.520$; therefore, $(M_H^*(0) - M_H(0))t \gg 1$ corresponds to $t \gg 1/(M_H^*(0) - M_H(0)) \approx 1.92$. We consider $6.0 \gg 1$ and shade the corresponding safe region $t > 6.0 \times 1.920 \approx 11.5$ in light gray.
  Finally $M_H(\theta)(T-2t) \gg 1$ can be solved with respect to $t$ resulting in $t \ll (T - 1/M_H(\theta))/2 \approx 463.6$. Clearly also this condition is fulfilled.

The effective mass plots shown in figure 5.2.3 are consistent with these estimates. There is nearly perfect agreement between the $1/V$ expansions of $M_{Q,T}^{\text{eff}}(t)$ and the exact results in the gray regions. On the other hand the difference of the effective mass at fixed topology and the mass at unfixed topology (the quantity one is finally interested in) is quite large. This clearly indicates that determining hadron masses from fixed topology simulations with standard methods (e.g. fitting a constant to an effective mass at large temporal separations) might lead to sizable systematic errors, which, however, can be reduced by orders of magnitude, when using the discussed $1/V$ expansions of $M_{Q,T}^{\text{eff}}(t)$ .

The number of parameters, in particular for the expansions derived up to $\mathcal{O}(1/V^3)$, i.e. eqs. (4.1.57) and (4.1.59), is quite large. This could be a problem, when fitting these expressions to lattice results for two-point correlation functions, where statistical accuracy is limited, e.g. for expensive QCD simulations. A possibility to benefit from the higher order expansions at least to some extent, while keeping at the same time the number of fit parameters small, is to use eqs. (4.1.57) and (4.1.59) (i.e. expansions up to $\mathcal{O}(1/V^3)$), but to set parameters, which are expected to be less important, to zero. In figure 5.2.4 we explore this possibility by restricting eqs. (4.1.57) and (4.1.59) to the parameters $\mathcal{E}_2$, $M_H(0)$, $M_H^{(2)}(0)$ and $\alpha(0)$, which are the **4 parameters** of eq. (4.1.61), the $1/V$ expansion from the seminal paper [8]. In detail the following curves are shown with the parameters taken from table 6.3.1:

- $M_{Q,T}^{\text{eff}}(t)$ from eq. (4.1.57).

- $M_{Q,T}^{\text{eff}}(t)$ from eq. (4.1.57), restricted to the **3 parameters** $\mathcal{E}_2$, $M_H(0)$ and $M_H^{(2)}(0)$:

$$C_{Q,V}(t) = \frac{\alpha(0)}{\sqrt{1+x_2/\mathcal{E}_2 V}} \exp\left( -M_H(0)t - \frac{1}{\mathcal{E}_2 V}\left(\frac{1}{1+x_2/\mathcal{E}_2 V} - 1\right)\frac{1}{2}Q^2\right) \tag{5.2.8}$$

  with $x_2 \equiv M_H^{(2)}t$.

- $M_{Q,T}^{\text{eff}}(t)$ from eq. (4.1.59).

- $M_{Q,T}^{\text{eff}}(t)$ from eq. (4.1.59), restricted to the **3 parameters** $\mathcal{E}_2$, $M_H(0)$ and $M_H^{(2)}(0)$:

$$\begin{aligned} C_{Q,V}(t) = \alpha(0) \\ \exp\left( -M_H(0)t - \frac{1}{\mathcal{E}_2 V}\frac{x_2}{2} + \frac{1}{(\mathcal{E}_2 V)^2}\left(\frac{x_2^2}{4} + \frac{x_2}{2}Q^2\right) - \frac{1}{(\mathcal{E}_2 V)^3}\left(\frac{x_2^3}{6} + \frac{x_2^2}{2}Q^2\right)\right) \end{aligned} \tag{5.2.9}$$

with $x_2 \equiv M_H^{(2)} t$.

- $M_{Q,T}^{\text{eff}}(t)$ from eq. (4.1.61), the $1/V$ expansion from [8].

Even though the number of parameters is identical, the "parameter restricted $\mathcal{O}(1/V^3)$ expansions", in particular eq. (5.2.8), are significantly closer to the exact result. In practice, when fitting to a correlator from fixed topology QCD simulations with statistical errors, where one is limited in the number of fit parameters, using eq. (5.2.8) might be the best compromise.

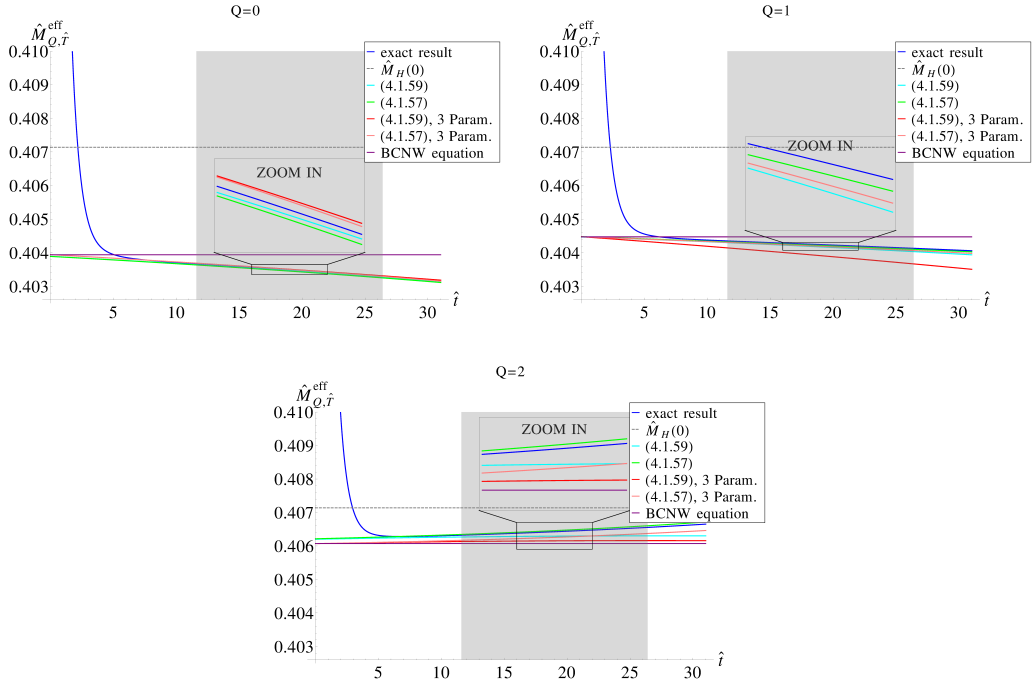


Figure 5.2.4: Effective masses $M_{Q,T}^{\text{eff}}(t)$ derived from (4.1.57) and (4.1.59) restricted to the parameters $\mathcal{E}_2$, $M_H(0)$ and $M_H^{(2)}(0)$ as functions of the temporal separation $t$ for different topological sectors $Q$ and $T = 6.0/\mathcal{E}_2 \approx 930.2$.

#### 5.2.1.4 Extracting hadron masses from fixed topology simulations

We now follow the two strategies suggested in section 5.1 starting with the first one to mimic the method to determine a physical hadron mass (i.e. at unfixed topology) from fixed topology computations using the quantum mechanical model. To this end we choose $t_M = 20.0$, i.e. a $t_M$ value inside the "safe gray regions" of figure 5.2.3 and figure 5.2.4. We use the exact result for the effective mass (shown e.g. in figure 5.2.2) in eq. (5.1.1) to generate $M_{Q,T}$ values for several topological charges $|Q| = 0, 1, 2, 3, 4$ and temporal extensions $T = 2.0/\mathcal{E}_2, 3.0/\mathcal{E}_2, \ldots, 10.0/\mathcal{E}_2$. Then we perform a single fit of either the expansion eq. (4.1.61) from [8] or our $1/V^3$ version restricted to three parameters (eq. (5.2.8)) inserted in eq. (5.1.1) to these masses $M_{Q,T}$, to determine $M_H(0)$ (the hadron mass at unfixed topology), $M_H^{(2)}(0)$ and $\mathcal{E}_2 = \chi_t$ (the curves in figure 5.2.5). Only those masses $M_{Q,\hat{T}}$ enter the fit, for which the conditions **(C1)** (we study both $1/\mathcal{E}_2 T, |Q|/\mathcal{E}_2 T \leq 0.5$ and $1/\mathcal{E}_2 T, |Q|/\mathcal{E}_2 T \leq 0.3$) and **(C2)** from section 4.3 are fulfilled. Both expansions give rather accurate results for $M_H(0)$ (cf. table 5.2.1, top, column "fitting to $M_{Q,T}$"; the relative errors are below $0.1\%$) and reasonable results for $\chi_t$ (cf. table 5.2.1, bottom, column "fitting to $M_{Q,T}$"; relative errors of a few percent). Note that the

relative errors for both $M_H(0)$ and $\chi_t$ are smaller, when using the $1/V^3$ version restricted to three parameters eq. (5.2.8).

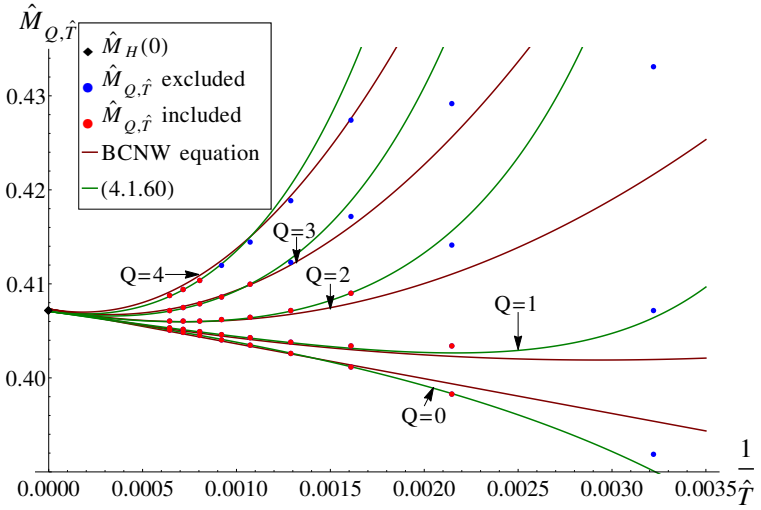


Figure 5.2.5: Determining the physical mass $M_H(0)$ (i.e. the mass at unfixed topology) from a fixed topology computation; only those masses $M_{Q,T}$ are included to the fit which fulfill $1/\mathcal{E}_2 T, |Q|/\mathcal{E}_2 T \leq 0.5$ (red points).

We apply the second strategy of section 5.1 to the quantum mechanical example using the same $|Q| = 0, 1, 2, 3, 4$ and $T = 2.0/\mathcal{E}_2, 3.0/\mathcal{E}_2, \ldots, 10.0/\mathcal{E}_2$ values as before. $t$ is limited to $12 \leqslant t \leqslant 26$ and sampled equidistantly. Since our input data is exact[3], i.e. has no statistical errors, the $\chi^2$ minimizing fit becomes an ordinary least squares fit. Again we compare the $1/V$ expansion from [8] eq. (4.1.61)) and our $1/V^3$ version restricted to three parameters eq. (5.2.8). As before, we find rather accurate results for $M_H(0)$ and $\chi_t$ (cf. table 5.2.1, columns "fitting to correlators"). Note that the relative errors for both $M_H(0)$ and $\chi_t$ are smaller, when using the $1/V^3$ version restricted to three parameters eq. (5.2.8). The relative errors are also smaller compared to the previously discussed method of "fitting to $M_{Q,T}$". An improvement using the $1/V^3$ version is also observed in figure B.2.1.

## 5.3 Results in 4D SU(2) Yang-Mills theory

As the next step towards QCD, we test the pure Yang-Mills theory. This theory is close to QCD without fermions and possesses the same topological structure. A brief description of the model and the setup can be read in the appendix A.2.2.

### 5.3.1 Computation of observables

We determine the topological charge $Q[U]$ for each gauge configuration $[U]$, as explained in section A.2.2. To compute observables at fixed topological charge $\nu$, we only use those gauge configurations, for which $Q[U] = \nu$.

The observable we focus on in the following is the static quark-antiquark potential $\mathcal{V}_{q\bar{q}}(r)$ for various quark-antiquark separations $r = a, 2a, \ldots, 6a$, which can be interpreted as the hadron mass of a static-static meson. To determine $\mathcal{V}_{q\bar{q}}(r)$, we consider temporal correlation functions of operators

$$O_{q\bar{q}} = \bar{q}(\mathbf{r}_1) U^{\text{APE}}(\mathbf{r}_1; \mathbf{r}_2) q(\mathbf{r}_2) \quad , \quad r = |\mathbf{r}_1 - \mathbf{r}_2|. \tag{5.3.1}$$

[3]Note that in QCD the non-pertubative correlator $C_{Q,V}(t)$ at fixed topological charge $Q$ and spacetime volume $V$ will be provided by lattice simulations, i.e. has statistical errors.

$M_H(0)$ results from fixed topology computations (exact result: $M_H = 0.40714$)

| | | fitting to $M_{Q,T}$ | | fitting to correlators | |
|---|---|---|---|---|---|
| | expansion | $M_H(0)$ result | rel. error | $M_H(0)$ result | rel. error |
| $\frac{1}{\chi_t V}, \frac{\lvert Q\rvert}{\chi_t V} \leq 0.5$ | (4.1.61) | 0.40733 | 0.047% | 0.40702 | 0.029% |
| | (5.2.8) | 0.40708 | 0.014% | 0.40706 | 0.019% |
| $\frac{1}{\chi_t V}, \frac{\lvert Q\rvert}{\chi_t V} \leq 0.3$ | (4.1.61) | 0.40739 | 0.062% | 0.40732 | 0.044% |
| | (5.2.8) | 0.40695 | 0.046% | 0.40713 | 0.002% |

$\chi_t$ results from fixed topology computations (exact result: $\chi_t = 0.00645$)

| | | fitting to $M_{Q,T}$ | | fitting to correlators | |
|---|---|---|---|---|---|
| | expansion | $\chi_t$ result | rel. error | $\chi_t$ result | rel. error |
| $\frac{1}{\chi_t V}, \frac{\lvert Q\rvert}{\chi_t V} \leq 0.5$ | (4.1.61) | 0.00586 | 9.1% | 0.00629 | 2.5% |
| | (5.2.8) | 0.00631 | 2.2% | 0.00633 | 1.9% |
| $\frac{1}{\chi_t V}, \frac{\lvert Q\rvert}{\chi_t V} \leq 0.3$ | (4.1.61) | 0.00590 | 8.5% | 0.00627 | 2.8% |
| | (5.2.8) | 0.00592 | 8.2% | 0.00630 | 2.3% |

Table 5.2.1: collection and comparison of results for $M_H(0)$ and $\chi_t$ from fixed topology computations; "rel. error" denotes the relative difference to the exact result, i.e. the systematic error associated with the determination of $M_H(0)$ and $\chi_t$ from two-point correlation functions at fixed topology.

$\bar{q}$ and $q$ are spinless static quarks and $U^{\text{APE}}(\mathbf{r}_1;\mathbf{r}_2)$ denotes a product of APE smeared spatial links along a straight line connecting $\mathbf{r}_1$ and $\mathbf{r}_2$. For the static quarks we use the HYP2 static action, which is designed to reduce UV-fluctuations and, therefore, leads to an improved signal-to-noise ratio [75–77]. These temporal correlation functions can be simplified analytically resulting in Wilson loop averages $\langle W(r,t)\rangle$ with APE smeared spatial and HYP2 smeared temporal lines of length $r$ and $t$, respectively, i.e.

$$\langle\Omega|O^{\dagger}_{\bar{q}q}(t)O_{\bar{q}q}(0)|\Omega\rangle \propto \Big\langle W(r,t)\Big\rangle. \tag{5.3.2}$$

The APE smearing parameters have been chosen to crudely optimize the overlap of $O_{\bar{q}q}|\Omega\rangle$ to the ground state of the static potential, $N_{\text{APE}} = 15$ and $\alpha_{\text{APE}} = 0.5$.

## 5.3.2 Numerical results

### 5.3.2.1 The static potential

In figure 5.3.1 we show results for the static potential[4] obtained at unfixed topology (i.e. for each $r$ and $t$ a single Wilson loop average has been computed on all available gauge configurations) for various volumes $\hat{V} \in \{12^4\,,\,14^4\,,\,15^4\,,\,16^4\,,\,18^4\}$. While the large volumes $14^4$, $15^4$, $16^4$ and $18^4$ yield identical results within statistical errors, the static potential corresponding to the $12^4$ volume differs by several $\sigma$ for quark-antiquark separations $r \geq 3a$. The conclusion is that the $12^4$ lattice leads to sizable ordinary finite volume effects (finite volume effects not associated with topology fixing), while for volumes $\hat{V} \geq 14^4$ these ordinary finite volume effects are negligible within statistical errors. Consequently to respect **(C3)**, we do not use the $12^4$ lattice in the following fixed topology studies. The effects of the ordinary finite volume effects on the BCNW-equation will be described in chapter 6.

In figure 5.3.2 we demonstrate for volume $15^4$ that static potentials obtained at fixed topology from different sectors $|Q| \in \{0\,,\,1\,,\,\ldots\,,\,5\}$, i.e. by only considering gauge configurations from a single sector, significantly

[4] $\mathcal{V}_{q\bar{q}}(r)$ has been determined by fitting constants to effective mass plateaux with the effective mass defined as $m_{\text{eff}}(r,t)a = \log(\langle W(r,t+a)\rangle/\langle W(r,t)\rangle)$.

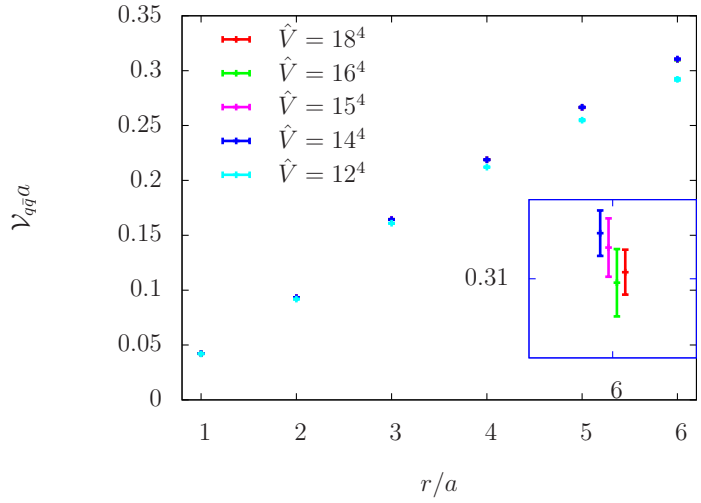


Figure 5.3.1: The static potential $\mathcal{V}_{q\bar{q}}(r)$ at unfixed topology for volumes $\hat{V} \in \{12^4\,,\, 14^4\,,\, 15^4\,,\, 16^4\,,\, 18^4\}$.

differ[5]. For example $\mathcal{V}_{q\bar{q}}(6a)$ at $Q = 0$ and at $|Q| = 4$ differ by more than $6\sigma$. They also differ from the corresponding unfixed topology result, which is larger than $\mathcal{V}_{q\bar{q}}(6a)$ at $Q = 0$ and at $|Q| = 1$ and smaller than $\mathcal{V}_{q\bar{q}}(6a)$ at $|Q| > 2$. These findings demonstrate the necessity to use specific analysis methods like those discussed in this thesis, when performing precise computations at fixed topology. Similar results for the static potential in SU(3) Yang-Mills theory have been reported in [78].

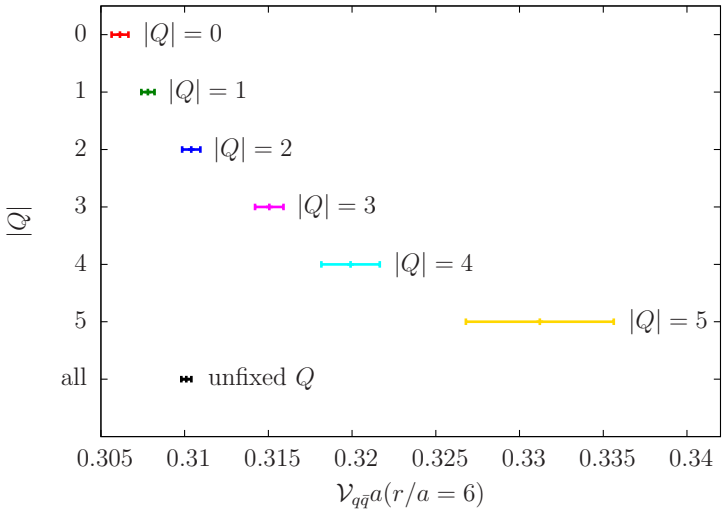


Figure 5.3.2: The static potential $\mathcal{V}_{q\bar{q}}(6a)$ for different topological sectors $|Q| \in \{0\,,\, 1\,,\, \ldots\,,\, 5\}$ at volume $\hat{V} = 15^4$.

To obtain the physical static potential (i.e. the static potential corresponding to unfixed topology) from Wilson loop averages separately computed in different topological sectors $|Q| \in \{0\,,\, 1\,,\, \ldots\,,\, 7\}$ and volumes

[5]Again we have determined $\mathcal{V}_{q\bar{q}}(r)$ by fitting constants to effective mass plateaux. Even though topology has been fixed, effective masses exhibit a constant behavior in $t$ at sufficiently large $t$ within statistical errors.

$\hat{V} \in \{14^4\,,\, 15^4\,,\, 16^4\,,\, 18^4\}$ denoted by $\langle W_{Q,V}(r,t)\rangle$, we proceed as discussed in detail in section 5.1.

- We perform $\chi^2$ minimizing fits of either the $1/V$ expansion of the correlation function associated to the BCNW-equation for the mass eq. (4.1.61):

$$C_{Q,V}(t) = \Big\langle W_{Q,V}(r,t)\Big\rangle = \\ = \alpha(r)\exp\bigg(-\bigg(\mathcal{V}_{q\bar{q}}(r) + \frac{1}{2}\mathcal{V}''_{q\bar{q}}(r)\frac{1}{V\chi_t}\bigg(1-\frac{Q^2}{V\chi_t}\bigg)\bigg)t\bigg) \tag{5.3.3}$$

  or the corresponding improved version:

$$C_{Q,V}(t) = \Big\langle W_{Q,V}(r,t)\Big\rangle = \\ = \frac{\alpha(r)}{\sqrt{1+\mathcal{V}''_{q\bar{q}}(r)t/\chi_t V}} \\ \exp\bigg(-\mathcal{V}_{q\bar{q}}(r)t - \frac{1}{\chi_t V}\bigg(\frac{1}{1+\mathcal{V}''_{q\bar{q}}(r)t/\chi_t V}-1\bigg)\frac{1}{2}Q^2\bigg) \tag{5.3.4}$$

  (cf. eq. (5.2.8)), with respect to their parameters $\mathcal{V}_{q\bar{q}}(r)$, $\mathcal{V}''_{q\bar{q}}(r)$, $\alpha(r)$ ($r = a, 2a, \ldots, 6a$) and $\chi_t$ (when using eq. (5.3.4) we also study the case, where $\chi_t$ is not a fit parameter, but fixed to $\chi_t a^4 = 7.0\times 10^{-5}$ as obtained in [63] at unfixed topology) to the numerical results for $\langle W_{Q,V}(r,t)\rangle$ in the range $t_{\text{min}} \leq t \leq t_{\text{max}}$, where $t_{\text{min}}$ and $t_{\text{max}}$ values are collected in table 5.3.1. This range has been chosen such that the resulting $\chi^2/\text{dof} \lesssim 1$ as well as the conditions **(C2)** and **(C4)** discussed in detail in section 4.3 are fulfilled. Moreover, we checked that the resulting fit parameters are stable within errors, when varying $t_{\text{min}}/a$ and $t_{\text{max}}/a$ by $\pm 1$.

| $\hat{V}$ | $t_{\text{min}}/a$ | $t_{\text{max}}/a$ | maximum $\lvert Q\rvert$ for $1/\chi_t V, \lvert Q\rvert/\chi_t V < 1.0$ | maximum $\lvert Q\rvert$ for $1/\chi_t V, \lvert Q\rvert/\chi_t V < 0.5$ |
|---|---|---|---|---|
| $14^4$ | 5 | 7 | 2 | 1 |
| $15^4$ | 5 | 7 | 3 | 1 |
| $16^4$ | 5 | 8 | 4 | 2 |
| $18^4$ | 5 | 8 | 7 | 3 |

Table 5.3.1: Temporal fitting ranges $t_{\text{min}}/a \ldots t_{\text{max}}/a$ and maximum topological charges $|Q|$ for the volumes $\hat{V}$ considered.

- The numerical results for $\langle W_{Q,V}(r,t)\rangle$ entering the fit are limited to those $Q$ and $V$ values, for which $1/\chi_t V, |Q|/\chi_t V < 1.0$ and $1/\chi_t V, |Q|/\chi_t V < 0.5$ , respectively with respect to condition **(C1)** (eqs. (5.3.3) and (5.3.4) are only valid for sufficiently large $\chi_t V$ and small $Q$; cf. section 4.3). For this selection we use $\chi_t a^4 = 7.0\times 10^{-5}$ from [63] . Cf. table 5.3.1 for a summary.

- We either perform a single fit to all considered separations $r = a, 2a, \ldots, 6a$ or six different fits, one for each of the six separations. In the latter case one obtains also six different results for the topological susceptibility $\chi_t$, which, however, agree within statistical errors in most cases (cf. section 5.3.2.2 for a detailed discussion).

In table 5.3.2 we have collected the corresponding results for $\mathcal{V}_{q\bar{q}}(r)$ from fixed topology computations (using four volumes $\hat{V} \in \{14^4\,,\, 15^4\,,\, 16^4\,,\, 18^4\}$) as well as from unfixed topology computations (at $\hat{V} = 18^4$). There is agreement between the majority of these results within statistical errors. Only for $r = a$ and when using the relaxed constraint $1/\chi_t V, |Q|/\chi_t V < 1.0$ there are a few cases with discrepancies larger than $3\sigma$, in particular for the expansion eq. (5.3.3) (the corresponding cells in table 5.3.2 are shaded in gray). The statistical errors

| method | $\mathcal{V}_{q\bar{q}}(a)$ | $\mathcal{V}_{q\bar{q}}(2a)$ | $\mathcal{V}_{q\bar{q}}(3a)$ | $\mathcal{V}_{q\bar{q}}(4a)$ | $\mathcal{V}_{q\bar{q}}(5a)$ | $\mathcal{V}_{q\bar{q}}(6a)$ |
|---|---|---|---|---|---|---|
| unfixed topology, $\hat{V} = 18^4$ | | | | | | |
| | 0.04229(1) | 0.09329(2) | 0.1646(1) | 0.2190(1) | 0.2664(2) | 0.3101(3) |
| fixed topology, $\hat{V} \in \{14^4, 15^4, 16^4, 18^4\}$, $1/\chi_t V, \lvert Q\rvert/\chi_t V < 1.0$ | | | | | | |
| (5.3.3)c | 0.04240(3) | 0.09343(8) | 0.1646(2) | 0.2189(3) | 0.2662(4) | 0.3097(5) |
| (5.3.3)s | 0.04241(3) | 0.09342(9) | 0.1646(2) | 0.2189(3) | 0.2662(4) | 0.3097(6) |
| (5.3.4)c | 0.04230(3) | 0.09324(8) | 0.1644(2) | 0.2187(3) | 0.2661(4) | 0.3098(6) |
| (5.3.4)s | 0.04240(3) | 0.09338(9) | 0.1645(2) | 02188(3) | 0.2661(4) | 0.3098(6) |
| (5.3.4)c$\chi_t$ | 0.04225(3) | 0.09326(8) | 0.1643(2) | 0.2186(3) | 0.2660(4) | 0.3097(6) |
| (5.3.4)s$\chi_t$ | 0.04225(3) | 0.09326(8) | 0.1643(2) | 0.2186(3) | 0.2660(4) | 0.3097(6) |
| fixed topology, $\hat{V} \in \{14^4, 15^4, 16^4, 18^4\}$, $1/\chi_t V, \lvert Q\rvert/\chi_t V < 0.5$ | | | | | | |
| (5.3.3)c | 0.04227(4) | 0.09326(14) | 01645(3) | 0.2190(5) | 0.2665(7) | 0.3103(10) |
| (5.3.3)s | 0.4226(4) | 0.09322(13) | 0.1644(3) | 0.2189(5) | 0.2666(8) | 0.3105(11) |
| (5.3.4)c | 0.04227(4) | 0.09326(14) | 0.1645(4) | 0.2190(5) | 0.2665(7) | 0.3104(10) |
| (5.3.4)s | 0.04226(4) | 0.9323(13) | 0.1645(3) | 0.2189(5) | 0.2665(8) | 0.3104(10) |
| (5.3.4)c$\chi_t$ | 0.04225(4) | 0.09317(12) | 0.1643(3) | 0.2186(4) | 0.2660(6) | 0.3096(8) |
| (5.3.4)s$\chi_t$ | 0.04225(3) | 0.09317(12) | 0.1643(3) | 0.2186(4) | 0.2660(6) | 0.3096(8) |

Table 5.3.2: Results for the static potential $\mathcal{V}_{q\bar{q}}(r)a$ for various separations $r = a, 2a, \ldots, 6a$ from unfixed and fixed topology computations. In the column "method" the equation number of the expansion is listed, "c" denotes a single combined fit for all separations $r = a, 2a, \ldots, 6a$, "s" denotes a separate fit for each separation and $\chi_t$ denotes that the topological susceptibility is not a fit parameter, but has been fixed to the value from [63], $\chi_t a^4 = 7.0 \times 10^{-5}$. Cells with fixed topology results, which differ by more than $3\sigma$ from the corresponding unfixed results, are shaded in gray.

of the fixed topology results are fairly independent of the expansion used (eqs. (5.3.3), (5.3.4) or (5.3.4) with $\chi_t a^4 = 7.0 \times 10^{-5}$ fixed). They are, however, larger by factors up to $\approx 2$, when using the stronger constraint $1/\chi_t V, |Q|/\chi_t V < 0.5$, which is expected, since less input data is used compared to $1/\chi_t V, |Q|/\chi_t V < 1.0$. All fits yield an uncorrelated $\chi^2/\text{dof} < 1$, indicating that the fixed topology lattice results are well described by both expansions eqs. (5.3.3) and (5.3.4).

For the extraction of the potential it seems to be make difference whether a single combined fit or six different fits are performed. Both the mean values and the statistical errors of $\mathcal{V}_{q\bar{q}}(r)$ are in most cases very similar. A single combined fit, however, seems somewhat advantageous, when also trying to determine the topological susceptibility (cf. section 5.3.2.2).

In figure 5.3.3 we compare the static potential obtained from fixed topology Wilson loops (using $\hat{V} \in \{14^4, 15^4, 16^4, 18^4\}$, $1/\chi_t V, |Q|/\chi_t V < 1.0$, expansion eq. (5.3.4) and a single combined fit) to the static potential computed without topology fixing (at $\hat{V} = 18^4$). As reflected by table 5.3.2 there is excellent agreement within statistical errors.

The expansion eq. (5.3.3) of fixed topology Wilson loop averages $\langle W_{Q,V}(r,t)\rangle$ is a decaying exponential in $t$. This suggests to define a static potential at fixed topological charge $|Q|$ and spacetime volume $\hat{V}$, denoted by $\mathcal{V}_{q\bar{q},Q,V}(r)$, via

$$\mathcal{V}_{q\bar{q},Q,V}(r) = -\frac{d}{dt} \ln\left(\left\langle W_{Q,V}(r,t)\right\rangle\right) \tag{5.3.5}$$

for some value of $t$, where eq. (5.3.3) is a rather precise approximation. Within statistical errors $\mathcal{V}_{q\bar{q},Q,V}(r)$ is independent of $t$ for $t_{\text{min}} \leq t \leq t_{\text{max}}$. Therefore, we determine $\mathcal{V}_{q\bar{q},Q,V}(r)$ by a $\chi^2$ minimizing fit of a constant to the right-hand-side of eq. (5.3.5) with the derivative replaced by a finite difference (this is the common definition of an effective mass) in the interval $t_{\text{min}} \leq t \leq t_{\text{max}}$. For $Q = 0, 1, \ldots 4$ and $V = 14^4, 15^4, 16^4, 18^4$

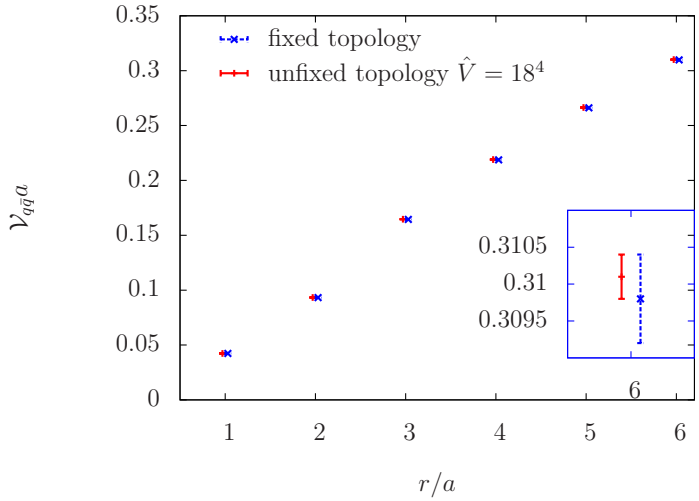


Figure 5.3.3: Comparison of static potential results obtained from fixed topology Wilson loops (using $\hat{V} \in \{14^4\,,\,15^4\,,\,16^4\,,\,18^4\}$, $1/\chi_t V, |Q|/\chi_t V < 1.0$, expansion eq. (5.3.4) and a single combined fit) and at unfixed topology (at $\hat{V} = 18^4$). Since unfixed and fixed topology results are identical within statistical errors, they have been shifted horizontally to the left and right, respectively, for better visibility.

the obtained values for $\mathcal{V}_{q\bar{q},Q,V}(r = 6a)$ are plotted in figure 5.3.4. As already shown in figure 5.3.2 there is a strong dependence of the static potential on the topological sector, which becomes increasingly prominent for smaller spacetime volumes. From the expansion eq. (5.3.3) the fixed topology static potential is expected to behave as

$$\mathcal{V}_{q\bar{q},Q,V}(r) = \mathcal{V}_{q\bar{q}}(r) + \frac{1}{2}\mathcal{V}''_{q\bar{q}}(r)\frac{1}{V\chi_t}\left(1 - \frac{Q^2}{V\chi_t}\right). \tag{5.3.6}$$

The corresponding curves for $|Q| = 0, 1, \ldots, 4$ with parameters $\mathcal{V}_{q\bar{q}}(r = 6a)$, $\mathcal{V}''_{q\bar{q}}(r = 6a)$ and $\chi_t$ determined by the previously discussed fits ($\hat{V} \in \{14^4\,,\,15^4\,,\,16^4\,,\,18^4\}$, $1/\chi_t V, |Q|/\chi_t V < 1.0$, expansion eq. (5.3.3) and a single combined fit) are also shown in figure 5.3.4. One can clearly see that eq. (5.3.6) nicely describes the numerical results for $\mathcal{V}_{q\bar{q},Q,V}(r = 6a)$.

We conclude that one can obtain a correct and accurate physical static potential (i.e. corresponding to unfixed topology) from Wilson loops separately computed in different topological sectors. The statistical errors, however, are larger by factors $\approx 2 \ldots 5$ (cf. table 5.3.2 for details) for a fixed topology computation using four ensembles ($\hat{V} \in \{14^4\,,\,15^4\,,\,16^4\,,\,18^4\}$) compared to a corresponding unfixed computations using a single ensemble ($\hat{V} = 18^4$) only.

#### 5.3.2.2 The topological susceptibility

In table 5.3.3 we present results for the topological susceptibility extracted from fixed topology Wilson loops $\langle W_{Q,V}(r,t)\rangle$. As in section 5.3.2.1 we use the $1/V$ expansions eqs. (5.3.3) and (5.3.4), the constraints $1/\chi_t V, |Q|/\chi_t V < 1.0, 0.5$ and either a single fit to all considered separations $r = a, 2a, \ldots, 6a$ or six different fits, one for each of the six separations. In the latter case one obtains also six different results for the topological susceptibility $\chi_t$.

Not all of the extracted $\chi_t a^4$ values perfectly agree with each other or with the result $\chi_t a^4 = 7.0 \times 10^{-5}$ from [63], which we take as an reference value. Using the rather relaxed constraint $1/\chi_t V, |Q|/\chi_t V < 1.0$ there seems to be a slight tension in form of $\approx 2\sigma$ discrepancies, when performing fits with eq. (5.3.3). The

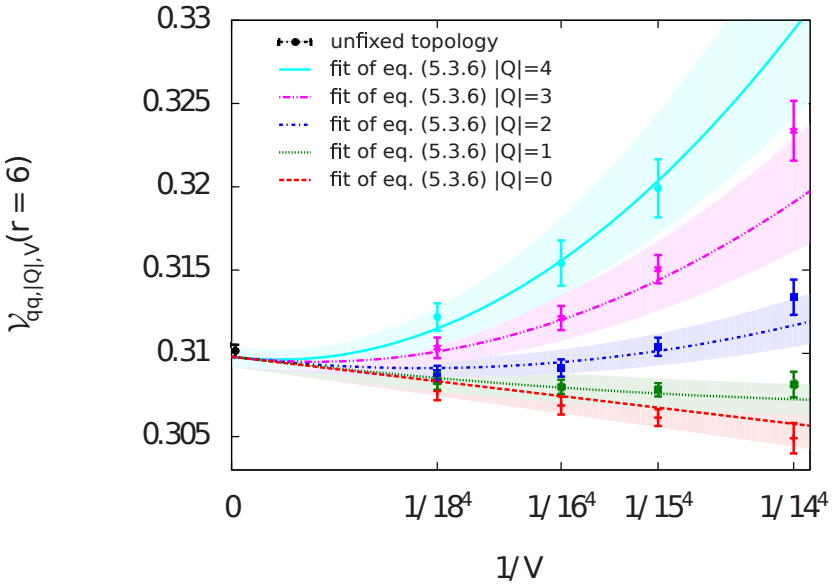


Figure 5.3.4: The fixed topology static potential $\mathcal{V}_{q\bar{q},Q,V}(r = 6a)$ for various $|Q| = 0, 1, \ldots 4$ as a function of $1/\hat{V}$ and the corresponding expansions eq. (5.3.6).

improved expansion eq. (5.3.4) gives slightly better results: no tension seems to be present, i.e. the majority of the extracted values are less than $1\sigma$ different from the reference value.

One might hope to further improve the results by using the stronger constraint $1/\chi_t V, |Q|/\chi_t V < 0.5$. Eqs. (5.3.3) and (5.3.4), which are expansions in $1/\chi_t V$ and $|Q|/\chi_t V$, should then be more accurate. Indeed there is then consistency with the reference value $\chi_t a^4 = 7.0 \times 10^{-5}$, but in most cases the statistical errors are extremely large, i.e. of the order of $\chi_t a^4$ itself or even larger. It seems that for $1/\chi_t V, |Q|/\chi_t V < 0.5$ the available fixed topology static potential data is not sufficiently precise to extract a reasonably accurate result for $\chi_t a^4$. Note that the statistical error for $\chi_t a^4$ obtained from a combined fit is significantly smaller compared to those from the separate fits to a single separation.

We conclude that in principle one can extract the topological susceptibility in Yang-Mills theory from the static potential at fixed topology using equations like eqs. (5.3.3) or (5.3.4). In practice, however, one needs rather precise data. Only, when a variation of the input data, e.g. by using different constraints with respect to $1/\chi_t V, |Q|/\chi_t V$, would lead to precise and stable $\chi_t a^4$ results, one should consider the result useful and trustworthy. The data used for this work is not sufficient to generate such a result. More promising methods to determine the topological susceptibility from simulations at fixed topology using the same lattice setup have been explored and results will be presented in chapter 7.

## 5.4 Results in the Schwinger model

Our next model on which we test the BCNW-equation is the Schwinger model. Some quick description of the model with the setups used for the numerical studies can be found in appendix A.2.1.2. The reason to study the model is to prepare the QCD tests. With this model we have a quantum field theory in two dimensions with fermions. It also has some properties as the quark confinement in common with QCD.

| method | $\mathcal{V}_{q\bar{q}}(a)$ | $\mathcal{V}_{q\bar{q}}(2a)$ | $\mathcal{V}_{q\bar{q}}(3a)$ | $\mathcal{V}_{q\bar{q}}(4a)$ | $\mathcal{V}_{q\bar{q}}(5a)$ | $\mathcal{V}_{q\bar{q}}(6a)$ |
|---|---|---|---|---|---|---|
| fixed topology, $\hat{V} \in \{14^4, 15^4, 16^4, 18^4\}$, $1/\chi_t V, \lvert Q\rvert/\chi_t V < 1.0$ | | | | | | |
| (5.3.3)c | 8.8(0.5) | | | | | |
| (5.3.3)s | 8.8(0.5) | 8.7(0.6) | 8.6(0.7) | 8.6(0.9) | 8.8(1.0) | 8.9(1.2) |
| (5.3.4)c | 7.1(0.6) | | | | | |
| (5.3.4)s | 8.6(0.5) | 8.2(0.7) | 7.7(0.8) | 7.3(0.9) | 7.0(1.0) | 6.7(1.1) |
| fixed topology, $\hat{V} \in \{14^4, 15^4, 16^4, 18^4\}$, $1/\chi_t V, \lvert Q\rvert/\chi_t V < 0.5$ | | | | | | |
| (5.3.3)c | 11.8(5.9) | | | | | |
| (5.3.3)s | 10.0(14.0) | 20.7(44.3) | 11.1(8.2) | 11.8(16.0) | 12.8(8.7) | 15.4(52.1) |
| (5.3.4)c | 11.9(5.4) | | | | | |
| (5.3.4)s | 10.2(21.8) | 10.7(12.5) | 11.3(8.7) | 11.8(5.8) | 13.0(9.7) | 14.6(12.2) |

Table 5.3.3: Results for the topological susceptibility $\chi_t a^4 \times 10^5$ from fixed topology computations of the static potential $\mathcal{V}_{q\bar{q}}(r)$ for various separations $r = a, 2a, \ldots, 6a$. In the column "method" the equation number of the expansion is listed, "c" denotes a single combined fit for all separations $r = a, 2a, \ldots, 6a$ and "s" denotes a separate fit for each separation. As reference value from an unfixed topology computation we use $\chi_t a^4 \times 10^5 = (7.0 \pm 0.9)$ [63].

### 5.4.1 Computation of observables

We determine the topological charge $Q[U]$ for each gauge configuration $U$ as explained in Section A.2.1. To compute observables at fixed topological charge $\nu$, we only use those gauge configurations, for which $Q[U] = \nu$.

The hadron masses we investigate in the following are the static potential $\mathcal{V}_{\bar{q}q}(r)$, which has been discussed already in the context of Yang-Mills theory (cf. section 5.3.1), and the pion mass $M_\pi$. A suitable hadron creation operator for the pion is

$$O_\pi \;=\; \sum_x \bar{\psi}^{(u)}(x)\gamma_5\psi^{(d)}(x), \tag{5.4.1}$$

where $\sum_x$ denotes a sum over space and $u$ and $d$ label the two degenerate fermion flavors (for an introduction regarding the construction of hadron creation operators cf. e.g. [79]). For the static potential we use

$$O_{q\bar{q}} = \bar{q}(\mathbf{r}_1)U(\mathbf{r}_1;\mathbf{r}_2)q(\mathbf{r}_2) \quad , \quad r = |\mathbf{r}_1 - \mathbf{r}_2| \tag{5.4.2}$$

as in section 5.3.1. Again $\bar{q}$ and $q$ are spinless static quarks and $U(\mathbf{r}_1;\mathbf{r}_2)$ denotes the product of spatial links connecting $\mathbf{r}_1$ and $\mathbf{r}_2$. In contrast to section 5.3.1, we do not use any gauge link smearing since there is only a single spatial dimension.

### 5.4.2 Numerical results

#### 5.4.2.1 The pion mass and the static potential

Figure 5.4.1 shows that pion masses obtained at fixed topology in different topological sectors differ significantly at finite spacetime volume ($\beta = 4.0$, $\hat{V} = 40^2$). For example $M_\pi$ at $Q = 0$ and at $Q = 3$ differ by more than $6\sigma$. Fixed topology pion masses also differ from the corresponding result at unfixed topology, i.e. the physically meaningful result (e.g. $M_\pi$ at $Q = 0$ and the unfixed topology $M_\pi$ differ by more than $7\sigma$). Figure 5.4.1, therefore, demonstrates (as figure 5.3.2 in the previous section) the necessity to use specific analysis methods like those discussed in this paper, when the Monte-Carlo algorithm is not able to generate sufficiently many changes in $Q$.

To obtain the physical pion mass and static potential (i.e. unfixed topology results) from correlation functions evaluated in single topological sectors, we proceed as above for Yang-Mills theory. We perform $\chi^2$ minimizing

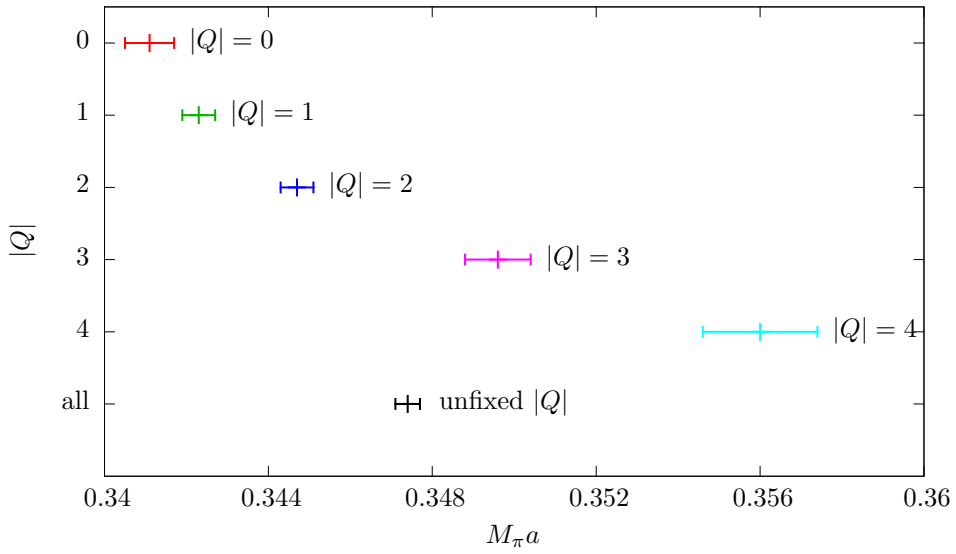


Figure 5.4.1: The pion mass $M_\pi$ for different topological sectors $|Q| \in \{0, 1, \ldots, 4\}$ at volume $\hat{V} = 40^2$.

| $\hat{V}$ | $t_{\text{min}}/a$ | $t_{\text{max}}/a$ | maximum $\lvert Q\rvert$ for $1/\chi_t V, \lvert Q\rvert/\chi_t V < 1.0$ | maximum $\lvert Q\rvert$ for $1/\chi_t V, \lvert Q\rvert/\chi_t V < 0.5$ |
|---|---|---|---|---|
| $40^2$ | 12 | 16 | 7 | 3 |
| $44^2$ | 12 | 18 | 9 | 4 |
| $48^2$ | 12 | 20 | 11 | 5 |
| $52^2$ | 12 | 22 | 13 | 6 |
| $56^2$ | 12 | 24 | 15 | 7 |
| $60^2$ | 12 | 24 | 17 | 8 |

Table 5.4.1: Temporal fitting ranges $t_{\text{min}}/a \ldots t_{\text{max}}/a$ and maximum topological charges $|Q|$ for the volumes $\hat{V}$ considered.

fits using both expansions eqs. (4.1.6) and (5.3.4) of correlation functions. We choose the volumes such that **(C3)** is respected and the temporal fitting range $t_{\text{min}} \ldots t_{\text{max}}$ such that the conditions **(C2)** and **(C4)** (cf. section 4.3) are fulfilled and that the resulting $\chi^2/\text{dof}$ is small, i.e. $\lesssim 1$. The stability of the resulting pion mass and static potential have been checked by varying $t_{\text{min}}/a$ and $t_{\text{max}}/a$ by $\pm 1$. The $t$ ranges used for the determination of the pion mass are collected in table 5.4.1.

We perform the fits in three slightly different ways: ("c") a single combined fit to all five observables ($M_\pi$, $\mathcal{V}_{q\bar{q}}(r = a)$, $\mathcal{V}_{q\bar{q}}(r = 2a)$, $\mathcal{V}_{q\bar{q}}(r = 3a)$, $\mathcal{V}_{q\bar{q}}(r = 4a)$); ("c$\mathcal{V}$") a single combined fit to the four static potential observables; ("s") five different fits, one to each of the five observables. In table 5.4.2 the corresponding results are collected together with reference values obtained at unfixed topology at volume $\hat{V} = 60^2$. The conclusions are essentially the same as for Yang-Mills theory discussed in the previous section. Results extracted indirectly from simulations at fixed topology are in agreement with those obtained directly at unfixed topology. The order of magnitude of the statistical errors is the same for the two expansions eqs. (4.1.6) and (5.3.4) and the fitting methods "c", "c$\mathcal{V}$" and "s". They are, however, larger by factors of $\approx 2$, when using the stronger constraint $1/\chi_t V, |Q|/\chi_t V < 0.5$, which is expected, since less input data is used as for $1/\chi_t V, |Q|/\chi_t V < 1.0$. The fits all yield uncorrelated $\chi^2/\text{dof} \lesssim 1$ indicating that the fixed topology lattice results are well described by both eqs. (4.1.6) and (5.3.4).

| method | $M_\pi$ | $\mathcal{V}_{q\bar{q}}(a)$ | $\mathcal{V}_{q\bar{q}}(2a)$ | $\mathcal{V}_{q\bar{q}}(3a)$ | $\mathcal{V}_{q\bar{q}}(4a)$ |
|---|---|---|---|---|---|
| unfixed topology, $\hat{V} = 60^2$ | | | | | |
| | 0.3474(3) | 0.1296(2) | 0.2382(5) | 0.3288(7) | 0.4045(10) |
| fixed topology, $\hat{V} \in \{40^2, 44^2, 48^2, 52^2, 56^2, 60^2\}$, $1/\chi_t V, \lvert Q\rvert/\chi_t V < 1.0$ | | | | | |
| (4.1.6)c | 0.3466(16) | 0.1293(19) | 0.2370(23) | 0.3261(29) | 0.4022(62) |
| (4.1.6)c$\mathcal{V}$ | | 0.1295(10) | 0.2372(12) | 0.3386(15) | 0.4052(16) |
| (4.1.6)s | 0.3477(8) | 0.1285(7) | 0.2371(9) | 0.3282(12) | 0.4050(16) |
| (5.3.4)c | 0.3467(10) | 0.1293(6) | 0.2377(9) | 0.3321(32) | 0.4059(69) |
| (5.3.4)c$\mathcal{V}$ | | 0.1295(5) | 0.2379(11) | 0.3392(14) | 0.4049(16) |
| (5.3.4)s | 0.3477(9) | 0.1294(5) | 0.2374(6) | 0.3288(12) | 0.4040(15) |
| fixed topology, $\hat{V} \in \{40^2, 44^2, 48^2, 52^2, 56^2, 60^2\}$, $1/\chi_t V, \lvert Q\rvert/\chi_t V < 0.5$ | | | | | |
| (4.1.6)c | 0.3454(32) | 0.1284(27) | 0.2364(28) | 0.3311(50) | 0.4049(80) |
| (4.1.6)c$\mathcal{V}$ | | 0.1282(12) | 0.2370(16) | 0.3312(35) | 0.4175(82) |
| (4.1.6)s | 0.3478(32) | 0.1292(12) | 0.2377(21) | 0.3275(61) | 0.4027(91) |
| (5.3.4)c | 0.3455(32) | 0.1285(16) | 0.2365(19) | 0.3310(49) | 0.4048(78) |
| (5.3.4)c$\mathcal{V}$ | | 0.1287(9) | 0.2371(23) | 0.3312(36) | 0.4073(83) |
| (5.3.4)s | 0.3482(35) | 0.1291(11) | 0.2376(13) | 0.3290(22) | 0.4036(55) |

Table 5.4.2: Results for the pion mass $M_\pi a$ and the static potential $\mathcal{V}_{q\bar{q}}(r)a$ for various separations $r = a, 2a, 3a, 4a$ from unfixed and fixed topology computations. In the column "method" the equation number of the expansion is listed, "c" denotes a single combined fit to all five observables, "c$\mathcal{V}$" denotes a single combined fit to the four static potential observables, "s" denotes a separate fit to each of the five observables.

Similar to eq. (5.3.5) one can define a pion mass at fixed topological charge $Q$ and spacetime volume $V$ by

$$M_{\pi,Q,V} = -\frac{d}{dt} \ln\left(\left\langle O_\pi^\dagger(t) O_\pi(0)\right\rangle\right) \tag{5.4.3}$$

for some value of $t$, where eq. (4.1.6) is a rather precise approximation. Within statistical errors $M_{\pi,Q,V}$ is independent of $t$ for $t_{\text{min}} \le t \le t_{\text{max}}$. Therefore, we determine $M_{\pi,Q,V}$ by a $\chi^2$ minimizing fit of a constant to the right-hand-side of eq. (5.4.3) with the derivative replaced by a finite difference in the interval $t_{\text{min}} \le t \le t_{\text{max}}$. For $|Q| = 0, 1, \ldots 4$ and $\hat{V} = 40^2, 44^2, 48^2, 52^2, 56^2, 60^2$ the obtained values for $M_{\pi,Q,V}$ are plotted in figure 5.4.2. Again we observe a strong dependence of the pion mass on the topological sector, in particular at small spacetime volumes. From the expansion eq. (4.1.6) the fixed topology pion mass is expected to behave as

$$M_{\pi,Q,V} = M_\pi + \frac{1}{2} M_\pi'' \frac{1}{V\chi_t}\left(1 - \frac{Q^2}{V\chi_t}\right). \tag{5.4.4}$$

The corresponding curves for $Q = 0, 1, \ldots 4$ with parameters $M_\pi$, $M_\pi''$ and $\chi_t$ determined by the previously discussed fit "(4.1.6)s" are also shown in figure 5.4.2. One can clearly see that eq. (5.4.4) nicely describes the fixed topology lattice results for $M_{\pi,Q,V}$.

We conclude, similar as for Yang-Mills theory in the previous section, that one can obtain correct and accurate values for the pion mass and the static potential from correlation functions computed in a number of fixed topological sectors. The statistical errors of such results are somewhat larger than for direct computation at unfixed topology: in our computation by factors of $\approx 2 \ldots 7$. This is partly due to the smaller amount of gauge configurations of the fixed $Q$ ensembles at different $V$ and partly due to the extrapolation to infinite volume.

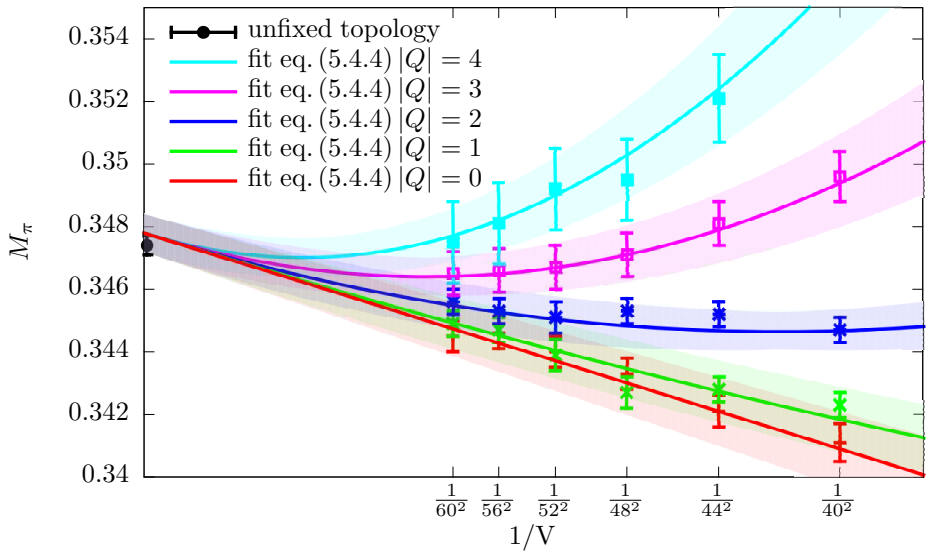


Figure 5.4.2: The fixed topology pion mass $M_{\pi,Q,V}$ for various $|Q| = 0, 1, ..., 4$ as a function of $1/\hat{V}$ and the corresponding expansions eq. (5.4.4).

#### 5.4.2.2 The topological susceptibility

In table 5.4.3 we present results for the topological susceptibility extracted from fixed topological computations of the pion mass and the static potential. These topological susceptibility results are obtained from the same fits, which lead to the pion mass and static potential results shown in table 5.4.2. These results for $\chi_t$ and their interpretation are quite similar to those obtained previously for Yang-Mills theory. We observe a slight tension of $\approx 2\sigma$ for some values, when using expansion eq. (4.1.6) and the relaxed constraint $(1/\chi_t V, |Q|/\chi_t V < 1.0)$. This tension disappears, when applying the improved expansion eq. (5.3.4). When imposing the strict constraint $(1/\chi_t V, |Q|/\chi_t V < 0.5)$, we encounter the same problem as in section 5.3.2.2: All results are in agreement with the reference value obtained at unfixed topology via $\chi_t = \langle Q^2 \rangle / V$, but statistical errors are extremely large.

The conclusion is that a reasonably accurate determination of the topological susceptibility from fixed topology pion and static potential correlation functions requires extremely precise data. The fixed topology ensembles and correlation functions we use in this work are not sufficient to extract a precise and stable value for $\chi_t$.

## 5.5 Conclusion about the BCNW-equation

We studied the method based on the BCNW-equation extensively for several models. The conclusion is that the method is efficient to extract the mass if the conditions **(C1)** to **(C4)** are respected. The method is unfortunately not efficient to extract the topological susceptibility. This problem is important not only to extract the topological susceptibility but also to evaluate the condition **(C1)** which is one of the most limiting ones. We will see in chapters 7 and 7.2 how we can extract the topological susceptibility and make sure that we respect the conditions to apply the BCNW-equation.

Another problem which appears in our simulation is the possibility to respect the condition **(C3)** i.e. to have ordinary finite volume effects. This condition is probably the bottleneck of the method for QCD as the simulation are extremely costly, in particular for chirally symmetric fermions. In the next chapter, we will describe how we overcome the problem and finally test the method on QCD.

| method | $M_\pi$ | $\mathcal{V}_{q\bar{q}}(a)$ | $\mathcal{V}_{q\bar{q}}(2a)$ | $\mathcal{V}_{q\bar{q}}(3a)$ | $\mathcal{V}_{q\bar{q}}(4a)$ |
|---|---|---|---|---|---|
| unfixed topology, $\hat{V} = 60^2$ | | | | | |
| 0.0048(1) | | | | | |
| fixed topology, $\hat{V} \in \{40^2, 44^2, 48^2, 52^2, 56^2, 60^2\}$, $1/\chi_t V, \lvert Q\rvert/\chi_t V < 1.0$ | | | | | |
| (4.1.6)c | 0.0038(5) | | | | |
| (4.1.6)c$\mathcal{V}$ | | 0.0042(5) | | | |
| (4.1.6)s | 0.0041(4) | 0.0038(5) | 0.0036(7) | 0.0038(11) | 0.0044(9) |
| (5.3.4)c | 0.0044(4) | | | | |
| (5.3.4)c$\mathcal{V}$ | | 0.0042(6) | | | |
| (5.3.4)s | 0.0046(5) | 0.0043(4) | 0.0045(7) | 0.0036(12) | 0.0038(8) |
| fixed topology, $\hat{V} \in \{40^2, 44^2, 48^2, 52^2, 56^2, 60^2\}$, $1/\chi_t V, \lvert Q\rvert/\chi_t V < 0.5$ | | | | | |
| (4.1.6)c | 0.0065(35) | | | | |
| (4.1.6)c$\mathcal{V}$ | | 0.0017(30) | | | |
| (4.1.6)s | 0.0014(38) | 0.0049(32) | 0.0057(31) | 0.0037(48) | 0.0032(27) |
| (5.3.4)c | 0.0067(32) | | | | |
| (5.3.4)c$\mathcal{V}$ | | 0.0018(33) | | | |
| (5.3.4)s | 0.0017(32) | 0.0043(34) | 0.0022(46) | 0.0015(38) | 0.0048(52) |

Table 5.4.3: Results for the topological susceptibility $\chi_t a^2$ from fixed topology computations of the pion mass $M_\pi$ and the static potential $\mathcal{V}_{q\bar{q}}(r)$ for various separations $r = a, 2a, 3a, 4a$. In the column "method" the equation number of the expansion is listed, "c" denotes a single combined fit to all five observables, "c$\mathcal{V}$" denotes a single combined fit to the four static potential observables, "s" denotes a separate fit to each of the five observables. The unfixed topology reference value shown at the top of the table has been obtained at volume $\hat{V} = 60^2$ using $\chi_t a^2 = \langle Q^2 \rangle / \hat{V}$.

# Chapter 6

# Ordinary and topological finite volume effects

In the previous chapter we have studied the possibility to use the BCNW-equation to extract masses from fixed topology simulations for several models. A necessary condition to apply the method is that ordinary finite volume effects have to be negligible (cf. **(C3)** of section 4.3). In QCD the situation is expected to be more difficult than for SU(2) because the lightest particle, the pion, is much lighter than the $J^{PC} = 0^{++}$ glueball of SU(2) Yang-Mills theory. And lattice simulations of QCD, in particular at large volumes, are extremely demanding with respect to high performance computer resources. Therefore, it is highly desirable to obtain an expression describing both topological and ordinary finite volume corrections to hadron masses.

## 6.1 Ordinary finite volume effects

Ordinary finite volume effects correspond to a shift of the value of the quantity that we want to measure. The problem arises as a particle has the possibility to interact with an image of itself when periodic boundary conditions are used. This self-interaction is artificial and one needs to be able to extract physical results in the presence of those non-desirable effects or at least be able to estimate them. Two different approaches exist to compute those effects. One is the Lüscher approach [80] and the other one is based on chiral pertubation theory (ChPT) [81]. We will briefly discuss both of them and apply them in case of fixed topology simulation.

### 6.1.1 The Lüscher Formula

For the Lüscher approach, we focus on particles that can travel around the spacetime volume. That implies that the particles should be stable and be able to propagate. Thus ordinary finite volume effects are dominated by the interaction with the lightest particle of the theory. That corresponds to the lightest glueball in the SU(N) or the pion in QCD as quarks and gluons are confined. To compute this interaction one has to compute Feynman diagrams with at least one loop around the spacetime.

In Lüscher's derivation of the asymptotic formula for the finite volume correction to particle masses [80] , the first step is a proof that the leading exponential term is given by the sum of all diagrams in which only one propagator is taken in finite volume. The three integrals which contribute are the following:

$$
\begin{aligned}
I_1 &= \int \frac{d^4p}{(2\pi)^4} 6e^{iq_1L} G(q+\frac{1}{2}p)G(-q+\frac{1}{2}p)\Gamma(-p,q+\frac{1}{2}p,-q+\frac{1}{2}p)\Gamma(p,-q-\frac{1}{2}p,q-\frac{1}{2}p) \\
I_2 &= \int \frac{d^4p}{(2\pi)^4} 6e^{iq_1L} G(q)G(0)\Gamma(-q,q,0)\Gamma(-p,p,0) \\
I_3 &= \int \frac{d^4p}{(2\pi)^4} 6e^{iq_1L} G(q)\Gamma(p,q,-p,-q),
\end{aligned}
\tag{6.1.1}
$$

where $G(q) = 1/(m^2+q^2)$ is the full propagator, $m$ the mass of the lightest particle and $\Gamma$ is the vertex function in infinite volume. The factor $k = 6e^{iq_1L}$ is the element which appears due to the periodicity and leads to the exponential prefactor. The integrals possess all a pole for $|q| = im$ giving a result proportional to an exponential factor $e^{-mL}$. $I_1$ also possesses a pole for $|q| = im \times \sqrt{3}/2$ leading to an exponential factor $e^{-\sqrt{3}/2.mL}$.

$I_1$ and $I_2$ are present for effective theories which allowed a three-point vertex, while $I_3$ needs a four-point vertex. For this reason, a theory which allows a three-point vertex will get a result proportional to $e^{-\frac{\sqrt{3}}{2}mL}$ due to the integral $I_1$ and a theory which do not allow a three-point vertex will get a result proportional to $e^{-mL}$.

In SU(N) gauge theory, the lightest particle is the $0^{++}$-glueball. In that case a three-point vertex is possible and the leading term will then be proportional to $e^{-\frac{\sqrt{3}}{2}mL}$. It is possible to completely solve the integral $I_1$. The result obtained is then:

$$
\Delta M = -\frac{3\lambda^2}{16\pi M^2 L} e^{-\frac{\sqrt{3}}{2}mL} + \mathcal{O}\left(\frac{1}{ML}e^{-mL}\right) \tag{6.1.2}
$$

where $\Delta M = M_L - M$, with $M$ the mass of the particle in which we are interested in at infinite volume, $M_L$ finite volume and $\lambda$ is defined such as:

$$
\lim_{\nu \to \pm\frac{1}{2}m_0} \left(\nu^2 - \frac{1}{4}m_0^2\right) F(\nu) = \frac{1}{2}\lambda^2, \tag{6.1.3}
$$

with $F$ the forward scattering amplitude. In SU(N), the glueball masses are rather large and higher orders are strongly suppressed.

In QCD the lightest particle is the pion. Due to parity symmetry a vertex with 3 pions is not possible and the integrals $I_1$ and $I_2$ do not exist. Then the leading term is proportional to $e^{-mL}$. The integral $I_3$ can be partially calculated and one obtains at leading order the following results:

$$
\Delta M = -\frac{3}{16\pi^2 ML}\int_{-\infty}^{+\infty} dy \mathcal{F}_p(iy) e^{-\sqrt{m_\pi^2+y^2}L} + \mathcal{O}\left(\frac{1}{ML}e^{-\sqrt{2}mL}, \frac{1}{ML}e^{-\bar{m}L}\right), \tag{6.1.4}
$$

with $\mathcal{F}_P$ the forward $p\pi$ scattering and $\bar{m}$ the mass of a heavier particle able to travel around the spacetime. Here it could be interesting to look at higher orders. A simple extension is to consider the case of the $n$ loops around the spacetime. Then the result is:

$$
\Delta M = -\frac{1}{32\pi^2 ML}\sum_{n=1}^{\infty}\frac{k(n)}{\sqrt{n}}\int_{-\infty}^{+\infty} dy \mathcal{F}_p(iy) e^{-\sqrt{n(m_\pi^2+y^2)}L} + \mathcal{O}\left(\frac{1}{ML}e^{-\bar{m}L}\right) \tag{6.1.5}
$$

where the first $k(n)$ are given by the table 6.1.1.

To take into account particles with higher mass, which also loop around the spacetime, one just has to add the different contributions.

| $n$ | 1 | 2 | 3 | 4 | 5 | 6 | 7 | 8 | 9 | 10 | 11 | 12 | 13 | 14 | 15 | 16 | 17 | 18 | 19 | 20 |
|---|---|---|---|---|---|---|---|---|---|---|---|---|---|---|---|---|---|---|---|---|
| $k(n)$ | 6 | 12 | 8 | 6 | 24 | 24 | 0 | 12 | 30 | 24 | 24 | 8 | 24 | 48 | 0 | 6 | 48 | 36 | 24 | 24 |

Table 6.1.1: List of $k(n)$ for ordinary finite volume effects

The same kind of calculus can be done for the decay constant [82]:

$$F_p(L) - F_p = -\frac{3}{8\pi^2 M_p L}\int_{-\infty}^{+\infty} dy \mathcal{N}_p(iy) e^{-\sqrt{m_\pi^2+y^2}L} + \mathcal{O}\left(\frac{1}{ML}e^{-\sqrt{2}m_\pi L}, \frac{1}{ML}e^{-\bar{m}L}\right), \tag{6.1.6}$$

with $\mathcal{N}_p(iy)$ is derived from the matrix element $\langle \pi\pi | A_\mu | P \rangle$.

## 6.1.2 The ChPT Formula

### 6.1.2.1 A brief word on ChPT

Chiral Perturbation Theory (ChPT) is a particularly useful effective theory of QCD at low energy. Its Lagrangian is constructed on hadronic degrees of freedom which are the members of the pseudo-scalar octet $(\pi, K, \eta)$. They are considered as the Goldstone bosons resulting to the spontaneous breaking of the chiral symmetry. ChPT is organized as an expansion in powers of the meson momenta and masses. The parameters of the theory are the quark masses and some low energy constants, such as the pion decay constant and the chiral condensate.

There is a strong relation between ChPT and lattice QCD. On one hand, lattice QCD can help by determining the different constants which appear in the ChPT Lagrangian and are not easily accessible by experiment. It can also test some predictions of ChPT and in this way determine the range of applications of the effective theory. On the other hand, lattice suffers from unphysical values of some parameters and that calculus are done in Euclidean space which cannot give access to scattering amplitudes. For both cases, ChPT allows some analytical continuation to obtain physical results.

The ChPT theory can be expanded in two different domains. The "$p$-expansion" which assumes that $m_\pi L \gg 1$ and the "$\epsilon$-expansion" done in the case of $m_\pi L \ll 1$. The most realistic expansion for lattice simulations is necessarily the "$p$-expansion" as we try generally to have a box as large as possible. In our case, we will be interested especially on how ChPT leads to the calculus of finite volume effects.

### 6.1.2.2 ChPT in finite volume

In QCD the physics of the infrared energy is controlled by chiral symmetry. This property is still true in a finite box as shown by Gasser and Leutwyler as long as the box is large enough that chiral symmetry is not restored [81]. They proved that for a box with periodic boundary conditions the finite-volume dependence comes in exclusively through the propagators as it is the case in Lüscher's approach. Thus the latter becomes periodic in space and can be expressed as:

$$G(x^0, \vec{x}) = \sum_n G_0(x^0, \vec{x} + \vec{n}L), \tag{6.1.7}$$

in the limit of $T \to \infty$. In order to apply ChPT in finite volume, we need to have

$$\frac{p}{4\pi F_\pi} \ll 1, \tag{6.1.8}$$

with a momentum given by $\vec{p} = 2\pi\vec{n}/L$ with $\vec{n}$ a vector of integers. Therefore one can apply ChPT in a finite box if

$$L \gg \frac{1}{2F_\pi}, \tag{6.1.9}$$

with $1/2F_\pi \approx 1fm$. In the opposite case there is no constraint on $M_\pi L$ and both the $p-$ and the $\epsilon$-regime seem possible. In this thesis, we will only have a look at the $p-$regime which corresponds to the same domain in which the Lüscher approach is valid. In this regime, the result has been obtained by Gasser and Leutwyler in a theory with $N_f^2 - 1$ degenerated pseudo-Goldstone bosons, and is expressed as:

$$m_{\pi,L} - m_\pi = \frac{m_\pi^2}{8N_f\pi^2 F_\pi^2 L}\sum_{n=1}^{\infty}\frac{k(n)}{\sqrt{n}}K_1(\sqrt{n}m_\pi L) \tag{6.1.10}$$

$$F_{\pi,L} - F_\pi = -\frac{N_f m_\pi}{8\pi^2 F_\pi L}\sum_{n=1}^{\infty}\frac{k(n)}{\sqrt{n}}K_1(\sqrt{n}m_\pi L), \tag{6.1.11}$$

where $K_1$ is the modified Bessel function of second kind.

In ChPT we can also obtain much more easily other quantities and one of particular interest for us is the topological susceptibility:

$$\chi_{t,L} - \chi_t = -\frac{m_\pi^3}{16\pi^2 L}\sum_{n=1}^{\infty}\frac{k(n)}{\sqrt{n}}K_1(\sqrt{n}m_\pi L). \tag{6.1.12}$$

The ChPT method has the advantage of an explicit formula which allows the estimation of the ordinary finite volume effects. However, the method can only be used in presence of light quasi- Nambu-Goldstone bosons . For example the calculus is not possible for the SU(N) pure Yang-Mills theory. Moreover, the calculus becomes much more complicated when one wants to investigate the errors coming from some additional mass (other particle traveling around the box). In that case, the Lüscher method is preferable.

We are now in a strange position where we have an explicit formula for which the improvement is difficult and a formula for which the expansion is easier but not explicit. A simple idea to overcome the problem has been described in [83]. The idea is to use the Lüscher formula in order to perform the calculus and to compute the integral using the ChPT. With this method, we obtain nicely the same result for the ordinary finite volume effects on the pion mass when only the pion is considered as a possible traveling particle.

In the following sections, we will use the Lüscher method as we are also interested in getting results for SU(2). However, for the pion mass, we will refer to the ChPT results to obtain an explicit formula as it has been proven that the results are equivalent.

### 6.1.3 Ordinary finite volume effects in the $\theta-$vacuum

Lüscher does not use any discrete symmetry to calculate the ordinary finite volume effects, thus we can apply the same reasoning. However, Lüscher's calculation is based on the Green's function. Therefore, we have to compute the Green's function in the $\theta$-vacuum.

Until now we have written the QCD action in a $\theta$-vacuum as $S[A,\Psi,\bar{\Psi}] + i\theta Q[A]$. But the $\theta$-dependence can also be moved in the quark mass matrix using a $U(1)_A$ chiral transformation [59],

$$\begin{aligned} S_\theta[A,\Psi,\bar{\Psi}] =& S_{YM} + \int \mathrm{d}^4\, x\bar{\Psi}_L[\gamma_\mu(A_\mu+\partial_\mu)]\Psi_L + \bar{\Psi}_R[\gamma_\mu(A_\mu+\partial_\mu)]\Psi_R \\ &+ \int \mathrm{d}^4\, x\bar{\Psi}_L\mathcal{M}e^{i\theta/N_f}\Psi_R + \bar{\Psi}_R\mathcal{M}^\dagger e^{-i\theta/N_f}\Psi_L, \end{aligned} \tag{6.1.13}$$

with $\mathcal{M} = \mathrm{diag}(m_u, m_d, \ldots, m_{N_f})$. Therefore $\theta$ appears as a phase in the determinant of the mass matrix and the mass of mesons depends of $\theta$ but their dynamics do not. This is consistent with a fact mentionned in section 1.2.4, that the $\theta$-term is a total derivative and does not modify the equations of motion. Thus the Green's function keeps the same form and the Lüscher method stays the same, only now the mass is $\theta$-dependent. Then for SU(N):

$$\Delta M(\theta) = -\frac{3\lambda(\theta)^2}{16\pi M(\theta)^2 L}e^{-\frac{\sqrt{3}}{2}m(\theta)L} + \mathcal{O}\left(\frac{1}{M(\theta)L}e^{-m(\theta)L}\right) \tag{6.1.14}$$

and for QCD:

$$\Delta m_\pi(\theta) = +\frac{m_\pi^2(\theta)}{8N_f\pi^2F_\pi^2(\theta)L}\sum_{n=1}^{\infty}\frac{k(n)}{\sqrt{n}}K_1(\sqrt{n}m_\pi(\theta)L) + \mathcal{O}\left(\frac{1}{m_\pi(\theta)L}e^{-\bar{m}(\theta)L}\right) \tag{6.1.15}$$

## 6.2 Finite volume effects at fixed topology

In the previous chapter we have computed the mass at fixed topology considering that the ordinary finite volume effects are negligible. That means that we have supposed that if we were measuring the value at unfixed topology the valued obtained will be the infinite volume mass (cf. eq. (4.1.45)). Now we consider that the ordinary finite volume effects are not negligible anymore. The idea of this section is to expand the BCNW-equation such that it contains also the ordinary finite volume effects. This allows the extraction of the mass from fixed topology simulation even if ordinary finite volume effects are present.

It is not necessary to redo the calculations of the BCNW-equation as one need only to change $M(\theta)$ to $M_L(\theta)$. One can modify the BCNW-equation to:

$$M_{Q,L} \approx M_L(0) + \frac{M_L^{(2)}(0)}{2\chi_{t,L}V}\left(1 - \frac{Q^2}{\chi_{t,L}V}\right), \tag{6.2.1}$$

where $M_L(0)$ (respectively $M_L^{(2)}(0)$) is the mass (the second derivative of the mass by $\theta$) at $\theta = 0$ in presence of ordinary finite volume effects. In order to have an applicable formula one has to insert the expression of the ordinary finite volume effects for the different quantities. This will lead to some formulae that are useful in case of simulations with ordinary finite volume effects. Let us start with the SU(N) case.

#### SU(N)

For simplicity we rewrite eq. (6.1.14) as:

$$\Delta M(\theta) = -\frac{A(\theta)}{M(\theta)^2L}e^{-\frac{\sqrt{3}}{2}m(\theta)L} + \mathcal{O}\left(\frac{1}{M(\theta)L}e^{-m(\theta)L}\right), \tag{6.2.2}$$

where $A = \frac{3\lambda^2}{16\pi}$ is a constant that depends only on $\theta$. The different terms of eq. (6.2.1) are:

$$M_{H,L}(0) = M_H(0) - \frac{A(0)}{M(0)^2L}e^{-\frac{\sqrt{3}}{2}m(\theta)L}, \tag{6.2.3}$$

$$M_{H,L}^{(2)}(0) = M_H^{(2)}(0) - \frac{A(0)}{M(0)^2L}\left(\frac{A^{(2)}(0)}{A(0)} - 2\frac{M^{(2)}(0)}{M(0)} - \frac{\sqrt{3}}{2}m^{(2)}(0)L\right)e^{-\frac{\sqrt{3}}{2}m(0)L} \tag{6.2.4}$$

and

$$\chi_{\mathrm{t},L} = \chi_{\mathrm{t}} - \frac{B}{L}e^{-\frac{\sqrt{3}}{2}m(0)L}, \tag{6.2.5}$$

where $B$ is a constant.

Here the finite volume dependence of topological susceptibility has not be derived in the case of pure Yang-Mills theory as we do not have the tools of the ChPT in this case. Nevertheless, this assumption has been done in analogy to QCD and numerical studies corroborate this assumption. Now inserting those relations in eq. (6.2.1), we obtain the following results:

$$
\begin{aligned}
M_{Q,L} \approx & M(0) + \frac{M^{(2)}(0)}{2\,\chi_t\,V}\left(1 - \frac{Q^2}{\chi_t V}\right) - \frac{A(0)}{M(0)^2 L} e^{-\frac{\sqrt{3}}{2}m(\theta)L} \\
& + \frac{1}{2\,\chi_t\,V L}\left(C\left(1 - \frac{2Q^2}{\chi_t V}\right) - D + EL\right)\left(1 - \frac{Q^2}{\chi_t V}\right) e^{-\frac{\sqrt{3}}{2}m(0)L} \\
& + \mathcal{O}\left(\frac{1}{\chi_t^2 V^2}, \frac{Q^2}{\chi_t^3 V^3}, e^{-m(0)L}\right),
\end{aligned}
\tag{6.2.6}
$$

where

$$
\begin{aligned}
C &= BM^{(2)}(0) \\
D &= \frac{A(0)}{M(0)^2}\left(\frac{A^{(2)}(0)}{A(0)} - 2\frac{M^{(2)}(0)}{M(0)}\right) \\
E &= \frac{\sqrt{3}}{2}\frac{A(0)}{M(0)^2} m^{(2)}(0)
\end{aligned}
\tag{6.2.7}
$$

are three independent constants. In the equation we can observe that leading terms correspond to the addition of the two finite volume effects. The two effects mix only the next-to-leading order. In a matter of visibility, the dominant terms are colored, in red are the topological finite volume effects, in blue the ordinary finite volume effects and the most important mixed terms in magenta.

**QCD (Pion Mass)**

We start from the ChPT results in order to not have to deal with the integral. The different terms which appear in eq. (6.2.1) are expressed as :

$$
m_{\pi,L}(0) = m_\pi(0) + \frac{m_\pi^2(0)}{8N_f\pi^2 F_\pi^2(0) L} K_1(m_\pi(0)L) + \mathcal{O}\left(\frac{1}{m_\pi(0)L} e^{-\sqrt{2}m_\pi(0)L}\right), \tag{6.2.8}
$$

$$
m_{\pi,L}^{(2)}(0) = m_\pi^{(2)}(0) + \frac{3}{16\pi L}\frac{m_\pi}{F_\pi^2}\left[\left(\frac{m_\pi^{(2)}}{m_\pi} - 2\frac{F_\pi^{(2)}}{F_\pi}\right) K_1(m_\pi L) - \frac{1}{2} m_\pi^{(2)} L\left(K_0(m_\pi L) + K_2(m_\pi L)\right)\right], \tag{6.2.9}
$$

$$
\chi_{T,L} = \chi_T - \frac{3m_\pi^3}{8\pi^2 L} K_1(m_\pi L) = \chi_T\left(1 - \frac{E}{m_\pi L} K_1(m_\pi L)\right). \tag{6.2.10}
$$

The following step corresponds to insert them in eq. (6.2.1) to obtain the following result using the notation $x = m_\pi L$:

$$
\begin{aligned}
m_{\pi,Q,L} = & m_\pi(0) + \frac{m_\pi^{(2)}(0)}{2\chi_T V}\left(1 - \frac{Q^2}{\chi_T V}\right) + \frac{3}{16\pi^2}\frac{m_\pi^2}{F_\pi^2}\frac{K_1(x)}{x} + \frac{m_\pi^{(2)} E}{2\chi_T V}\left(1 - \frac{2Q^2}{\chi_T V}\right)\frac{K_1(x)}{x} \\
& + \frac{3}{32\pi^2\chi_T V}\frac{m_\pi^2}{F_\pi^2}\left(1 - \frac{Q^2}{\chi_T V}\right)\left[\left(\frac{m_\pi^{(2)}}{m_\pi} - 2\frac{F_\pi^{(2)}}{F_\pi}\right)\frac{K_1(x)}{x} - \frac{1}{2}\frac{m_\pi^{(2)}}{m_\pi}\left(K_0(x) + K_2(x)\right)\right] \\
& + \mathcal{O}\left(\frac{1}{\chi_t^2 V^2}, \frac{Q^2}{\chi_t^3 V^3}, K_1(\sqrt{2}x)\right).
\end{aligned}
\tag{6.2.11}
$$

Here we observe the addition of the two effects for the leading order. The other terms correspond to the mixing of the ordinary and topological finite volume effects. To underline the dominant terms of the equation, we color them with the same color code than for SU(2). The consideration of a higher number of loops modifies the

| | $\hat{\mathcal{V}}_{q\bar{q},Q,V}(r=3a)$ | $\hat{m}$ | $\hat{\chi}_t \times 10^5$ |
|---|---|---|---|
| fit results, eq. (6.2.6) | 0.16437(15) | 0.67(10) | 9.5(2.0) |
| unfixed topology results [63, 84] | 0.16455(7) | 0.723(23) | 7.0(0.9) |

Table 6.3.1: Results for the static potential $\hat{\mathcal{V}}_{q\bar{q}}(r=3a)$, the mass $\hat{m}$ of the $J^{PC}=0^{++}$ glueball, and the topological susceptibility $\hat{\chi}_t$, obtained by a fit of eq. (6.2.6) to fixed topology lattice results $\hat{\mathcal{V}}_{q\bar{q},Q,V}(r=3a)$.

results to:

$$\begin{aligned} m_{\pi,Q,L} = {} & m_\pi(0) + \frac{m_\pi^{(2)}(0)}{2\chi_t V}\left(1-\frac{Q^2}{\chi_t V}\right) + \frac{3}{16\pi^2}\frac{m_\pi^2}{F_\pi^2}\frac{1}{x}\sum_{n=1}^{\infty}\frac{m(n)}{\sqrt{n}}K_1(\sqrt{n}x) \\ & + \frac{m_\pi^{(2)}E}{2\chi_t V}\left(1-\frac{2Q^2}{\chi_T V}\right)\frac{1}{x}\sum_{n=1}^{\infty}\frac{m(n)}{\sqrt{n}}K_1(\sqrt{n}x) \\ & + \frac{3}{32\pi^2\chi_T V}\frac{m_\pi^2}{F_\pi^2}\left(1-\frac{Q^2}{\chi_T V}\right)\left[\left(\frac{m_\pi^{(2)}}{m_\pi}-2\frac{F_\pi^{(2)}}{F_\pi}\right)\frac{1}{x}\sum_{n=1}^{\infty}\frac{m(n)}{\sqrt{n}}K_1(\sqrt{n}x)\right. \\ & \left. -\frac{1}{2}\frac{m_\pi^{(2)}}{m_\pi}\sum_{n=1}^{\infty}m(n)\left(K_0(\sqrt{n}x)+K_2(\sqrt{n}x)\right)\right] + \mathcal{O}\left(\frac{1}{\chi_t^2V^2},\frac{Q^2}{\chi_t^3V^3},K_1(m'L)\right). \end{aligned} \tag{6.2.12}$$

## 6.3 Numerical tests of BCNW-equation with finite volume effects

### 6.3.1 Numerical tests in pure Yang-Mills SU(2) theory

In the SU(2) example discussed in section 5.3, it is possible to analyze fixed topology results using eq. (4.1.61) in a meaningful way, i.e. without taking ordinary finite volume effects into account. Since the mass of the lightest particle, the $J^{PC}=0^{++}$ glueball, is quite large, ordinary finite volume effects are strongly suppressed for large volumes. As indicated by the figure. 5.3.1 and explained in section A.2.2, one just has to discard volumes with $\hat{L}<14$.

In figure. 6.3.1 (top) we show a plot similar to figures 5.2.5, 5.4.2 and 5.3.4, this time for $\hat{\mathcal{V}}_{q\bar{q},Q,V}(r=3a)$. Moreover, also results for small volumes $\hat{V}=11^4,12^4,13^4$ are included. The curves correspond to eq. (4.1.61) with the fit parameters $M$, $M''$ and $\chi_t$ determined by a fit to the large volumes $\hat{V}=14^4,15^4,16^4,18^4$ where ordinary finite volume effects are negligible. There is a strong discrepancy between these curves and the lattice results for the small volumes $\hat{V}=11^4,12^4,13^4$. This is expected since ordinary finite volume corrections are not part of eq. (4.1.61) in particular for small Q.

In figure 6.3.1 (bottom) we show the same lattice results for $\hat{\mathcal{V}}_{q\bar{q},Q,V}(r=3a)$. This time, however, the curves correspond to eq. (6.2.6) with the fit parameters $M$, $M''$, $\hat{\chi}_t$, $m$, $m''$, $A$ and $A''$ determined by a fit to all seven volumes $\hat{V}=11^4,12^4,13^4,14^4,15^4,16^4,18^4$. There is almost perfect agreement, even at small volumes and for $Q=0$ and $|Q|=1$. However, a small discrepancy for $|Q|=2$ appears which is expected as the condition **(C1)** is not respected for those points. The extracted "hadron mass" $\hat{\mathcal{V}}_{q\bar{q},Q,V}(r=3a)$ is consistent with a corresponding computation at unfixed topology and also the glueball mass $\hat{m}$ and the topological susceptibility $\hat{\chi}_t$ obtained by the fit are in fair agreement with reference values, cf. table 6.3.1.

### 6.3.2 Test in QCD

To perform our most important test we use the configurations of the ensemble described in the appendix A.2.3.2. This ensemble suffers from ordinary finite volume effects as we have three volumes such that $\hat{m}_\pi\hat{L}=3.66$ for $\hat{L}=14$ and $\hat{m}_\pi\hat{L}=3.93$ for $\hat{L}=15$ and $\hat{m}_\pi\hat{L}=4.19$ for $\hat{L}=16$. Those rather small volumes correspond to the typical lattice size for overlap simulations. The choice of the volumes is designed to obtain a number of

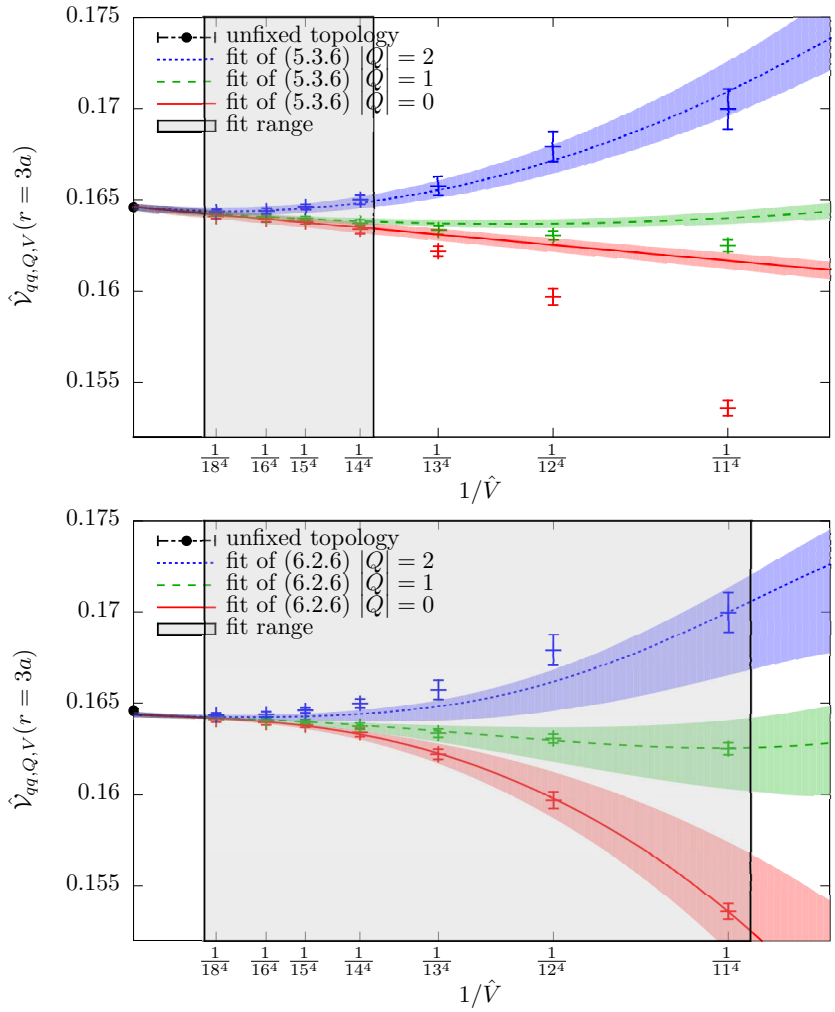


Figure 6.3.1: $\hat{\mathcal{V}}_{q\bar{q},Q,V}(r = 3a)$ as a function of $1/\hat{V}$. **(top)**: The curves represent the fit of eq. (A.2.6) to the lattice static potential results for large volumes $\hat{V} = 14^4, 15^4, 16^4, 18^4$. There is a strong discrepancy between these curves and the lattice results for the small volumes $\hat{V} = 11^4, 12^4, 13^4$. **(bottom)**: The curves represent the fit of eq. 6.2.6 to the lattice static potential results for all volumes $\hat{V} = 11^4, \ldots, 18^4$. There is almost perfect agreement even at small volumes and $Q = 0$.

| | fit | $2\tau_0$ | $4\tau_0$ | $8\tau_0$ |
|---|---|---|---|---|
| $\hat{m}_\pi$ | 1 | 0.256(5) | 0.256(6) | 0.255(6) |
| | 2 | 0.25601(65) | 0.25605(55) | 0.25564(64) |
| | 3 | 0.25568(64) | 0.25574(53) | 0.25555(62) |

Table 6.3.2: Pion mass from fixed topology

configurations per topological sectors similar to those obtained for a typical simulation $\mathcal{O}(1000)$ and such that the topological sectors are represented such that we can obtained unfixed topological results by averaging over them. Unfortunately, we just have a crude results for the volume $\hat{V} = 15^3 \times 30$ at unfixed topology and no results at fixed topology as the computations are ongoing.

We have first determined the infinite volume limit at unfixed topology by a fitting of eq. (6.1.15) to the unfixed topology results for our three volumes. We limit ourself to the one loop formula, i.e. the terms for $n \geq 2$ are neglected as in eq. (6.2.11). This leads to an infinite volume limit of $\hat{m}_\pi = 0.2556(2)$. Here the error is particularly small due to the lack of data on our ensemble with a spatial extension of $\hat{L} = 15$.

In order to extract the result from fixed topology simulations we compute the value of the pion mass at fixed topology for the topological charges $|Q| = \{0, 1, 2, 3\}$ for the two different volumes corresponding to $\hat{L} = 14$ and $\hat{L} = 16$. For all sectors used for the fit, the condition **(C1)** is respected such that $|Q|/\chi_t V < 0.5$. The conditions **(C2)** and **(C4)** are fulfilled as a clear plateau for the masses is observed for all the values. We were then in the condition to apply the BCNW-method. Here we test different equations with different numbers of parameters.

1. The leading order of the eq. (6.2.11) (i.e. blue and red terms):

$$m_{\pi,Q,L} = m_\pi(0) + \frac{m_\pi^{(2)}(0)}{2\chi_t V}\left(1 - \frac{Q^2}{\chi_t V}\right) + c\frac{K_1(x)}{x}, \tag{6.3.1}$$

   with parameters $m_\pi(0)$, $m_\pi^{(2)}(0)$, $\chi_t$ and $c$

2. The same equation with the topological susceptibility fixed to its unfixed topology results (cf. appendix A.2.3.2), i.e. the parameters are $m_\pi(0)$, $m_\pi^{(2)}(0)$ and $c$.

3. The next-to-leading order equation of eq. (6.2.11):

$$\begin{aligned} m_{\pi,Q,L} =& m_\pi(0) + \frac{m_\pi^{(2)}(0)}{2\chi_t V}\left(1 - \frac{Q^2}{\chi_t V}\right) + \frac{3}{16\pi^2}\frac{m_\pi^2}{F_\pi^2}\frac{K_1(x)}{x} \\ & - \frac{1}{2}\frac{m_\pi^{(2)}}{m_\pi}\left(K_0(x) + K_2(x)\right)\frac{3}{32\pi^2\chi_t V}\frac{m_\pi^2}{F_\pi^2}\left(1 - \frac{Q^2}{\chi_t V}\right), \end{aligned} \tag{6.3.2}$$

   with the same parameter than for 2.

The results for the pion mass are given in table 6.3.2. There is agreement of all the results extracted from fixed topology with the unfixed topology result. The results for the fit 1 leads to much larger statistical errors. This could be expected as there is one more parameter in the fit but mainly because there is a large error on the topological susceptibility as well. The other fits give extremely precise results with a rather small difference between them.

Figure 6.3.2 represents the fit of item 2. for $\tau = 4\tau_0$ which appears to be very accurate. However, it is clear on the figure that one more volume would be better. Another important aspect is the separation of the topological sectors that is visible for the smaller volumes. If the statistics are not sufficient for $\hat{L} = 16$ to clearly separate them, we can still observe a clear tendency.

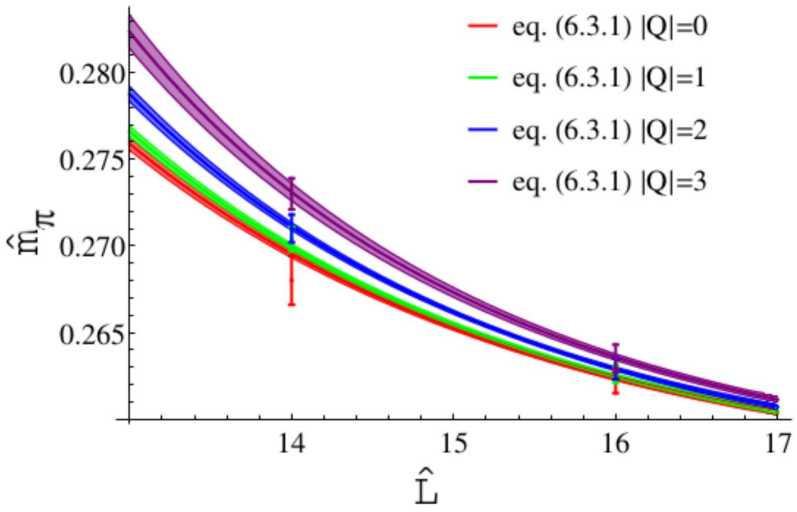


Figure 6.3.2: Pion mass as the function of the spatial extension $\hat{L}$ for $\hat{L} = 14$ and $\hat{L} = 16$ at flow time $4\tau_0$. The points are the values of the mass at fixed topology and for a given volume, the continuous lines correspond to the fits of eq. (6.3.1) with the topological susceptibility fixed at its unfixed topology results.

| $\times 10^5$ | $2\tau_0$ | $4\tau_0$ | $8\tau_0$ |
|---|---|---|---|
| $\chi_t$ | 6.3(4.1) | 6.2(4.3) | 6.2(4.7) |

Figure 6.3.3: Topological susceptibility from the BNCW method for the fit (1)

The result is given for different flow times. It is important to notice that the pion mass is always computed at flow time equal zero. Only the topological charge is computed at different flow times. This could lead to different attributions of topological sectors for a small number of configurations. It is not possible to compute the pion mass on 4D-smooth configurations (gradient flow different than zero) as it leads to a very large additive renormalization mass.

We have also mentioned that the topological susceptibility is a parameter of the first fit. We obtain similar results as in the previous sections, i.e. the results are in agreement with the reference value but the statical errors is larger than 50% of the values obtained. This clearly demonstrates that the method is not appropriate to extract the topological susceptibility. The results are summarised in table 6.3.3.

# Chapter 7

# The topological susceptibility

## 7.1 The AFHO-method

### 7.1.1 The method

The method is based on a simple formula, that we first demonstrate following [11]. We have already seen in section 4.2 that if we consider the parity mixing applied to the $\eta$ particle operator we obtain a mixing with the vacuum leading to constant term in the correlator (cf. eq. (4.2.30)). Here we will work with a similar result, however, we will focus on a strictly bosonic correlator instead of a fermionic one: the topological charge density two-point function. The BCNW-equation for an observable applied to the topological charge density correlator leads to:

$$\langle q(x)q(0)\rangle_Q = \langle q(x)q(0)\rangle(\theta=0) + \frac{\langle q(x)q(0)\rangle^{(2)}(\theta=0)}{2\,\chi_{\rm t}\,V}\left(1-\frac{Q^2}{\chi_{\rm t}\,V}\right) + \mathcal{O}\left(\frac{1}{{\chi_{\rm t}}^2\,V^2}\right) \tag{7.1.1}$$

with $q(x)$ is the topological charge density on $x$. For large $x$, $\langle q(x)q(0)\rangle(\theta=0)=0$ as the parity is conserved for $\theta=0$. The unknown parameter $\langle q(x)q(0)\rangle^{(2)}(\theta=0)$ can now be computed as

$$\begin{aligned}
\langle q(x)q(0)\rangle^{(2)} &= \frac{\partial^2}{\partial\theta^2}\langle q(x)q(0)\rangle \\
&= \frac{\partial^2}{\partial\theta^2}\frac{\int DA\,D\psi\,D\bar\psi e^{-S+i\theta Q}(q(x)q(0))}{\int DA\,D\psi\,D\bar\psi e^{-S+i\theta Q}} \\
&= \frac{\int DA\,D\psi\,D\bar\psi e^{-S+i\theta Q}(-Q^2q(x)q(0))}{\int DA\,D\psi\,D\bar\psi e^{-S+i\theta Q}} \\
&\quad + \frac{\int DA\,D\psi\,D\bar\psi e^{-S+i\theta Q}(q(x)q(0))\int DA\,D\psi\,D\bar\psi e^{-S+i\theta Q}Q^2}{\left(\int DA\,D\psi\,D\bar\psi e^{-S+i\theta Q}\right)^2} \\
&= -\left\langle Q^2q(x)q(0)\right\rangle + \langle q(x)q(0)\rangle\langle Q^2\rangle,
\end{aligned} \tag{7.1.2}$$

where we have used that $\langle Q\rangle\,(\theta=0)=0$, for all observables $G$. As already observed we have $\langle q(x)q(0)\rangle(\theta=0)=0$. Thus:

$$\langle q(x)q(0)\rangle^{(2)}(\theta=0) = -\left\langle Q^2q(x)q(0)\right\rangle. \tag{7.1.3}$$

$$\begin{aligned}\left\langle Q^2 q(x)q(0)\right\rangle &= \int d^4y d^4z \langle q(z)q(y)q(x)q(0)\rangle \\ &= \int d^4y d^4z \left[\langle q(z)q(y)q(x)q(0)\rangle_c + \langle q(z)q(y)\rangle\langle q(x)q(0)\rangle\right. \\ &\quad \left. + \langle q(0)q(y)\rangle\langle q(x)q(z)\rangle + \langle q(0)q(z)\rangle\langle q(x)q(y)\rangle\right],\end{aligned} \tag{7.1.4}$$

where $\langle \ldots \rangle_c$ is the connected vacuum expectation value. The first and the second terms vanish as $|x| \to \infty$ due to parity reasons. Therefore we have:

$$\begin{aligned}\left\langle Q^2 q(x)q(0)\right\rangle &= \int d^4y d^4z \left[\langle q(0)q(y)\rangle\langle q(x)q(z)\rangle + \langle q(0)q(z)\rangle\langle q(x)q(y)\rangle\right] \\ &= 2\int d^4y \langle q(0)q(y)\rangle \int d^4z \langle q(x)q(z)\rangle \\ &= 2\,{\chi_{\mathrm{t}}}^2,\end{aligned} \tag{7.1.5}$$

where we used the translation invariance to compute the second integral. This calculus leads to the following result:

$$\langle q(x)q(0)\rangle_Q = -\frac{\chi_{\mathrm{t}}}{V}\left(1 - \frac{Q^2}{\chi_{\mathrm{t}} V}\right) + \mathcal{O}\left(\frac{1}{{\chi_{\mathrm{t}}}^2 V^2}, e^{-m_\eta x}\right). \tag{7.1.6}$$

With this equation the method is straightforward. In eq. (7.1.6), we know the volume which is a parameter of our simulation and the topological charge of the topological sector in which the simulation is fixed. Then the only free parameter is the topological susceptibility. To extract it using the equation (7.1.6), one can easily compute the topological charge density correlator from the simulation. If the volume is large enough and the statistical errors not too large one will observe a plateau for a large value of $x$. By fitting the plateau, we extract the topological susceptibility.

### 7.1.2 Test in 4D SU(2) gauge theory

The first test is done in 4D SU(2) gauge theory. The numerical setups are given in the appendix A.2.2. We proceeded by computing the correlation function of the topological charge density $\langle q(x)q(0)\rangle_Q$ for several topological charges $|Q| \in \{0, 1, \ldots, 4\}$ and volumes $\hat{V} \in \{14^4, 16^4, 18^4\}$.

The normalization factor on the right-hand-side of eq. (7.1.6) is given by the inverse volume. The corresponding suppressed signal in a large volume is often the bottleneck in the application of the AFHO-method. In order to compensate this suppression which is worrisome in a 4D volume we now determined $\langle q(x)q(0)\rangle$ by measuring all-to-all correlations in each configuration, thus taking advantage of the discrete translational and rotational invariance.

In a second step we fit to these lattice results the right-hand-side of eq. (7.1.6) with respect to $\chi_{\mathrm{t}}$ at sufficiently large separations $x$ where $\langle q(x)q(0)\rangle_Q$ exhibits a plateau.

Figure 7.1.1 illustrates the determination of $\hat{\chi}_{\mathrm{t}}$ after $N_{\mathrm{cool}} = 10$ cooling sweeps, in the three lattice volumes under consideration. Clearly the correlation function $\langle q(x)q(0)\rangle_Q$ is different for each topological sector $|Q|$. These differences are more pronounced for smaller volumes $V$ and larger topological charges $Q$ which show that the splitting according to eq. (7.1.6) can indeed be resolved from our data. Hence the statistics, drastically enhanced by the all-to-all correlations, is indeed sufficient to reveal the relevant signal.

In particular, for $\hat{V} = 14^4$ the maximally available on-axis separations $|x| = 6, 7, 8$ are at the border-line which allows us to observe plateaux of $\langle q(x)q(0)\rangle_Q$. For $\hat{V} = 16^4$ plateaux are visible in the range $|x| = 7, 8, 9$ and in $\hat{V} = 18^4$ even five points, $7 \leq |x| \leq 11$, are consistent with a plateau.

Since the signal, i.e. the differences between the plateau values, increases for smaller volumes a promising strategy might be to use anisotropic volumes. For example the volumes of a $14^4$ and a $12^3 \times 24$ lattice are similar (i.e. both should exhibit a similar signal quality), but the latter allows to study larger separations (on-axis up to $|x| = 12$, though not with the entire statistics of all-to-all correlations).

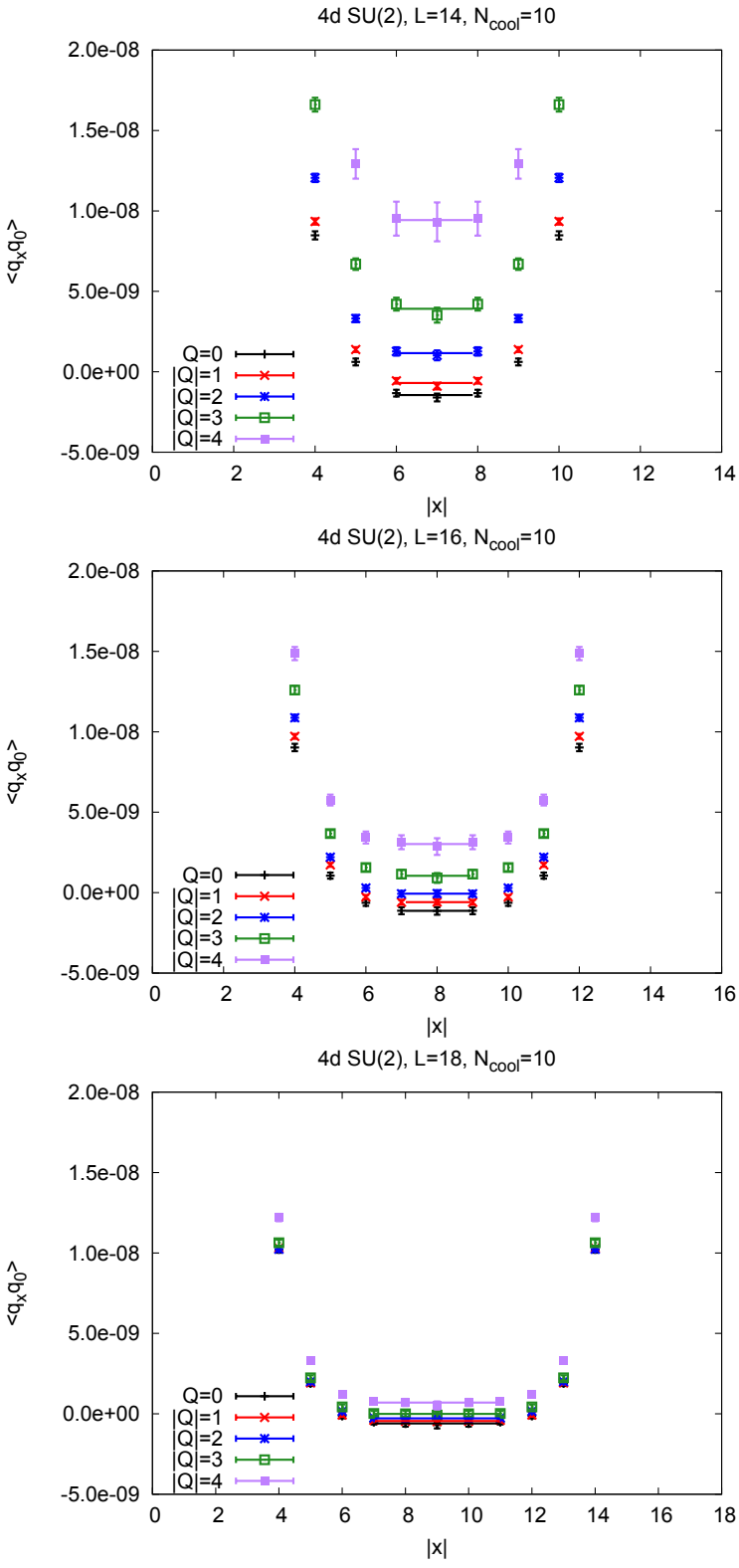


Figure 7.1.1: The correlation $\langle q(x)q(0)\rangle_Q$ as a function of the on-axis separation $|x|$, after $N_{\rm cool} = 10$ cooling sweeps, for the lattice volumes $\hat{V} = 14^4\,,\ 16^4\,,\ 18^4$. Fits of the right-hand-side of eq. (7.1.6) with respect to $\chi_{\rm t}$ are indicated by the horizontal solid lines.

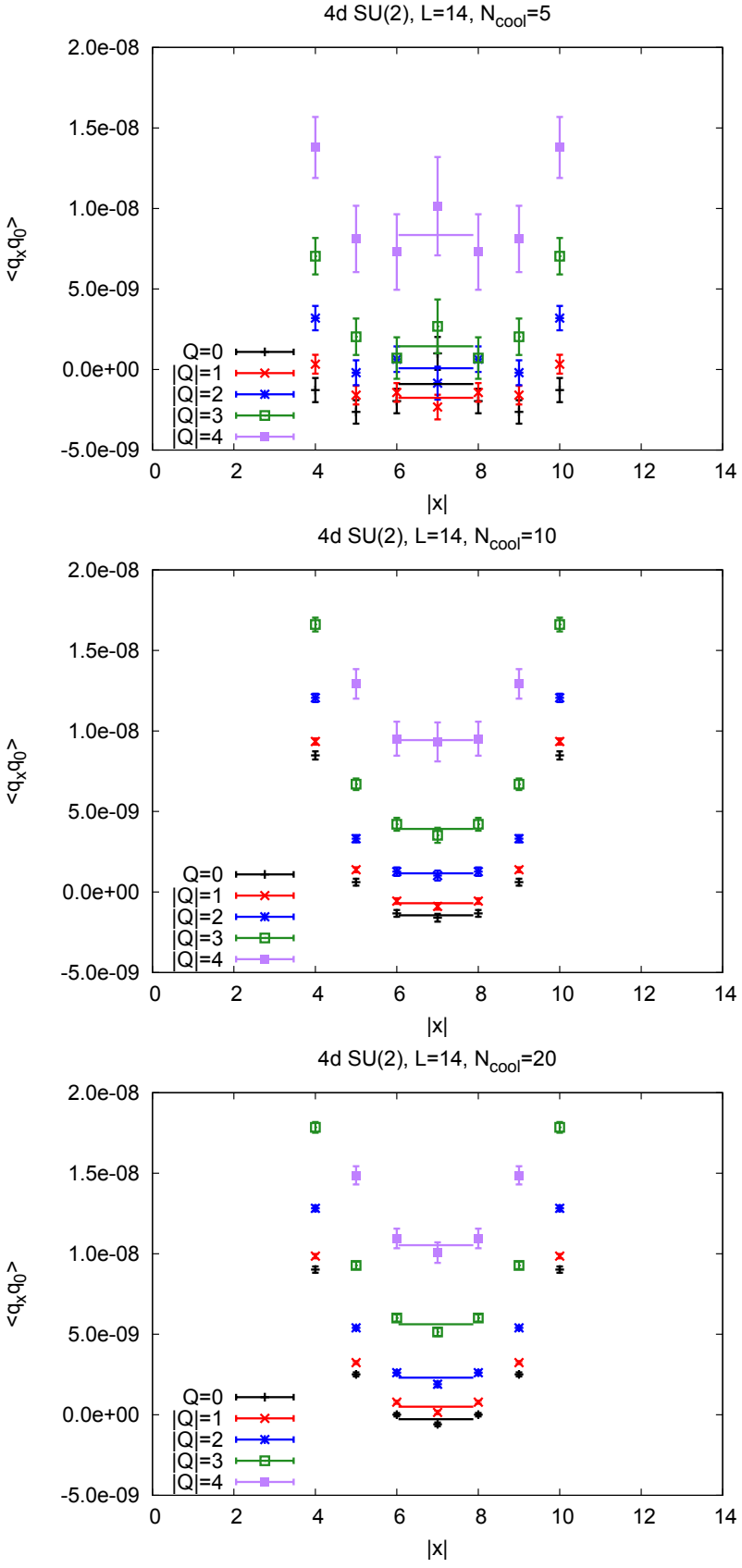


Figure 7.1.2: The correlation $\langle q(x)q(0)\rangle_Q$ as a function of the on-axis separation $|x|$ for different numbers of cooling sweeps, $N_{\rm cool} = 5\,,\ 10\,,\ 20$, and lattice volume $\hat{V} = 14^4$.

In figure 7.1.2 we show determinations of $\hat{\chi}_{\rm t}$ using the volume $\hat{V} = 14^4$ and compare different numbers of cooling sweeps, $N_{\rm cool} = 5\ ,\ 10\ ,\ 20$. For a small number such as $N_{\rm cool} = 5$, the correlation function $\langle q(x)q(0)\rangle_Q$ is rather noisy. This is a consequence of strong UV-fluctuations, which are manifest in the topological charge density $q(x)$, and which are not filtered out appropriately at small $N_{\rm cool}$. For a large number of cooling sweeps like $N_{\rm cool} = 20$, statistical errors are significantly smaller, but the correlation function $\langle q(x)q(0)\rangle_Q$ exhibits plateaux only at larger separations $|x|$.

This effect becomes plausible when considering the structure of the states contributing to $\langle q(x)q(0)\rangle_Q$. This correlation function is the Fourier transform of an analogous correlation function, summed over all topological sectors at a finite vacuum angle $\theta$ (for a detailed discussion, see chapter 4). The plateau values arise due to the non-vanishing vacuum expectation value $\langle q(x)\rangle$ at $\theta \neq 0$. Deviations from these plateaux are predominantly caused by low-lying excitations which correspond to glueballs in Yang-Mills theory. Due to the glueball size the overlap with $q(x)|\Omega\rangle$ (where $|\Omega\rangle$ is the vacuum state) increases when using extensive cooling (then $q_x$ is an extended operator resembling a low-lying glueball), compared to little or no cooling (then $q(x)$ is a highly local operator). Consequently, cooling enhances the contribution of excitations to the correlation function $\langle q(x)q(0)\rangle_Q$ and, hence, causes stronger deviations from the plateaux. In practice one should search for an optimal compromise, an intermediate number of cooling steps, such as $N_{\rm cool} = 8$ or $N_{\rm cool} = 10$, as we used in the examples in figure 7.1.1 and table 7.1.1.

Numerical results for the larger volumes, $\hat{V} = 16^4$ and $18^4$, and moderate cooling, $N_{\rm cool} = 8$ or 10, where a reasonably accurate determination of $\hat{\chi}_{\rm t}$ seems possible, are summarized in table 7.1.1. Fits have been restricted to sectors $|Q|$ fulfilling $|Q|/(\chi_{\rm t}V) < 0.5$, which is the small expansion parameter in the derivation of eq. (7.1.6) (cf. conditions **(C1)** of section 4.3). The resulting values for the topological susceptibility agree within the errors with a previous straight determination (without topology fixing), which obtained $\hat{\chi}_{\rm t} \times 10^5 = 7.0(9)$ [63].

| $\hat{V}$ | $N_{\rm cool}$ | $Q = 0$ | $\lvert Q\rvert = 1$ | $\lvert Q\rvert = 2$ | $\lvert Q\rvert = 3$ | combined |
|---|---|---|---|---|---|---|
| $16^4$ | 8 | 6.1(9) | 5.5(9) | 7.1(8) | | 6.3(6) |
| | 10 | 7.4(10) | 5.4(7) | 6.5(9) | | 6.3(5) |
| $18^4$ | 8 | 7.1(14) | 5.8(10) | 7.4(12) | 9.2(19) | 7.3(17) |
| | 10 | 6.2(10) | 5.9(10) | 6.6(9) | 8.7(11) | 7.9(13) |

Table 7.1.1: Results for the topological susceptibility $\hat{\chi}_{\rm t} \times 10^5$ extracted from fits to a single sector $|Q|$, or combined fits to several sectors ($0 \leq |Q| \leq 2$ for $\hat{V} = 16^4$, $0 \leq |Q| \leq 3$ for $\hat{V} = 18^4$). A corresponding study at unfixed topology [63] arrived at $\hat{\chi}_{\rm t} \times 10^5 = 7.0(9)$.

### 7.1.3 Test in QCD

In a way similar to the previous section, we now study the practicability of this method on full QCD. The numerical setups are summed-up in the appendix A.2.3.2. In addition to changing from SU(2) to QCD which is already an important step forward, we use here an anisotropic lattice with a volume of $16^3 \times 32$. This volume is even bigger than the previous ones used ($\approx 1.3$ times bigger that the volume $18^4$) and as it is asymmetric an all-to-all correlation doesn't make sens. It is then particularly important to smooth our configurations to extract the topological charge density in the aim of computing $\langle q(t)q(0)\rangle_Q$. Here the gradient flow technique is used which allowed to preserve the topology.

The topological susceptibility is extracted by fitting to the lattice results the right-hand-side of eq. (7.1.6) with respect to $\hat{\chi}_{\rm t}$, at sufficiently large separations $t$, i.e where $\langle q(t)q(0)\rangle_Q$ exhibits a plateau. In table 7.1.2, we summarise our results for different gradient flow times. The errors included the systematic ones due to the choice of the plateau. The results obtained for $|Q| < 3$ are in good agreement with unfixed topology results. Especially the combined fit of the three lowest plateaux gives extremely good results. For $|Q| = 3$ we observe a small discrepancy but still smaller than $2\sigma$. We also observe that the error is still rather large for each measurement, approximately $10\%$ for a single sector and $5\%$ for a combined fit to several sectors.

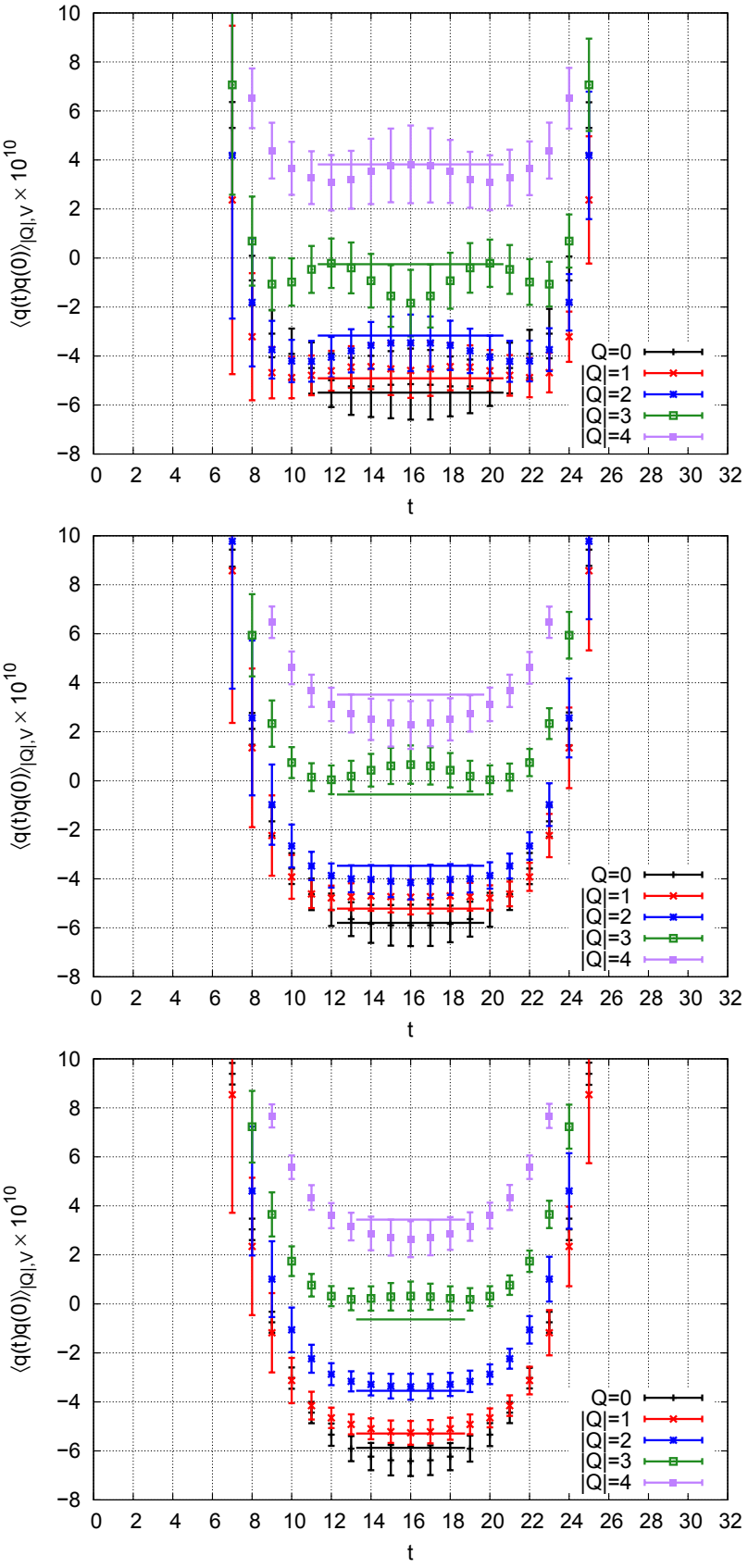


Figure 7.1.3: The correlation $\langle q(t)q(0)\rangle_Q$ as a function of the on-axis separation $t$ for different flow times $2\tau_0, 4\tau_0$ and $8\tau_0$, and lattice volume $\hat{V} = 16^3 \times 32$.

| $\tau_0$ | $Q=0$ | $\lvert Q\rvert=1$ | $\lvert Q\rvert=2$ | $\lvert Q\rvert=3$ | combined (0-2) | combined (0-3) |
|---|---|---|---|---|---|---|
| 4 | 7.6(7) | 6.9(6) | 8.3(6) | 6.3(9) | 7.6(4) | 7.3(4) |
| 6 | 8.2(7) | 7.5(5) | 7.4(5) | 6.6(6) | 7.7(3) | 7.4(3) |

Table 7.1.2: Results for the topological susceptibility $\hat{\chi}_{\rm t} \times 10^5$ extracted from fits to a single sector $|Q|$, or combined fits to several sectors ($0 \leq |Q| \leq 2$ "combined (0-2)", $0 \leq |Q| \leq 3$ "combined (0-3)"). The unfixed topology results gives $\hat{\chi}_{\rm t} \times 10^5 = 7.76(20)$.

We also study the effects of the gradient flow, as it can be observed from figure 7.1.3. One can conclude that the method for QCD with the gradient flow has a similar behavior as for SU(2) with cooling. For small gradient flow time the errors are important and the extraction of the topological susceptibility is difficult. The increase of the flow time leads to a reduction of the errors but also to a smaller plateau to fit. As for SU(2) the reason of this effect is an increase of the overlap of our correlator which excitation. In this case of QCD with 2 flavors, the excitation corresponds to the $\eta$-mesons (cf. section 4.2). In order to maintain a reasonable plateau and a statistical error as small as possible, a compromise has to be found. In our case, it appears that a good compromise is to take the flow time between $4\tau_0$ and $6\tau_0$.

Concerning the application of this method for large topological charge, it seems from that $|Q| = 3$ is the limit in our case. With $\hat{\chi}_{\rm t}\hat{V} \approx 10$ that leads to a condition **(C1)** restricted to $|Q|/\hat{\chi}_{\rm t}\hat{V} \leq 0.3$ which is quite limiting.

### 7.1.4 Conclusion on the AFHO-method

We have tested successfully the AFHO-method for the 4D gauge theory. The bottleneck of the theory which is a signal proportional to the inverse volume seems not to be worrisome for intermediate volumes. As we have observed, it can still be problematic for a large volume as figure 7.1.1 show us for the largest volume. However, the definition of large volumes (volumes too big to apply the method) is strongly linked to the precision that we obtain for the correlator. We have also seen that to obtain a proper result, it is important to have a strong control on the smoothing method used and to find a good compromise for the fit between precision of the correlators and size of the plateau, is necessary.

An important constraint is the condition **(C1)** that seems to limit the topological sectors usable such as $|Q|/\chi_t V \leq 0.3$ for QCD. However, this is not a main issue as the lowest topological charge are the most represented statically. It is not a problem either when a topology fixing actions [56–58] is used as the topological sector in which the simulation is performed can be chosen.

To conclude, this is an efficient method to extract the topological susceptibility for intermediate volumes.

## 7.2 The Slab-method

### 7.2.1 The derivation

Previously we observed that the topological charge distribution is close to a normal distribution, both from a theoretical point of view (cf. section 1.2.5) and from a numerical point of view (cf. section 3.1.2.1). Here the method assumes that the topological charge distribution is perfectly Gaussian. The method is based on the computation of the topological charge on spacetime subvolumes $xV$, $x \in [0, 1]$ called "Slabs".

Not all boundaries of those subvolumes are periodic, which implies that the topological charge $\bar{Q}$ of the Slab is a real and not an integer. The probability to have a charge $\bar{Q}$ on a subvolume of a configuration of charge $Q$ is given by:

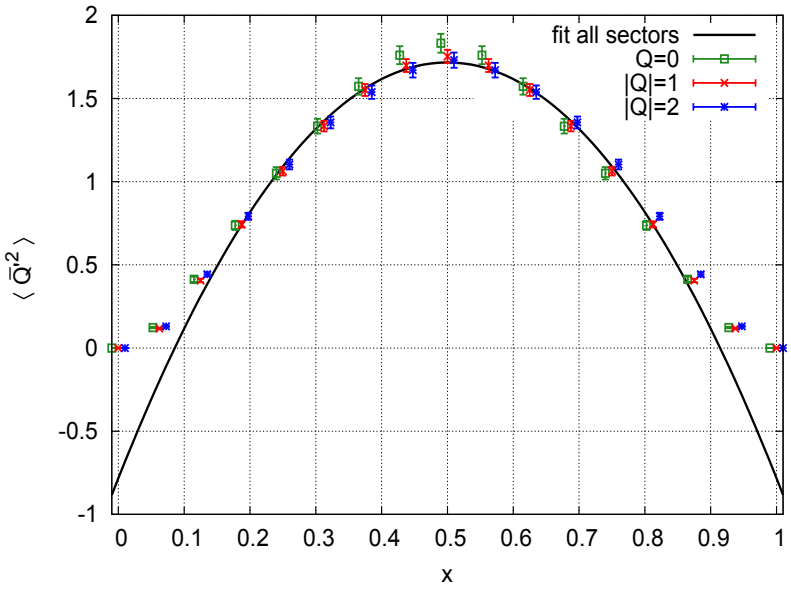


Figure 7.2.1: $\langle \bar{Q}'^2 \rangle$ as a function of $x$ at flow time $t = 5t_0$ for different values of the topological charge $Q$ (for better visibility points for $Q = 0$ ($|Q| = 2$) are slightly shifted to the left (right)). The black curve represents the fit of eq. (7.2.3) with an additive constant to the data points.

$$p(\bar{Q})p(Q-\bar{Q})\Big|_{xV,Q} \propto \exp\left(-\frac{\bar{Q}^2}{2\chi_t V x}\right) \times \exp\left(-\frac{(Q-\bar{Q})^2}{2\chi_t V(1-x)}\right). \tag{7.2.1}$$

Defining $\bar{Q}' = \bar{Q} - xQ$ allows to simplify (7.2.1),

$$p(\bar{Q})p(Q-\bar{Q})\Big|_{xV,Q} \propto \exp\left(-\frac{\bar{Q}'^2}{2\chi_t V x(1-x)}\right). \tag{7.2.2}$$

From this expression one can read off

$$\left\langle \bar{Q}'^2 \right\rangle = \chi_t V x(1-x). \tag{7.2.3}$$

The method to extract the topological susceptibility is then straightforward: One has to compute $\langle \bar{Q}'^2 \rangle$, the average of $\bar{Q}'^2$ on the available gauge link configurations with topological charge $Q$, for several values of $x$. The resulting points should be consistent with the parabola eq. (7.2.3), i.e. $\hat{\chi}_\mathrm{t}$ can be obtained with a corresponding fit.

### 7.2.2 Test in QCD

We perform our test on the same configurations as those used for the test of the AFHO-method on QCD. The Slabs are constructed to have a temporal extent $x\hat{T}$ and spatial volume $\hat{L}^3$, periodic in space.

In figure 7.2.1, we observe that the data points are not fully consistent with the quadratic curve eq. (7.2.3). In particular at small $x$ and small $1-x$ there are strong discrepancies. On the other hand, the data points in the interval $0.2 \leq x \leq 0.8$ can be described nicely with eq. (7.2.3) if one allows for an additive constant. Moreover, the corresponding result, $\hat{\chi}_\mathrm{t} = 7.83(14) \times 10^{-5}$, is then in agreement with the unfixed topology result from $\hat{\chi}_\mathrm{t} = 7.76(20) \times 10^{-5}$. Another important observation is the fact that the different topological sectors nicely agree for small topological charges. For larger topological charges the method does not seem to work so well

| $\tau$ | $\tau_0$ | $2\tau_0$ | $3\tau_0$ | $4\tau_0$ | $5\tau_0$ |
|---|---|---|---|---|---|
| $\hat{\chi}_t \times 10^5$ | 7.97(18) | 7.99(20) | 7.73(30) | 7.87(30) | 7.89(20) |

Table 7.2.1: Results of the topological susceptibility for different flow time $\tau$ for $|Q| = 1$. The unfixed topology results gives $\hat{\chi}_t \times 10^5 = 7.76(20)$.

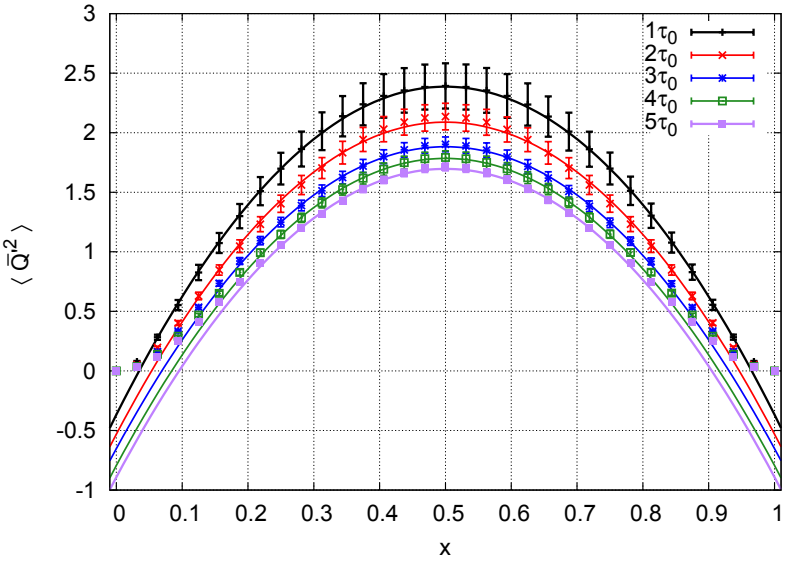


Figure 7.2.2: $\langle \bar{Q}'^2 \rangle$ as a function of $x$ for different values of the flow time for $|Q| = 1$.The continuous curve represents the fit of eq. (7.2.3) with an additive constant to the data points.

anymore and some parabola distortion appears. Similar effects are reported for low dimensional theories [13].

To study the deviation from a parabola at small $x$ and small $1-x$ and the appearance of the constant, we have first studied the effect of the smoothing on the curve. In figure 7.2.2, we can observe the results of $\left\langle \bar{Q}'^2 \right\rangle$ for different flow time $\tau \in \{\tau_0, 2\tau_0, \ldots, 5\tau_0\}$ in the topological sector $|Q| = 1$. The continuous lines correspond to the fit of eq. (7.2.3) with an additive constant. The results for the topological susceptibility can be found in table 7.2.1. The results nicely agree with the unfixed topology result.

In figure 7.2.2 the deviation from eq. (7.2.3) increases with the flow time. To understand if the smoothing process is the only reason and how this modifies the curves, we have to study in detail the two different aspects of the deviation, i.e. the deviation from a parabola at small $x$ and the additive constant.

As the gradient flow is a diffusion mechanism, we can expected that the distortion from the expected parabola due to the gradient flow is proportional to the square root of the gradient flow. The limits of the distortion when the flow time goes to zero inform us about the part due to the gradient flow. The additive constants are easy to study and it is possible to extract them from the fit of the curves of figure 7.2.2. Their values are plotted in figure 7.2.3 as a function of the gradient flow for $\tau \in \{\tau_0, \ldots, 8\tau_0\}$. The plot clearly shows the increase of the value with the flow time as already observed before. We fitted our values with a function proportional to the square root of the flow time. The result from the fit, which is represented by the continuous line in figure 7.2.3, matches very well the data points obtained. Moreover one can observe that the curve converges to zero for a flow time equal to zero, strongly supporting the hypothesis that the constant value is due to the smoothing process. This could also explain why in $\sigma$-model tests, where no smoothing is needed, the same effect has not been observed [13]. A possible explanation can be suggested considering the trivial picture of instantons gas. Due to the process of gradient flow, the instantons and anti-instantons are moving, making the annihilation of the instanton-anti-instanton pairs particularly easy, reducing for a Slab the value of $\langle \bar{Q}'^2 \rangle(x)$ but

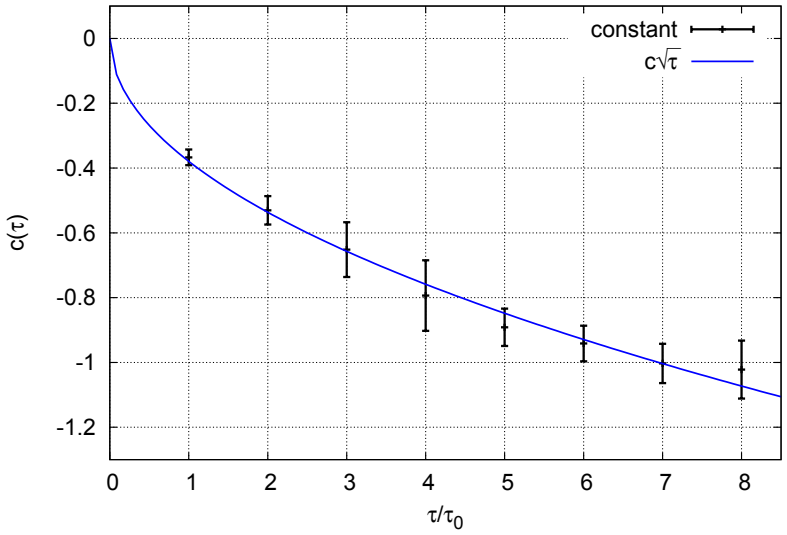


Figure 7.2.3: The additive constant extracted from fit as a function of the flow time and fit of the data point by a function proportional to the square root of the flow time.

not the value of $\langle Q^2 \rangle$ as the topological charge on the complete volume is kept unchanged by the annihilation.

The study of the distortions from small $x$ and how they are related to the gradient flow is more difficult to analyze. It is clear that the separation between the parabola and the value obtained for small Slabs decreased exponentially with $x$. This behavior corresponds to ordinary finite volume effects (cf. chapter 6). Moreover, the gradient flow is a diffusion process and with an increasing flow time, the ordinary finite volume effects are probably enhanced.

Using an ansatz inspired by [85], we describe successfully the distortion by the function:

$$f(x,\tau) = -c(\tau)e^{-(k_1\tau + k_2/\tau)x}, \tag{7.2.4}$$

where $c(\tau)$ is the additive constant computed before, $k_1$ and $k_2$ are constant that have to be fitted, $\tau$ is the flow time and $x$ is the volume on the Slab over the complete volume as figure 7.2.4 attests. However, this ansatz is somehow arbitrary and no proper justification has been found yet.

### 7.2.3 Conclusion on the Slab method

The Slab method seems to be an efficient method to determine the topological susceptibility at fixed topology. The results are in agreement with the expected results from unfixed topology if one adds this constant to eq. (7.2.3). Practically the addition of this constant is not a problem, as it appears that we are able to extract the topological susceptibility with a reasonable error. However, theoretically one needs to study the problem deeper. Our study of the variation of the constant with the gradient flow tome seems to show that this is only due to gradient flow and a possible explanation has been suggested. The deviation from a parabola at small Slabs volume can be considered as a finite volume effect and has been expected but a deeper study of the phenomena should be performed. To conclude, the method seems to work pretty well and one can use it, however, the user has to keep in mind the additive constant.

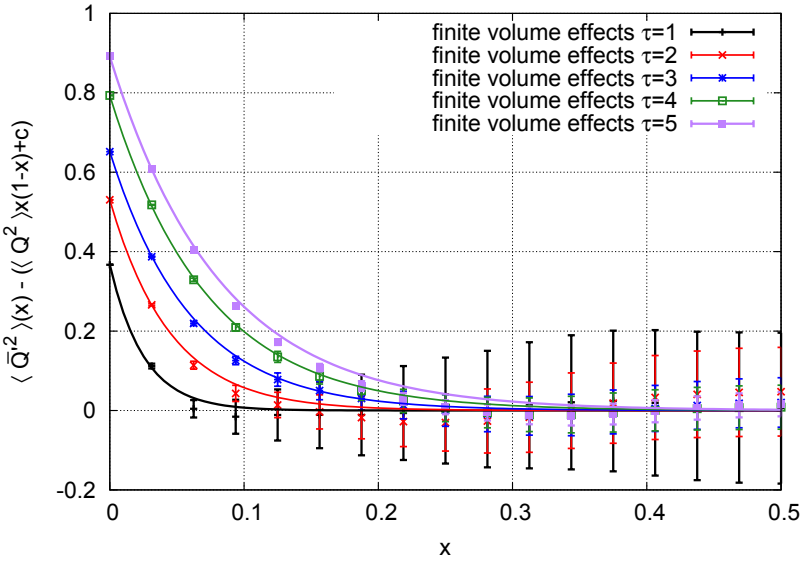


Figure 7.2.4: Deviation from the parabola formula eq. (7.2.3) as the a function of $x$, the ratio between the Slab volume and the complete volume.

# Conclusion

Lattice QCD is a particularly interesting tool to study QCD as it allows non-perturbative computations. However, to obtain physical results, make predictions and confront the results with experiments one has to look at the continuum limit of the computed observables. Having configurations with a small lattice spacing is particularly interesting in that case in order to gain in precision. However, for small lattice spacings the problem of the topology freezing is worrisome to extract e.g. masses without uncontrolled systematic errors. This is particularly true for overlap fermions which currently can only be simulated in small volumes.

Recently several methods have been suggested to overcome the problem. In this thesis we study the relation between variables computed at fixed topology and at unfixed topology. The formula is known as the BCNW-equation. The procedure to extract physical results from those computations has the advantage to be simple to apply and not breaking symmetries such as translation invariance.

The main aim of the thesis was to make a rather complete investigation of the procedure for QCD, in order to know if the method is practically useful and suitable for lattice simulations. This study also gave the possibility to learn which criteria are critical and what the limits of applications of the method are. In particular, we focused most of our tests on the extraction of the mass of a particle and the topological susceptibility.

We have first studied the method theoretically. A careful analysis of the realized approximations to calculate the formula has led to the identification of four criteria ((**C1**), **(C2)**, **(C3)** and **(C4)**) for the extraction of the mass. **(C1)** is limiting the volume range of application of the method and the topological sectors, **(C2)** gives the maximum value of the Euclidean time separation for the extraction of the mass, **(C3)** corresponds to the possibility to neglect ordinary finite volume effects imposing a minimum spatial extent and **(C4)** avoids the contamination of the results by excited states giving a minimum time for the extraction of the mass.

Then our second step was to push the calculation of the equation to third order in $1/V$ in order to gain precision or to evaluate the errors made when a lower order equation is used. In addition, we studied the consequences of parity breaking due to fixed topology on the parity partner correlators. In particular, we have proven that fixing the topology leads to $1/V$ corrections for quantities having a lighter parity partner. In that case one has to fit a matrix instead of a single correlator.

The following step was to perform a series of tests on different models. The tests were first done in the O(2) model with a square well potential which actually was not a simulation but a direct computation with arbitrary precision. This has allowed us to precisely study all the parameters and the consequences of non-respecting the suggested criteria. We were also able to test the expansion of the BCNW-equation up to third order and to show the improvement that one achieves. Then, in order to study the problem, we have performed tests on models closer to QCD, one with fermions and confinement, i.e. the Schwinger model and one in four dimensions, i.e. pure Yang-Mills theory. On those models our statistics was not sufficient to prove the effect of the improvement of the BCNW-equation. However, we were able to identify the troublesome criteria. From our results it appears that the conditions **(C2)** and **(C4)** are easy to fulfill. On the contrary, **(C1)** is a problem if the simulation is trapped in a high topological charge sector. However, this is rather unlikely as we have a Gaussian distribution reducing quickly the probability to have a large value of the topological charge. Also it is possible to use an action which fixes the topology in order to choose the sector such that it respects **(C1)**. The last condition, **(C3),** is not specific to fixed topology simulations; the problem is known as the ordinary finite volume effects and solutions exist for those effects at unfixed topology. This problem is particularly important for expensive

simulations as those made with overlap fermions, which are also those for which the freezing of the topology is the most severe. Our tests have identified this condition as the most restrictive one, in order to apply the method in QCD. Thus we searched and found a solution for the **(C3)** condition to be less limiting. Our solution consists of calculating the ordinary finite volume effects at fixed topology. This has resulted in a new equation that we were able to test in SU(2) and QCD with success.

The conclusions of all those tests are the following:

**(C1)** To be on the safe side to apply the BCNW-method, one needs: $|Q|/(\chi_{\rm t}V) < 0.5$

**(C2)** Here two cases have to be considered: the first one corresponds to the case where the statistics is not enough to see the time dependence of the mass. Then the mass at fixed topology can be extracted from a plateau and the condition **(C2)** is respected. The second case corresponds to the case where the statistics is good enough to see the time dependence, then respecting the condition corresponds to finding the range of time for which the dependence is linear. Here the correlator has to be fitted and not the mass.

**(C3)** To be on the safe side when the basic BCNW-equation is used, the lattice spatial extend has to respect $m_\pi(\theta = 0)L \gtrsim 5$. Otherwise either eq. (6.3.1) or eq. (6.3.2) has to be used.

**(C4)** Here it corresponds to identifying a minimum time $t_{min}$ such that for $t > t_{min}$ there is no time exponential dependence. That generally corresponds to use large $t$ values being careful that **(C2)** is still respected**.**

We have also mentioned that we wanted to extract the topological susceptibility, at least to check if the condition **(C1)** is fulfilled. The procedure to extract the mass is supposed to also give us the topological susceptibility. However, it has been observed that the statistical errors that result from this method are very large on this quantity. The method is not suitable to extract the topological susceptibility. We have then looked at two different methods. Both approaches have the advantage that they only need one volume and one topological sector.

The first one tested is the AFHO-method. This method is based on the BCNW-equation, and so the same conditions need to be fulfilled. The method consists of computing the topological charge density correlator at fixed topology and was tested in SU(2) and in QCD. All the tests allow us to conclude that the results obtained are in agreement with unfixed topology simulations and with small statistical errors compared to the topological susceptibility extracted from the BCNW-equation. It appears that the condition **(C1)** has to be a bit stricter in that case, with $|Q|/(\chi_{\rm t}V) < 0.3$, partly due to an influence of the gradient flow which is necessary to extract the correlator value.

The second method that was tested was the Slab method. This method is based on a computation in subvolumes and is not constrained by the same conditions as the BCNW based method. The main condition here is that the kurtosis should be equal to zero or small enough to be negligible. A priori each topological sector can be used and no restriction on the volume exists. We have tested the method on our QCD configurations and several conclusions were drawn. The method does not work as expected: a constant value has to be subtracted from the theoretical formula, some deviation appears also for small subvolumes and for a large topological charge $Q \geq 4$. Those discrepancies have been studied. For the constant it appears that this is due to the smoothing of the configurations and the deviation for small subvolumes corresponds to ordinary finite volume effects enhanced by the gradient flow. However, taking these remarks into account it has been possible to extract the topological susceptibility with success. The only problem remaining is the lack of theoretical explanation for those deviations even if some ideas have been suggested.

To conclude the BCNW-method is efficient to extract physical results from fixed topology simulation. Its application can be made in two steps:

1. We first need to compute the topological susceptibility to know which topological sectors fulfill the condition **(C1)**. Here both methods (AFHO and Slab) can be used for intermediate volumes. If the AFHO-method is used, one has to check afterwards if the condition **(C1)** is satisfied.

2. Then we can apply the BCNW-method with respect to the four conditions with the value of the topological susceptibility fixed to the value computed in the first step.

Let us finish by giving some directions for further work. They can be divided in two areas. The first one concerns directly the BCNW-method while the second one concerns the extraction of the topological susceptibility. Concerning the BCNW-method:

- The tests in QCD should be extended to insert a third volume (on-going).
- The second test that still needs to be done is to extract the mass of two parity partners.

Concerning the topological susceptibility:

- A complete study of the ordinary finite volume effects on the AFHO-method should be done.
- A theoretical study of the deviation in the Slab method.

To summarize, the results of this work prove that simulations at fixed or frozen topology can be done using the BCNW-equation. In particular, we have determined the conditions for which this method can be considered as valid and performed improvements of the method allowing a large range of applicability. Two methods to extract the topological susceptibility have also been studied and tested with success. Thus we believe that the methods will be often used in the next years.

# Appendix A

# Convention and Setup

## A.1 Notation and Conventions

This appendix describes the notation used in the thesis.

### A.1.1 Metric, Indices and Units

For the spacetime Minkowski metric, the metric $\eta_{\mu\nu} = \text{diag}(1, -1, -1, -1)$ represents flat four-dimensional spacetime. Four-dimensional coordinates are written as $x^\mu = (t, x, y, z)$ and $\partial_\mu = (\partial/\partial t, \vec{\nabla})$ is used.

Lorentzian indices are always denoted by Greek letters and the Einstein convention is used (implicit summation over repeated indices). Purely spatial coordinates are defined by Latin letter. The Minkowski indices are $\{0, 1, 2, 3\}$, the time being $0$. The Euclidean indices are $\{1, 2, 3, 4\}$ with $4$ the Euclidean time.

The antisymmetric tensor is defined to be unity when all of its indices are upper and in numerical order. Thus $\epsilon^{123} = \epsilon^{0123} = \epsilon^{1234} = 1$.

In the continuum, units used are natural units with $c$, $\hbar$ equal to unity. All dimensionful lattice quantities are expressed in units of $a$, denoted by a hat $\hat{}$, e.g. $\hat{m} = ma$.

### A.1.2 Gauge fields

In non-Abelian gauge theories, the gauge field is written as a Hermitian element of the Lie algebra:

$$A_\mu = A_\mu^a T^a, \tag{A.1.1}$$

where the hermitian generators of the SU(N) algebra $T^a$ are normalized according to:

$$\text{Tr}(T^a T^b) = \frac{1}{2}\delta^{ab} \quad \text{and} \quad [T^a, T^b] = i f^{abc} T^c \tag{A.1.2}$$

where $f^{abc}$ is the completely antisymmetric structure constant.

## A.2 Setup

### A.2.1 Schwinger model

#### A.2.1.1 Brief description

The Schwinger model describes 2D quantum electrodynamics. The continuum Lagrangian is

$$\mathcal{L}(\psi,\bar{\psi},A)=\sum_{f=1}^{N_f}\bar{\psi}^{(f)}\Big(\gamma_\mu(\partial_\mu+igA_\mu)+m^{(f)}\Big)\psi^{(f)}+\frac{1}{4}F_{\mu\nu}F_{\mu\nu}, \tag{A.2.1}$$

where $N_f$ is the number of fermion flavors. The Schwinger model is a widely used toy model, which shares several important features with QCD. In particular the $U(1)$ gauge theory in two spacetime dimensions allows for topologically non-trivial gauge configurations, which are similar to instantons in 4D Yang-Mills theory or QCD. The corresponding topological charge is given by

$$Q[A]=\frac{1}{\pi}\int d^2x\,\epsilon_{\mu\nu}F_{\mu\nu}. \tag{A.2.2}$$

Moreover, for $N_f=2$ its low lying energy eigenstates contain a rather light iso-triplet composed of quasi Nambu-Goldstone bosons, the analogues of pions in QCD. The model also provides fermion confinement.

#### A.2.1.2 Setups

Numerically we study the Schwinger model on a periodic spacetime lattice with extension $L=\hat{L}a$. The spacetime volume is $V=L^2$. We use $N_f=2$ flavors of mass-degenerate Wilson fermions, $m=m^{(1)}=m^{(2)}$, and the standard plaquette gauge action.

We use a geometric definition of topological charge on the lattice [86, 87],

$$Q[U] \;=\; \frac{1}{2\pi}\sum_P\phi(P), \tag{A.2.3}$$

where $\sum_P$ denotes the sum over all plaquettes $P=e^{i\phi(P)}$ with $-\pi<\phi(P)\leq+\pi$. With this definition $Q$ is an integer for any given gauge configuration with periodic boundary conditions.

**Setup Schwinger 1: Topology freezing.**

Simulations where performed at various values of $\beta$, $\hat{m}$ and $\hat{L}$ using a Hybrid Monte-Carlo (HMC) algorithm with multiple timescale integration and mass preconditioning [88]. The majority of simulations are rather short ($\approx 50\,000\ldots100\,000$ HMC trajectories), have been performed using small lattice sizes ($\hat{V}=8^2\ldots28^2$) and are mainly used to investigate the probability for a transition to another topological sector per HMC trajectory. This probability is plotted in figure 2.3.1 versus $\hat{g}=1/\sqrt{\beta}$ and $\hat{m}/\hat{g}=\hat{m}\sqrt{\beta}$, while $\hat{g}\hat{L}=\hat{L}/\sqrt{\beta}=24/\sqrt{5}$ is kept constant. $\hat{g}$ is proportional to the lattice spacing $a$. $\hat{m}/\hat{g}$ is proportional to $\hat{m}/a$ and, therefore, proportional to $m$, the bare quark mass in physical units.

**Setup Schwinger 2: Physical mass extraction from frozen topology.**

To explore the possibility to extract physical energy levels (i.e. hadron masses in the Schwinger model at unfixed topology) from simulations at fixed topology, we generate such fixed topology results with rather small statistical errors. We focus on a single lattice spacing and a single quark mass (corresponding to $\beta=4.0$ and a bare quark mass $\hat{m}=0.10$) and perform long simulations (500 000 HMC trajectories) for several spacetime volumes $\hat{V}\in\{40^2,44^2,48^2,52^2,56^2,60^2\}$.

### A.2.2 Simulation setup SU(2)

In the continuum the pure SU(2) Yang-Mills Lagrangian is

$$\mathcal{L}(A) = \frac{1}{4g^2} F^a_{\mu\nu} F^a_{\mu\nu}. \tag{A.2.4}$$

In 4 spacetime dimensions gauge field configurations may have a non-trivial topological structure. The corresponding topological charge is

$$Q[A] = \frac{1}{32\pi^2} \int d^4x \, \epsilon_{\mu\nu\rho\sigma} F^a_{\mu\nu} F^a_{\rho\sigma}. \tag{A.2.5}$$

Following section 3.1.2, we use an improved field theoretical definitions, to determine the topological charge of a lattice gauge configuration $[U]$,

$$Q[U] = \frac{1}{32\pi^2} \sum_x \sum_{\mu\nu\rho\sigma} \epsilon_{\mu\nu\rho\sigma} \sum_{\square=1,2,3} \frac{c_\square}{\square^4} F^{(\square\times\square)}_{x,\mu\nu}[U] F^{(\square\times\square)}_{x,\rho\sigma}[U], \tag{A.2.6}$$

where $F^{(\square\times\square)}_{x,\mu\nu}[U]$ denotes the dimensionless lattice field strength tensor clover averaged over loops of size $\square \times \square$ and $c_1 = +1.5$, $c_2 = -0.6$ and $c_3 = +0.1$. We apply eq. (A.2.6), after performing a number of cooling sweeps with the intention to remove local fluctuations in the gauge configurations, while keeping topological structures intact. The topological charge has been assigned after performing $N_{\text{cool}} = 10$ cooling sweeps leading to the statistics given in table A.2.1 for the sectors $|Q| \leq 4$.

| $V$ | $Q=0$ | $\lvert Q\rvert=1$ | $\lvert Q\rvert=2$ | $\lvert Q\rvert=3$ | $\lvert Q\rvert=4$ |
|---|---|---|---|---|---|
| $14^4$ | 1023 | 1591 | 893 | 350 | 103 |
| $16^4$ | 722 | 1371 | 942 | 574 | 248 |
| $18^4$ | 622 | 1079 | 898 | 616 | 402 |

Table A.2.1: Number of configurations for three volumes $V$ in each topological sector $0 \leq |Q| \leq 4$. The topological charge has been assigned after performing $N_{\text{cool}} = 10$ cooling sweeps.

The lattice action used for the simulations is the standard plaquette action. Simulations have been performed using a heatbath algorithm as explained in [89]. We decided for $\beta = 2.5$, which corresponds to the lattice spacing $a \approx 0.073\,\text{fm}$, when the scale is set by identifying the Sommer parameter $r_0$ with $0.46\,\text{fm}$ [90]. This value of $a$ is in the range of lattice spacings $0.05\,\text{fm} \lesssim a \lesssim 0.15\,\text{fm}$ nowadays typically used for QCD simulations. We have generated gauge configurations for various spacetime volumes, $\hat{V} = V/a^4 \in \{11^4\,,\, 12^4\,,\, 13^4\,,\, 14^4\,,\, 15^4\,,\, 16^4\,,\, 18^4\}$. For each volume observables have been computed on 4000 gauge configurations, which are separated by 100 heatbath sweeps guaranteeing statistically essentially independent gauge configurations. In particular there is no correlation regarding the topological charge $Q$ (the autocorrelation time of $Q$ is smaller than 20 heatbath sweeps).

### A.2.3 Simulation setup for QCD.

The theory of QCD is briefly introduced in chapter 1 and no more explanations will be given here. However, we used for our lattice simulations two different ensembles, with different setups that will be summarized here. The first ensemble of configurations which appears is B39.16 which is an ensemble generated by the ETMC collaboration. We used it for the comparison of the topological charge in chapter 3. The second ensemble is the ensemble B150 which has been used to test the different methods presented in this thesis.

| | $\hat{L}=14$ | $\hat{L}=16$ |
|---|---|---|
| Total | 40000 | 20000 |
| $Q=0$ | 6500 | 2500 |
| $\|Q\|=1$ | 12000 | 4700 |
| $\|Q\|=2$ | 9400 | 4100 |
| $\|Q\|=3$ | 6200 | 3200 |

Table A.2.2: Number of configurations per ensemble and per topological sector for the ensembles B150. The total number is exact but the number per topological sector is rounded to the nearest hundred configurations.

| $\times 10^5$ | $\hat{L}=14$ | $\hat{L}=16$ |
|---|---|---|
| $\hat{\chi}_{\mathrm{t}}$ | 7.88(12) | 7.76(20) |

Table A.2.3: Topological susceptibility for the ensembles B150.

#### A.2.3.1 B39.16

This corresponds to a single ensemble of maximally twisted mass fermions with 2 flavours where $\beta$ is equal to 3.9. We have an asymmetric lattice with a spatial length of $\hat{L}=16$ and a temporal extend of $\hat{T}=32$. The bare quark mass has been chosen at $\hat{\mu}=0.004$ which corresponds to a pion mass of approximatively 340 MeV in infinite volume. The lattice spacing is $a\approx 0.079$fm, hence a small physical volume of $L\approx 1.3$ fm. The complete ensemble contains 545 configurations barely not correlated. More details about this ensemble can be found in [91].

#### A.2.3.2 B150

The second setup corresponds to three ensembles of maximally twisted mass fermions with 2 flavours and $\beta$ equals to 3.9. We have two different asymmetric lattices with a spatial length of $\hat{L}=14$ and 16 and a temporal extend of $\hat{T}=2\hat{L}$. The bare quark mass has been chosen at $\hat{\mu}=0.015$ which corresponds to a pion mass of approximatively 650 MeV in infinite volume. The lattice spacing is $a\approx 0.079$fm.

The total amount of configurations is summed-up in table A.2.2. For each configuration, the topological charge has been computed via gradient flow for $\tau_0, 2\tau_0, 3\tau_0, ..., 7\tau_0$ and $8\tau_0$ using a clover definition for the topological charge operator and where the rescaling method has been used. The number of configurations per topological sectors has been listed in A.2.2. Note that only a rounded number appears as the values slightly differ with different flow times.

The topological susceptibility has also been computed at unfixed topology using the straightforward expression:

$$\chi_t = \frac{\langle Q^2\rangle}{V}. \tag{A.2.7}$$

The errors have been computed with bootstrap technique and the differences between different flow times have been considered as systematic errors. The results is summarized in table A.2.3.

# Appendix B

# An analytically solvable case, the 1D O(2) model

## B.1 Partition function and correlators at fixed topology

In the free case the eigenfunctions $\psi_n$ and eigenvalues $E_n$ of $H_\theta$ can be determined analytically,

$$H_\theta \psi_n(\varphi) = E_n \psi_n(\varphi) \quad \rightarrow \quad \psi_n(\varphi) = \frac{e^{+in\varphi}}{\sqrt{2\pi}} \quad , \quad E_n(\theta) = \frac{1}{2\beta}\left(n + \frac{\theta}{2\pi}\right)^2. \tag{B.1.1}$$

The partition function $Z_{Q,T}$ is the Fourier transform of $\mathcal{Z}_{\theta,T}$ (cf. eq. ((4.1.4))). After inserting the eigenvalues $E_n(\theta)$ and changing the variables of integration according to $\theta \rightarrow \theta' = \theta + 2\pi n$ one obtains a Gaussian integral, which is analytically solvable,

$$Z_{Q,T} = \sqrt{\frac{2\pi\beta}{T}} \exp\left( - \frac{2\pi^2\beta}{T} Q^2 \right). \tag{B.1.2}$$

This exact result can be compared with the approximation (4.1.24) after inserting $E_0(0, V_s) \rightarrow E_0(\theta = 0) = \theta^2/8\pi^2\beta|_{\theta=0} = 0$, $\mathcal{E}_2 = E_0^{(2)}(\theta = 0) = 1/4\pi^2\beta$ and $\mathcal{E}_n = 0$ for $n \neq 2$,

$$Z_{Q,T} = \sqrt{\frac{2\pi\beta}{T}} \exp\left( - \frac{2\pi^2\beta}{T} Q^2 \right) + \mathcal{O}\left( \frac{1}{\mathcal{E}_2^4 T^4} \, , \, \frac{1}{\mathcal{E}_2^4 T^4} Q^2 \, , \, \frac{1}{\mathcal{E}_2^4 T^4} Q^4 \right). \tag{B.1.3}$$

Even though power corrections proportional to $1/T^4$ and exponentially suppressed corrections have been neglected, the approximation is identical to the exact result eq. (B.1.2).

To extract the BCNW-equation we used $E_n(+\theta) = E_n(-\theta)$. While the spectrum fulfills this $+\theta \leftrightarrow -\theta$ symmetry, it is clearly violated by our mathematical parameterization eq. (B.1.1) for $n \neq 0$, (cf. figure B.1.1).

To compute the two-point correlation function $C_{Q,T}(t)$ we use the creation operator $O \equiv \sin(\varphi)$ (on a circle operators must be $2\pi$-periodic in $\varphi$). $C_{Q,T}(t)$ is the Fourier transform of $\mathcal{C}_{\theta,T}(t)$, which can be expanded in terms of energy eigenstates (cf. eqs. (4.1.43) and (4.1.44)). After inserting the eigenvalues $E_n(\theta)$ (eq. (B.1.1)), using $\langle \psi_m; \theta | O | \psi_n; \theta \rangle = (\delta_{m,n+1} + \delta_{m,n-1})/2$ and changing the variables of integration according to $\theta \rightarrow \theta + 2\pi n$ as in eq. (B.1.2), one again obtains a Gaussian integral, which can be solved exactly,

$$C_{Q,T}(t) = \frac{1}{2} \exp\left( - \frac{t(T-t)}{2\beta T} \right) \cos\left( \frac{2\pi Q t}{T} \right). \tag{B.1.4}$$

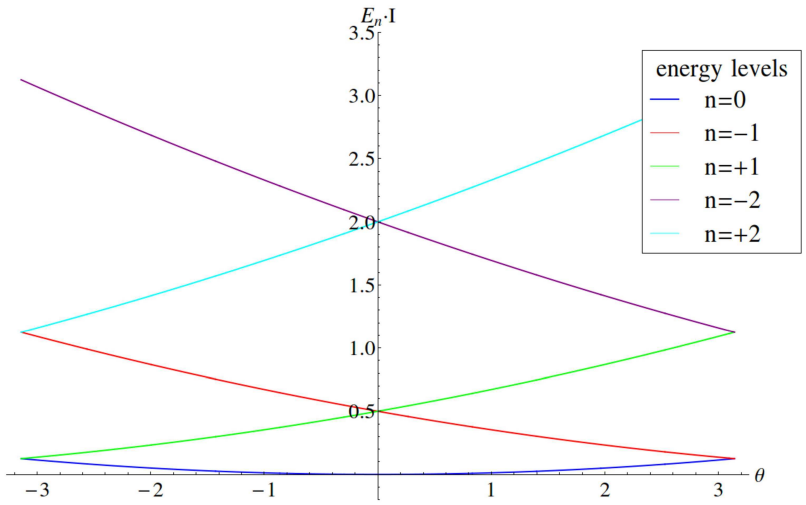


Figure B.1.1: The low lying spectrum of the free O(2) model: $E_n\beta$ as a function of $\theta$ (eq. (B.1.1))

Here, it is clear that the mass is not following the BCNW-equation which is a consequence of $E_n(+\theta) \neq E_n(-\theta)$. However, if the symmetry is not realized for each energy level independently it is realized when all the energy levels are considered together: $\sum_n E_n(+\theta) = \sum_n E_n(-\theta)$. Due to this some observables with no time dependence can still follow the BCNW-equation.

## B.2 Magnetic susceptibility

### B.2.1 Theoretical calculus

In this section we derive an exact analytical expression for the magnetic susceptibility at fixed topology in the $O(2)$-model. Then we prove that this quantity follows the BCNW-equation and we compare both with numerical results.

The magnetic susceptibility can be calculated as the sum of the magnetic susceptibility in one direction and an orthogonal direction:

$$\begin{aligned}\langle\chi_m\rangle_Q &= \langle\chi_y\rangle_Q + \langle\chi_x\rangle_Q \\ &= \int_0^T dt\, \langle \sin(\varphi(t))\sin(\varphi(0))\rangle_Q + \int_0^T dt\, \langle \cos(\varphi(t))\cos(\varphi(0))\rangle_Q \\ &= 2 \times \int_0^T dt\, \langle \sin(\varphi(t))\sin(\varphi(0))\rangle_Q \,.\end{aligned} \tag{B.2.1}$$

Using the eq. (B.1.4), it is easy to calculate an exact analytic expression for $\langle\chi_m\rangle_Q$:

$$\begin{aligned}\langle\chi_m\rangle_Q &= 4 \times \int_0^{T/2} dt\, \frac{1}{2} \exp\left(-\frac{t(T-t)}{2\beta T}\right) \cos\left(\frac{2\pi Q t}{T}\right) \\ &= 2 \times \int_0^{T/2} dt\, \exp\left(-\frac{t(T-t)}{2\beta T}\right) \cos\left(\frac{2\pi Q t}{T}\right) \\ &= \sqrt{\frac{\pi\beta T}{2}} e^{\frac{2\pi^2\beta Q^2}{T} - \frac{T}{8\beta}} e^{-i\pi Q} \left(\text{Erfi}\left(\frac{4i\pi Q\beta + T}{2\sqrt{2\beta T}}\right) - \text{Erfi}\left(\frac{4i\pi Q\beta - T}{2\sqrt{2\beta T}}\right)\right),\end{aligned} \tag{B.2.2}$$

where Erfi is the complex error function. The eq. (B.2.2) is the exact solution but it is difficult to conclude anything in this form. As a test for our solution, the limit $T \to \infty$ is interesting. In chapter 4, we have observed that fixed topology effects are finite size effects. If this is true, they should vanish and $\langle \chi_m \rangle_Q$ should converge to its unfixed topological value $4\beta$. The limit of eq. (B.2.2) is given by:

$$\begin{aligned}\lim_{T\to\infty} \langle \chi_m \rangle_Q &= \lim_{T\to\infty} \sqrt{\frac{\pi\beta T}{2}} e^{-\frac{T}{8\beta}} \times 2\text{Erfi}\left(\frac{T}{2\sqrt{2\beta T}}\right) \\ &= \lim_{T\to\infty} \sqrt{\frac{\pi\beta T}{2}} e^{-\frac{T}{8\beta}} \times 2\left(-i + e^{\frac{T}{8\beta}}\left(\frac{2\sqrt{2\beta}}{\sqrt{\pi T}}\right)\right). \\ &= 4\beta.\end{aligned} \tag{B.2.3}$$

Then the obtained result corresponds to its undixed topology result. The question that we are interested in now, is if the magnetic susceptibility follows the BCNW-equation. This question is legitimate as eq. (B.1.4) is not following the BCNW-equation especially due to its time dependence, when the magnetic susceptibility is not time dependent.

Let us have a look at the Taylor expansion for large $T$. The function Erfi can be developed as:

$$\begin{aligned}\text{Erfi}\left(\frac{4i\pi Q\beta + T}{2\sqrt{2\beta T}}\right) &= \text{Erfi}\left(\frac{\sqrt{T}}{\sqrt{8\beta}}\left(1 + \frac{4i\pi Q\beta}{T}\right)\right) \\ &= e^{\frac{T}{8\beta}\left(1+\frac{4i\pi Q\beta}{T}\right)^2}\left[\frac{\sqrt{8\beta}}{\sqrt{\pi T}}\left(1+\frac{4i\pi Q\beta}{T}\right)^{-1} + \frac{4\beta}{T}\frac{\sqrt{8\beta}}{\sqrt{\pi T}}\left(1+\frac{4i\pi Q\beta}{T}\right)^{-3}\right. \\ &\qquad \left. + \frac{48\beta^2}{T^2}\frac{\sqrt{8\beta}}{\sqrt{\pi T}} + \mathcal{O}\left(\frac{1}{T^3}\right)\right] \\ &= e^{\frac{T}{8\beta}} e^{i\pi Q} e^{-\frac{2\pi^2 Q^2 \beta}{T}}\left[\frac{\sqrt{8\beta}}{\sqrt{\pi T}}\left(1 - \frac{4i\pi Q\beta}{T} - \frac{16\pi^2 Q^2\beta^2}{T^2}\right) + \frac{4\beta}{T}\frac{\sqrt{8\beta}}{\sqrt{\pi T}}\left(1 - \frac{12i\pi Q\beta}{T}\right)\right. \\ &\qquad \left. + \frac{48\beta^2}{T^2}\frac{\sqrt{8\beta}}{\sqrt{\pi T}} + \mathcal{O}\left(\frac{1}{T^3}\right)\right] \\ &= e^{\frac{T}{8\beta}} e^{i\pi Q} e^{-\frac{2\pi^2 Q^2 \beta}{T}}\left[\frac{\sqrt{8\beta}}{\sqrt{\pi T}}\left(1 - \frac{4i\pi Q\beta}{T} + \frac{4\beta}{T} - \frac{16\pi^2 Q^2\beta^2}{T^2} - \frac{48i\sqrt{\pi}Q\beta^2}{T^2}\right.\right. \\ &\qquad \left.\left. + \frac{48\beta^2}{T^2}\right) + \mathcal{O}\left(\frac{1}{T^3}\right)\right].\end{aligned} \tag{B.2.4}$$

Changing $Q$ to $-Q$ we have:

$$\begin{aligned}\text{Erfi}\left(\frac{T - 4i\pi Q\beta}{2\sqrt{2\beta T}}\right) = e^{\frac{T}{8\beta}} e^{-i\pi Q} e^{-\frac{2\pi^2 Q^2 \beta}{T}}&\left[\frac{\sqrt{8\beta}}{\sqrt{\pi T}}\left(1 + \frac{4i\pi Q\beta}{T} + \frac{4\beta}{T} - \frac{16\pi^2 Q^2\beta^2}{T^2}\right.\right. \\ &\left.\left. + \frac{48i\sqrt{\pi}Q\beta^2}{T^2} + \frac{48\beta^2}{T^2}\right) + \mathcal{O}\left(\frac{1}{T^3}\right)\right].\end{aligned} \tag{B.2.5}$$

We can now use the antisymmetry of the function:

$$\begin{aligned}&\text{Erfi}\left(\frac{4i\pi Q\beta + T}{2\sqrt{2\beta T}}\right) - \text{Erfi}\left(\frac{4i\pi Q\beta - T}{2\sqrt{2\beta T}}\right) \\ &\qquad = 2e^{\frac{T}{8\beta}} e^{i\pi Q} e^{-\frac{2\pi^2 Q^2 \beta}{T}}\left[\frac{\sqrt{8\beta}}{\sqrt{\pi T}}\left(1 + \frac{4\beta}{T} - \frac{16\pi^2 Q^2\beta^2}{T^2} + \frac{48\beta^2}{T^2}\right) + \mathcal{O}\left(\frac{1}{T^3}\right)\right].\end{aligned} \tag{B.2.6}$$

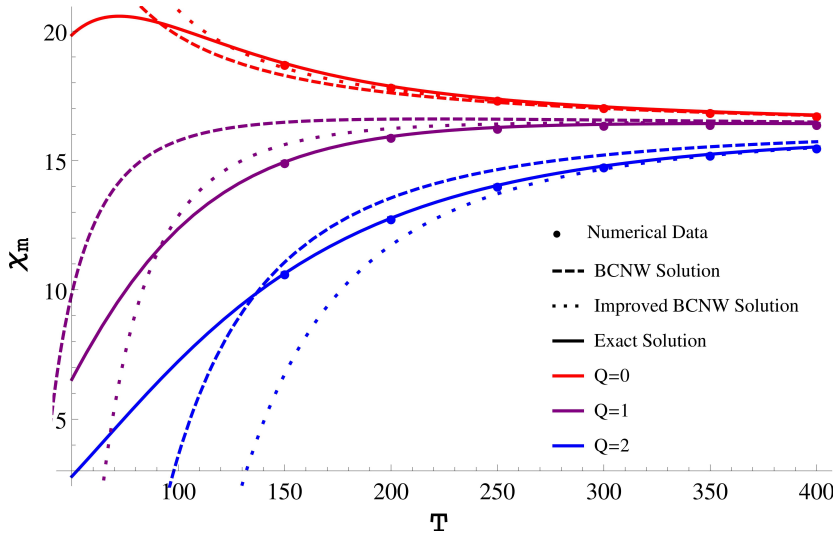


Figure B.2.1: Plot of the magnetic susceptibility as a function of the volume for different topological charge: $|Q| = 0, 1, 2$. Points are numerical results by Christoph Hofmann. Large dashed curves are the results of the BCNW-equation with the exact value of the parameter as entry, small dashed is the $1/T^3$ improved BCNW-equation and plain curves are the exact results.

We can apply this results to our equation eq. (B.2.2) to obtain:

$$\begin{aligned}\langle\chi_m\rangle_Q &= 2\sqrt{\frac{\pi\beta T}{2}}\left[\frac{\sqrt{8\beta}}{\sqrt{\pi T}}\left(1+\frac{4\beta}{T}-\frac{16\pi^2Q^2\beta^2}{T^2}+\frac{48\beta^2}{T^2}\right)+\mathcal{O}\left(\frac{1}{T^3}\right)\right]\\ &= 4\beta\left(1+\frac{4\beta}{T}-\frac{16\pi^2Q^2\beta^2}{T^2}+\frac{48\beta^2}{T^2}\right)+\mathcal{O}\left(\frac{1}{T^3}\right)\\ \langle\chi_m\rangle_Q &= 4\beta+\frac{4\beta}{\pi^2\chi_t T}\left(1-\frac{3/\pi^2-Q^2}{\chi_t T}\right)+\mathcal{O}\left(\frac{1}{T^3}\right).\end{aligned} \tag{B.2.7}$$

Here we obtain that the magnetic susceptibility follows the BCNW-equation.

### B.2.2 Comparison to numerical computations

Knowing the exact results and the BCNW-equation allows us to look a the convergence of the latter. Moreover, numerical results computed by Christoph Hofmann have been computed [16]. We present the results in the figure B.2.1. We observe the perfect agreement between numerical values and the exact equations. The BCNW equation converge only for large volumes which is expected as the condition **(C1)** has to be respected. Here it corresponds to $T \gg 160$ for $Q = 0$ and $Q = 1$ and $T \gg 320$ for $Q = 2$. In the plot it appears that considering the case $|Q|/\chi_t V < 0.8$ leads to a maximum of $5\%$ of error and for $|Q|/\chi_t V < 0.6$ leads to a maximum of $1\%$ of error. We can also observe in the plots the BCNW-equation improved to the third order in $1/T$. It clearly shows a much better convergence to the exacts values.

## B.3 Topological susceptibility

Here, it is also interesting to see if the topological susceptibility follows the AFHO-method. In the O(2) model the topological charge is given by:

$$Q = \int \mathrm{d}\, t \frac{\dot{\varphi}(t)}{2\pi} \tag{B.3.1}$$

This corresponds to the fact that the topological charge density is given by:

$$q(t) = \frac{\dot{\varphi}(t)}{2\pi}. \tag{B.3.2}$$

Thus the quantum operator associated to it in the $\theta$-vacuum, is given by

$$q_{op} = -\frac{1}{2\pi\beta}\left(\frac{\partial}{\partial\varphi} - \frac{i\theta}{2\pi}\right). \tag{B.3.3}$$

Therefore, the correlator in the $\theta$-vacuum is given by:

$$\begin{aligned} Z_\theta \langle q(t)q(0)\rangle_\theta &= \sum_{n,m} \langle n|\hat{q}|m\rangle\langle m|\hat{q}|n\rangle e^{-E_m(\theta)t} e^{-E_n(\theta)(T-t)} \\ &= -\sum_m \frac{\left(\frac{\theta}{2\pi} - m\right)^2}{4\pi^2\beta^2} e^{-E_m(\theta)T} \end{aligned} \tag{B.3.4}$$

The correlator at fixed topology is then given by the Fourier transform:

$$\begin{aligned} \langle q(t)q(0)\rangle_Q &= \frac{1}{Z_Q}\int_{-\pi}^{\pi} d\theta Z_\theta \langle q(t)q(0)\rangle_\theta e^{-i\theta Q} \\ &= -\frac{1}{Z_Q}\int_{-\pi}^{\pi} d\theta \sum_m \frac{\left(\frac{\theta}{2\pi} - m\right)^2}{4\pi^2\beta^2} e^{-E_m(\theta)T} e^{-i\theta Q} \\ &= -\frac{1}{Z_Q}\int_{-\pi}^{\pi} d\theta \sum_m \frac{\left(m - \frac{\theta}{2\pi}\right)^2}{4\pi^2\beta^2} e^{-\frac{T}{2\beta}\left(m - \frac{\theta}{2\pi}\right)^2} e^{-i\theta Q}. \end{aligned} \tag{B.3.5}$$

Making the change of variable: $\frac{\theta'}{2\pi} = \frac{\theta}{2\pi} - m$ and defining $\alpha = \frac{T}{8\pi^2\beta}$, we get:

$$\begin{aligned} \langle q(t)q(0)\rangle_Q &= -\frac{1}{Z_Q}\sum_m \int_{-\pi-2m\pi}^{\pi-2m\pi} d\theta' \frac{\left(\frac{\theta'}{2\pi}\right)^2}{4\pi^2\beta^2} e^{-\frac{T}{2\beta}\left(\frac{\theta'}{2\pi}\right)^2} e^{-i\theta' Q} \\ &= -\frac{1}{Z_Q}\frac{1}{16\pi^4\beta^2}\sum_m \int_{-\pi-2m\pi}^{\pi-2m\pi} d\theta' \theta'^2 e^{-\alpha\theta'^2} e^{-i\theta' Q} \\ &= -\frac{1}{Z_Q}\frac{e^{-\frac{Q^2}{4\alpha}}}{16\pi^4\beta^2}\sum_m \int_{-\pi-2m\pi}^{\pi-2m\pi} d\theta' \theta'^2 e^{-\alpha\left(\theta' - \frac{iQ}{2\alpha}\right)^2} \\ &= -\frac{1}{Z_Q}\frac{e^{-\frac{Q^2}{4\alpha}}}{16\pi^4\beta^2}\int_{-\infty}^{+\infty} d\theta' \theta'^2 e^{-\alpha\left(\theta' - \frac{iQ}{2\alpha}\right)^2} \end{aligned} \tag{B.3.6}$$

Here we have used that $\sum_m \int_{-\pi-2m\pi}^{\pi-2m\pi} = \int_{-\infty}^{+\infty}$. And now if we are making the change of variable $\vartheta = \theta' - \frac{iQ}{2\alpha}$, we obtain:

$$\begin{aligned}
\langle q(t)q(0)\rangle_Q &= -\frac{1}{Z_Q}\frac{e^{-\frac{Q^2}{4\alpha}}}{16\pi^4\beta^2}\int_{-\infty-i\frac{Q}{2\alpha}}^{+\infty-i\frac{Q}{2\alpha}} d\vartheta\left(\vartheta+i\frac{Q}{2\alpha}\right)^2 e^{-\alpha\vartheta^2} \\
&= -\frac{1}{Z_Q}\frac{e^{-\frac{Q^2}{4\alpha}}}{16\pi^4\beta^2}\int_{-\infty}^{+\infty} d\vartheta\left(\vartheta+i\frac{Q}{2\alpha}\right)^2 e^{-\alpha\vartheta^2} \\
&= -\frac{1}{Z_Q}\frac{e^{-\frac{Q^2}{4\alpha}}}{16\pi^4\beta^2}\left[\int_{-\infty}^{+\infty} d\vartheta\vartheta^2 e^{-\alpha\vartheta^2} + i\frac{Q}{2\alpha}\int_{-\infty}^{+\infty} d\vartheta 2\vartheta e^{-\alpha\vartheta^2} - \frac{Q^2}{4\alpha^2}\int_{-\infty}^{+\infty} d\vartheta e^{-\alpha\vartheta^2}\right] \\
&= -\frac{1}{Z_Q}\frac{e^{-\frac{Q^2}{4\alpha}}}{16\pi^4\beta^2}\left[\frac{\sqrt{\pi}}{2}\alpha^{-3/2} + 0 - \frac{Q^2}{4\alpha^2}\sqrt{\pi}\alpha^{-1/2}\right]
\end{aligned} \tag{B.3.7}$$

Using $\chi_t = \frac{1}{4\pi^2\beta}$, and $Z_Q = \sqrt{\pi}\alpha^{-1/2}e^{-\frac{Q^2}{4\alpha}}$, with $\alpha = \frac{1}{2}\chi_t T$

$$\langle q(t)q(0)\rangle_Q = -\chi_t^2\left[\frac{\alpha^{-1}}{2} - \frac{Q^2}{4}\alpha^{-2}\right] \quad . \tag{B.3.8}$$

$$\langle q(t)q(0)\rangle_Q = -\frac{\chi_t}{T} + \frac{Q^2}{T^2}. \tag{B.3.9}$$

Finally in the case of the 1D O(2) model we prove the AFHO formula. Here the result is exact. Meaning that this is valid whatever the volume is. This has been observed in our article [16].

# Appendix C

# The $\mathcal{O}(\mathbf{V}^{-3})$ expansion of the parity mixing equations

For information and potential use we add the $\mathcal{O}(V^{-3})$ expansion of the parity mixing equations (eq. (4.2.26), eq. (4.2.27) and eq. (4.2.28)). The calculus can be found in [14] and the notation has been defined in section (4.2).

The equation (4.2.26) at $\mathcal{O}(V^{-3})$ is given by:

$$
\begin{aligned}
C^{--}_{Q,V}(t) = \alpha^{--}_{-}(0)\exp\Bigg[ & - M_{H_-}(0)t - \frac{1}{\mathcal{E}_2 V}\frac{x^{--}_{2,-}}{2} - \frac{1}{(\mathcal{E}_2 V)^2}\Bigg(\frac{x^{--}_{4,-} - 2(\mathcal{E}_4/\mathcal{E}_2)x^{--}_{2,-} - 2(x^{--}_{2,-})^2}{8} - \frac{x^{--}_{2,-}}{2}Q^2\Bigg) \\
& - \frac{1}{(\mathcal{E}_2 V)^3}\Bigg(\frac{16(\mathcal{E}_4/\mathcal{E}_2)^2 x^{--}_{2,-} + x^{--}_{6,-} - 3(\mathcal{E}_6/\mathcal{E}_2)x^{--}_{2,-} - 8(\mathcal{E}_4/\mathcal{E}_2)x^{--}_{4,-}}{48} \\
& + x^{--}_{2,-}\frac{9(\mathcal{E}_4/\mathcal{E}_2)x^{--}_{2,-} - 6x^{--}_{4,-} + 4(x^{--}_{2,-})^2}{24} - \frac{x^{--}_{4,-} - 3(\mathcal{E}_4/\mathcal{E}_2)x^{--}_{2,-} - 2(x^{--}_{2,-})^2}{4}Q^2\Bigg)\Bigg] \\
+ \frac{\alpha^{--,(2)}_{+}(0)}{2\mathcal{E}_2 V}\exp\Bigg[ & - M_{H_+}(0)t - \frac{1}{\mathcal{E}_2 V}\Bigg(\frac{(\mathcal{E}_4/\mathcal{E}_2) + 3x^{--}_{2,+}}{2} + Q^2\Bigg) \\
& - \frac{1}{(\mathcal{E}_2 V)^2}\Bigg(\frac{3(\mathcal{E}_6/\mathcal{E}_2) - 13(\mathcal{E}_4/\mathcal{E}_2)^2 - 30(\mathcal{E}_4/\mathcal{E}_2)x^{--}_{2,+} + 15x^{--}_{4,+} - 18(x^{--}_{2,+})^2}{24} \\
& - \frac{2(\mathcal{E}_4/\mathcal{E}_2) + x^{--}_{2,+}}{2}Q^2 + \frac{1}{2}Q^4\Bigg)\Bigg] + \mathcal{O}\Bigg(\frac{1}{(\mathcal{E}_2 V)^4}\Bigg).
\end{aligned}
$$

The equation (4.2.27) at $\mathcal{O}(V^{-3})$ is given by:

$$
\begin{aligned}
C^{++}_{Q,V}(t) = \alpha^{++}_{+}(0)\exp\Bigg[ & - M_{H_+}(0)t - \frac{1}{\mathcal{E}_2 V}\frac{x^{++}_{2,+}}{2} - \frac{1}{(\mathcal{E}_2 V)^2}\Bigg(\frac{x^{++}_{4,+} - 2(\mathcal{E}_4/\mathcal{E}_2)x^{++}_{2,+} - 2(x^{++}_{2,+})^2}{8} - \frac{x^{++}_{2,+}}{2}Q^2\Bigg) \\
& - \frac{1}{(\mathcal{E}_2 V)^3}\Bigg(\frac{16(\mathcal{E}_4/\mathcal{E}_2)^2 x^{++}_{2,+} + x^{++}_{6,+} - 3(\mathcal{E}_6/\mathcal{E}_2)x^{++}_{2,+} - 8(\mathcal{E}_4/\mathcal{E}_2)x^{++}_{4,+}}{48} \\
& + x^{++}_{2,+}\frac{9(\mathcal{E}_4/\mathcal{E}_2)x^{++}_{2,+} - 6x^{++}_{4,+} + 4(x^{++}_{2,+})^2}{24} - \frac{x^{++}_{4,+} - 3(\mathcal{E}_4/\mathcal{E}_2)x^{++}_{2,+} - 2(x^{++}_{2,+})^2}{4}Q^2\Bigg)\Bigg] \\
+ \frac{\alpha^{++,(2)}_{-}(0)}{2\mathcal{E}_2 V}\exp\Bigg[ & - M_{H_-}(0)t - \frac{1}{\mathcal{E}_2 V}\Bigg(\frac{(\mathcal{E}_4/\mathcal{E}_2) + 3x^{++}_{2,-}}{2} + Q^2\Bigg) \\
& - \frac{1}{(\mathcal{E}_2 V)^2}\Bigg(\frac{3(\mathcal{E}_6/\mathcal{E}_2) - 13(\mathcal{E}_4/\mathcal{E}_2)^2 - 30(\mathcal{E}_4/\mathcal{E}_2)x^{++}_{2,-} + 15x^{++}_{4,-} - 18(x^{++}_{2,-})^2}{24} \\
& - \frac{2(\mathcal{E}_4/\mathcal{E}_2) + x^{++}_{2,-}}{2}Q^2 + \frac{1}{2}Q^4\Bigg)\Bigg] + \mathcal{O}\Bigg(\frac{1}{(\mathcal{E}_2 V)^4}\Bigg).
\end{aligned}
$$

The equation (4.2.28) at $\mathcal{O}(V^{-3})$ is given by:

$$
\begin{aligned}
C^{\mp\pm}_{Q,V}(t) = \frac{i\alpha^{\mp\pm,(1)}_{-}(0)Q}{\mathcal{E}_2 V}\exp\Bigg[ & - M_{H_-}(0)t - \frac{1}{\mathcal{E}_2 V}\Bigg(\frac{(\mathcal{E}_4/\mathcal{E}_2) + 3x^{\mp\pm}_{2,-}}{2}\Bigg) \\
& - \frac{1}{(\mathcal{E}_2 V)^2}\Bigg(\frac{3(\mathcal{E}_6/\mathcal{E}_2) - 13(\mathcal{E}_4/\mathcal{E}_2)^2 - 30(\mathcal{E}_4/\mathcal{E}_2)x^{\mp\pm}_{2,-} + 15x^{\mp\pm}_{4,-}}{24} \\
& - \frac{3}{4}(x^{\mp\pm}_{2,-})^2 - \frac{(\mathcal{E}_4/\mathcal{E}_2) + 3x^{\mp\pm}_{2,-}}{6}Q^2\Bigg)\Bigg] \\
+ \frac{i\alpha^{\mp\pm,(1)}_{+}(0)Q}{\mathcal{E}_2 V}\exp\Bigg[ & - M_{H_+}(0)t - \frac{1}{\mathcal{E}_2 V}\Bigg(\frac{(\mathcal{E}_4/\mathcal{E}_2) + 3x^{\mp\pm}_{2,+}}{2}\Bigg) \\
& - \frac{1}{(\mathcal{E}_2 V)^2}\Bigg(\frac{3(\mathcal{E}_6/\mathcal{E}_2) - 13(\mathcal{E}_4/\mathcal{E}_2)^2 - 30(\mathcal{E}_4/\mathcal{E}_2)x^{\mp\pm}_{2,+} + 15x^{\mp\pm}_{4,+}}{24} \\
& - \frac{3}{4}(x^{\mp\pm}_{2,+})^2 - \frac{(\mathcal{E}_4/\mathcal{E}_2) + 3x^{\mp\pm}_{2,+}}{6}Q^2\Bigg)\Bigg] + \mathcal{O}\Bigg(\frac{1}{(\mathcal{E}_2 V)^4}\Bigg).
\end{aligned}
$$

# Acknowledgements

First of all, I would like to thank my supervisor Marc Wagner, which introduced me to Lattice QCD and was always patient in answering all my questions. Thank you for your guidance, your honesty and your trust.

A special thank for Wolfgang Bietenholz for the fruitfully collaboration which has led to many of my PhD results, for sharing his great experience and for the valuable discussions, suggestions and corrections.

I am thankful to Krzysztof Cichy for is effectiveness during our collaboration, for the valuable and interesting discussions and for answering a lot of my naive questions.

I would like also to thank my office colleagues to endure my mess quietly, for answering my small questions immediately, for the valuable discussions and the nice working atmosphere throughout these years: Antje Peters, Christopher Czaban, Martin Kalinowski and Joshua Berlin. Also more generally I would like to thank everyone in the Lattice group for the atmosphere.

I am also indebted to Andrea Obermeyer for her helps and her guidance through the maze of the administration as for her constant good mood which contributes to the nice atmosphere of the group.

A big thanks goes to people who contributed to make this thesis readable by correcting my poor English: Antje Peters and Savvas Zafeiropoulos. A great thanks also to Christopher Czaban for the German abstract.

I am grateful to the "coffee temple" and its members for helping me to be productive after lunch time.

I acknowledge support by the Emmy Noether Programme of the DFG (German Research Foundation), grant WA 3000/1-1.

This work was supported in part by the Helmholtz International Center for FAIR within the framework of the LOEWE program launched by the State of Hesse. Calculations on the LOEWE-CSC high-performance computer of Johann Wolfgang Goethe-University Frankfurt am Main were conducted for this research. I would like to thank HPC-Hessen, funded by the State Ministry of Higher Education, Research and the Arts, for programming advice.

Last but not the least, I would like to thank my familly and my girlfriend who never fail to support me during these four years.

# Bibliography


[1] K. G. Wilson, "Confinement of Quarks," Phys. Rev. D **10**, 2445 (1974)

[2] M. Creutz, "Monte Carlo Study of Quantized SU(2) Gauge Theory" Phys. Rev. D **21** (1980) 2308

[3] L. Del Debbio, G. M. Manca and E. Vicari, "Critical slowing down of topological modes," Phys. Lett. B **594**, 315 (2004) doi:10.1016/j.physletb.2004.05.038 [hep-lat/0403001].

[4] S. Schaefer *et al.* [ALPHA Collaboration], "Critical slowing down and error analysis in lattice QCD simulations," Nucl. Phys. B **845** (2011) 93 doi:10.1016/j.nuclphysb.2010.11.020 [arXiv:1009.5228 [hep-lat]].

[5] S. Schaefer, "Status and challenges of simulations with dynamical fermions," PoS LATTICE **2012**, 001 (2012) [arXiv:1211.5069 [hep-lat]].

[6] W. Bietenholz, "Hadron Physics from Lattice QCD," arXiv:1605.08103 [hep-ph].

[7] M. Lüscher and S. Schaefer, "Lattice QCD without topology barriers," JHEP **1107**, 036 (2011) [arXiv:1105.4749 [hep-lat]].

[8] R. Brower, S. Chandrasekharan, J. W. Negele and U. J. Wiese, "QCD at fixed topology," Phys. Lett. B **560**, 64 (2003) doi:10.1016/S0370-2693(03)00369-1 [hep-lat/0302005].

[9] W. Bietenholz, I. Hip, S. Shcheredin and J. Volkholz, A Numerical Study of the 2-Flavour Schwinger Model with Dynamical Overlap Hypercube Fermions *Eur. Phys. J.* **C 72** (2012) 1938. arXiv:1109.2649 [hep-lat].

[10] W. Bietenholz and I. Hip, Topological Summation of Observables Measured with Dynamical Overlap Fermions, *PoS LATTICE2008 (2008) 079; J. Phys. Conf. Ser.* **378** (2012) 012041.

[11] S. Aoki, H. Fukaya, S. Hashimoto and T. Onogi, "Finite volume QCD at fixed topological charge," Phys. Rev. D **76**, 054508 (2007) [arXiv:0707.0396 [hep-lat]].

[12] P. de Forcrand, M. Garcia Perez, J. E. Hetrick, E. Laermann, J. F. Lagae and I. O. Stamatescu, "Local topological and chiral properties of QCD," Nucl. Phys. Proc. Suppl. **73**, 578 (1999) doi:10.1016/S0920-5632(99)85143-3 [hep-lat/9810033].

[13] W. Bietenholz, P. de Forcrand and U. Gerber, "Topological Susceptibility from Slabs," JHEP **1512**, 070 (2015) [arXiv:1509.06433 [hep-lat]].

[14] A. Dromard and M. Wagner, "Extracting hadron masses from fixed topology simulations," Phys. Rev. D **90**, no. 7, 074505 (2014) doi:10.1103/PhysRevD.90.074505 [arXiv:1404.0247 [hep-lat]].

[15] I. Bautista, W. Bietenholz, A. Dromard, U. Gerber, L. Gonglach, C. P. Hofmann, H. Mejía-Díaz and M. Wagner, "Measuring the Topological Susceptibility in a Fixed Sector," Phys. Rev. D **92**, no. 11, 114510 (2015) doi:10.1103/PhysRevD.92.114510 [arXiv:1503.06853 [hep-lat]].

[16] W. Bietenholz, C. Czaban, A. Dromard, U. Gerber, C. P. Hofmann, H. Mejía-Díaz and M. Wagner, "Interpreting Numerical Measurements in Fixed Topological Sectors," Phys. Rev. D **93**, no. 11, 114516 (2016) doi:10.1103/PhysRevD.93.114516 [arXiv:1603.05630 [hep-lat]].

[17] K. Cichy, A. Dromard, E. Garcia-Ramos, K. Ottnad, C. Urbach, M. Wagner, U. Wenger and F. Zimmermann, "Comparison of different lattice definitions of the topological charge," PoS LATTICE **2014**, 075 (2014) [arXiv:1411.1205 [hep-lat]].

[18] A. Dromard, W. Bietenholz, U. Gerber, H. Mejía-Díaz and M. Wagner, "Simulations at fixed topology: fixed topology versus ordinary finite volume corrections," Acta Phys. Polon. Supp. **8**, no. 2, 391 (2015) doi:10.5506/APhysPolBSupp.8.391 [arXiv:1505.03435 [hep-lat]].

[19] A. Dromard, W. Bietenholz, U. Gerber, H. Mejía-Díaz and M. Wagner, "Combining ordinary and topological finite volume effects for fixed topology simulations," arXiv:1510.08809 [hep-lat].

[20] A. Dromard, W. Bietenholz, K. Cichy and M. Wagner, "Computing the topological susceptibility from fixed topology QCD simulations," arXiv:1605.08637 [hep-lat].

[21] A. Athenodorou, K. Cichy, A. Dromard "Matching topological charge field definitions" ,in preparation

[22] A. Athenodorou, K. Cichy, A. Dromard, C. Urbach, U. Wenger and F. Zimmermann, "Comparison of different lattice definitions of the topological charge", in preparation

[23] K. Cichy, A. Dromard "The BCNW-method in QCD", in preparation

[24] M. E. Peskin and D. V. Schroeder, "An Introduction to quantum field theory," Reading, USA: Addison-Wesley (1995)

[25] K. Osterwalder and R. Schrader, "Axioms For Euclidean Green's Functions 1 & 2," Commun. Math. Phys. **31**, 83 (1973). Commun. Math. Phys. **42**, 281 (1975). doi:10.1007/BF01645738

[26] M. Lüscher, "Construction of a Selfadjoint, Strictly Positive Transfer Matrix for Euclidean Lattice Gauge Theories," Commun. Math. Phys. **54**, 283 (1977). doi:10.1007/BF01614090

[27] E. J. Weinberg, "Classical solutions in quantum field theory : Solitons and Instantons in High Energy Physics,"

[28] S. R. Coleman, "The Uses Of Instantons," Subnucl. Ser. **15**, 805 (1979).

[29] R. Rajaraman, "Solitons And Instantons. An Introduction To Solitons And Instantons In Quantum Field Theory," Amsterdam, Netherlands: North-Holland ( 1982)

[30] M. Nakahara, "Geometry, topology and physics," Boca Raton, USA: Taylor & Francis (2003)

[31] R. D. Peccei and H. R. Quinn, "CP Conservation in the Presence of Instantons," Phys. Rev. Lett. **38**, 1440 (1977). doi:10.1103/PhysRevLett.38.1440

[32] R. D. Peccei and H. R. Quinn, "Constraints Imposed by CP Conservation in the Presence of Instantons," Phys. Rev. D **16**, 1791 (1977). doi:10.1103/PhysRevD.16.1791

[33] E. Witten, "Current Algebra Theorems for the U(1) Goldstone Boson," Nucl. Phys. B **156**, 269 (1979). doi:10.1016/0550-3213(79)90031-2

[34] G. Veneziano, "U(1) Without Instantons," Nucl. Phys. B **159**, 213 (1979). doi:10.1016/0550-3213(79)90332-8

[35] R. Kitano and N. Yamada, "Topology in QCD and the axion abundance," JHEP **1510**, 136 (2015) doi:10.1007/JHEP10(2015)136 [arXiv:1506.00370 [hep-ph]].

[36] I. Montvay and G. Münster, "Quantum fields on a lattice," Cambridge University Press (1994)

[37] H. J. Rothe, "Lattice gauge theories: An Introduction," World Sci. Lect. Notes Phys. **43**, 1 (1992)

[38] C. Gattringer and C. B. Lang, "Quantum chromodynamics on the lattice," Lect. Notes Phys. **788**, 1 (2010). doi:10.1007/978-3-642-01850-3

[39] H. B. Nielsen and M. Ninomiya, "No Go Theorem for Regularizing Chiral Fermions," Phys. Lett. B **105**, 219 (1981). doi:10.1016/0370-2693(81)91026-1

[40] P. H. Ginsparg and K. G. Wilson, "A Remnant of Chiral Symmetry on the Lattice," Phys. Rev. D **25**, 2649 (1982). doi:10.1103/PhysRevD.25.2649

[41] R. Frezzotti *et al.* [Alpha Collaboration], "Lattice QCD with a chirally twisted mass term," JHEP **0108**, 058 (2001) [hep-lat/0101001].

[42] R. Frezzotti and G. C. Rossi, "Chirally improving Wilson fermions. 1. O(a) improvement," JHEP **0408**, 007 (2004) doi:10.1088/1126-6708/2004/08/007 [hep-lat/0306014].

[43] P. Boucaud *et al.* [ETM Collaboration], "Dynamical Twisted Mass Fermions with Light Quarks: Simulation and Analysis Details," Comput. Phys. Commun. **179**, 695 (2008) doi:10.1016/j.cpc.2008.06.013 [arXiv:0803.0224 [hep-lat]].

[44] H. Fukaya *et al.* [JLQCD Collaboration], "Two-flavor lattice QCD simulation in the epsilon-regime with exact chiral symmetry," Phys. Rev. Lett. **98**, 172001 (2007) doi:10.1103/PhysRevLett.98.172001 [hep-lat/0702003].

[45] S. Duane, A. D. Kennedy, B. J. Pendleton and D. Roweth, "Hybrid Monte Carlo," Phys. Lett. B **195**, 216 (1987). doi:10.1016/0370-2693(87)91197-X

[46] M. Wagner and C. Wiese [ETM Collaboration], "The static-light baryon spectrum from twisted mass lattice QCD," JHEP **1107**, 016 (2011) [arXiv:1104.4921 [hep-lat]].

[47] M. Kalinowski and M. Wagner [ETM Collaboration], "Strange and charm meson masses from twisted mass lattice QCD," PoS ConfinementX , 303 (2012) [arXiv:1212.0403 [hep-lat]].

[48] M. Kalinowski and M. Wagner [ETM Collaboration], "Masses of mesons with charm valence quarks from 2+1+1 flavor twisted mass lattice QCD," Acta Phys. Polon. Supp. **6**, no. 3, 991 (2013) [arXiv:1304.7974 [hep-lat]].

[49] M. Kalinowski and M. Wagner [ETM Collaboration], "Twisted mass lattice computation of charmed mesons with focus on $D^{**}$," PoS LATTICE **2013**, 241 (2013) [arXiv:1310.5513 [hep-lat]].

[50] A. Chowdhury, A. Harindranath and J. Maiti, "Open Boundary Condition, Wilson Flow and the Scalar Glueball Mass," JHEP **1406**, 067 (2014) doi:10.1007/JHEP06(2014)067 [arXiv:1402.7138 [hep-lat]].

[51] S. Mages, B. C. Toth, S. Borsanyi, Z. Fodor, S. Katz and K. K. Szabo, "Lattice QCD on Non-Orientable Manifolds," arXiv:1512.06804 [hep-lat].

[52] G. McGlynn and R. D. Mawhinney, "Diffusion of topological charge in lattice QCD simulations," Phys. Rev. D **90**, no. 7, 074502 (2014) doi:10.1103/PhysRevD.90.074502 [arXiv:1406.4551 [hep-lat]].

[53] A. Amato, G. Bali and B. Lucini, "Topology and glueballs in SU(7) Yang-Mills with open boundary conditions," arXiv:1512.00806 [hep-lat].

[54] K. Cichy, G. Herdoiza and K. Jansen, "Continuum Limit of Overlap Valence Quarks on a Twisted Mass Sea," Nucl. Phys. B **847**, 179 (2011) [arXiv:1012.4412 [hep-lat]].

[55] K. Cichy, V. Drach, E. Garcia-Ramos, G. Herdoiza and K. Jansen, "Overlap valence quarks on a twisted mass sea: a case study for mixed action Lattice QCD," Nucl. Phys. B **869**, 131 (2013) [arXiv:1211.1605 [hep-lat]].

[56] H. Fukaya, S. Hashimoto, T. Hirohashi, K. Ogawa and T. Onogi, *Phys. Rev.* **D 73** (2006) 014503. arXiv:hep-lat/0510116.

[57] W. Bietenholz, K. Jansen, K.-I. Nagai, S. Necco, L. Scorzato and S. Shcheredin, *JHEP* **0603** (2006) 017. hep-lat/0511016.

[58] F. Bruckmann, F. Gruber, K. Jansen, M. Marinkovic, C. Urbach and M. Wagner *Eur. Phys. J.* **A 43** (2010) 303. arXiv:0905.2849 [hep-lat].

[59] E. Vicari and H. Panagopoulos, "Theta dependence of SU(N) gauge theories in the presence of a topological term," Phys. Rept. **470**, 93 (2009) doi:10.1016/j.physrep.2008.10.001 [arXiv:0803.1593 [hep-th]].

[60] A.F. Atiyah and I.M. Singer, *Ann. Math.* **87** (1968) 484.

[61] L. Del Debbio, H. Panagopoulos and E. Vicari, "theta dependence of SU(N) gauge theories," JHEP **0208**, 044 (2002) doi:10.1088/1126-6708/2002/08/044 [hep-th/0204125].

[62] P. Weisz, "Continuum Limit Improved Lattice Action for Pure Yang-Mills Theory. 1.," Nucl. Phys. B **212**, 1 (1983). doi:10.1016/0550-3213(83)90595-3

[63] P. de Forcrand, M. Garcia Perez and I.-O. Stamatescu, "Topology of the SU(2) vacuum: A Lattice study using improved cooling," Nucl. Phys. B **499**, 409 (1997) [hep-lat/9701012].

[64] Y. Iwasaki, K. Kanaya, T. Kaneko and T. Yoshie, "Scaling in SU(3) pure gauge theory with a renormalization group improved action," Phys. Rev. D **56**, 151 (1997) doi:10.1103/PhysRevD.56.151 [hep-lat/9610023].

[65] A. Di Giacomo and E. Vicari, "Renormalization and topological susceptibility on the lattice," Phys. Lett. B **275**, 429 (1992). doi:10.1016/0370-2693(92)91613-E

[66] B. Berg, "Dislocations and Topological Background in the Lattice O(3) $\sigma$ Model," Phys. Lett. B **104**, 475 (1981). doi:10.1016/0370-2693(81)90518-9

[67] M. Albanese *et al.* [APE Collaboration], "Glueball Masses and String Tension in Lattice QCD," Phys. Lett. B **192**, 163 (1987). doi:10.1016/0370-2693(87)91160-9

[68] M. Lüscher, "Properties and uses of the Wilson flow in lattice QCD," JHEP **1008**, 071 (2010) Erratum: [JHEP **1403**, 092 (2014)] doi:10.1007/JHEP08(2010)071, 10.1007/JHEP03(2014)092 [arXiv:1006.4518 [hep-lat]].

[69] C. Bonati and M. D'Elia, "Comparison of the gradient flow with cooling in $SU(3)$ pure gauge theory," Phys. Rev. D **89**, no. 10, 105005 (2014) doi:10.1103/PhysRevD.89.105005 [arXiv:1401.2441 [hep-lat]].

[70] C. Alexandrou, A. Athenodorou and K. Jansen, "Topological charge using cooling and the gradient flow," Phys. Rev. D **92**, no. 12, 125014 (2015) doi:10.1103/PhysRevD.92.125014 [arXiv:1509.04259 [hep-lat]].

[71] C. Bonati, M. D'Elia, H. Panagopoulos and E. Vicari, "Change of theta dependence in 4D SU(N) gauge theories across the deconfinement transition," Phys. Rev. Lett. **110**, 252003 (2013) [arXiv:1301.7640 [hep-lat]].

[72] K. Jansen *et al.* [ETM Collaboration], "The Static-light meson spectrum from twisted mass lattice QCD," JHEP **0812**, 058 (2008) [arXiv:0810.1843 [hep-lat]].

[73] C. Michael, A. Shindler and M. Wagner [ETM Collaboration], "The continuum limit of the static-light meson spectrum," JHEP **1008**, 009 (2010) [arXiv:1004.4235 [hep-lat]].

[74] R. Baron *et al.* [ETM Collaboration], "Computing K and D meson masses with $N_f$ = 2+1+1 twisted mass lattice QCD," Comput. Phys. Commun. **182**, 299 (2011) [arXiv:1005.2042 [hep-lat]].

[75] A. Hasenfratz and F. Knechtli, "Flavor symmetry and the static potential with hypercubic blocking," Phys. Rev. D **64**, 034504 (2001) [hep-lat/0103029].

[76] M. Della Morte *et al.* [ALPHA Collaboration], "Lattice HQET with exponentially improved statistical precision," Phys. Lett. B **581**, 93 (2004) [Erratum-ibid. B **612**, 313 (2005)] [hep-lat/0307021].

[77] M. Della Morte, A. Shindler and R. Sommer, "On lattice actions for static quarks," JHEP **0508**, 051 (2005) [hep-lat/0506008].

[78] F. Bruckmann, F. Gruber, K. Jansen, M. Marinkovic, C. Urbach and M. Wagner, "Comparing topological charge definitions using topology fixing actions," Eur. Phys. J. A **43**, 303 (2010) [arXiv:0905.2849 [hep-lat]].

[79] M. Wagner, S. Diehl, T. Kuske and J. Weber, "An introduction to lattice hadron spectroscopy for students without quantum field theoretical background," arXiv:1310.1760 [hep-lat].

[80] M. Lüscher, "Volume Dependence of the Energy Spectrum in Massive Quantum Field Theories. 1. Stable Particle States," Commun. Math. Phys. **104**, 177 (1986). doi:10.1007/BF01211589

[81] J. Gasser and H. Leutwyler, "Spontaneously Broken Symmetries: Effective Lagrangians at Finite Volume," Nucl. Phys. B **307**, 763 (1988). doi:10.1016/0550-3213(88)90107-1

[82] G. Colangelo and C. Haefeli, "An Asymptotic formula for the pion decay constant in a large volume," Phys. Lett. B **590**, 258 (2004) doi:10.1016/j.physletb.2004.03.080 [hep-lat/0403025].

[83] G. Colangelo, S. Durr and C. Haefeli, "Finite volume effects for meson masses and decay constants," Nucl. Phys. B **721**, 136 (2005) doi:10.1016/j.nuclphysb.2005.05.015 [hep-lat/0503014].

[84] M. J. Teper, "Glueball masses and other physical properties of SU(N) gauge theories in D = (3+1): A Review of lattice results for theorists," hep-th/9812187.

[85] M. Bruno *et al.* [ALPHA Collaboration], "Topological susceptibility and the sampling of field space in $N_f$ = 2 lattice QCD simulations," JHEP **1408**, 150 (2014) doi:10.1007/JHEP08(2014)150 [arXiv:1406.5363 [hep-lat]].

[86] M. Lüscher, "Topology of Lattice Gauge Fields," Commun. Math. Phys. **85**, 39 (1982).

[87] C. R. Gattringer, I. Hip and C. B. Lang, "Topological charge and the spectrum of the fermion matrix in lattice QED in two-dimensions," Nucl. Phys. B **508**, 329 (1997) [hep-lat/9707011].

[88] `https://github.com/urbach/schwinger`.

[89] M. Creutz, "Quarks, gluons and lattices," Cambridge Monographs On Mathematical Physics (1983)

[90] O. Philipsen and M. Wagner, "On the definition and interpretation of a static quark anti-quark potential in the colour-adjoint channel," Phys. Rev. D **89**, 014509 (2014) [arXiv:1305.5957 [hep-lat]].

[91] K. Cichy, G. Herdoiza and K. Jansen, "Continuum Limit of Overlap Valence Quarks on a Twisted Mass Sea," Nucl. Phys. B **847** (2011) 179 doi:10.1016/j.nuclphysb.2011.01.021 [arXiv:1012.4412 [hep-lat]].